UC San Diego
UC San Diego Electronic Theses and Dissertations

Title
Hybrid Bonded Silicon Photonic and Lithium Niobate Platform for Low-voltage & High-speed Electro-optic Modulators in the Infrared to Visible Wavelengths

Permalink
https://escholarship.org/uc/item/39w118mt

Author
Valdez, Forrest Glenn

Publication Date
2023

Peer reviewed|Thesis/dissertation

eScholarship.org Powered by the California Digital Library
University of California

UNIVERSITY OF CALIFORNIA SAN DIEGO

Hybrid Bonded Silicon Photonic and Lithium Niobate Platform for Low-voltage & High-speed Electro-optic Modulators in the Infrared to Visible Wavelengths

A Dissertation submitted in partial satisfaction of the requirements
for the degree Doctor of Philosophy

in

Electrical Engineering (Photonics)

by

Forrest Glenn Valdez

Committee in charge:

Professor Shayan Mookherjea, Chair
Professor Joseph Ford
Professor James Friend
Professor George Papen
Professor Gabriel Rebeiz

2023

Copyright

Forrest Glenn Valdez, 2023

All rights reserved.

The Dissertation of Forrest Glenn Valdez is approved, and it is acceptable in quality and form for publication on microfilm and electronically.

University of California San Diego

2023

DEDICATION

To my love Juliana, for being my lifeline throughout these years.

To my brothers Aidan, Carson, and Santiago, for our unbreakable bond.

To my family, found and given, for supporting and loving me throughout my life.

EPIGRAPH

If dreams can’t come true, then why not pretend?

−Over the Garden Wall, The Blasting Company

TABLE OF CONTENTS

Dissertation Approval Page iii

Dedication iv

Epigraph v

Table of Contents vi

List of Figures ix

List of Tables xix

Acknowledgements xx

Vita xxvi

Abstract of the Dissertation xxviii

Chapter 1 1

1.1 Motivation 1
1.1.1 CMOS Compatible Electro-optic Mach-Zehnder Modulators 1
1.1.2 The Hybrid Bonded Silicon (Nitride)/Lithium Niobate Platform 4
1.2 Overview of this Dissertation 6

Chapter 2 9

2.1 Figures of Merit for Electro-Optic Mach-Zehnder Modulators 9
2.1.1 High-speed Traveling Wave Modulator Response Theory 10
2.1.2 Half-wave Driving Voltage of Lithium Niobate Mach-Zehnder Modulators 13
2.1.3 RF-Photonic Link Gain and Noise Factor 16
2.2 Hybrid Bonded Si(N)/LN MZM Design and Principle 18
2.2.1 The Optimized Si(N)/LN Cross Section 19
2.2.2 Transitioning Between the Feeder and Hybrid Modes 29
2.2.3 Edge Couplers 35
2.2.4 Single Mode Feeder Waveguides 37
2.2.5 2x2 MMI Couplers 38
2.3 SiN/LN Modulators with CMOS-compatible Buried Electrode Layers 41
2.4 A SiN/LN Platform for Low-Voltage Modulators from the Visible to Telecom Wavelengths 43
2.5 Acknowledgments 49

Chapter 3 51

3.1 Coplanar Waveguides 51
3.2 Slow-wave Electrodes for High-speed Modulation 57
3.3 Modelling the EO Response with CPW and SWE Traveling Wave Electrodes .. 62
3.4 SWE Impact on $V_{\pi}L$? 65
3.5 Acknowledgments 67

Chapter 4 68

4.1 Fabrication of Si/LN Photonic Chips 68
4.2 Fabrication of SiN/LN Photonic Chips 72
4.3 Passive Feature Characterizations 75
4.4 Acknowledgments 79

Chapter 5 80

5.1 High-speed SWE Electrical Characterization 86
5.2 Si/LN On-chip Insertion Loss 89
5.3 High-speed Si/LN EO Response 90
5.4 Low-speed $V_{\pi}L$ Measurements 93
5.5 O-band and C-band Si/LN EOM Comparison 96
5.6 RF Impedance Mismatch 98
5.7 Integrated O-band and C-band Si/LN MZMs Summary 101
5.8 Acknowledgments 102

Chapter 6 103

6.1 Introduction 103
6.1 High Optical Power Handling: Theory 104
6.2 High Optical Power Handling: Measurements 109
6.3 High Optical Power Handling: Discussion 116
6.4 Acknowledgments 123

Chapter 7 124

7.1 High-speed O-band SiN/LN MZM Characterization 124
7.2 Acknowledgments 130

Chapter 8 131

8.1 Introduction 131
8.2 BE vs TE SiN/LN: Comparison of RF Design 132
8.3 BE vs TE SiN/LN: Comparison of EO Operation 134
8.2 Acknowledgments 137

Chapter 9 139

9.1 Introduction 139
9.2 NIR SiN/LN EO Measurement Results 142

9.3 NIR SiN/LN Discussion 146
9.4 Acknowledgments 149

Chapter 10 150

10.1 DC Bias Drift: Preliminary Study and Observations 151
10.2 Integration of Hybrid MZMs with Silicon Photonic Devices 158
10.2.1 Integrated High Quality Factor Microrings 158
10.3 A Design for Si/LN EO Modulators Integrated with Lasers 161
10.4 Acknowledgments 164

Appendix A 166

A.1 Half-wave Voltage-length Derivation 166

Appendix B 171

B.1 Measuring the Modulator Response using an OSA 171
B.2 Measuring the Modulator Response using a Sampling Oscilloscope 175
B.3 RF Power Calibrations 177
B.4 Acknowledgments 180

Bibliography 182

LIST OF FIGURES

Figure 1.1: Cross sections of LN waveguides fabricated via (a) proton exchange on bulk LN substrates (b) etched TFLN (c) deposited materials on LNOI and (d) hybrid bonded TFLN to SOI rib-waveguides. 5

Figure 2.1: A top-view diagram of an EOM modulating a continuous wave (CW) laser input with push-pull traveling wave electrodes driven by an RF source and terminated with a load impedance, Z_L. 10

Figure 2.2: The calculated 3-dB bandwidth vs MZM V_π (inverse to L_{ps}) using Eq. (2.1) assuming the MZM is RF-loss limited (i.e, $\Delta n = 0\%$ and $Z_c = Z_L = 50\ \Omega$) for different values of $\alpha_m(f = 110\text{ GHz})$. The assumed $V_\pi L$ of this MZM is 2.86 V.cm. 13

Figure 2.3: The simulated (a) RF CPW mode $|E_{RF}|^2$ at 100 GHz and (b) hybrid optical mode $|E_o|^2$ at 1550 nm for a SiN/LN cross section using Lumerical Mode Solutions. 14

Figure 2.4: The simulated $V_\pi L$ (blue, left y-axis) and α_{opt} (orange, right y-axis) of a SiN/LN MZM with h_{LN} = 400 nm (solid traces) and a Si/LN with h_{LN} = 600 nm (dashed traces) as a function of electrode gap, G. In this example, the SiN waveguide is 900 nm wide by 200 nm thick, the Si waveguide is 225 nm wide by 150 nm thick, h_{cmp} is 50 nm. 15

Figure 2.5: (a) A block diagram of a generalized RF-photonic link with an external MZM. (b) A diagram of an MZM transfer function (black curve) biased at quadrature with via an external DC voltage bias (V_b). An RF signal (blue curve) drives the device in the small-signal regime which modulates the optical signal (red curve). 16

Figure 2.6: (a) Singulation of the SOI and LNOI dies. The SOI is patterned with photonic waveguide features while the LNOI is unpatterned and unetched. (b) An example of the hybrid bonded Si/LN EO chip with multiple MZM structures and passive integrated Si photonic components. (c) A diagram (not to scale). 18

Figure 2.7: (a) The cross section diagram of the Si(N)/LN MZM with electrodes above the bonded TFLN layer. G: electrode gap. h_{cmp}: CMP oxide thickness. h_{box}: Buried oxide thickness. h_{LN}: LN film thickness. h_e: electrode thickness. w_s: signal electrode width. $w_{Si(N)}$: the Si(N) waveguide width. $h_{Si(N)}$: the Si(N) waveguide thickness. (b). 19

Figure 2.8: The simulated (a) n_{eff}, (b) A_{eff}, and (c) Γ_{LN} of a Si/LN hybrid mode as a function of Si waveguide dimensions with a TFLN thickness of 600 nm at λ = 1550 nm. The simulated (d) n_{eff}, (e) A_{eff}, and (f) Γ_{LN} of a SiN/LN hybrid mode as a function of SiN waveguide dimensions with a TFLN thickness of 200 nm at λ = 1550 nm. 22

Figure 2.9: (a,b) The simulated FoM [Eq. (2.13)] of a hybrid Si/LN mode operating at (a) 1550 nm and (b) 1310 nm as a function of Si waveguide width and CMP oxide thickness when h_{Si} = 150 nm, h_{LN} = 600 nm, G = 8 μm. (c,d) The simulated FoM of a hybrid SiN/LN mode operating at (a) 1550 nm and (b) 1310 nm as a function of Si. 24

Figure 2.10: The simulated (circles) and fitted (lines) data of the fraction $R = \Gamma mo \Gamma LN$ as the electrode gap distance, G, and h_{LN} are varied for a (a) hybrid Si/LN and (b) SiN/LN cross section with h_{cmp} = 0 nm, λ = 1550 nm, and f_{RF} = 100 GHz. 25

Figure 2.11: (a) The simulated $V_{\pi}L_{app}$ as a function of Si waveguide width and CMP oxide thickness at λ = 1550 nm. (b) The simulated $V_{\pi}L_{app}$ as a function of Si waveguide width and CMP oxide thickness at λ = 1310 nm. The constant parameters of the Si/LN waveguide are h_{Si} = 150 nm, h_{LN} = 600 nm, G = 8 μm, and. (c) The. 26

Figure 2.12: (a) The simulated α_{opt} as a function of Si waveguide width and CMP oxide thickness at λ = 1550 nm. (b) The simulated α_{opt}, as a function of Si waveguide width and CMP oxide thickness at λ = 1310 nm. The constant parameters of the Si/LN waveguide are h_{Si} = 150 nm, h_{LN} = 600 nm, G = 8 μm, and. (c) The simulated α_{opt} 27

Figure 2.13: (a) The simulated n_g as a function of Si waveguide width and CMP oxide thickness at λ = 1550 nm. (b) The simulated n_g as a function of Si waveguide width and CMP oxide thickness at λ = 1310 nm. The constant parameters of the Si/LN waveguide are h_{Si} = 150 nm, h_{LN} = 600 nm, G = 8 μm, and. (c) The simulated n_g 29

Figure 2.14: Top-view schematic (not to scale) of the Si/LN transition region and phase shifter (one arm of MZM). The transition region consists of the transition waveguide and adiabatic tapers (shown in green), and the phase shifter section consists of the hybrid waveguide (shown in red). Cross-sectional simulated Poynting vector of the (b) 30

Figure 2.15: (a) A side-view (not to scale) of the Si/LN transition across the bonded region with an adiabatic taper section to the hybrid mode. The simulated S-parameters (transmission and reflection) as a function of (b) taper length and (c) number of modes per cell in the taper section for operation wavelengths at 1550 nm (C) and 1310 nm (O). 31

Figure 2.16: (a) A perspective view of a single layer SiN waveguide transitioning across the bonded MgO:LN film. (b) The simulated interface loss due to mode and neff mismatch at the Air-LN interface as a function of SiN waveguide width and LN film thickness for an operation λ of 1550 nm. The SiN thickness is 200 nm. (c). 32

Figure 2.17: (a) A side-view diagram of the proposed single layer SiN/LN transition with a deposited cladding oxide before the bonded region. (b) A top-view diagram of the proposed single layer SiN/LN transition. The simulated $|S_{21}|^2$ of the transition shown in panel (a) for 1310 nm (blue) and 1550 nm (red) operational wavelengths. 34

Figure 2.18: The simulated edge coupling loss (per facet) as a function of taper tip width for (a) a single layer Si waveguide that is 150 nm thick and (b) a single layer SiN waveguide that is 200 nm thick at different operational wavelengths. 36

Figure 2.19: (a) A cross section of the Si feeder waveguide section with 150 nm thick Si clad with SiO_2. The simulated n_{eff} as of the cross section in panel (a) as a function of Si waveguide (WG) width at (b) λ = 1550 nm and (c) λ = 1310 nm, showing the guided modes. (d) A cross section of the SiN feeder waveguide section with. 38

Figure 2.20: (a) A top-view schematic of a 2x2 MMI coupler of width W_{mmi}. (b) The simulated L_{3dB} (left, blue) and total loss at the output ports (right, orange) as a function of W_{mmi} at λ = 1550 nm. (c) The simulated L_{3dB} (left, blue) and total loss at the output ports (right, orange) as a function of W_{mmi} at λ = 1310 nm. (d) A top-view power. 40

Figure 2.21: (a) A top-view schematic of the angled 2x2 MMI coupler. (b) FDTD simulations of the power reflected to the input ports (1 and 2) of the angled 2x2 MMI designed in the O-band. 41

Figure 2.22: (a) A cartoon cross-section of a SiN/LN MZM which uses buried electrodes (M1 CMOS layer) as opposed to Au electrodes patterned above the LN film. There is an additional layer of oxide (labelled h_{buff}) between the buried metal and the SiN waveguides. (b) The simulated hybrid optical mode at λ = 1550 nm. (c). 42

Figure 2.23: The simulated $V_{\pi}L$ as a function of electrode gap spacing, G, and hbuff of the cross-section in Fig for (a) l = 1550 nm and (b) l = 1310 nm. The simulated α_{opt} as a function of G and h_{buff} of the cross-section in Fig for (a) λ = 1550 nm and (b) λ = 1310 nm. The assumed constants are w_{SiN} = 900 nm, h_{SiN} = 200 nm,. 43

Figure 2.24: The simulated optical modes of the SiN/LN phase-shifter section at the following operation wavelengths: (a) 1550 nm, (b) 1310 nm, (c) 775 nm, and (d) 633 nm. The MgO:LN film thickness is 200 nm and the SiN waveguide is 900 nm wide by 180 nm thick for all four simulations. The simulated n_{eff}, A_{eff}, and Γ_{LN} are inset. 45

Figure 2.25: The simulated $V_{\pi}L$ of SiN/LN MZMs designed for the following operation wavelengths with different G: (a) 1550 nm, (b) 1310 nm, (c) 775 nm, and (d) 633 nm. The MgO:LN film thickness is 200 nm and the SiN waveguide is 900 nm wide by 180 nm thick for all four panels. 46

Figure 2.26: The simulated α_{opt} of SiN/LN MZMs designed for the following operation wavelengths and different G: (a) 1550 nm, (b) 1310 nm, (c) 775 nm, and (d) 633 nm. The MgO:LN film thickness is 200 nm and the SiN waveguide is 900 nm wide by 180 nm thick for all four panels. The dashed horizontal lines correspond to an α_{opt}. 47

Figure 2.27: The simulated n_g of SiN/LN MZMs designed for the following operation wavelengths: (a) 1550 nm, (b) 1310 nm, (c) 775 nm, (d) 633 nm. The MgO:LN film thickness is 200 nm and the SiN waveguide is 900 nm wide by 180 nm thick for all four simulations. 48

Figure 2.28: The simulated n_{eff} of the first three guided modes of a 200 nm thick SiN feeder waveguide clad in 2 mm of SiO2 at (a) λ = 775 nm and (b) λ = 633 nm. A cross section of the waveguide is in Figure 2.19(d). 49

Figure 3.1: The simulated (a) n_m, (b) Z_c, and (c) α_m as a function of electrode gap distance, G, and signal width, w_s, when f_{RF} = 100 GHz, h_{LN} = 600 nm, h_{BOx} = 2 µm, he = 1 µm for a Si/LN cross section with an HR-Si substrate. The dashed line is panel (a) corresponds to an example n_g of 2.252. The dashed line in panel (b) corresponds to. 52

Figure 3.2: An example of a simulated CPW mode at 100 GHz for a Si/LN MZM cross section from EMPro. The color of the vector points correspond to the E_{RF} magnitude and the arrow dictates the direction. The green arrow in between the electrodes is an 'impedance line' defined in EMPro to guide the solver in finding the CPW mode..... 53

Figure 3.3: The simulated (a) $n_m(f)$, (b) $Z_c(f)$, and (c) $\alpha_m(f)$ assuming three different Si substrate resistivities. 54

Figure 3.4: The simulated (a) n_m, (b) Z_c, and (c) α_m of a SiN/LN MZM phase shifter using buried electrodes (see Figure 2.24(a) for cross section) of varying thickness from 1 GHz to 150 GHz. The assumed cross-sectional parameters are h_{LN} = 200 nm, G = 4 um, w_s = 12 um, h_{BOx} = 3 um, and h_{buff} = 250 nm. 56

Figure 3.5: The calculated 3-dB bandwidth vs V_π of SiN/LN MZMs using buried electrodes at (a) 1550 nm operational wavelength and (b) 1310 nm operational wavelength. The different traces correspond to different thicknesses of electrode, h_e. The assumed cross-sectional parameters are h_{LN} = 200 nm, G = 4 um, w_s = 12 um, h_{BOx}. 57

Figure 3.6: A top-view layout of the (a) Slot SWE and (b) T-rail SWE with G-S-G probing pads with 100 μm pitch and 100 μm tapers to the main phase shifting section. The zoomed in diagrams detail the (a) Slot and (b) T-rail parameters of the periodic unit cells...... 59

Figure 3.7: The simulated n_m as a function of SWE parameters (a) t and (b) h for T-rail and Slot structures at 110 GHz. The other T-rail parameters are L = 30 μm, t = 6 μm, c = 2 μm, w = 5 μm, G = 8 μm, and w_s = 55 μm. The other parameters for the Slot SWE are L = 24 μm, t = 24 μm, c = 2 μm, w = 5 μm, G = 8 μm, and w_s = 55 μm. 62

Figure 3.8: The simulated RF (a) n_m, (b) Z_c, and (c) α_m for a Si/LN MZM with Slot SWEs (L = 20 μm, t = 20 μm, h = 4 μm, w = 5 μm, G = 9 μm) and 600 nm TFLN. The dashed line in panel (a) corresponds to the simulated n_g of a Si/LN mode at 1550 nm. (d) The calculated EO response using the results of panels (a)-(c) assuming. 63

Figure 3.9: (a)-(c) The simulated RF characteristics of a SiN/LN MZM with buried T-rail (blue to red λs) and Slot (λ = 775 nm) electrodes (250 nm below the SiN waveguides). (d) The calculated 3-dB bandwidth as a function of V_π (inverse phase shifter length) for the visible to NIR wavelength designs resulting in greater than 100 GHz speeds............ 65

Figure 3.10: (a) A perspective-view of a T-rail unit cell being discretized along the propagation direction. The numbers correspond to the labelled numbers for the (b) calculated VpL as a function of distance along the unit cell. 67

Figure 4.1: The interpolated CMP oxide thickness contour maps of three SOI wafers with single layer Si features after planarization based on ellipsometer measurements (red 'x's). The dashed lines correspond to the individual reticle areas, totaling 26 reticles per wafer. The average CMP oxide thickness is (a) 40 nm, (b) 28 nm, and (c) 40 nm...... 69

Figure 4.2: The fabrication process flow of the hybrid bonded Si/LN EOM chips. 70

Figure 4.3: A photograph of a hybrid bonded Si/LN photonic chip with a section dedicated to hybrid bonded MZMs and a section dedicated to standard Si photonic components. . 72

Figure 4.4: A cross-section of the hybrid bonded SiN/LN MZM showing that the traveling wave electrodes can be formed with the buried metal layer (M1) during the SOI wafer development, or post-fabricated using a gold layer above the bonded LN surface. 73

Figure 4.5: The interpolated contour maps of the (a) buffer oxide thickness, (b) SiN layer thickness, and (c) CMP oxide layer thickness based on ellipsometer measurements (red 'x's) of the 8-inch SiN wafer with buried metal. (d) The 25.4 mm by 30.8 mm reticle layout for the SiN MZMs and passive structures. The purple shaded.............. 74

Figure 4.6: Examples of the hybrid bonded SiN/LN photonic chips with (a) 0.5 cm long phase-shifters and (b) 1.0 cm long phase-shifters.. 75

Figure 4.7: (a) The normalized measured passive optical transmission as a function of laser l for a Si/LN asymmetric MZM (no voltage bias applied) showing a 30 dB ER. (b) The normalized transmission of cutback waveguides of varying length to determine the linear absorption loss of the feeder Si waveguides (650 nm wide by 150. 77

Figure 4.8: (a) The measured passive transmission of the Thru (blue trace) and Cross (orange trace) ports of an asymmetric SiN/LN MZM before edge polishing. (b) The measured passive transmission of the Thru (blue trace) and Cross (orange trace) ports of a symmetric SiN/LN MZM before edge polishing. (c) The optical............................... 78

Figure 5.1: (a) A perspective-view schematic (not to scale) of the hybrid bonded Si/LN 82

Figure 5.2: (a) An SEM image of a T-rail SWE design used in this work with the SWE parameters labelled. (b) The top-view schematic of the periodic inductively loaded slot feature with slow-wave design parameters used for devices CN and ON. (c) The top-view schematic of the periodic capacitively loaded T-rail feature used for the................... 84

Figure 5.3: (a) A block diagram of the RF S-parameter measurements using a Keysight 2-port PNA-X and frequency extenders to measure from 100 MHz to 118 GHz. The measured S-parameters of the 1.0 cm and 0.54 cm long SWEs with the following designs: (a) T-rail and G = 6 μm, (b) T-rail and G = 7 μm, and (c) Slot and.............. 87

Figure 5.4: The extracted RF characteristics of each of the SWE devices from the measured S-parameters. (a) RF effective index of the four 1.0 cm long SWEs. (b) RF propagation loss of each of the four 1.0 cm long SWEs. (c) RF driving impedance of each of the four 1.0 cm long SWEs. (d) RF effective index of the four 0.54 cm long SWE.......... 89

Figure 5.5: The measured (blue) and modelled (red) EO responses of the hybrid bonded Si/LN MZMs designed for C-band. (a) T-rail SWE with G = 7 μm and L = 0.54 cm. (b) T-rail SWE with G = 7 μm and L = 1.0 cm. (c) Slot SWE with G = 8 μm and L = 0.54 cm. (d) Slot SWE with G = 8 μm and L = 1.0 cm... 91

Figure 5.6: The measured (blue) and modelled (red) EO responses of the hybrid bonded Si/LN MZMs designed for O-band. (a) T-rail SWE with G = 6 μm and L = 0.54 cm. (b) T-rail SWE with G = 6 μm and L = 1.0 cm. (c) Slot SWE with G = 8 μm and L = 0.54 cm. (d) Slot SWE with G = 8 μm and L = 1.0 cm. 92

Figure 5.7: (a) A block diagram of the V_π measurement of the Si/LN MZMs using sinusoidal frequencies from a waveform generator. The modulated signals were detected with a photodetector (PD: Newfocus 1611-FC). (b) The applied electrical signal (orange trace) and the modulated signal (blue trace) were monitored with 93

Figure 5.8: The measured normalized optical power as a function of applied voltage to the hybrid bonded Si/LN MZMs for (a) CW MZMs with G = 7 μm. (b) CN MZMs with G = 8 μm, (c) OW MZMs with G = 6 μm, (d) and ON MZMs with G = 8 μm. The blue traces correspond to the 0.54 cm long modulators and the red traces. 94

Figure 5.9: The calculated RF V_π as a function of driving frequency using Eq. (5.1) for the following Si/LN MZMs: (a) CW MZMs with G = 7 μm. (b) CN MZMs with G = 8 μm, (c) OW MZMs with G = 6 μm, (d) and ON MZMs with G = 8 μm. The blue traces correspond to the 0.54 cm long modulators and the red traces. 96

Figure 5.10: Summary bar graphs of the measured (a) $V_\pi L$, (b) 3-dB bandwidth (BW), (c) EO S_{21} slope (from 10 GHz to 110 GHz), and (d) 3-dB BW-to-V_π ratio for the hybrid bonded Si/LN C-band and O-band MZMs of the fabricated chip. 97

Figure 5.11: The measured (blue) EO responses of the hybrid bonded Si/LN MZMs designed for: (a) O-band, Slot SWE with G = 8 μm and L = 1.0 cm. (b) C-band, Slot SWE with G = 8 μm and L = 1.0 cm. (c) O-band, Slot SWE with G = 8 μm and L = 0.54 cm. (d) C-band, Slot SWE with G = 8 μm and L = 0.54 cm. The red. 100

Figure 5.12: The measured (solid) and modelled (dashed) EO response normalized to 0.1 GHz for the ON devices with 8 μm gap slot SWEs. 101

Figure 6.1: The simulated n_{eff} (top) of the first three modes of the Si/LN hybrid waveguide and confinement factor (bottom) in the LN film (blue) and Si waveguide (red) regions as a function of Si waveguide width. 106

Figure 6.2: (a) The calculated IL due to TPA as a function of peak optical power in the hybrid waveguide mode (solid) and the transition mode (dashed) assuming different lengths. (b) The change in refractive index due to additional carriers generated via TPA as a function of peak optical power for different waveguide widths. (c). 107

Figure 6.3: (a) An optical microscope image of the hybrid bonded Si/LN chip with gold SWEs used for high optical power modulation measurements with short feeder sections. (b) A stitched optical microscope image of the 5 mm long SWE. (c) A scanning electron microscope image of the inductively loaded slot features of the SWE. 109

Figure 6.4: A photograph of the hybrid bonded MZM EO test station. 110

Figure 6.5: (a) The measured passive (no voltage applied) transmission of the asymmetric Si/LN MZM in the C-band. (b) The block diagram of the V_π measurement for the Si/LN MZM using a pulse pattern generator to drive the device. (c) An example of the trapezoidal driving signal (blue dashed trace) and the measured. 111

Figure 6.6: A (not to scale) schematic of the hybrid bonded Si/LN MZM showing the total measured insertion loss and the loss attributed to the edge coupler (EC), transition, hybrid, and phase shifter sections. 113

Figure 6.7: A schematic block diagram of the quasi-CW high power electro-optic response measurement setup. Active RF multipliers were used for generating f > 50 GHz. PM-EDFA: Polarization Maintaining Erbium Doped Amplifier. VOA: Variable Optical Attenuator. 114

Figure 6.8: The OSA-measured (blue points) EOR of the hybrid bonded Si/LN MZM with Lps = 0.5 cm using no RF multiplier (circles), a 4x multiplier (diamonds), and a 6x multiplier (squares) resulting in a measured 3-dB bandwidth of 110 GHz for both: (a) Low power, CW optical input with 4 mW of power; and (b). 116

Figure 6.9: (a) Stitched IR camera images (20x objective) of the propagating light through the damaged Si/LN MZM after 150 mW of peak on-chip optical power was coupled. Large scattering before the TFLN edge (dashed line) indicates the points of damage. (b) The optical transmission measurements as a function of laser. 121

Figure 6.10: (a) An IR camera image of the input edge coupler of a Si/LN MZM that has experienced optically induced damage which causes large amounts of scattering (encircled). (b) An IR camera image of the other port of the Si/LN MZM which has not experienced damage and propagates the light to the device. 122

Figure 7.1: (a) A digital camera image of the fabricated SiN/LN bonded MZM chip. (b) Passive normalized transmission measurements of the hybrid EOM (b) asymmetric and (c) symmetric devices in the O-band with (red dotted lines) and without (blue solid lines) voids. 126

Figure 7.2: The measured normalized optical power as a function of applied voltage using a pulse pattern generator at 1310 nm, resulting in a voltage-driven ER of 25 dB and a V_π of 2.9 V for the 0.93 cm long phase-shifter. The blue trace is a cosine-squared fit to the data (black circles). 127

Figure 7.3: A block diagram detailing the different equipment used to measure the EO modulator response from 1 to 110 GHz of a SiN/LN MZM designed for wavelengths in the O-band. For frequencies greater than 10 GHz the OSA method can be used to track the modulated sideband peaks. For frequencies less than 10 GHz 128

Figure 7.4: Measured EO response of the 0.93 cm long SiN-LN MZM referenced to the 1 GHz value using a high-speed sampling oscilloscope (blue stars), an OSA (red circles), and active multipliers (yellow diamonds and purple squares). 129

Figure 8.1: The simulated (a) RF effective index, n_{RF}, (b) RF loss, and (c) characteristic impedance of a SiN-LN MZM with buried electrodes (BE) CPW structure (solid) and top Au electrodes (TE) using standard CPW structures (dotted line) and a SWE structure (dashed line). The dash-dot black line in (a) corresponds. 132

Figure 8.2: A top-view schematic of the (a) BE CPW MZM and (b) TE SWE MZM. (c) A stitched optical microscope image showing the 0.5 cm long SiN-LN MZM with buried M1 electrodes. (d) A stitched optical microscope image showing the 0.4 cm long SiN-LN MZM with top Au electrodes. 134

Figure 8.3: The normalized measured optical power (black) as a function of applied voltage when driven with a 100 kHz trapezoidal waveform for the (a) BE and (b) TE SiN/LN devices. The electro-optic response (referenced to 1 GHz) of the (c) BE and (d) TE SiN/LN devices. 136

Figure 9.1: (a) A top-view schematic of the hybrid bonded SiN-TFLN modulator (not to scale). (b) The simulated n_g, and Γ_{LN} as a function of the SiN waveguide width. The vertical dot-dashed red line corresponds to the mode shown in panel (e). The horizontal dashed black line corresponds to the simulated RF index at 110 GHz. 140

Figure 9.2: (a,b) The normalized optical power measured as a function of applied voltage for the hybrid MZM with length 0.4 cm [panel (a)] and 0.8 cm [panel (b)]. The solid lines are fits to the data using the squared-cosine functional form, which yields V_π. (c) A magnified portion of the data in panel (b) with a logarithmic 143

Figure 9.3: (a) Schematic for measurement of the EO response. (b,d) EO response measurements over 1 to 110 GHz of a hybrid TFLN-SiN MZM with phase-shift length 0.4 cm and 0.8 cm, respectively. The four colors for the data points represent the four RF measurement bands as described in the text. Each trace is. 144

Figure 9.4: (a) A block diagram of the high-speed serial PRBS-15 data measurement using the NIR SiN/LN MZM. (b) The measured eye diagram from a PRBS-15 signal at 25 Gbps with no precompensation or signal processing. 145

Figure 9.5: Scatter plot of 3-dB EO Bandwidth (GHz) versus half-wave voltage (V) for various MZM devices with slope lines at 1, 10, 50 and 100 GHz/V indicated. The correspondence between the numerical labels for the data points and the citation-list numbers is provided in Table 9.1. Labels 1 and 2 are this work. 146

Figure 10.1: A cross-sectional example of an integrated system with a suspended optical isolator, III-V/Si quantum well laser, hybrid SiN/LN MZM, and Ge photodetector. 151

Figure 10.2: A schematic block diagram showing the measurement of the DC bias drift of a hybrid bonded Si(N)/LN MZM using a high-speed bias-t and a programmable DC bias source. The modulated signals are monitored using the OSA method described in Appendix B.1 152

Figure 10.3: (a) The applied DC bias voltage as a function of time. It is stepped from 0 V to 5 V in 1 V increments and held for 2 minutes before each consecutive step. V_{dc} = 5 V is held for the remainder of the measurement. (b) The tracked carrier signal peak as a function of time. From 630 seconds onward, the variation in Pc is from. 153

Figure 10.4: The same measured ϕ from Figure 6.2(f) but zoomed into the 'hold' regime (V_{dc} = 5 V for 3000 s). There is an initial overshoot in ϕ in the first 4.5 minutes from changing the bias from 4 to 5 V (seen in every step). Then ϕ is stable at 1.0 ± 0.01 radian for 12 minutes before decaying by 0.2 radians over a span of 12 minutes. 154

Figure 10.5: The flow-chart diagram of the Si(N)/LN MZM DC bias drift control using an OSA to monitor the modulated sidebands and resulting phase. 156

Figure 10.6: (a) The applied DC voltage and (b) extracted phase as a function of time to the symmetric SiN/LN MZM under test. First a coarse voltage sweep is done to map out the MZM transfer function (blue data points). Then a finer sweep (red data points) is performed around the quadrature point (3.5 V to 5 V in this case) 157

Figure 10.7: (a) The applied DC voltage and (b) extracted phase as a function of time to the symmetric SiN/LN MZM under test. First a coarse voltage sweep is done to map out the MZM transfer function (blue data points). Then a finer sweep (red data points) is performed around the quadrature point (3.5 V to 5 V in this case) 158

Figure 10.8: (a) Schematic representation of a hybrid bonded thin-film MZM integrated with microring resonator based filters. (b) The measured transmission of a three stage second-order coupled microring filter cascaded with a ring resonator and symmetric hybrid bonded MZI fabricated using 150 nm thick Si waveguides........................... 160

Figure 10.9: A fabrication process flow for integrating hybrid Si/LN EO modulators with hybrid Si/III-V gain sections with the same single layer patterned SOI............................... 162

Figure 10.10: The simulated (a) n_{eff}, (b) n_g, (c) α_{opt}, and (d) Γ_{LN} of the fundamental TE_0 and TM_0 Si/LN hybrid modes as a function of Si waveguide width. The waveguide thickness is 250 nm, LN film is 400 nm, G = 4 μm, and λ = 1550 nm for these calculations. 163

Figure 10.11: (a) The simulated Si/LN hybrid mode cross-sectional |E|2 with a 250 nm wide by 250 nm thick Si waveguide, 400 nm thick LN film, Au electrodes spaced 4 μm apart, operating at λ = 1550 nm. The simulated (b) Γ_{LN}, Γ_{mo} and Γ_{Si}, (c) α_{opt}, and (d) $V_\pi L$ as a function of G. 164

Figure B.1: The measured spectra of a 1550 nm Si/LN MZM being modulated with tones from 1 to 50 GHz in 1 GHz steps (overlaid) using a high-resolution OSA. Modulating at f_{RF} GHz generates first-order sidebands at $\pm f_{RF}$ from the carrier frequency (f_c). Each color pair represents one modulation tone. The black circles are the peak. 173

Figure B.2: An example of the measured spectrum using an low resolution OSA (Ando AQ6317B) showing the first sideband o carrier ratio (FSCR) and second-sideband to carrier ratio (SSCR) which were generated by modulating a SiN/LN MZM at 100 GHz. 175

Figure B.3: Time domain method block diagrams for measuring the frequency response of (a) MZMs operating in the O-band and (b) MZMs operating in the NIR. PD: Photodetector, DFB: Distributed Feedback Laser, BOA: Optical Amplifier. 176

Figure B.4: The modulated optical waveforms measured with a high-speed photodetector and sampling oscilloscope when driven with sinusoidal tones at the following frequencies: (a) 1 GHz, (b) 10 GHz, (c) 20 GHz, and (d) 30 GHz. 177

Figure B.5: The RF connection setups for high-speed frequency measurements of EO modulators in the (a) 1 – 50 GHz range and (b) 47 – 111 GHz range using 110 GHz rated G-S-G RF probes with 1.0 mm connectors (Picoprobe 110H). P_I (input RF power) is defined as the RF power before the input-side probe and P_{chip}. 178

Figure B.6: The measured RF power output from the (a) X4 and (b) X6 active RF multipliers as a function of their respective frequency ranges at various input RF powers. When the RF input power is greater than 0 dBm the output is more stable with frequency. 179

Figure B.7: The RF power delivered to the chip under test (P_{chip}) as a function of frequency for the four different measurement configurations in (a) Figure B.5(a) with an RF input power setting of -3 dBm, (b) Figure B.5(a) with an RF input power setting of 15 dBm, (c) Figure B.5(c) with an RF input power setting of 3 dBm, and (d) 180

LIST OF TABLES

Table 2.1: The Si(N) waveguide dimensions chosen for fabrication in the hybrid phase-shifter section of the MZMs at the O- and C-bands. 29

Table 5.1: The Si/LN MZM design parameters for the O-band and C-band structures on the chip 86

Table 6.1: Comparison of recent TFLN-based MZM Performance Metrics 118

Table 9.1: References for data points in Figure 9.5. 148

ACKNOWLEDGEMENTS

First and foremost, I would like to sincerely thank my advisor Professor Shayan Mookherjea for his guidance throughout the many years of my university experience at UCSD. I am incredibly grateful for his support, his patience in me, and for all the rewarding discussions we have had. I believe Shayan is one of the greatest teachers I have had the pleasure of meeting. It is a great honor to graduate from his group and I am truly happy to have been given this opportunity to be a part of his group.

I would also like to thank Professor George Papen and Professor Saharnaz Baghdadchi for their mentorship and always having their doors open to me for quick discussions about photonics and for advice. They gave me the opportunity to teach as a Teaching Assistant which I truly enjoyed. And a special thanks to Sahar for pushing me to go out of my comfort zone and become more involved with the SPIE student chapter.

I would like to sincerely thank all my fellow integrated photonics groupmates over the years: Dr. Peter O. Weigel, Dr. Hannah R. Grant, Dr. Chaoxuan (Ellen) Ma, Dr. Jie Zhao, Dr. Michael Rusing, Dr. Xiaoxi (Josh) Wang, Dr. Viphretuo Mere, Mr. Reed Rouland, Mr. Ferrill Rushton, and Mr. Carson Valdez. I had an absolutely wonderful time having the privilege to work with such amazing people. Thank you to Peter for the initial groundwork he had put in to developing the hybrid bonded Silicon/Lithium Niobate platform. He helped me get started in modelling the devices we would end up fabricating. I am grateful to Hannah for her mentorship when I was an undergraduate just getting started in Photonics as my TA. She always made time for me whenever I was confused and had questions. She continued to be a

great friend and gave support when I joined the group and took over her role as a Photonics TA. A very special thanks go to Josh and Viphretuo, without them I would not be where I am today. Josh taught me everything I know about being an experimentalist. There was a time when I would have to bug Josh every time I was about to start a measurement to make sure my plan was sound. He has instilled a confidence in me that was not there before. And without Viphretuo, this work would not exist! I am incredibly grateful to him for the countless hours that he has spent in the cleanroom fabricating the devices I have designed. I truly enjoy working with Viphretuo, he makes being in the lab a fun experience as we share music, videos, and ideas. Viphretuo has made these last few years of my graduate studies a joy and I am grateful to have him as a friend and colleague.

A very special thank you to my favorite groupmate (nepotism always wins), my brother Carson. I was overjoyed when you moved to San Diego, you made this place feel like home. It was a dream come true to be able to work with you. I have always thought you have the most potential of us four to do great things, and I still do. If I can somehow make it through this, you will breeze through these next few years no problem. I am so proud of you, and I hope we can continue to work together in the future.

Thank you to the Sandia National Laboratories team led by Dr. Anthony Lentine for supporting my doctoral work. I would like to particularly thank Tony for his kindness and support through our many discussions we have had over the years. I would also like to thank Dr. Nicholas Boynton for his help and always open ear for discussion anytime I requested.

Thank you to our collaborators at Keysight Technologies, namely, Dr. Chris Coleman, Dr. Ryan Scott, Dr. Greg Lee, Dr. Bogdan Szafraniec, Dr. Greg Vanwiggeren, Dr. Valentina Moskalenko, and Dr. Kamal Khalil Abdelsalam, for the many years of insightful discussions

and support. In particular, I would like to thank Chris and Greg. They were always available to offer advice whenever I had questions. Greg shared with me his insights and knowledge of high-speed RF modelling which I used to design my devices. I am greatly appreciative of Chris for his many invitations to visit them, his hospitality, and his aid in measuring our fabricated devices.

To my homies Tevon Hodges and Chris Lee for their comradery and friendship for all these years. We have been friends since undergrad days at UCSD and I hope we remain friends forever. Thank you for all the distractions, the inhumane number of hours of super smash bros, and your companionship.

To my family for the love and support they have given me my entire life. Thank you for being a haven for me to return to when I need a break from the struggles of the lab. Thank you Mom, Dad, Nana, Papa, Aidan, Carson, and Santiago for always believing in me, for leading me to this point, and for your unquestioning love.

Finally, my sincerest gratitude goes to my love, Juliana. I am so sorry for all the late, sleepless nights. Without you I would not have survived these years in the slightest. Thank you for all the songs we sing, the silly jokes we make, the games we play, our long walks through the neighborhood, and the adventures we take. You are my greatest friend, the one I share absolutely everything with. I am truly fortunate that you choose to share your life with me. I can happily say that we can now move on to the future. Let’s finally get outta here!

Forrest Valdez

San Diego, CA

2023

Chapter 2, in part, is a reprint of the material that appears in the following: Peter O. Weigel, Forrest Valdez, Jie Zhao, Huiyan Li, and Shayan Mookherjea, “Design of high-bandwidth, low-voltage and low-loss hybrid lithium niobate electro-optic modulators”, Journal of Physics: Photonics 3, no. 1 (2020) The dissertation author, together with his advisor and colleagues, led the research efforts for this work and co-authored the paper.

Chapter 3, in part, is a reprint of the material that appears in the following: Peter O. Weigel, Forrest Valdez, Jie Zhao, Huiyan Li, and Shayan Mookherjea, “Design of high-bandwidth, low-voltage and low-loss hybrid lithium niobate electro-optic modulators”, Journal of Physics: Photonics 3, no. 1 (2020) and Forrest Valdez, Viphretuo Mere, Xiaoxi Wang, and Shayan Mookherjea, “Integrated O- and C-band silicon-lithium niobate Mach-Zehnder modulators with 100 GHz bandwidth, low voltage, and low loss” Optics Express 31, no. 4 pg 5273-5289 (2023). The dissertation author, together with his advisor and colleagues, led the research efforts for this work and co-authored the papers.

Chapter 4, in part, is a reprint of the material that appears in the following: Forrest Valdez, Viphretuo Mere, Nicholas Boynton, Thomas A. Friedmann, Shawn Arterburn, Christina Dallo, Andrew T. Pomerene, Andrew L. Starbuck, Douglas C. Trotter, Anthony L. Lentine, and Shayan Mookherjea, “110 GHz, 110 mW hybrid silicon-lithium niobate Mach-Zehnder modulator”, Scientific Reports 12, 18611, (2022), Viphretuo Mere, Forrest Valdez, Xiaoxi Wang, and Shayan Mookherjea, “A modular fabrication process for thin-film lithium niobate modulators with silicon photonics” Journal of Physics: Photonics 4, no. 2 (2022). The dissertation author, together with his advisor and colleague, led the research efforts for this work and co-authored the papers.

Chapter 5, in part, is a reprint of the material that appears in the following: Forrest Valdez, Viphretuo Mere, Xiaoxi Wang, and Shayan Mookherjea, "Integrated O- and C-band silicon-lithium niobate Mach-Zehnder modulators with 100 GHz bandwidth, low voltage, and low loss" Optics Express 31, no. 4 pg 5273-5289 (2023). The dissertation author, together with his advisor and colleague, led the research efforts for this work and co-authored the papers.

Chapter 6, in part, is a reprint of the material that appears in the following: Forrest Valdez, Viphretuo Mere, Nicholas Boynton, Thomas A. Friedmann, Shawn Arterburn, Christina Dallo, Andrew T. Pomerene, Andrew L. Starbuck, Douglas C. Trotter, Anthony L. Lentine, and Shayan Mookherjea, "110 GHz, 110 mW hybrid silicon-lithium niobate Mach-Zehnder modulator", Scientific Reports 12, 18611, (2022). The dissertation author, together with his advisor and colleague, led the research efforts for this work and co-authored the papers.

Chapter 7, in part, is a reprint of the material that appears in the Journal of the Optical Society of America B: Viphretuo Mere, Forrest Valdez, and Shayan Mookherjea, "Improved fabrication of scalable hybrid silicon nitride – thin-film lithium niobate electro-optic modulators", JOSAB 40, no. 5 (2023). The dissertation author, together with his advisor and colleague co-authored the paper.

Chapter 8, in part, has been submitted for publication of the material as it may appear in Photonic Technology Letters 2023. Forrest Valdez, Viphretuo Mere, Nicholas Boynton, Thomas A. Friedmann, Shawn Arterburn, Christina Dallo, Andrew T. Pomerene, Andrew L. Starbuck, Douglas C. Trotter, Anthony L. Lentine, Ashok Kodigala, and Shayan Mookherjea, "Buried-electrode Hybrid Bonded Thin-film Lithium Niobate Electro-optic Mach-Zehdner

Modulators" PTL 2023 (under review). The dissertation author, together with his advisor and colleague, led the research efforts for this work and co-authored the paper.

Chapter 9, in part, is a reprint of the material that appears in arxiv 2022 and has been submitted for publication of the material as it may appear in Optica. Forrest Valdez, Viphretuo Mere, and Shayan Mookherjea, "100 GHz, 1 V Near-infrared Electro-optic Mach-Zehnder Modulator" arXiv:2211.13348 2022. The dissertation author, together with his advisor and colleague, led the research efforts for this work and co-authored the paper.

Chapter 10, in part, is a reprint of the material that appears in the following: Viphretuo Mere, Forrest Valdez, Xiaoxi Wang, and Shayan Mookherjea, "A modular fabrication process for thin-film lithium niobate modulators with silicon photonics" Journal of Physics: Photonics 4, no. 2 (2022). The dissertation author, together with his advisor and colleagues, led the research efforts for this work and co-authored the papers.

Appendix B, in part, is a reprint of the material that appears in arxiv 2022 and has been submitted for publication of the material as it may appear in Optica. Forrest Valdez, Viphretuo Mere, and Shayan Mookherjea, "100 GHz, 1 V Near-infrared Electro-optic Mach-Zehnder Modulator" arXiv:2211.13348 2022. The dissertation author, together with his advisor and colleague, led the research efforts for this work and co-authored the paper.

VITA

2017 Bachelor of Science in Engineering Physics, University of California San Diego

2019 Master of Science in Electrical Engineering (Photonics), University of California San Diego

2023 Doctor of Philosophy in Electrical Engineering (Photonics), University of California San Diego

PUBLICATIONS

Forrest Valdez, Viphretuo Mere, and Shayan Mookherjea. "100 GHz Bandwidth, 1 Volt Near-infrared Electro-optic Mach-Zehnder Modulator." arXiv preprint arXiv:2211.13348 (2022). (Manuscript Under Review)

Forrest Valdez, Viphretuo Mere, Nicholas Boynton, Thomas A. Friedmann, Shawn Arterburn, Christina Dallo, Andrew Pomerene, Andrew Starbuck, Douglas Trotter, Anthony Lentine, Ashok Kodigal, and Shayan Mookherjea. "Buried-electrode Hybrid Bonded Thin-film Lithium Niobate Electro-optic Mach-Zehnder Modulators" Photonic Technology Letters (2023) (Manuscript Under Review)

Forrest Valdez, Viphretuo Mere, Xiaoxi Wang, Nicholas Boynton, Thomas A. Friedmann, Shawn Arterburn, Christina Dallo, Andrew T. Pomerene, Andrew T. Starbuck, Douglas C. Trotter, Anthony L. Lentine, and Shayan Mookherjea. "110 GHz, 110 mW hybrid silicon-lithium niobate Mach-Zehnder modulator." Scientific Reports 12, 18611, 1-11 (2022).

Forrest Valdez, Viphretuo Mere, Xiaoxi Wang, and Shayan Mookherjea. "Integrated O-and C-band Silicon-Lithium Niobate Mach-Zehnder Modulators with 100 GHz Bandwidth, Low Voltage, and Low Loss." Optics Express, 31(4) 5273-5289 (2023).

Viphretuo Mere, Forrest Valdez, Xiaoxi Wang, and Shayan Mookherjea. "A modular fabrication process for thin-film lithium niobate modulators with silicon photonics." Journal of Physics: Photonics 4, no. 2, 024001 (2022).

Viphretuo Mere, Forrest Valdez, and Shayan Mookherjea. "Improved Fabrication of Scalable Hybrid Silicon Nitride – Thin-film Lithium Niobate Electro-optic Modulators" Journal of the Optical Society B 40, no. 5 (2023).

Xiaoxi Wang, Forrest Valdez, Viphretuo Mere, and Shayan Mookherjea. "Monolithic Integration of 110 GHz Thin-film Lithium Niobate Modulator and High-Q Silicon Microring

Resonator for Photon-Pair Generation." In 2022 Conference on Lasers and Electro-Optics (CLEO), pp. 1-2. IEEE, 2022., **Post-Deadline Paper**

Xiaoxi Wang, Forrest Valdez, Viphretuo Mere, and Shayan Mookherjea. "Integrated thin-silicon passive components for hybrid silicon-lithium niobate photonics." Optics Continuum 1, no. 10, 2233-2244 (2022).

Nicholas A. Boynton, Forrest G. Valdez, Thomas A. Friedmann, Shawn C. Arterburn, Christina M. Dallo, Andrew T. Pomerene, Andrew L. Starbuck, Michael R. Gehl, Christopher T. DeRose, Shayna Mookherjea, and Anthony L. Lentine. "RF Waveguide Pattern Engineering to Mitigate Bonding Surface Nonuniformities in CMOS Compatible Fabrication Processes." IEEE Transactions on Components, Packaging and Manufacturing Technology 12, no. 11, 1729-1739 (2022).

Peter O. Weigel, Forrest Valdez, Jie Zhao, Huiyan Li, and Shayan Mookherjea. "Design of high-bandwidth, low-voltage and low-loss hybrid lithium niobate electro-optic modulators." Journal of Physics: Photonics 3, no. 1, 012001 (2020).

ABSTRACT OF THE DISSERTATION

Hybrid Bonded Silicon Photonic and Lithium Niobate Platform for Low-voltage & High-speed Electro-optic Modulators in the Infrared to Visible Wavelengths

by

Forrest Glenn Valdez

Doctor of Philosophy in Electrical Engineering (Photonics)

University of California San Diego, 2023

Professor Shayan Mookherjea, Chair

Electro-optic modulators (EOMs) are essential components for communications systems, enabling light to be encoded with information and distributed to the world. Data traffic has grown tremendously in recent years which puts strain on current communication links to operate at high bandwidths and require little power. This dissertation discusses the design and optimization of hybrid bonded silicon (nitride) / lithium-niobate [Si(N)/LN] EOMs

for high-speed, low-voltage, and high optical power handling operations. The heterogeneous combination of Silicon-on-insulator (SOI) wafers with thin-film lithium niobate (TFLN) offers a platform that takes advantage of the large EO Pockels effect of TFLN, as well as the low-cost, scalable, and well-established SOI foundry technology. By carefully designing the Si(N) waveguide dimensions and introducing periodic slow-wave features in the traveling wave electrodes, broad frequency modulation is demonstrated across operational wavelengths from the telecom to the visible regimes. The results presented here pave way for record-breaking modulator efficiencies and a map for integration with a host of Si photonic components.

Chapter 1

Introduction

1.1 Motivation

1.1.1 CMOS Compatible Electro-optic Mach-Zehnder Modulators

Mach-Zehnder Interferometers (MZIs) are widely used optical structures that involve splitting an input optical waveform into two equally weighted waveguide arms, and recombining the paths after propagating a certain distance, L. They are used to implement quasi-unitary gate operations, path switching, amplitude modulation, filtering, analog computing and simulation, and other photonic signal processing functionalities that are important in both the classical and quantum regimes. MZIs are typically passive photonic circuits that have a fixed phase relation, $\Delta\phi = \frac{2\pi n_{eff}\Delta L}{\lambda}$, where ΔL is a path-length difference between the MZI arms. Upon recombination with a second coupler, the output signal experiences constructive and destructive interference, following a sinusoidal transfer function:

$$I_{out} = \frac{|E_o|^2}{2}\cos^2(\Delta\phi) \tag{1.1}$$

In this example, the MZI optical response varies with the operational wavelength, λ, as the number of 2π revolutions changes at the recombiner. However, the interferometer can become actively modulated by imparting a user-controlled phase-shift (typically between 0 and π

radians) by thermo-optic, electro-optic, or mechanical means. In such cases the MZI is known as a Mach-Zehnder modulator (MZM).

Electro-optic (EO) modulation is a key functionality for both classical and quantum photonics, and has widespread applications in communications, switching, radio frequency (RF) waveform generation and pulse shaping [1–6]. Integrated high-bandwidth EO modulators (EOMs) can be useful to quantum photonic applications such as time-to-frequency conversion in large-alphabet quantum key distribution where a phase modulator follows a dispersive element [7], and applying a time-dependent phase-shift to photons based on the measurement result of a prior stage [8]. In these cases, the 3-dB EO modulation bandwidth should exceed the bandwidth of the filtered photons, which is typically around 50 GHz if standard telecommunications (telecom)-grade optical filters at 1550 nm are used in the experiment [9]. In the classical domain, RF-photonic analog communication links utilize EOMs to encode an optical carrier wave (i.e, a laser source) with electrical information from an RF source to modulate the phase and amplitude of the input optical signal (if using in an MZI configuration). For such links, the faster the EO MZM can switch the light from off to on states without impacting the integrity of the signal itself (i.e, higher bandwidth), the more information can be imparted to the signal. This increasing demand for high-bandwidth operation by a diverse set of end users requires high performance EOMs to be designed and fabricated on a scalable integrated platform.

Silicon-on-insulator (SOI) based MZMs have been fabricated at the wafer scale (200 mm wafers) in commercial complementary-metal-oxide-semiconductor (CMOS) foundries for decades. These CMOS fabrication techniques allow for a scalable, low-cost, and high-yield platform for photonic chips that can be co-integrated with electronic circuits. However, silicon (Si) EO MZMs that are carrier based [10] are typically RC-limited, with reported 3-dB

bandwidths less than 60 GHz [11–15]. Furthermore, the introduction of these carriers to the optical waveguide result in significant amounts of optical loss, which requires shorter devices to limit the insertion loss and reduced extinction ratios (ERs) [16,17]. Additionally, Si waveguides have issues with handling high optical powers due to two-photon absorption (TPA) in the telecom regime. TPA is an intensity dependent nonlinear effect that generates carriers in Si waveguides which then lead to additional loss and dispersion. This puts intrinsic limits on the optical power handling of Si based RF-photonic links.

Silicon nitride (SiN) is another CMOS compatible material which has shown low loss integrated photonics [18,19] and has a much larger transparency window, from the visible to mid-infrared wavelengths, compared to Si. However, SiN is a centrosymmetric material with no linear EO effect and furthermore is an insulator which cannot take advantage of carrier-based plasma dispersion effects like Si. Nevertheless, SiN EO modulation has been demonstrated via heterogeneous integration with other EO materials such as lithium niobate (LN) [20,21] and lead zirconate titanate (PZT) [22]. These works resulted in rather low 3-dB bandwidths of 30 GHz and only show operation in the telecom wavelength regime.

In fact, visible light communicatinos systems typically employ direct modulation techniques (in which the laser source output is modulated via the applied current driving the laser itself) which limits the high-speed functionality at these wavelengths to a few GHz. Here a roadmap is shown using thin-film LN (TFLN) EOM devices designed and made without etching or patterning the LN film, co-integrated on a Si(N) photonics platform with optimized 3-dB bandwidths exceeding the available measurable limit of 110 GHz and low half-wave voltages (ranging sub-volt to 6 V) across the visible to telecom wavelengths.

1.1.2 The Hybrid Bonded Silicon (Nitride)/Lithium Niobate Platform

Lithium niobate (LN) is a versatile nonlinear anisotropic material with a host of extraordinary physical phenomena such as the EO (Pockels effect, i.e a change in refractive index with applied voltage), piezoelectric (a change in elasticity with applied voltage), pyroelectric (a build-up of charge with change in temperature), and ferroelectric effects. Because of such adept functionalities, it has been used as a workhorse material in many applications, but most suitably as an EOM as it possesses a quite large EO coefficient of 30.8 pm/V [23]. Since the 1980s, bulk LN substrates (100s of μm thick) have been used to develop waveguide and EOM technologies [24–26]. However, due to fabrication limitations, waveguides developed on LN substrates (for example via Titanium diffusion [27–30], Figure 1.1(a)) yield a small index variation for optical mode confinement, leading to effective areas on the order of 10 μm or larger. This inherently places a limitation on the modulation efficiency of the devices as the required voltage to incur a π phase-shift (V_{π}) is directly proportional to the spacing, G, between the ground and signal electrodes. If G is too narrow for a given waveguide mode, then the mode will be absorbed by the metal electrodes and the EOM will incur heavy optical losses, and in the worst case render it useless.

A crystal-ion-slicing technique combined with direct wafer bonding [31–33] and chemical-mechanical-polishing (CMP) has led to the development of LN-on-insulator (LNOI), with LN thicknesses less than 1 μm, which preserves many of the properties of bulk LN crystals [34,35]. TFLN allows a much smaller, more confined optical mode (effective areas on the order of 1 μm^2 or less) which in turn allows more compact device footprints and higher efficiency devices compared to traditional LN devices [36,37]. Figure 1.1 shows 2-D cross sections of LNOI based waveguides that have been published in recent years. Etching of LNOI [Figure

1.1(b)] has quickly become a popular method to fabricate waveguides via patterning and dry-etching the LNOI surface [38]. While many researchers have shown state-of-the-art EOMs with low-voltage and high 3-dB bandwidths [36,39–42], etching LNOI is not a simple process. One challenge is the redeposition of etched composites that buildup on the etched surface and are difficult to remove at low temperatures. Additionally, integration of other photonic components, such as lasers and detectors, requires a full design kit to be developed on the LNOI platform, which is not CMOS compatible and cannot take advantage of scalable and well-defined CMOS processing, unlike Si photonic circuits.

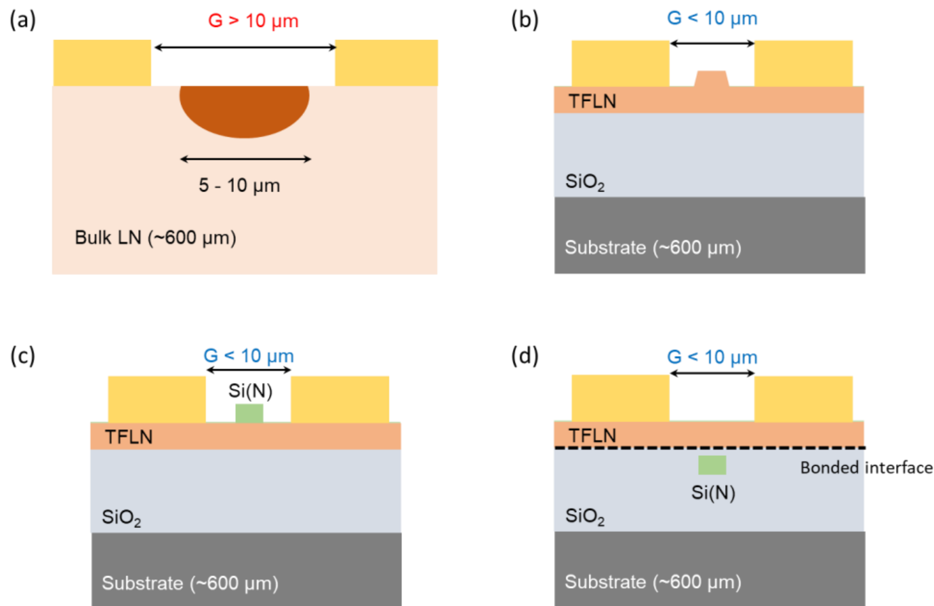

Figure 1.1: Cross sections of LN waveguides fabricated via (a) proton exchange on bulk LN substrates (b) etched TFLN (c) deposited materials on LNOI and (d) hybrid bonded TFLN to SOI rib-waveguides.

The conflict of etching LN and front-end-of-line processing can be mitigated by designing hybrid optical modes using rib-loaded LN films. Figure 1.1(c) and Figure 1.1(d) are cross sections of heterogeneous methods of developing LN waveguides via material deposition [Figure 1.1(c)] or heterogeneous bonding [Figure 1.1(d)]. Rib-loaded LN waveguides have been demonstrated via depositing other materials such as SiN, tantala, amorphous Si, or chalcogenide

glass [21,43–46]. However, to avoid damaging the LN film, the materials must be deposited at low temperatures which often result in amorphous materials. This increases the chances of trapped charges, nonlinear carrier effects, and nonideal material properties [47].

Heterogeneous bonding is a hydrophilic process that transfers the TFLN layer to a planarized photonic circuit with Si or SiN patterned features fabricated in a CMOS foundry [48–52]. The guided optical mode is distributed between the etched Si(N) waveguide and the LN film to form a hybrid optical mode based on the waveguide dimensions without needing to etch or pattern the TFLN. The waveguide routing, splitting, combining, tapering, and bending can all be performed via the underlying Si or SiN layer within or outside of the bonded region. Once the guided light is within the bonded LN region, the underlying rib waveguides are adiabatically tapered to push the fraction of light into the LN layer for an optimal phase shifter. Such hybrid bonded Si/LN and SiN/LN MZMs have been demonstrated to show EO 3-dB bandwidths of > 106 GHz [50] and 30 GHz [20], respectively; however, with a high $V_\pi > 13$ V with a phase shifter length of only 0.5 cm. To meet the ever-increasing demands of data centers and long-haul communications, the Si(N)/LN platform must be enhanced to achieve both broadband and low-voltage operations.

1.2 Overview of this Dissertation

This dissertation discusses how to optimize the hybrid bonded Si(N)/LN platform not only in terms of low-voltage and high bandwidth but will do so for multiple wavelength regimes from the telecom wavelengths (O-band to C+L band) to the visible and near-infrared (NIR) regime (400 nm – 800 nm) by using carefully designed slow-wave electrode (SWE) structures. Chapter 2 introduces the concepts of Mach Zehnder EO modulators, their figures of merit, and

how best to develop such a hybrid Si(N)/LN device in terms of optical design. Chapter 3 discusses the high frequency RF electrode design of traveling wave electrodes for driving modulation. SWEs are introduced by including periodic features along the inner edges of the electrodes to slow the RF wave velocity; providing additional design parameters to achieve velocity matching to the hybrid optical wave and thus, high-speed modulation. Chapter 4 discusses the fabrication of hybrid bonded Si/LN and SiN/LN chips, as well as passive measurement tests. Chapter 5 reports on the electrical and electro-optic characterization of high-speed Si/LN MZMs designed for O-band and C-band operation. SWEs are used to achieve velocity matching between the RF and optical waves to less than 1% mismatch, resulting in 100 GHz class modulators in both the C-band and O-band with low driving voltage. In Chapter 6 I will demonstrate that Si/LN modulators can withstand high input optical powers (> 110 mW) while modulating at high speeds (> 110 GHz), which far surpasses the expectations and capabilities of standard Si MZMs, ultimately benefitting RF-photonic links. Chapter 7 reports on the characterization of hybrid bonded SiN/LN chips with MZMs developed for telecom regimes. In Chapter 8 a CMOS compatible modulator is fabricated using a buried metal layer as the traveling wave electrodes instead of post-CMOS processed gold, which achieves > 100 GHz modulation speed for a comparable V_π of 5.6 V. Chapter 9 demonstrates the world's first modulator (of any type) to simultaneously achieve 100 GHz 3-dB bandwidth with a driving voltage of 1 V is demonstrated on the SiN/LN platform in the near-infrared (NIR) wavelengths (784 nm). Lastly, Chapter 10 discusses preliminary findings concerning the long-term DC bias drift effects of the hybrid Si(N)/LN platform and shows a means to control such drift. An outlook of future possibilities, such as integration with other photonic components for a full system on-chip are proposed.

Chapter 2

Hybrid Bonded LN EOM: Principles and Optical Design

2.1 Figures of Merit for Electro-Optic Mach-Zehnder Modulators

To fully understand how to optimize the design of hybrid bonded Si(N)/LN modulators, the key figures of merit must first be defined. The primary aspects that describe the performance of an EO MZM are its modulation efficiency, high-frequency response 3-dB bandwidth, optical insertion loss, and optical power handling capability. All of which are not only important for standalone modulator performance, but can also determine the overall system performance of an RF-photonic data link.

2.1.1 High-speed Traveling Wave Modulator Response Theory

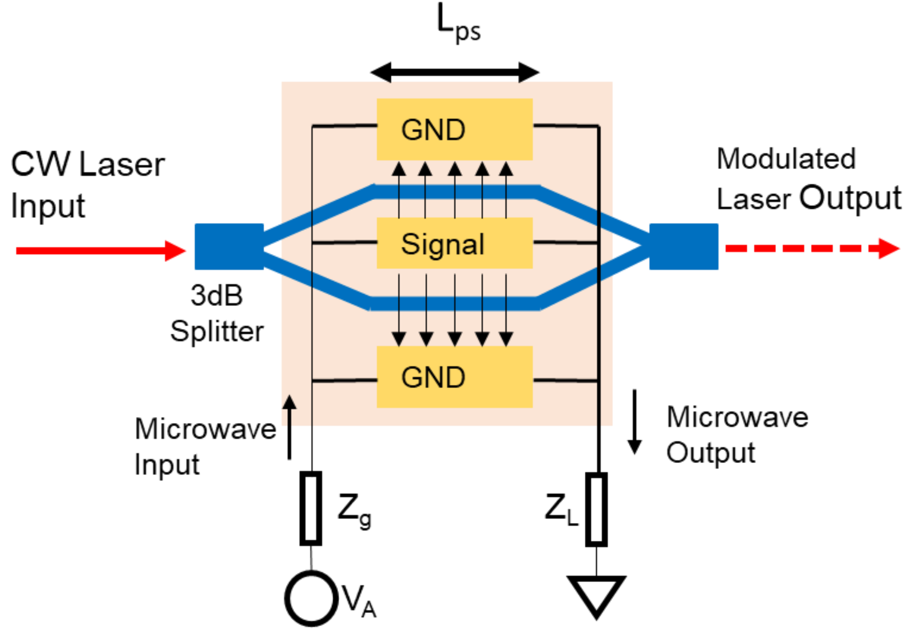

Figure 2.1: A top-view diagram of an EOM modulating a continuous wave (CW) laser input with push-pull traveling wave electrodes driven by an RF source and terminated with a load impedance, Z_L.

Figure 2.1 shows a top-view generalized diagram of an EOM with traveling wave electrodes of length L_{ps} that are driven with a generated voltage with source impedance and resistance (Z_G and R_G), and a load impedance and resistance (Z_L and Z_R). The small-signal modulator response describes how the device reacts when driven with RF sinusoidal tones at high frequencies (typically f > 100 MHz) when it is biased in the linear regime of the MZM transfer function. The small-signal frequency response is described by the following equations (where the full derivation is provided in [53]):

$$m(\omega) = \frac{R_L + R_G}{R_L} \left|\frac{Z_{in}}{Z_{in} + Z_G}\right| \left|\frac{(Z_L + Z_c)F(u_+) + (Z_L - Z_c)F(u_-)}{(Z_L + Z_c)\exp[\gamma_m L_{ps}] + (Z_L - Z_c)\exp[-\gamma_m L_{ps}]}\right| \quad (2.1)$$

$$Z_{in} = Z_c \frac{Z_L + Z_c \tanh(\gamma_m L_{ps})}{Z_c + Z_L \tanh(\gamma_m L_{ps})} \quad (2.2)$$

$$\gamma_m = \alpha_m + \frac{j\omega}{c} n_m \tag{2.3}$$

$$F(u_\pm) = \frac{1 + \exp[u_\pm]}{u_\pm} \tag{2.4}$$

$$u_\pm = \pm\alpha_m L_{ps} + \frac{j\omega}{c}(\pm n_m - n_g)L_{ps} \tag{2.5}$$

Where ω is the radial frequency ($2\pi f_{RF}$), $Z_{in,c}$ are the input and characteristic impedances and γ_m is the complex propagation constant of the RF wave along the transmission line. This EO response (EOR) is one of the standard measures of modulators as it describes how fast the device can switch between on and off states before losing excessive amounts of power. The point at which the EOR decays to half of the low-frequency magnitude is termed the 3-dB bandwidth and is a common reported metric by research groups and industry alike. The higher a modulators 3-dB bandwidth is, the more information can be encoded and transmitted before losing power and degrading the signal; thus, devices with high-speed are coveted.

For a given material dielectric stack (i.e, MZM cross section), high speed EO modulation depends on three main design criteria: 1) matching the velocities of the traveling RF and optical waves; 2) matching the transmission line, source, and load impedances ($Z_c = Z_G = Z_L$, typically 50 Ω); and 3) minimizing the RF propagation loss (α_m) [53]. To ensure that the first criterion is met, the RF effective index (n_m) and the optical group index (n_g) must be designed to be equal. Furthermore, each of the three design rules must be held as functions of frequency. The microwave velocity, characteristic impedance, and loss are frequency dependent parameters of the RF transmission line characteristics which are determined by the dimensions and material composition of the dielectric stack and the electrode geometry [54,55]. These three criteria put a restriction on the fabricated phase-shifter length (L_{ps}), because if there is a mismatch between the

RF and optical velocities (described by $\Delta n = n_g - n_m$), then the waves will become out of phase as they propagate and the EO effect will be reduced. If there is a mismatch in the various impedances, then there will be unwanted RF reflections in the system which result in oscillations in the frequency response. The RF loss of coplanar waveguide electrodes generally follows a square-root dependence of the driving frequency (from conductive skin loss) and a linear dependence from dielectric loss at high frequencies:

$$\alpha_m = \alpha_{sd} f^{0.5} + \alpha_{die} f \tag{2.6}$$

For a well-designed EOM, the index and impedance matching conditions are met and the EO response becomes RF loss limited. Figure 2.2 is a plot of the calculated 3-dB bandwidth of an EO modulator response (from Eq. (2.1)) that is index matched ($\Delta n = 0$) and impedance matched to a 50 Ω load, with different assumed RF loss coefficients as a function of the MZM V_π (inverse to the phase-shifter length). This means that if the MZM has a V_π of 6 V (L_{ps} ~ 0.5 cm), then the expected 3-dB bandwidth ranges from 110 GHz to nearly 5 THz as the RF loss at 110 GHz (α_m(f=110 GHz)) decreases from 10 dB/cm to 2 dB/cm. For longer devices the higher RF loss weakens the overall EO response which reduces the 3-dB bandwidth; thus, for L_{ps} = 1 cm (V_π ~ 3V), the 3-dB bandwidth ranges from 60 GHz to 1 THz.

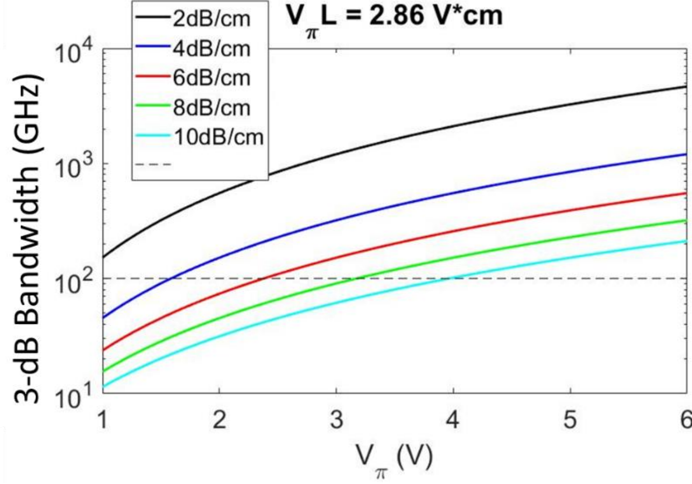

Figure 2.2: The calculated 3-dB bandwidth vs MZM V_π (inverse to L_{ps}) using Eq. (2.1) assuming the MZM is RF-loss limited (i.e, $\Delta n = 0\%$ and $Z_c = Z_L = 50\ \Omega$) for different values of $\alpha_m(f = 110\text{ GHz})$. The assumed $V_\pi L$ of this MZM is 2.86 V.cm.

2.1.2 Half-wave Driving Voltage of Lithium Niobate Mach-Zehnder Modulators

The modulation efficiency of an EO MZM is defined in terms of the amount of driving voltage required to yield a π phase-shift between its two optical pathways, which is deemed the half-wave voltage (V_π). This is important as it determines the amount of DC and RF power required from driving circuits or power supplies to enable modulation. This metric is most often reported as the half-wave voltage-length product, $V_\pi L$, which gives the additional information of the phase-shifter length (i.e, the traveling wave electrode length). $V_\pi L$ for an EO MZM with x-cut LN driven by CPWs is defined as

$$V_\pi L = \frac{n_{eff}\lambda_0 G}{2n_e^4 r_{33}\Gamma_{mo}} \tag{2.7}$$

where a factor of 1/2 is included to account for single-drive push-pull configuration (equal amplitude and opposite phase voltage applied to each arm) of the MZM arms as shown in Figure

2.1. A more detailed derivation is included in Appendix A.1. Here n_{eff} is the effective index of the optical guided mode, λ_0 is the operational wavelength in vacuum, G is the spacing between the ground and signal electrodes, n_e is the extraordinary index of LN, and r_{33} is the EO coefficient of LN (30.8 pm/V). Γ_{mo} is the RF-to-optical mode overlap integral, defined as

$$\Gamma_{mo} = \frac{G}{V_A} \frac{\iint_{LN} E_{RF}(x,z)|E_o(x,z)|^2 dxdz}{\iint |E_o(x,z)|^2 dxdz}, \tag{2.8}$$

where E_{RF} is the applied RF E-field to the phase-shifter, E_o is the optical mode E-field and V_A is the applied voltage. This is a cross-sectional integral over the EO region (which is LN in this case). Figure 2.3(a) is an example of a simulated RF mode at 100 GHz for a CPW structure on a hybrid Si/LN MZM cross section. The mode is confined and concentrated between the ground and signal electrodes and strongly interacts with the x-cut TFLN directly underneath. With the hybrid waveguides centered between the electrodes, as shown by the simulated mode in Figure 2.3(b), Γ_{mo} (which depends on the Si(N) waveguide design and TFLN thickness) can reach values upwards of 0.85 (discussed further in Section 2.2.1) to enable efficient modulation.

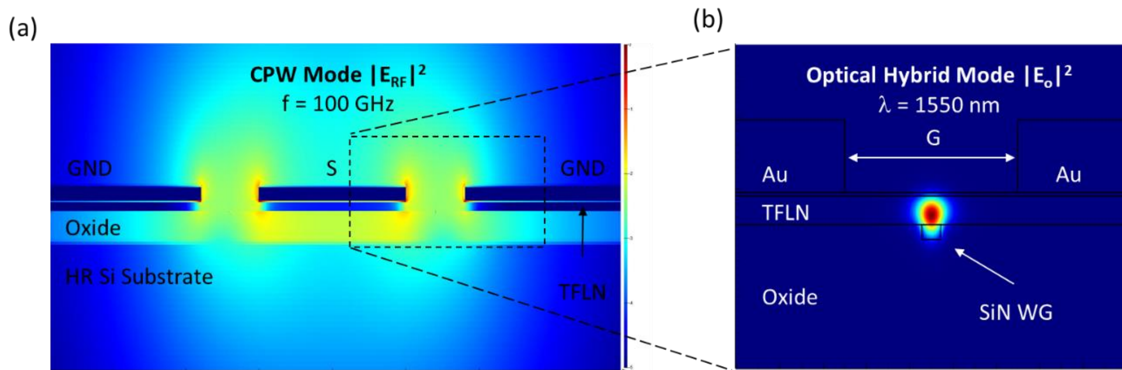

Figure 2.3: The simulated (a) RF CPW mode $|E_{RF}|^2$ at 100 GHz and (b) hybrid optical mode $|E_o|^2$ at 1550 nm for a SiN/LN cross section using Lumerical Mode Solutions.

From Eq. (2.7), the $V_\pi L$ of a push-pull EO MZM is proportional to many material constants but in practice is primarily limited by the spacing G. Ideally G should be made as narrow as possible to within fabrication limits; however, there is a caveat that the optical mode intensity should not interact with the driving electrodes. Metal features cause large amounts of optical propagation loss, α_{opt}, if the evanescent tail of the mode interferes with the metal boundaries. Thus there is an inherent trade-off between designing low-voltage and low-loss modulator, which is demonstrated by Figure 2.4 as a function of G at 1550 nm for the Si/LN (dashed lines) and SiN/LN (solid lines) MZMs with LN film thicknesses of 600 nm and 400 nm, respectively. The Si waveguide is 225 nm wide which does not confine the large optical mode (at 1550 nm) well enough and leads to higher optical losses. The SiN waveguide is 900 nm wide which results in $\alpha_{opt} < 1$ dB/cm at G = 8 μm and a $V_\pi L$ of 3.2 V.cm.

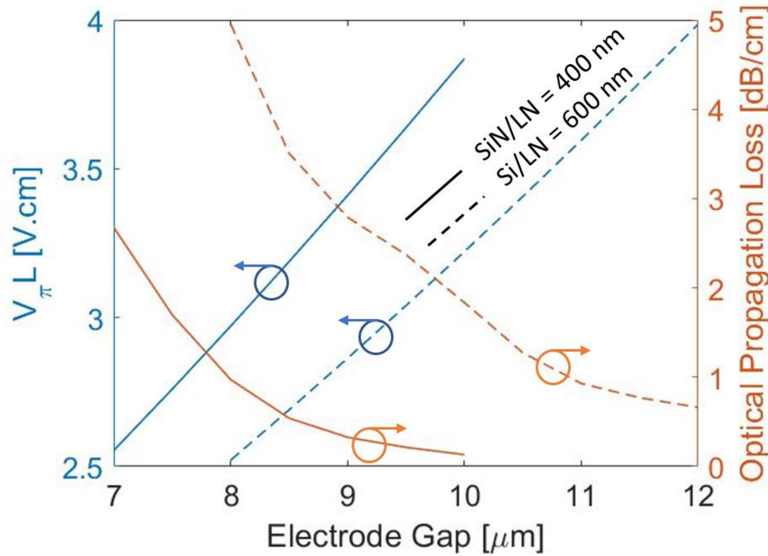

Figure 2.4: The simulated $V_\pi L$ (blue, left y-axis) and α_{opt} (orange, right y-axis) of a SiN/LN MZM with h_{LN} = 400 nm (solid traces) and a Si/LN with h_{LN} = 600 nm (dashed traces) as a function of electrode gap, G. In this example, the SiN waveguide is 900 nm wide by 200 nm thick, the Si waveguide is 225 nm wide by 150 nm thick, h_{cmp} is 50 nm, and λ = 1550 nm.

2.1.3 RF-Photonic Link Gain and Noise Factor

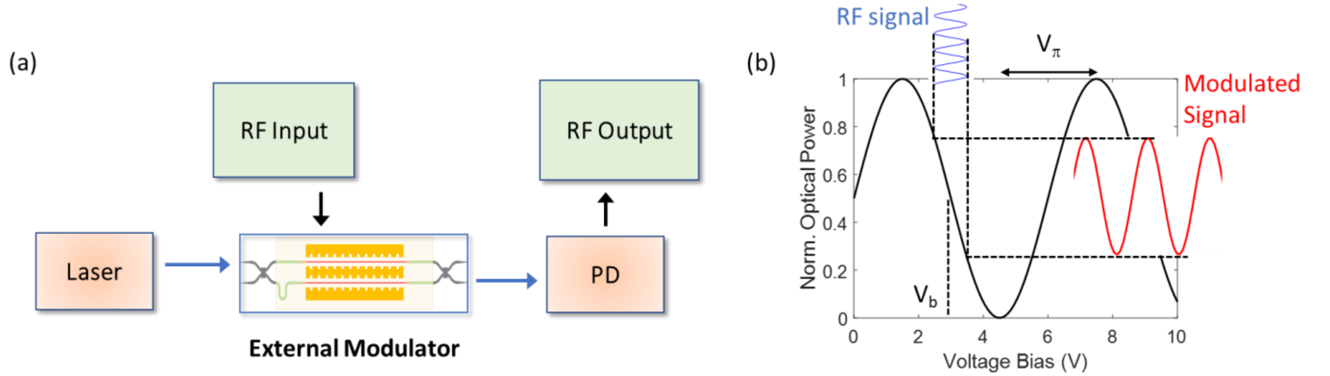

Figure 2.5: (a) A block diagram of a generalized RF-photonic link with an external MZM. (b) A diagram of an MZM transfer function (black curve) biased at quadrature with via an external DC voltage bias (V_b). An RF signal (blue curve) drives the device in the small-signal regime which modulates the optical signal (red curve).

RF-photonic links have been employed to transmit RF analog signals over optical fibers for decades [1,56], with commercial applications in cable television, antenna remoting and, more recently, optical phased arrays. A general block diagram of an RF-photonic link is shown in Figure 2.5(a), where an optical light source (laser) is imparted with amplitude and/or phase information via external modulation from an RF source. This modulated signal is transmitted over optical fiber and then converted to voltage using a photodetector. An example of such a small-signal modulation of an optical signal is demonstrated by Figure 2.5(b), where an MZM is used to modulate, hence the cosine-squared transfer function. Two main figures of merit for such links are the RF gain, G_{RF}, and the noise factor, NF. The link gain is important as it describes the overall performance of the system. When using an MZM to modulate, G_{RF} is defined as [57]

$$G_{RF} = \frac{P_{RF,O}}{P_{RF,I}} = \left(P_{opt}T'\eta\right)^2 r_d R_m = \left(\frac{\pi P_{opt}\eta}{2V_\pi}\right)^2 r_d R_m \qquad (2.9)$$

where P_{opt} is the optical power, T' is the modulator linear region slope efficiency (a factor of V_π for an MZM biased at quadrature), η is the efficiency of the modulator and the fiber-to-fiber losses, r_d is the photodetector responsivity, and R_m is the modulator resistance. From this expression it can be clearly seen that the link gain increases as the optical power increases, the modulation efficiency (V_π) decreases, the insertion loss of the modulator decreases, and the photodetector responsivity increases. As this dissertation is mainly concerned with modulator design, it is of the utmost importance to optimize the hybrid bonded devices to have low half-wave voltages and be able to handle as much optical power as possible. Furthermore, to enable greater bandwidth of the RF-photonic link, the modulator must also be designed for high-speed operation.

The RF-photonic link NF is a merit of how much the signal-to-noise ratio decreases in the face of all potential sources of noise in the system. For an MZM the NF is defined as [1]

$$NF = 10\log\left(1 + C + \frac{4V_\pi^2}{\pi^2 r_d^2 \eta^2 P_{opt}^2 R_s^2} + \frac{V_\pi^2 RIN}{\pi^2 k T_0 R_s} + \frac{4qV_\pi^2}{\pi^2 k T_0 r_d \eta P_{opt} R_s}\right) \qquad (2.10)$$

where C is a constant from unavoidable thermal noise, the second term corresponds to added thermal noise from the link gain, the third term corresponds to laser noise or relative intensity noise (RIN), and the last term corresponds to shot noise. Again, it is clearly seen from Eq. (2.10) that optimizing the hybrid bonded modulator for low-voltage operation (which also maximizes the RF gain) helps minimize the NF of the system.

Increasing the optical power transmitted through the RF-photonic link also benefits both the GRF and NF. The simplest method of optimizing these figures of merit would be to just blast the link with as much optical power as possible. Unfortunately, Si photonic circuits suffer from intensity dependent losses and dispersion from a multiphoton interaction, two-photon absorption

(TPA). TPA increases the number of photogenerated carriers in Si waveguides which lead to additional optical losses from free carrier effects. Thus, for a Si-based MZM, the optical power handling is limited and cannot simply be increased to maximize RF gain. The hybrid bonded Si/LN platform offers a solution to the power handling issue of standard Si based modulators as the optical intensity is split between the Si and LN regions (LN having negligible TPA in the telecom wavelengths). This will be further discussed in Section 2.3.

2.2 Hybrid Bonded Si(N)/LN MZM Design and Principle

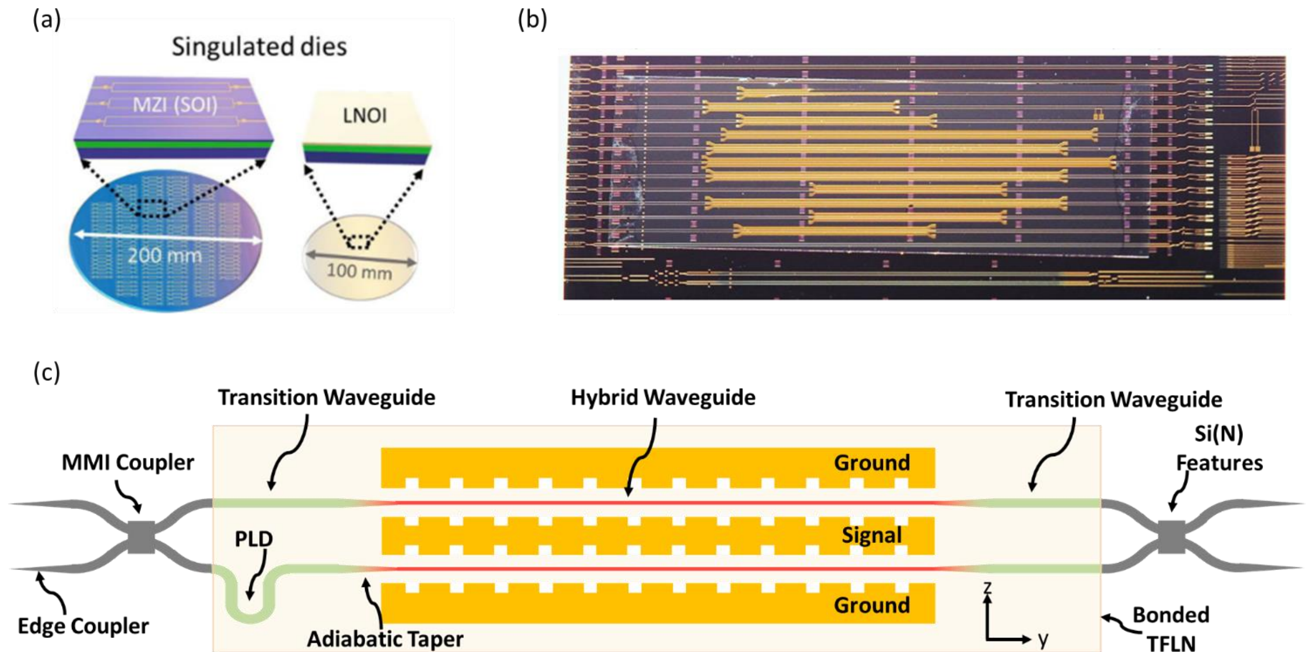

Figure 2.6: (a) Singulation of the SOI and LNOI dies. The SOI is patterned with photonic waveguide features while the LNOI is unpatterned and unetched. (b) An example of the hybrid bonded Si/LN EO chip with multiple MZM structures and passive integrated Si photonic components. (c) A diagram (not to scale) of the hybrid bonded Si(N)/LN MZM showing the relevant features such as edge couplers, MMI couplers, tapers, and transitions. PLD is an optional path-length-difference which can incur a constant phase difference between the MZM arms.

The proposed heterogeneous platform consists of two hybrid bonded dielectric stacks, one being silicon-on-insulator (SOI) which consists of planarized Si(N) circuits on a high-

resistivity Si substrate developed in a CMOS foundry, and the other being commercially procured x-cut LNOI with a less than 1 µm film of LN. Bonding of TFLN to patterned Si(N) waveguides offers a site-specific, modular, and scalable approach for realizing hybrid photonic circuits. This integration process requires minimal processing of the LN film (i.e, no patterning or etching) and yields additional EO functionality to the mature SOI photonic system. As the LN film is not etched or patterned at all, the waveguiding functionality of this platform is provided by the Si(N) layer, while the diced LN region is bonded as needed in specific areas as shown in Figure 2.6(a)-(b). The waveguide coupling, routing, tapering, and bending can all be performed in the Si(N) circuit (outside of the bonded region), while the high-speed and low-voltage EO effect can be imparted in the hybrid bonded phase-shifting section as shown by Figure 2.6(c). Lumerical Mode simulations were performed to design single-mode waveguides, low-loss bends, MMI 3-dB couplers, adiabatic tapers, and the hybrid phase-shifter section, all of which are components of the Si(N)/LN MZM.

2.2.1 The Optimized Si(N)/LN Cross Section

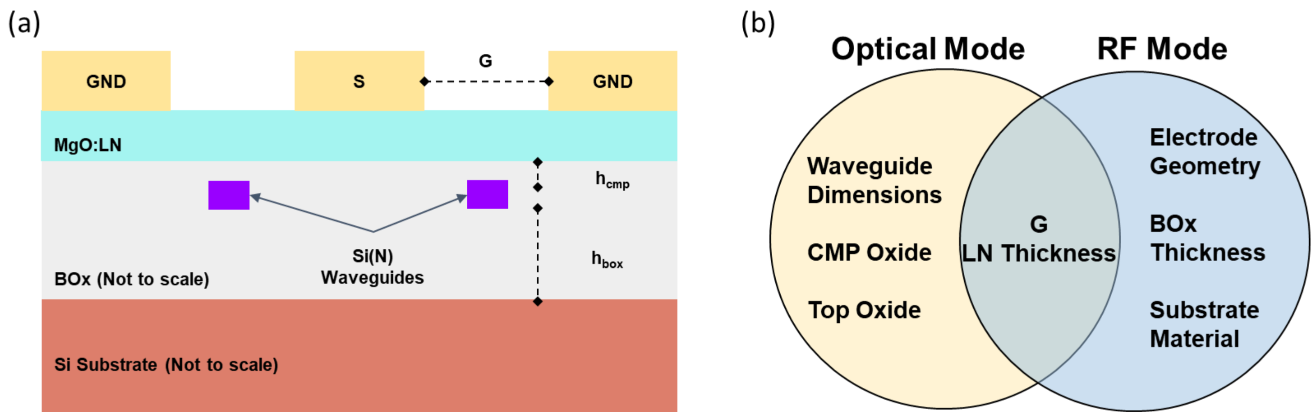

Figure 2.7: (a) The cross section diagram of the Si(N)/LN MZM with electrodes above the bonded TFLN layer. G: electrode gap. h_{cmp}: CMP oxide thickness. h_{box}: Buried oxide thickness. h_{LN}: LN film thickness. h_e: electrode thickness. w_s: signal electrode width. $w_{Si(N)}$: the Si(N) waveguide width. $h_{Si(N)}$: the Si(N) waveguide thickness. (b) A Ven diagram describing whether the labelled parameters affect the optical mode, RF mode, or both.

Figure 2.7(a) is a schematic generalized cross section of the hybrid bonded Si(N)/LN MZM with the various design parameters labelled. As this is an EO device, some of these parameters affect both the optical and RF mode properties. The optical characteristics of the hybrid mode (i.e, the n_{eff}, n_g, A_{eff}) are heavily dependent on the underlying waveguide dimensions (width and thickness), the LN film thickness, and the narrow amount of oxide between the TFLN and Si(N) layers. This thin oxide (SiO_2) layer is a planarized surface from a chemical-mechanical polish (CMP) process performed at the wafer scale in a CMOS foundry. On the other hand, the characteristics of the RF mode is primarily determined by the permittivity and loss of the dielectric stack as well as the electrode geometry. Figure 2.7(b) is a Ven diagram detailing which of the various design parameters affect either the optical or RF fields (or both in some cases).

Because the Si(N) waveguides are developed in a CMOS foundry, the waveguide width ($w_{Si(N)}$) can be tapered and tailored with high precision across all devices in the wafer. This allows for simple low optical loss transitions from the unbonded region to the bonded region of the modulator [48]. Furthermore, once in the hybrid region, the fraction of light (i.e, the Poynting vector magnitude percentage) can be transferred from the Si(N) rib waveguide to a hybrid Si(N)/LN region by simply narrowing the underlying waveguide width. Contour maps of the simulated n_{eff}, A_{eff}, and optical confinement factor, Γ, in the and LN region for Si/LN and SiN/LN hybrid modes are shown in Figure 2.8 as a function of Si(N) waveguide width and thickness at an operational λ of 1550 nm. The optical confinement factor is defined as

$$\Gamma_{\mathrm{LN}} = \frac{\iint_{LN} |E_o|^2 dA}{\iint |E_o|^2 dA} \tag{2.11}$$

$$\Gamma_{\mathrm{Si(N)}} = \frac{\iint_{Si(N)} |E_o|^2 dA}{\iint |E_o|^2 dA} \tag{2.12}$$

where $|E_o|^2$ is the optical field intensity which is integrated over the cross-sectional area of interest. Because the refractive index of Si is higher than that of LN, the optical mode resides primarily in the Si rib waveguide. Thus, as the Si waveguide width increases, n_{eff}, n_g, and Γ_{Si} increase; whereas A_{eff} and Γ_{LN} decrease. The refractive index of SiN is similar to that of LN, resulting in less modal control as a function of waveguide dimension. The SOI wafers used in this dissertation were processed and developed by Sandia National Laboratories, which has a standard Si thickness of 250 nm and SiN thickness of 200 nm. Sandia allowed a thinner Si layer of 150 nm which yields a higher Γ_{LN} for a wider range of w_{Si} [Figure 2.8(c)] for our wafers. These are the target thicknesses of the Si and SiN wafers for the works presented in this dissertation and from this point will be assumed to be fixed.

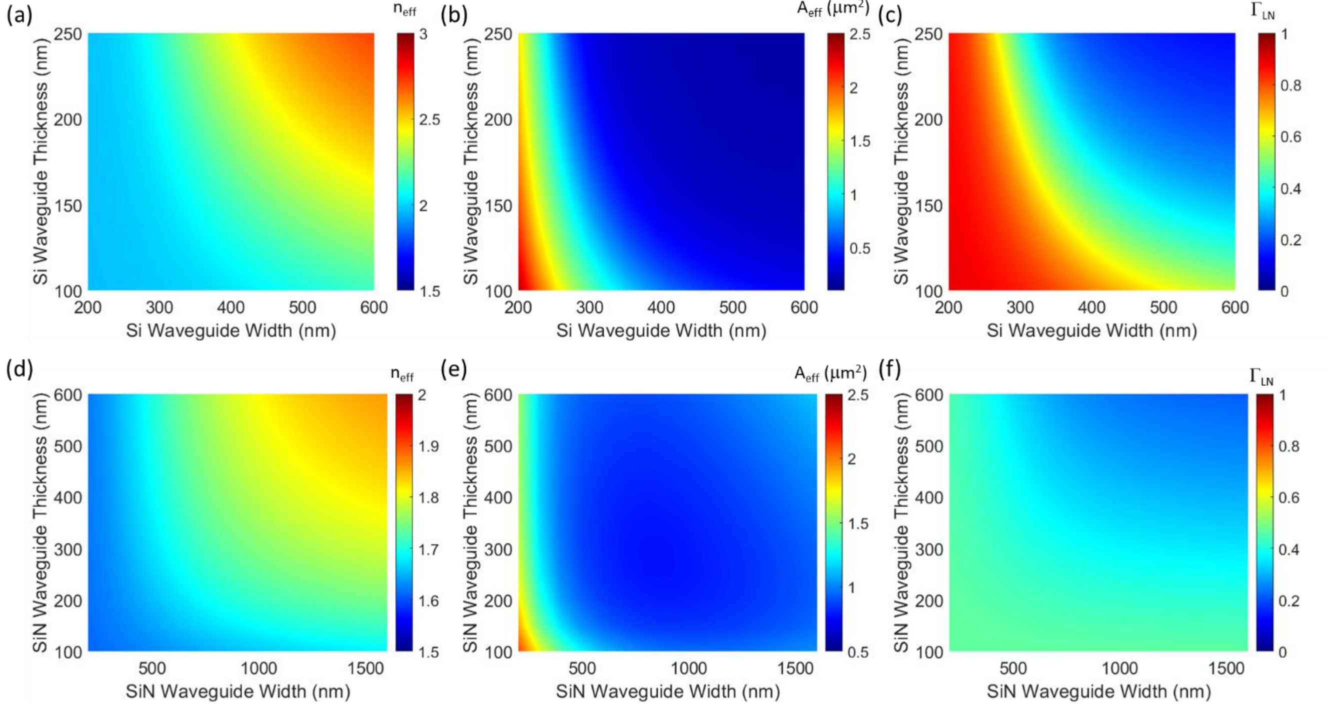

Figure 2.8: The simulated (a) n_{eff}, (b) A_{eff}, and (c) Γ_{LN} of a Si/LN hybrid mode as a function of Si waveguide dimensions with a TFLN thickness of 600 nm at $\lambda = 1550$ nm. The simulated (d) n_{eff}, (e) A_{eff}, and (f) Γ_{LN} of a SiN/LN hybrid mode as a function of SiN waveguide dimensions with a TFLN thickness of 200 nm at $\lambda = 1550$ nm.

The amount of light confined to the LN region of the hybrid region directly impacts the modulation efficiency ($V_{\pi}L$) of the MZM via the RF-to-optical mode overlap integral. In the limit that the applied RF field is constant and perfectly polarized in the direction of the optical field, then the E_{RF} term in Eq. (2.7) can be simplified as $\frac{V_A}{G}$ and pulled out of the integral. Thus, the RF-to-optical mode field overlap integral (Γ_{mo}) can be approximated as simply the confinement factor of light in the LN film (Γ_{LN}), and $V\pi L$ simplifies to the following Figure-of-Merit (FoM):

$$FoM = \frac{n_{eff}\lambda G}{2n_e^4 r_{33}\Gamma_{LN}} \tag{2.13}$$

Note that this approximation reduces $V_\pi L$ to a function of material constants, operational wavelength, and optical mode properties defined by the geometry of the hybrid waveguide. Thus, FoM can be rapidly simulated all in an optical mode environment (Lumerical MODE FDE) without needing to simulate the RF field which can be lengthy due to the increased wavelength and simulation area. Typically, each 2D hybrid mode optical simulation takes 10 seconds or less per geometry and wavelength, while the 2D RF mode simulation can take minutes per geometry and frequency. A blind search in the RF parameter space to optimize $V_\pi L$ would quickly get out of hand in terms of simulation time. Figure 2.9 shows the results of an all-optical simulation resulting in FoM as a function of w_{Si} and h_{cmp} for a Si/LN mode (assuming h_{Si} = 150 nm, h_{LN} = 600 nm, G = 8 μm) and SiN/LN mode (assuming h_{SiN} = 200 nm, h_{LN} = 200 nm, G ~ 6 μm) at λ = 1550 nm and 1310 nm, respectively. As expected, FoM increases (the device becomes less modulation efficient) as the Si waveguide width increases, because there is more light confined in the non-Pockels Effect material and Γ_{LN} decreases. In the extreme cases with $w_{Si} > 500$ nm, the FoM is as large as 10 V.cm and greater which is comparable to bulk LN modulators. But if w_{Si} is kept narrower than 325 nm in the phase-shifter section, then FoM is less than 2.5 V.cm. As the CMP oxide layer thickness increases the hybrid mode diffuses/spreads into the other dielectric layers and the A_{eff} increases which improves FoM. The SiN waveguide provides less modal confinement and thus less tuning of the FoM with SiN waveguide width but is still expected to achieve efficient modulation with FoM < 3 V.cm for $w_{SiN} < 1000$ nm.

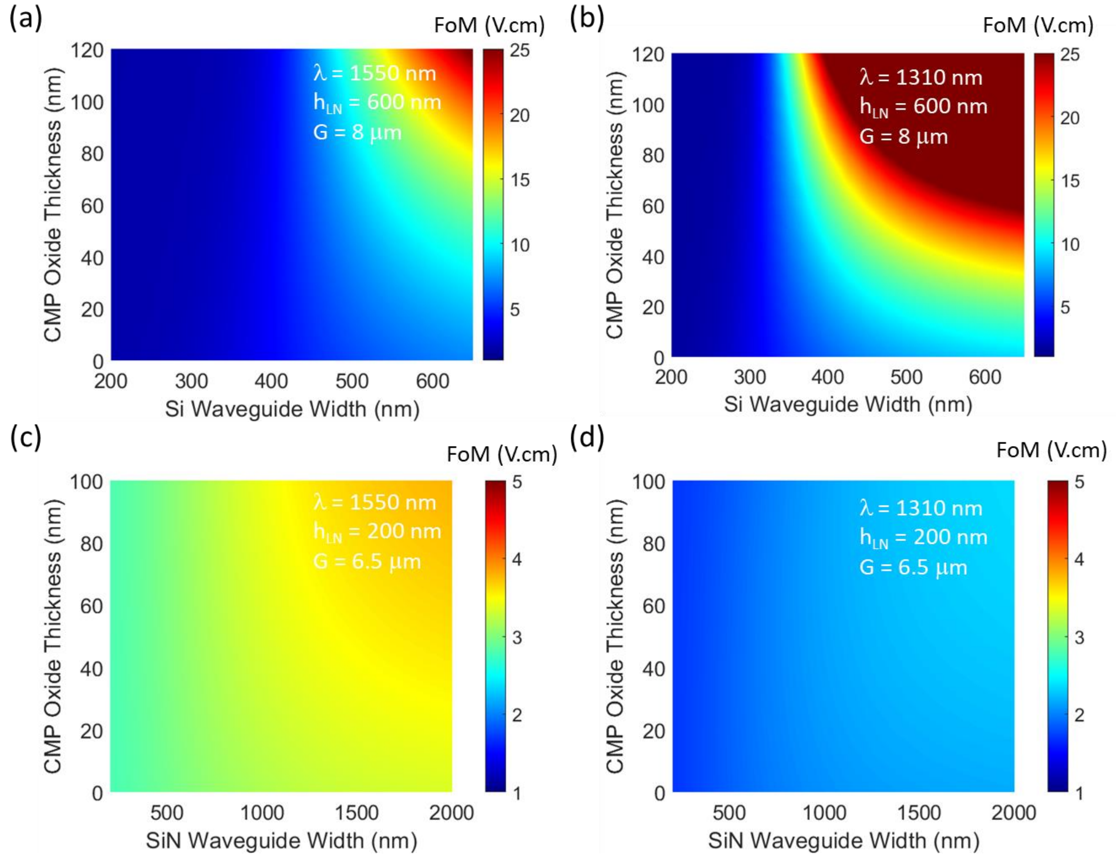

Figure 2.9: (a,b) The simulated FoM [Eq. (2.13)] of a hybrid Si/LN mode operating at (a) 1550 nm and (b) 1310 nm as a function of Si waveguide width and CMP oxide thickness when h_{Si} = 150 nm, h_{LN} = 600 nm, G = 8 μm. (c,d) The simulated FoM of a hybrid SiN/LN mode operating at (a) 1550 nm and (b) 1310 nm as a function of Si waveguide width and CMP oxide thickness when h_{SiN} = 200 nm, h_{LN} = 200 nm and G = 6.5 μm and 5.5 mm, respectively.

This simplified FoM will, in the worst case, underestimate $V_\pi L$ by a factor of

$$R = \frac{\Gamma_{mo}}{\Gamma_{LN}} = A + B\exp\left(-C * G\right) + D * G \tag{2.14}$$

from the assumption that the RF field is constant in the vicinity of the hybrid optical mode, where A, B, and C are fitting parameters. To attain a more accurate simulated value of $V_\pi L$, the RF mode must also be simulated. However, now that a local minimum of FoM can be determined swiftly, specific RF modes can be evaluated in the region of this optimized FoM as

opposed to blindly searching over the vast parameter space. Figure 2.10 shows the underestimation factor, R, as a function of G for different LN film thickness (as these are the two variable parameters in the cross section, Figure 2.7, that impact the RF mode). With these specific R values determined, the $V_\pi L$ can be approximated very quickly based on the optical simulation sweeps that generated Figure 2.8 and Figure 2.9 as

$$V_\pi L_{app} = \frac{FoM}{R} = \frac{n_{eff}\lambda G}{2n_e^4 r_{33} R \Gamma_{LN}} \tag{2.15}$$

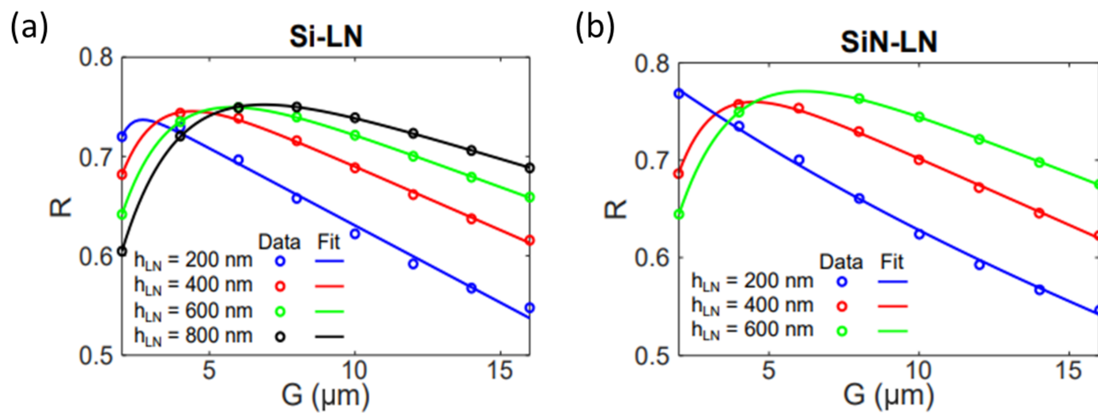

Figure 2.10: The simulated (circles) and fitted (lines) data of the fraction $R = \frac{\Gamma_{mo}}{\Gamma_{LN}}$ as the electrode gap distance, G, and h_{LN} are varied for a (a) hybrid Si/LN and (b) SiN/LN cross section with $h_{cmp} = 0$ nm, $\lambda = 1550$ nm, and $f_{RF} = 100$ GHz.

From Figure 2.10(a) and Figure 2.10(b), using FoM underestimates $V_\pi L$ by a factor of 0.75 (0.7) when G = 8 μm (6 μm) and $h_{LN} = 600$ nm (200 nm) for the Si(N)/LN hybrid MZMs. This factor can then be applied to the simulated FoM as a function of waveguide width and h_{cmp} to generate Figure 2.11 to determine the optimal design for low-voltage hybrid bonded MZMs in the C-band and O-band.

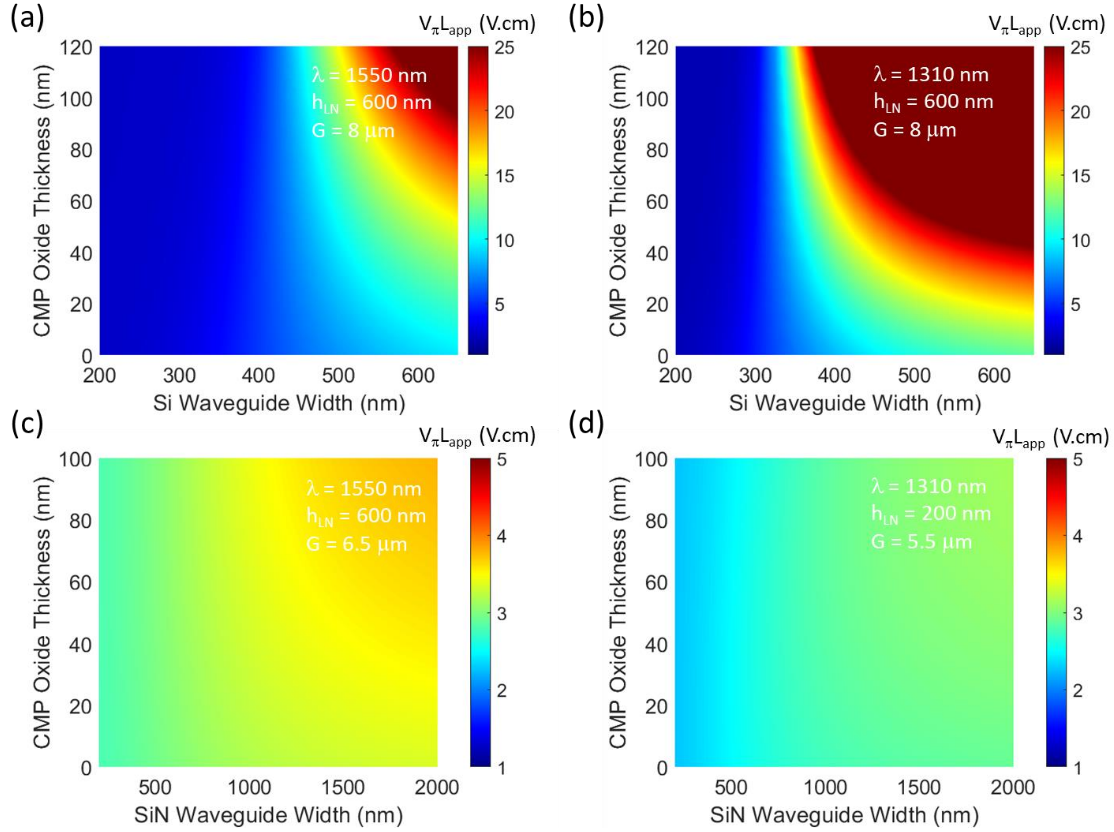

Figure 2.11: (a) The simulated $V_\pi L_{app}$ as a function of Si waveguide width and CMP oxide thickness at $\lambda = 1550$ nm. (b) The simulated $V_\pi L_{app}$ as a function of Si waveguide width and CMP oxide thickness at $\lambda = 1310$ nm. The constant parameters of the Si/LN waveguide are $h_{Si} = 150$ nm, $h_{LN} = 600$ nm, G = 8 μm, and. (c) The simulated $V_\pi L_{app}$ as a function of SiN waveguide width and CMP oxide thickness at $\lambda = 1550$ nm. (d) The simulated $V_\pi L_{app}$ as a function of SiN waveguide width and CMP oxide thickness at $\lambda = 1310$ nm. The constant parameters of the SiN/LN waveguide are $h_{SiN} = 200$ nm, $h_{LN} = 200$ nm, G = 6.5 μm and 5.5 μm, respectively.

Judging from the results shown in Figure 2.11, the naïve designer would state that the optimal design would be to minimize the Si waveguide width to the narrowest possible fabrication limit and have a thick CMP oxide separating the TFLN and Si layers in order to optimize $V_\pi L$. While at the surface this is true, this choice completely neglects optical propagation loss due to the mode interacting with the metal electrodes. Electrodes act as perfect electrical conductors, and as such, absorb electromagnetic fields causing large amounts of loss. Figure 2.12 shows the simulated optical propagation loss, α_{opt}, as $w_{Si(N)}$ and h_{cmp} are varied for

the Si/LN and SiN/LN modes at 1550 nm and 1310 nm operational wavelengths, respectively. As can be seen, α_{opt} increases as A_{eff} increases for this constant electrode gap width (G = 8 µm and ~6 µm). For this example, to maintain $\alpha_{opt} < 1$ dB/cm, then $w_{Si} > 250$ nm and $h_{cmp} < 80$ nm and $w_{SiN} > 800$ nm and $h_{cmp} < 60$ nm (as noted by the dark red regions in Figure 2.12). Again, this is for the specified 8 µm gap and 600 (400) nm thick LN film on a single layer of Si(N) waveguides. These ranges are subject to change as these parameters change.

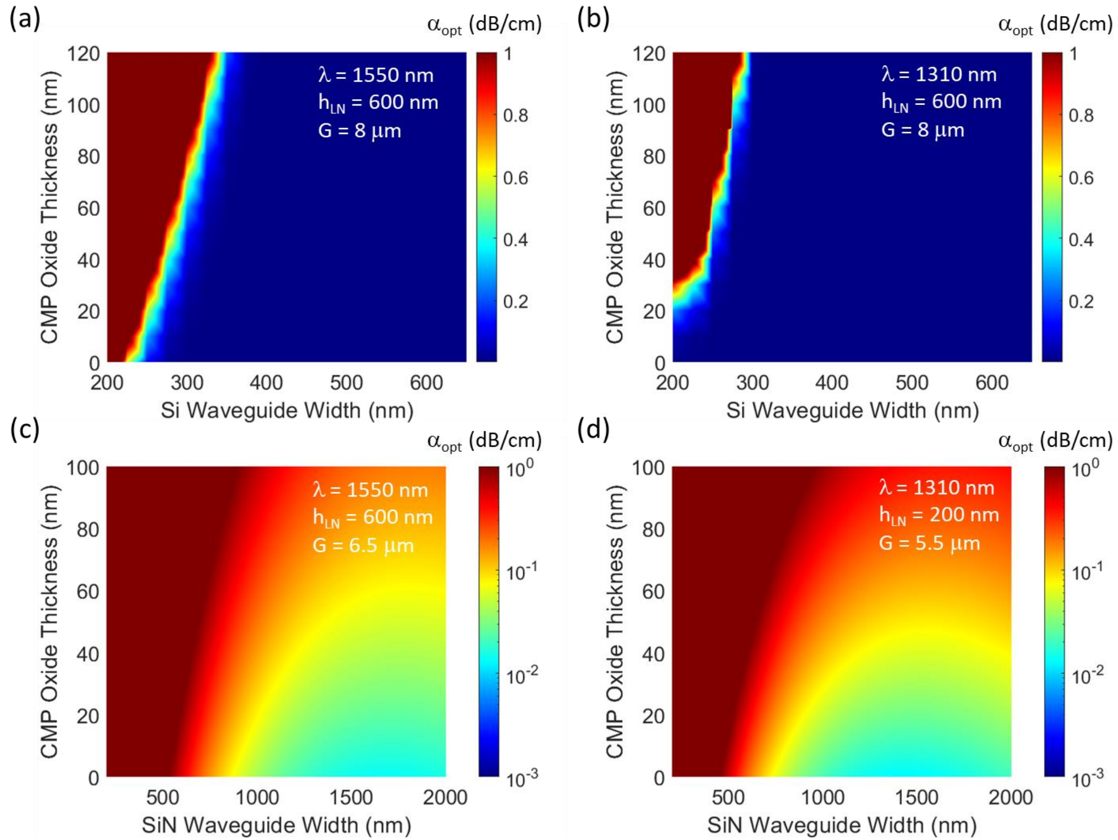

Figure 2.12: (a) The simulated α_{opt} as a function of Si waveguide width and CMP oxide thickness at λ = 1550 nm. (b) The simulated α_{opt}, as a function of Si waveguide width and CMP oxide thickness at λ = 1310 nm. The constant parameters of the Si/LN waveguide are h_{Si} = 150 nm, h_{LN} = 600 nm, G = 8 µm, and. (c) The simulated α_{opt} as a function of SiN waveguide width and CMP oxide thickness at λ = 1550 nm. (d) The simulated α_{opt}, as a function of SiN waveguide width and CMP oxide thickness at λ = 1310 nm. The constant parameters of the SiN/LN waveguide are h_{SiN} = 200 nm, h_{LN} = 200 nm, G = 6.5 µm and 5.5 µm, respectively.

With the waveguide widths determined in mind of minimizing $V_\pi L$ and α_{opt}, this sets a constraint on the optical group index, n_g, of the hybrid modes. Figure 2.13 show the n_g as a function of waveguide width and CMP oxide thickness for the Si/LN and SiN/LN with 600 nm LN and 200 nm LN film thicknesses, respectively at the C- and O-bands. The n_g of a waveguide follows the trend of the n_{eff} because $n_g = n_{eff} - \lambda \frac{dn_{eff}}{d\lambda}$. Thus, as the underlying Si(N) waveguide width increases and more of the hybrid mode resides in the waveguide core, then n_g increases. This effect is seen much more dramatically in the Si/LN case as $n_{Si} > n_{LN}$ which offers a much stronger dispersion control via Si waveguide tuning compared to the SiN/LN counterpart. To achieve high-speed modulation the RF traveling wave electrodes need to be designed in such a way to yield an RF effective index, n_m, that equates to n_g ideally for all frequencies and across all CMP oxide thicknesses. For example, if the RF effective index (n_m) was expected to be 2.23, then looking at Figure 2.13, the optimal w_{Si} would be less than 300 nm and the h_{cmp} must be around 50 nm; whereas the optimal w_{SiN} would be between 800 nm and 1400 nm, but the h_{cmp} must be less than 20 nm thick. However, to maintain low α_{opt}, then w_{Si} cannot be narrower than 250 nm. It is important to keep all aspects of the modulator design in mind to achieve low-voltage, high bandwidth, and low-loss operation. Table 2.1 details the parameters chosen for the Si and SiN phase-shifter sections to be fabricated. Multiple Si waveguide widths were chosen to account for potential variations in hcmp from the target value of 40-50 nm.

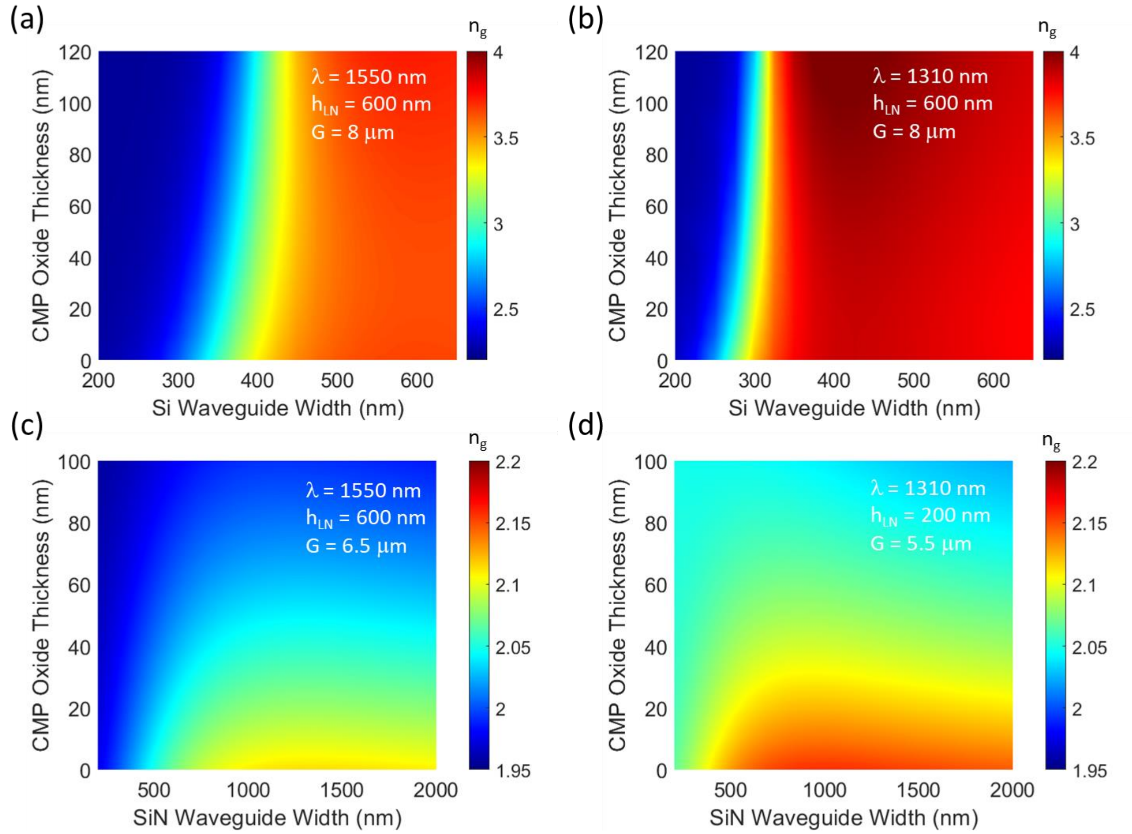

Figure 2.13: (a) The simulated n_g as a function of Si waveguide width and CMP oxide thickness at λ = 1550 nm. (b) The simulated n_g as a function of Si waveguide width and CMP oxide thickness at λ = 1310 nm. The constant parameters of the Si/LN waveguide are h_{Si} = 150 nm, h_{LN} = 600 nm, G = 8 µm, and. (c) The simulated n_g as a function of SiN waveguide width and CMP oxide thickness at λ = 1550 nm. (d) The simulated n_g, as a function of SiN waveguide width and CMP oxide thickness at λ = 1310 nm. The constant parameters of the SiN/LN waveguide are h_{SiN} = 200 nm, h_{LN} = 200 nm, G = 6.5 µm and 5.5 µm, respectively.

Table 2.1: The Si(N) waveguide dimensions chosen for fabrication in the hybrid phase-shifter section of the MZMs at the O- and C-bands.

MZM λ-band	w_{Si}	h_{Si}	w_{SiN}	h_{SiN}
O-band	225 nm	150 nm	900 nm	200 nm
	250 nm			
C-band	275 nm			
	300 nm			

2.2.2 Transitioning Between the Feeder and Hybrid Modes

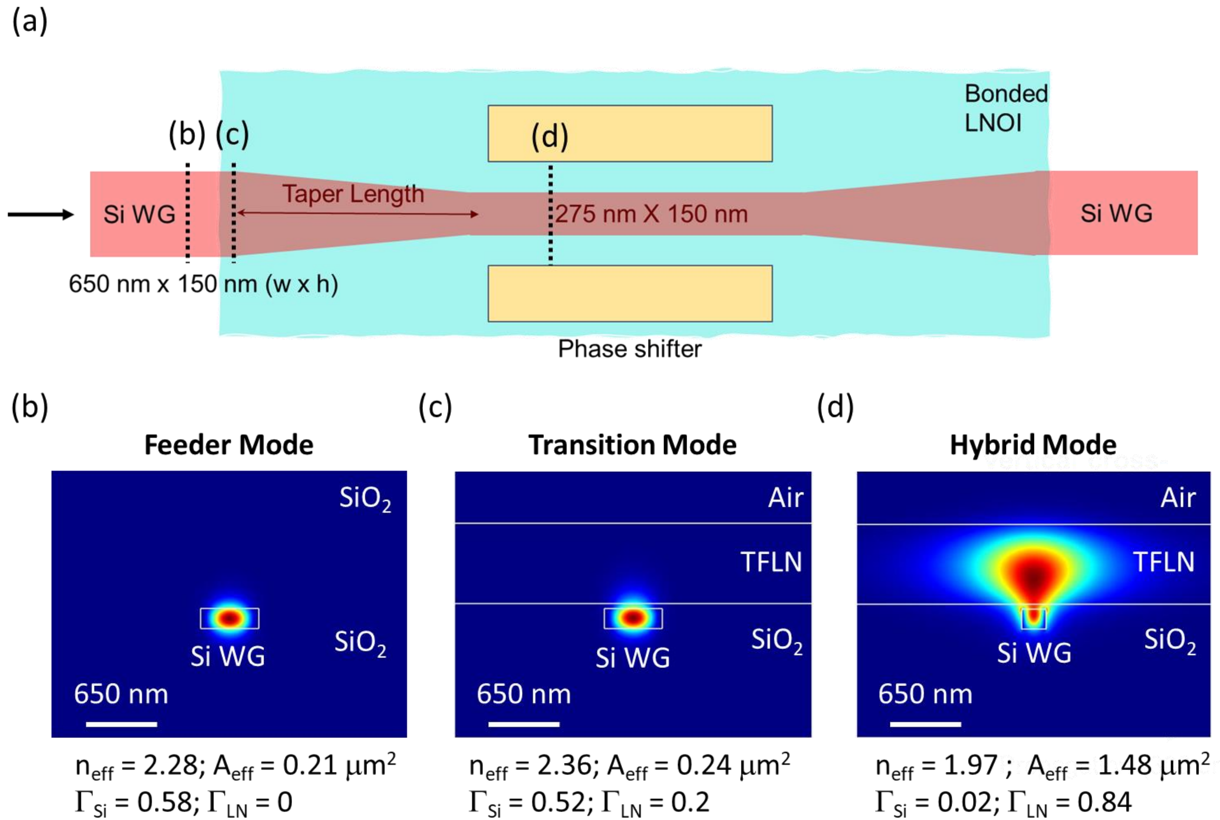

Figure 2.14: Top-view schematic (not to scale) of the Si/LN transition region and phase shifter (one arm of MZM). The transition region consists of the transition waveguide and adiabatic tapers (shown in green), and the phase shifter section consists of the hybrid waveguide (shown in red). Cross-sectional simulated Poynting vector of the (b) feeder Si waveguide (no LN film), (c) transition Si waveguide, and (d) hybrid Si/LN waveguide.

As shown in Figure 2.14(a), the light transitions from a feeder section (outside of the bonded region) to the hybrid mode (within the bonded region). For the Si/LN platform, this transition can be quite simple because the refractive index of Si is higher than that of LN ($n_{Si} > n_{LN}$). This means that for the wide Si waveguide width in the feeder section (further described in Section 2.2.4), the majority of the mode resides in the Si core (58%). There will be an amount of loss at the initial air-to-LN interface from Fresnel reflections and slight modal overlap differences. Figure 2.14(b) and Figure 2.14(c) show the simulated modes before and after the bonded LN interface at 1550 nm as an example and below the cross-sections are the simulated

modal characteristics. The difference in n_{eff} between these modes is 0.08 which results in an expected loss of only about 0.074 dB. Because the mode fraction in Si (Γ_{Si}) is similar, it is not expected that this loss will change significantly at higher optical powers when the refractive index of Si changes slightly.

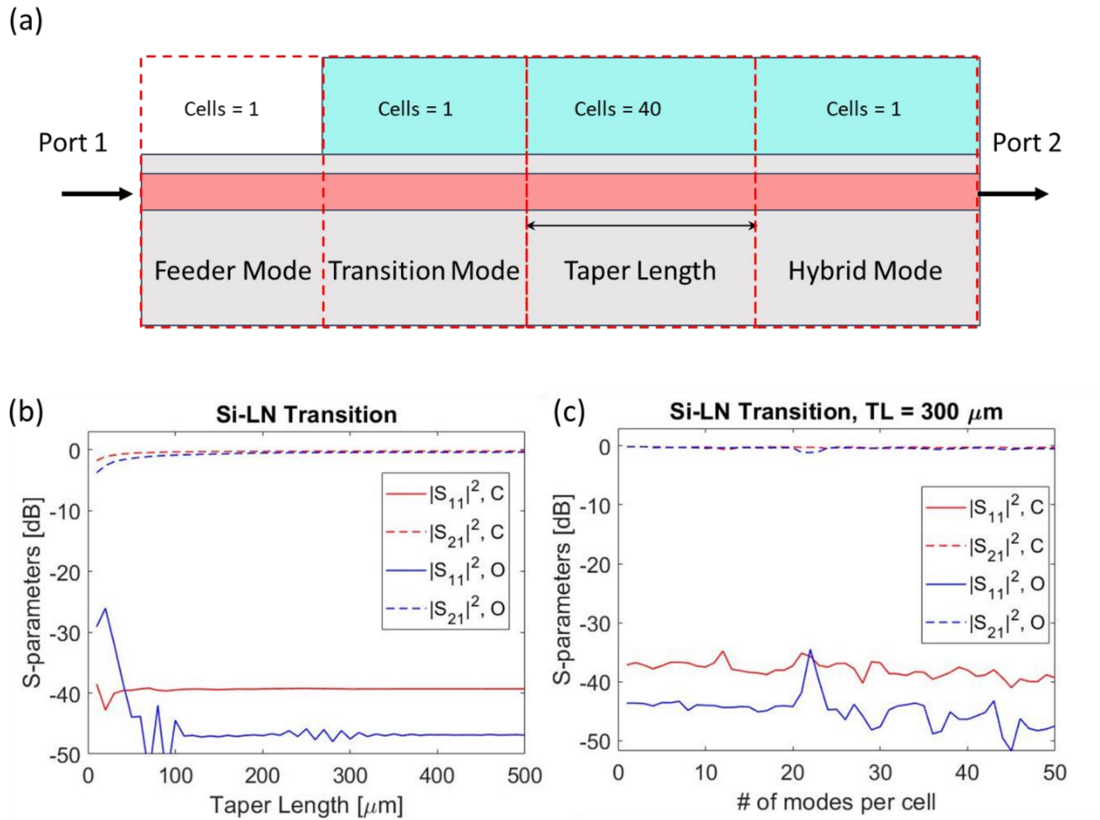

Figure 2.15: (a) A side-view (not to scale) of the Si/LN transition across the bonded region with an adiabatic taper section to the hybrid mode. The simulated S-parameters (transmission and reflection) as a function of (b) taper length and (c) number of modes per cell in the taper section for operation wavelengths at 1550 nm (C) and 1310 nm (O) using Lumerical's EME solver.

Once beyond the TFLN bonded edge, the Si waveguide can be adiabatically tapered to the optimized hybrid waveguide width determined from the modelling of Section 2.2.1. A side-view of one of the MZM arms at the bonded LN interface is shown in Figure 2.15(a), which includes an adiabatic taper section to narrow the underlying Si waveguide to the designed hybrid mode. Lumerical's Eigenmode Expansion (EME) solver was used to model this transition which

includes the Air-LN interface loss (mode and n_{eff} mismatch) as well as the adiabatic taper loss. EME splits the structure into user-defined cells along the propagation direction and solves for the optical mode characteristics per cell. The modes are then compared cell-to-cell to determine the amount of power that transmits from port 1 to port 2 in Figure 2.15(a). The S-parameters of such a transition and taper as a function of taper length (Figure 2.15(b)) and the number of optical modes (Figure 2.15(c)) for C-band (red traces) and O-band (blue traces) incident light. The results of which are transition losses less than 0.5 dB for taper lengths greater than 100 μm.

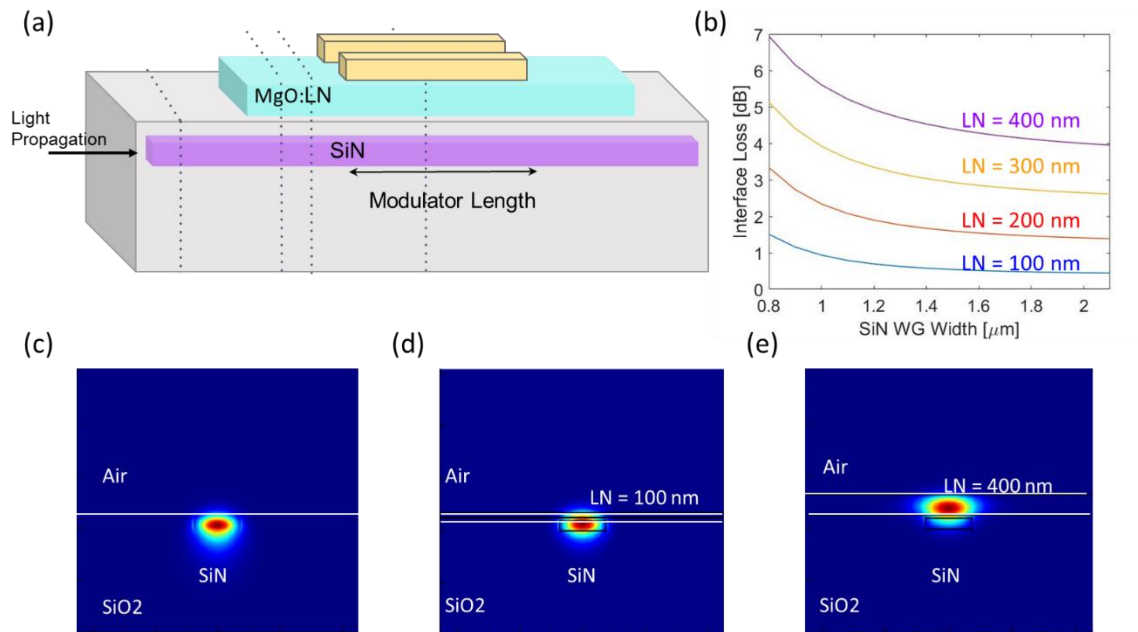

Figure 2.16: (a) A perspective view of a single layer SiN waveguide transitioning across the bonded MgO:LN film. (b) The simulated interface loss due to mode and neff mismatch at the Air-LN interface as a function of SiN waveguide width and LN film thickness for an operation λ of 1550 nm. The SiN thickness is 200 nm. (c) The simulated SiN mode in the feeder section. (d) The simulated SiN/LN mode with hLN = 100 nm. (e) The simulated SiN/LN mode with hLN = 400 nm.

While such transitions are simple for the Si/LN platform, the single layer SiN/LN structures (Figure 2.16(a)) require more design and intuition as the refractive index of SiN is approximate to that of LN ($n_{SiN} \sim n_{LN}$). Figure 2.16(b) is the calculated loss from the Air-LN interface of a SiN/LN structure for different LN film thicknesses as a function of SiN waveguide

width when the SiN waveguide is 200 nm thick and the CMP oxide layer is 50 nm thick. The weaker refractive index of SiN compared to Si yields less modal confinement and control by simply tapering the SiN waveguide, resulting in large modal mismatch as shown by Figure 2.16(c)-(d). Thicker LN films, such as 400 nm, can result in 4 dB of loss per transition even if the SiN waveguide is 2 μm wide. For LN film thicknesses less than 200 nm, the interface loss reduces to less than 2 dB.

Low loss transitions in a SiN/LN platform have been demonstrated by introducing a secondary Si-rich SiN layer to act as the feeder section [20]. This additional layer is vertically separated from the LN film by about 600 nm, which makes the interface loss from the bonded edge minimal. A vertical directional coupler was then implemented to bring the propagating mode into the hybrid phase shifting section. Others have shown that using much thicker SiN layers can reduce the interface losses as well [58]. Unfortunately, due to time and fabrication cost restrictions, I was limited to using only a single layer of SiN for the wafers allocated by Sandia National Laboratories; as such, the optical insertion losses of the fabricated SiN/LN devices reported in this dissertation may be impacted by this.

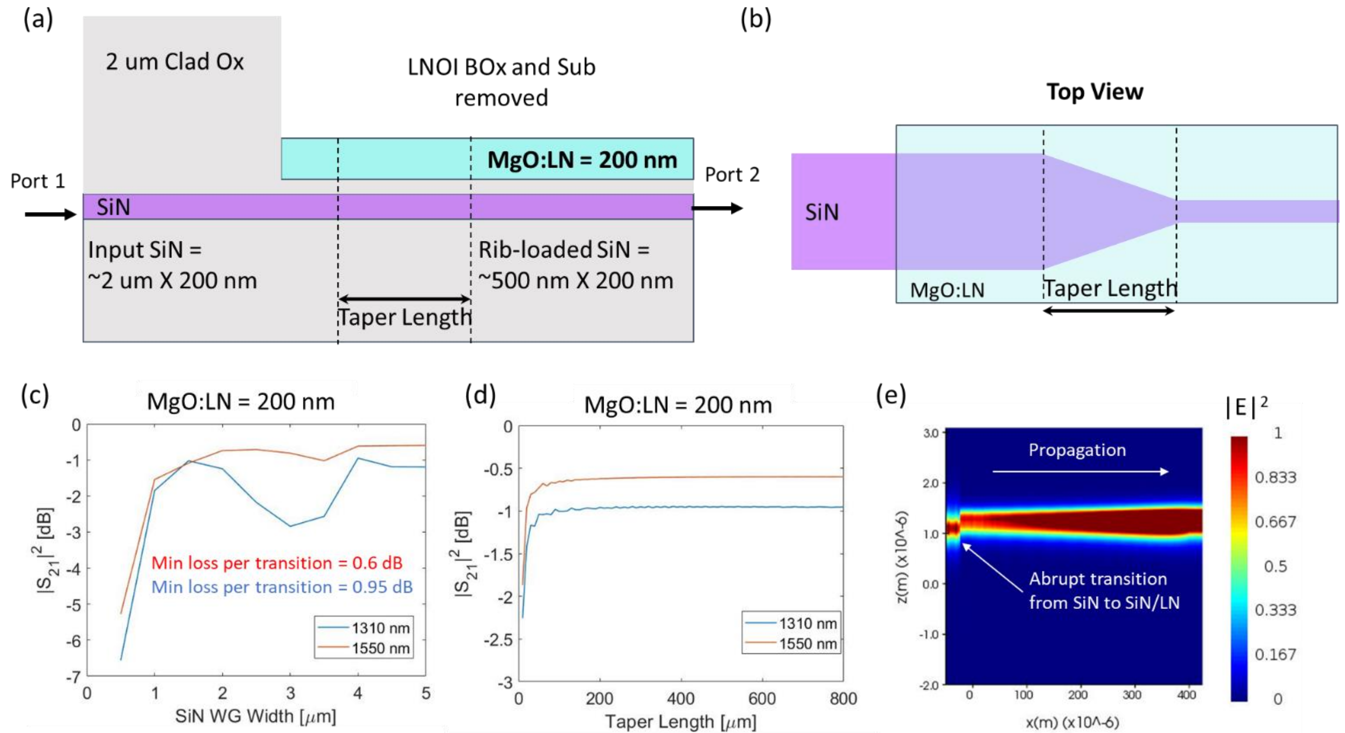

Figure 2.17: (a) A side-view diagram of the proposed single layer SiN/LN transition with a deposited cladding oxide before the bonded region. (b) A top-view diagram of the proposed single layer SiN/LN transition. The simulated $|S_{21}|^2$ of the transition shown in panel (a) for 1310 nm (blue) and 1550 nm (red) operational wavelengths as a function of (c) SiN waveguide width and (d) adiabatic taper length. (e) The simulated E-field intensity of the optical mode as a function propagation distance (x-axis) as it propagates from left-to-right.

This limit of only having a single layer of SiN waveguides to route into and out of the hybrid bonded region puts a limit on the bonded LN film thickness to maintain low optical losses to less than 200 nm. Furthermore, a deposited oxide layer may help reduce these interface losses as shown in Figure 2.17. The cladding oxide before the bonded LN film helps reduce the mode and n_{eff} mismatch between the feeder and transition modes. With this an inverse taper can also be used to widen the SiN waveguide (see Figure 2.17(b) for a top-view diagram). Figure 2.17(c) and (d) are EME simulation results of the transmission, $|S_{21}|^2$, of the diagrams shown in Figure 2.17(a) and Figure 2.17(b) for incident light at 1550 nm (red traces) and 1310 nm (blue traces). These simulations predict a minimum loss per transition of 0.6 dB and 0.95 dB for 1550 nm and

1310 nm operation wavelengths, respectively. Figure 2.17(e) is an EME mode power monitor simulation showing light propagation from left-to-right. There is an abrupt transition from the SiN feeder waveguide to the transition waveguide from the vertical separation between the SiN waveguide mode and the hybrid SiN/LN mode [which causes the loss in Figure 2.17(a) and Figure 2.17(b)], but still power transfers to the hybrid SiN/LN mode efficiently.

2.2.3 Edge Couplers

Efficient edge coupling of optical power from single-mode fibers to photonic chips requires modal and refractive index matching between the gaussian fiber mode and the waveguide mode. Typical single-mode fibers have mode field diameters (MFDs) on the order of 9 µm at 1550 nm, while Si(N) waveguides have MFDs on the order of 100 – 1000 nm. Lensed tapered fibers or high numerical aperture fibers can be used to lessen the MFD mismatch, but to further improve efficiency inverse tapers at the edges of the Si photonic chips (labelled in Figure 2.6(c)) can be applied which pushes the mode into the surrounding SiO_2 and increases the modal A_{eff}. Figure 2.18(a) and Figure 2.18(b) are the simulated edge coupling loss (which takes into account mode matching and refractive index differences) as the Si and SiN waveguide tip narrows, respectively, where the different colors correspond to different operational wavelengths.

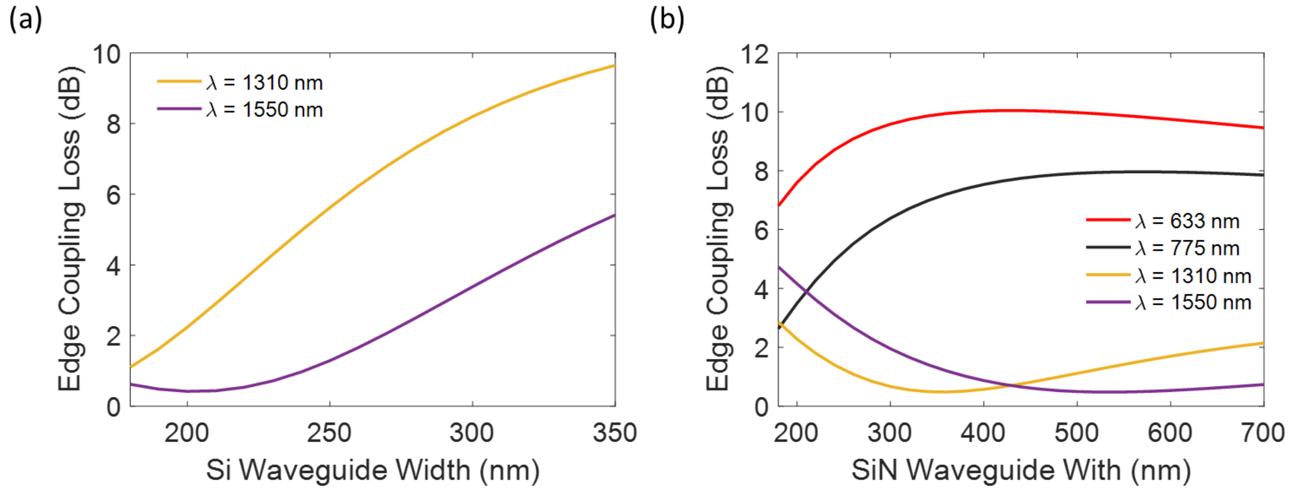

Figure 2.18: The simulated edge coupling loss (per facet) as a function of taper tip width for (a) a single layer Si waveguide that is 150 nm thick and (b) a single layer SiN waveguide that is 200 nm thick at different operational wavelengths.

From Figure 2.18(a) and Figure 2.18(b), the Si taper tip width (at the edge of the chips) should be 180 - 200 nm wide to obtain the best modal overlap and power coupling from a fiber with a MFD of 2.5 μm when the input λ is 1310 nm or 1550 nm. The minimum waveguide taper tip width of 180 nm was limited by the resolution requirements of the foundry process provided for the SOI wafers. Lower edge coupling losses can be achieved with smaller resolution or by using different types of edge couplers which require further fabrication steps [59–62]. The SiN taper tips do not need to be at the resolution limit like the Si counterparts because of the lower refractive index of SiN. The simulations at 1310 nm and 1550 nm show that the tip width should be 400 nm and 600 nm wide, respectively. However, at shorter visible wavelengths, the optical mode becomes more confined at narrower waveguide widths, which yields a much larger edge coupling loss unless the taper tip width is reduced to the minimum. Others have shown that an array of SiN inverted tapers can also reduce edge coupling losses to larger MFD fibers [63–65], however multiple layers of SiN were not feasible at the time of SOI production for these wafers.

2.2.4 Single Mode Feeder Waveguides

Once light is coupled to the Si(N) photonic chips, it must be routed to the phase-shifting section. These sections are denoted the 'feeder' waveguides in this dissertation (see Figure 2.19(a) and Figure 2.19(b) for cross sections of the Si and SiN feeder sections, respectively). Single-mode operation waveguides are defined as structures that only propagate the fundamental TE and TM modes. Figure 2.19(c)-(d) and Figure 2.19(e)-(f) show the simulated n_{eff}, of the first few modes as a function of waveguide width for both Si and SiN waveguides for operational wavelengths in the C-band and O-band. The Si waveguide thickness is set to 150 nm, while the SiN waveguide thickness is set to 200 nm. From these simulations, the feeder waveguide sections are chosen to be 650 nm wide for the O- and C-band Si devices to guide the fundamental TE_0 mode; whereas, the SiN feeder waveguides are set to 1200 nm and 1600 nm for the O-band and C-band devices, respectively.

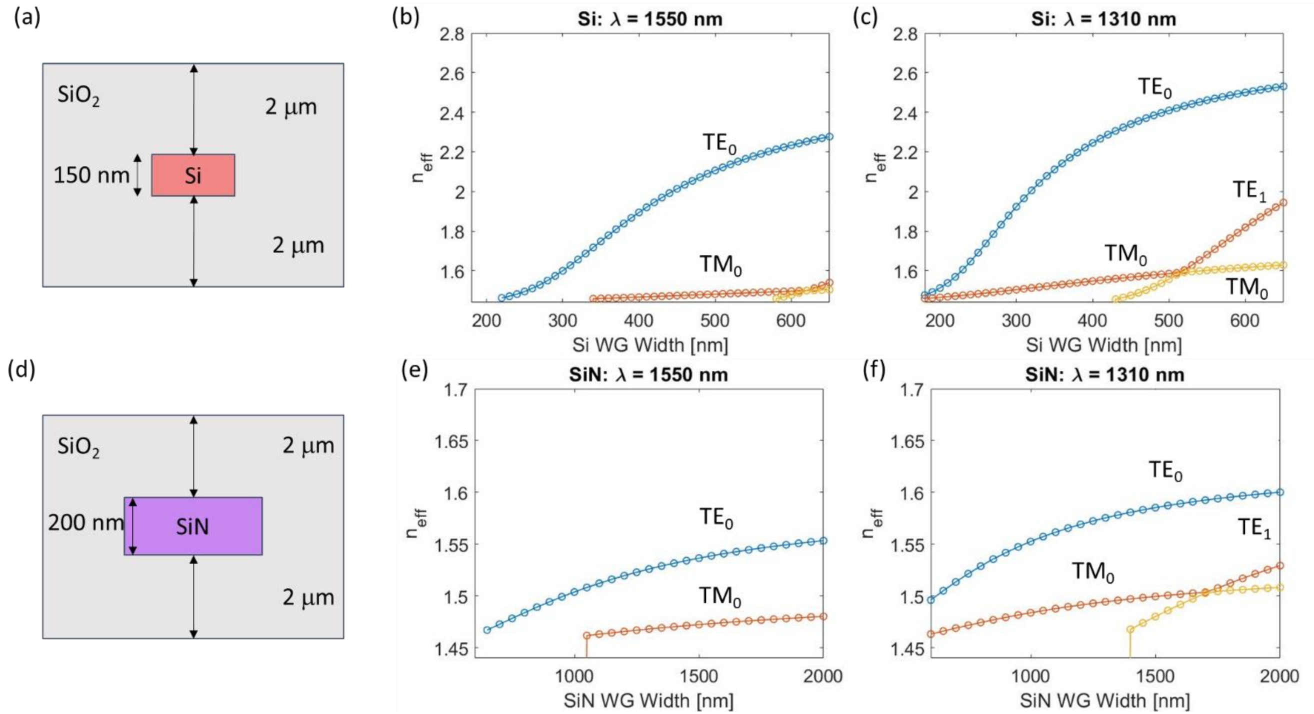

Figure 2.19: (a) A cross section of the Si feeder waveguide section with 150 nm thick Si clad with SiO_2. The simulated n_{eff} as of the cross section in panel (a) as a function of Si waveguide (WG) width at (b) λ = 1550 nm and (c) λ = 1310 nm, showing the guided modes. (d) A cross section of the SiN feeder waveguide section with 200 nm thick SiN clad with SiO_2. The simulated n_{eff} as of the cross section in panel (d) as a function of Si waveguide (WG) width at (e) λ = 1550 nm and (f) λ = 1310 nm, showing the guided modes.

2.2.5 2x2 MMI Couplers

MZMs operate by splitting the optical power in one waveguide into two equal paths, then recombined after the phase-shifting section to produce interference. This equal splitting can be achieved via directional couplers [48], y-splitters [66], or multi-mode interference couplers (MMIs) [67], the latter of which are used in the hybrid MZM structures reported in this dissertation. Figure 2.20(a) shows a top view schematic of a 2x2 MMI which consists of two tapered inputs and outputs with a central wide multimode core section. MMIs work under the principle of self-imaging interference where the input mode is decomposed into multiple higher order modes in the core, the length of which dictates the power in each output [68]. For a 2x2

MMI with the input and output waveguides symmetrically placed at $\frac{W_{mmi}}{3}$ as shown, then the length to acquire a 3-dB split at the outputs is given by

$$L_{3dB} = \frac{L_\pi}{2} = \frac{\pi}{\beta_0 - \beta_1} \approx \frac{4nW_{mmi}^2}{3\lambda} \tag{2.16}$$

where L_π is the beat length of the two lowest order modes in the core, $\beta_{0,1}$ is the propagation constants of the two lowest order modes, and W_{mmi} is the MMI core width [68].

EME simulations were performed to determine the optimal L_{3dB} for the Si(N) MZMs assuming thicknesses of 150 nm and 180 nm, respectively, and at various operational wavelengths. Figure 2.20(b) and Figure 2.20(c) shows L_{3dB} and the total loss at the output ports as a function of W_{mmi} for Si 2x2 MMIs at 1550 nm and 1310 nm, respectively. As an example, if the MMI width is 6 µm, then the length to achieve a 3-dB split at the outputs is 39 µm at 1550 nm and 48.9 µm at 1310 nm. Figure 2.20(d) shows the simulated power flow for a 6 µm wide by 39 µm long MMI where the light with wavelength of 1550 nm is input at port 1 and the output ports (3 and 4) have half the power.

Due to the dispersion of the 3-dB MMI splitters (inverse relation of L_{3dB} in Eq. (2.16)), there is a limit to the ideal 3-dB coupling ratio as the input source strays from the designed operational wavelength. Typically, researchers and industry alike quote a 3-dB MMI's 1 dB bandwidth to signify the wavelength range of which the output ports result in a 1 dB drop from the ideal output (4 dB in this case). As can be seen in Figure 2.20(e), the designed MMIs with 6 µm width each have 1 dB bandwidths greater than 100 nm around the designed operation wavelengths of 1250 nm (magenta), 1310 nm (blue), 1450 nm (cyan), 1550 nm (green), 1650 nm

(red), and 2000 nm (black) where for each the only difference in design is the MMI core length (labelled in the inset).

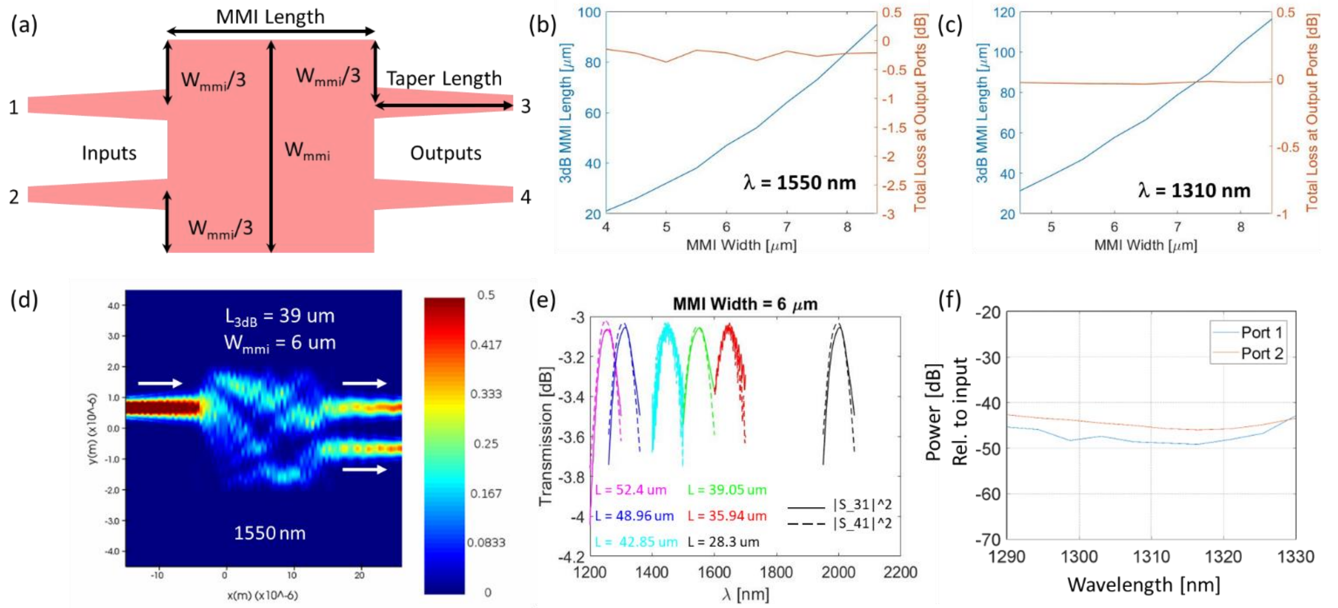

Figure 2.20: (a) A top-view schematic of a 2x2 MMI coupler of width W_{mmi}. (b) The simulated L_{3dB} (left, blue) and total loss at the output ports (right, orange) as a function of W_{mmi} at λ = 1550 nm. (c) The simulated L_{3dB} (left, blue) and total loss at the output ports (right, orange) as a function of W_{mmi} at λ = 1310 nm. (d) A top-view power flow simulation using EME for a 6 µm wide by 39 µm long MMI 3-dB splitter. (e) The simulated output transmissions of different MMIs designed for 3-dB splitting ratios with central λs of 1250, 1310, 1450, 1550, 1650, and 2000 nm. (f) FDTD simulations of the reflections ($|S_{11}|^2$ and $|S_{21}|^2$) for a 2x2 MMI designed for O-band operation.

2x2 MMI couplers are chosen here as opposed to 1x2 MMIs because they result in negligible reflections at the input port [69] . This is particularly important for potential integrated lasers with MZMs as reflections back to the light source will need to be minimized to avoid damage. Figure 2.20(f) shows the simulated reflections back to the input ports (1 and 2) when the input is at port 1 for a 2x2 SiN MMI designed for O-band operation using FDTD, resulting in $|S_{11}|^2$ and $|S_{21}|^2$ less than -40 dB. To further reduce these reflections, the edges of the MMI can be angled as shown in Figure 2.21(a) [70]. Such angled 2x2 MMIs result in $|S_{11}|^2$ and $|S_{21}|^2$ less than -60 dB [see Figure 2.21(b)].

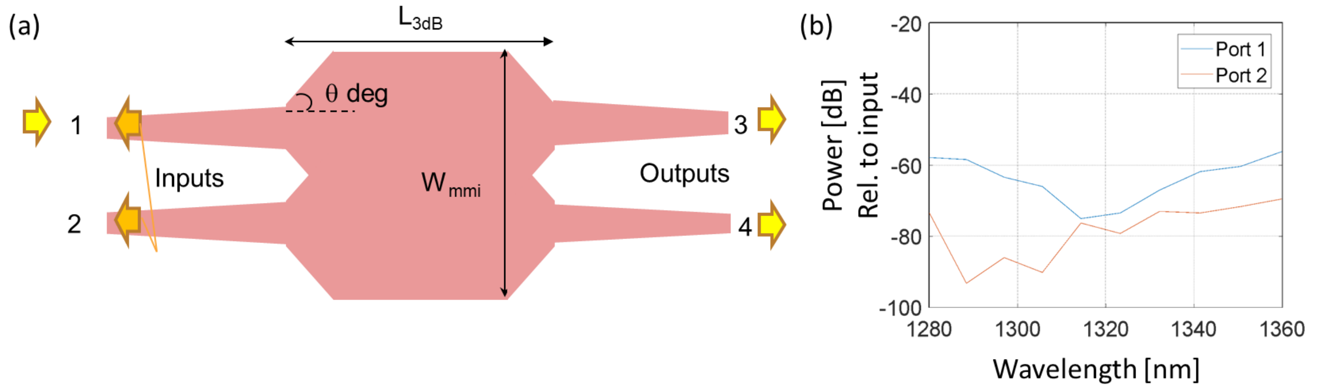

Figure 2.21: (a) A top-view schematic of the angled 2x2 MMI coupler. (b) FDTD simulations of the power reflected to the input ports (1 and 2) of the angled 2x2 MMI designed in the O-band.

2.3 SiN/LN Modulators with CMOS-compatible Buried Electrode Layers

A more general CMOS processed photonic circuit can contain multiple layers of materials including metal, Si(N) waveguides, dopants, and planarized oxides. In fact, standard Si photonic carrier-based MZMs use these buried metal layers (contacted using vias or pad openings) to apply external E-fields to the devices as opposed to Au (because Au is not offered in CMOS facilities) [11,13,71]. These buried metal layers can similarly be leveraged in our hybrid bonded platform to enable a fully CMOS compatible high-speed and low-voltage MZM (besides the final bonding stage). A cross-section of such a hybrid SiN/LN MZM with buried metal is demonstrated in Figure 2.22(a). The only difference between this design and the previous design with metal above the LN film is the placement of the driving electrodes. Thus the optical design would remain the same as Section 2.2.1 because the hybrid mode will be unchanged, as shown by the simulated hybrid modes at 1550 nm and 1310 nm in Figure 2.22(b) and Figure 2.22(c) for a 900 nm wide by 200 nm thick SiN waveguide and 200 nm thick TFLN. The metal CPWs would be defined and patterned below the patterned SiN layer, resulting in a

"buffer" SiO_2 layer between them (more details of fabrication in Section 4.2). This separation, and the further separation from the CMP layer between SiN and TFLN means the CPW mode will also be further from the EO material.

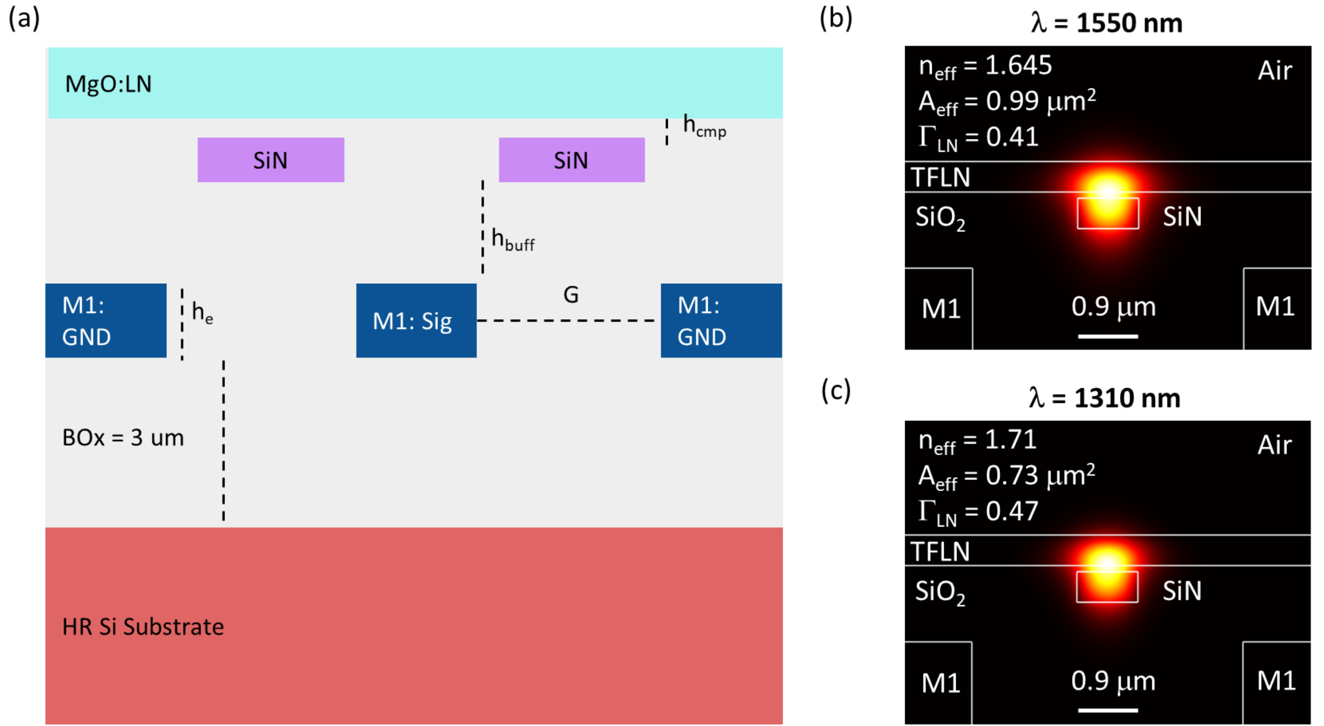

Figure 2.22: (a) A cartoon cross-section of a SiN/LN MZM which uses buried electrodes (M1 CMOS layer) as opposed to Au electrodes patterned above the LN film. There is an additional layer of oxide (labelled h_{buff}) between the buried metal and the SiN waveguides. (b) The simulated hybrid optical mode at λ = 1550 nm. (c) The simulated hybrid optical mode at λ = 1310 nm. The constant SiN/LN parameters are w_{SiN} = 900 nm, h_{SiN} = 200 nm, h_{cmp} = 40 nm, h_{buff} = 220 nm, h_{LN} = 200 nm, and G = 4 μm.

Figure 2.23(a) and Figure 2.23(b) shows the simulated $V_\pi L$ of such a buried electrode (BE) modulator with 200 nm thick LN a SiN waveguide that is 900 nm wide by 200 nm thick as a function of G and the buffer SiO2 thickness, h_{buff} at 1550 nm and 1310 nm, respectively. If h_{buff} can be maintained to less than 250 nm, then there is only a small impact (< 10% variation) in the expected modulation efficiency per G. However, the electrodes being vertically separated from the hybrid mode (and particularly away from the larger lobe near the top of the LN film) does

help reduce phase-shifter α_{opt} [Figure 2.23(c) and Figure 2.23(d)]. This reduction in α_{opt} from the metal interaction allows G to be reduced compared to a SiN/LN MZM made with electrodes above the LN film (Section 2.2.1) before reaching $\alpha_{opt} > 1$ dB/cm. The performance of such buried metal SiN/LN MZMs will be further demonstrated in Chapter 8.

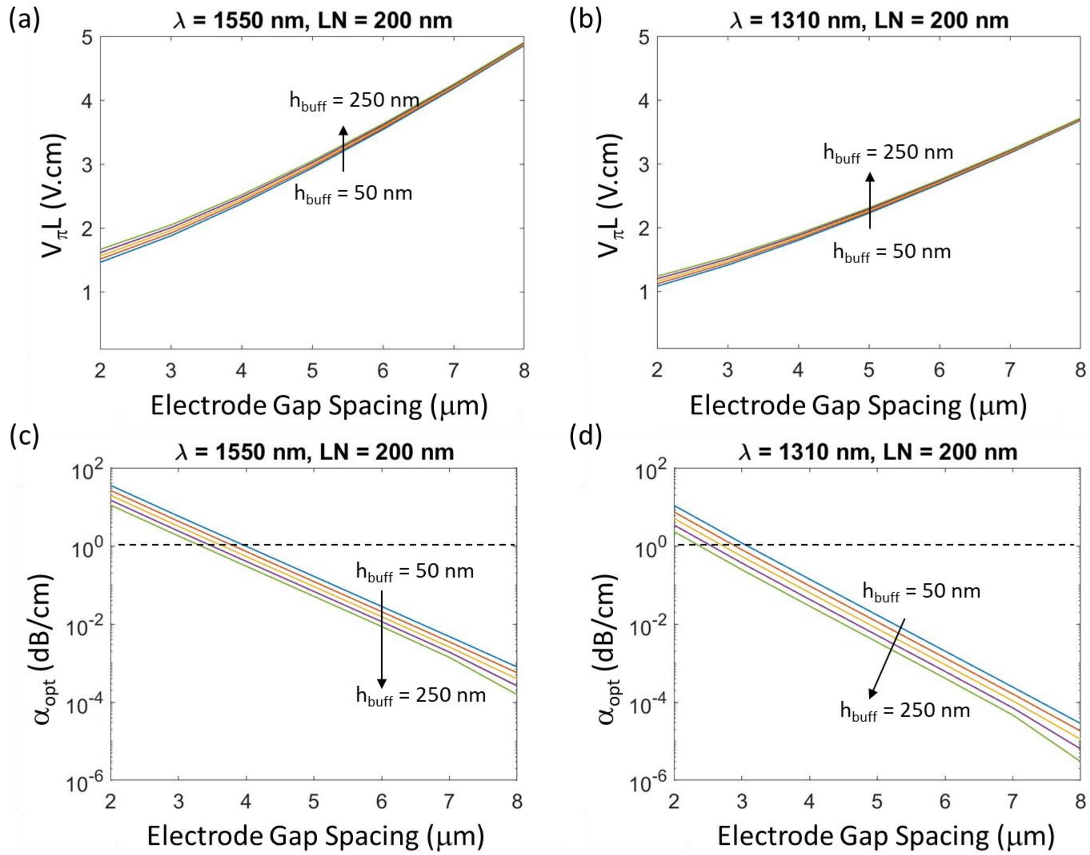

Figure 2.23: The simulated $V_{\pi}L$ as a function of electrode gap spacing, G, and hbuff of the cross-section in Fig for (a) l = 1550 nm and (b) l = 1310 nm. The simulated α_{opt} as a function of G and h_{buff} of the cross-section in Fig for (a) λ = 1550 nm and (b) λ = 1310 nm. The assumed constants are w_{SiN} = 900 nm, h_{SiN} = 200 nm, h_{cmp} = 50 nm, h_{LN} = 200 nm, h_e = 0.87 μm, and h_{BOx} = 3 μm.

2.4 A SiN/LN Platform for Low-Voltage Modulators from the Visible to Telecom Wavelengths

One major benefit of utilizing SiN as opposed to Si features is the fact that SiN has a transparency window that matches that of LN (350 nm - 4500 nm), whereas Si becomes highly

absorbing for $\lambda < 1100$ nm. The majority of high-speed EO modulators have been demonstrated in the telecom regime (particularly the C-band) as optical gain from Erbium-doped fiber amplifiers (EDFAs) is readily available and single-mode optical fibers have low attenuation in this regime. Visible to near infrared (NIR) photonics could drastically benefit communications, spectroscopy, biomedical sciences, quantum information processing and laser technology [72–76]. Visible light communications primarily utilize direct modulation techniques (of the laser diodes) which limit the 3-dB bandwidths to less than a few GHz and data rates less than 10 Gbps [77–79]. To date there has been little progress in developing visible-to-NIR EO modulators with low-voltage and high-speed performance. Here I will demonstrate a SiN/LN hybrid bonded modulator designs for V_π in the sub-volt range operating in the red (633 nm) and NIR (~780 nm) wavelength ranges.

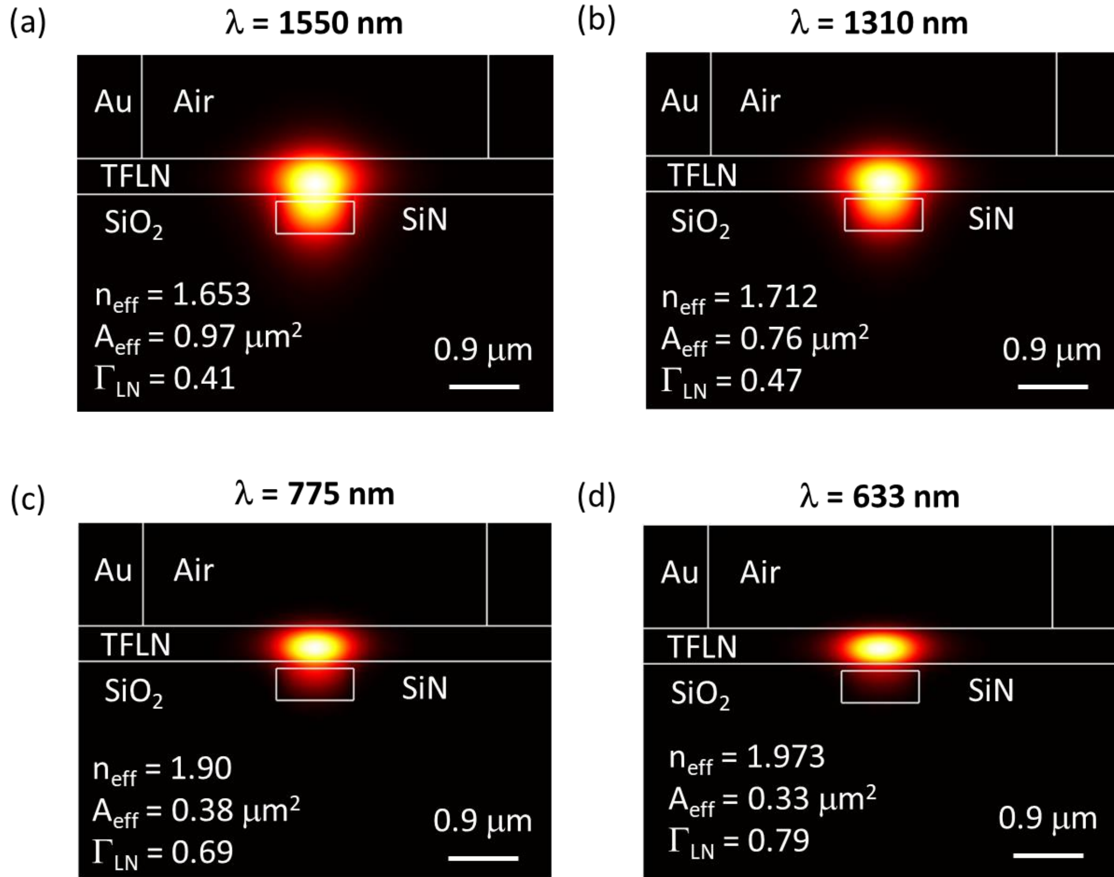

Figure 2.24: The simulated optical modes of the SiN/LN phase-shifter section at the following operation wavelengths: (a) 1550 nm, (b) 1310 nm, (c) 775 nm, and (d) 633 nm. The MgO:LN film thickness is 200 nm and the SiN waveguide is 900 nm wide by 180 nm thick for all four simulations. The simulated n_{eff}, A_{eff}, and Γ_{LN} are inset.

As can be seen in Eq. (2.7), the V_π of an EO modulator is directly dependent on the operation wavelength that is being modulated. Thus, compared to a SiN/LN MZM designed for 1550 nm operation, a 775 nm modulator is already a factor of 2 more efficient. This efficiency increases further however because as λ decreases, so does the hybrid mode A_{eff} (as shown by the simulated hybrid SiN/LN modes in Figure 2.24)and thus the optical loss due to interaction with the driving electrodes. This means that the electrode gap, G, can also be reduced for further improvements to the modulation efficiency in a short wavelength device. Figure 2.25 are the simulated $V_\pi L$ of SiN/LN MZMs with 200 nm MgO:LN films, SiN waveguides that are 900 nm

wide by 180 nm thick as a function of CMP oxide thickness and G for operation λ in the telecom and visible ranges.

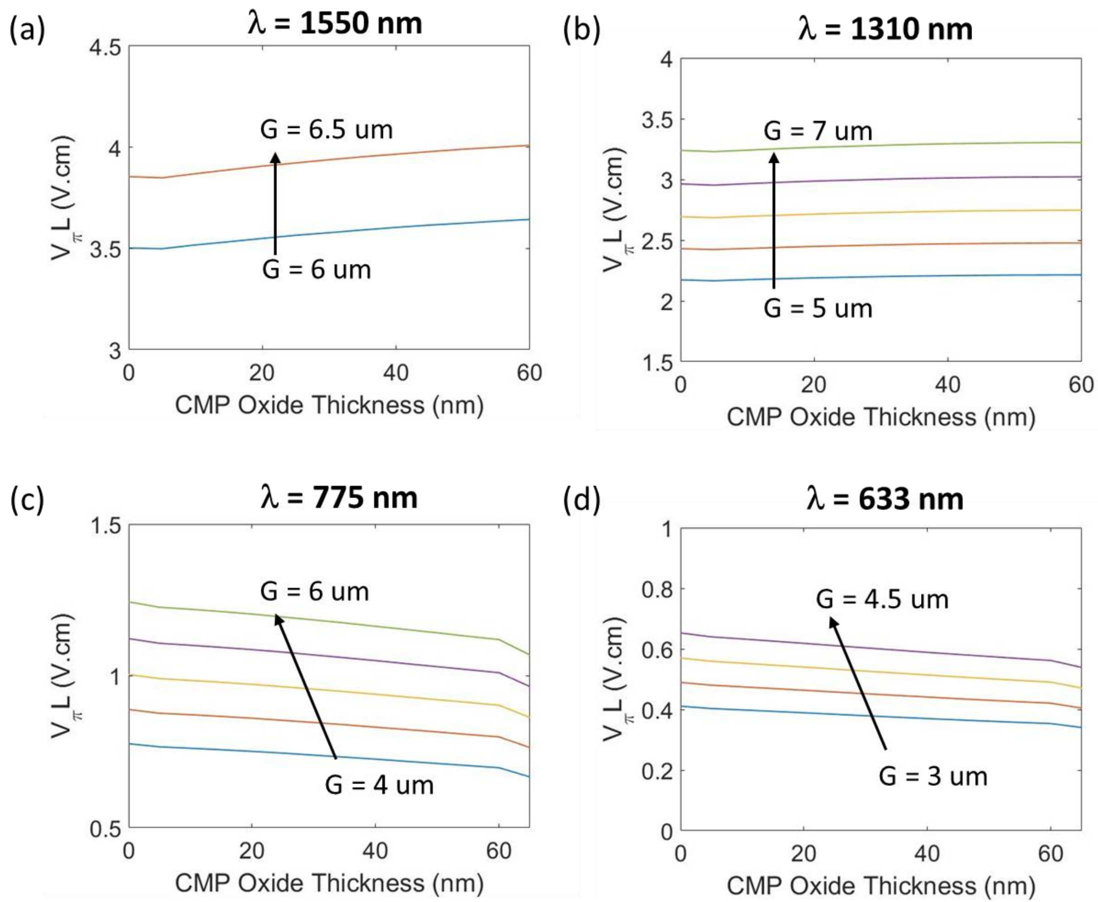

Figure 2.25: The simulated $V_\pi L$ of SiN/LN MZMs designed for the following operation wavelengths with different G: (a) 1550 nm, (b) 1310 nm, (c) 775 nm, and (d) 633 nm. The MgO:LN film thickness is 200 nm and the SiN waveguide is 900 nm wide by 180 nm thick for all four panels.

The lower-limit G used in each simulation was chosen in accordance with Figure 2.26 which show the α_{opt} due to the hybrid mode interfering with the G-S-G metal layers. As expected, the visible wavelength designs can have a further reduced G on the order of 3 to 4 μm as opposed to the telecom regime designs which must have G > 5 μm to maintain $\alpha_{opt} < 1.0$ dB/cm (dashed lines in Figure 2.26). The combination of wavelength reduction and electrode gap reduction can bring the $V_\pi L$ of the SiN/LN MZM to the sub-1 V.cm regime (~0.75 V.cm for λ =

775 nm and G = 4 μm; ~0.45 V.cm for λ = 633 nm and G = 4 μm). Such efficiency would allow the shortening of the phase-shifter section to less than 1 cm and still maintain CMOS level voltages required to achieve π phase shifts. This is an overall net positive as it decreases device footprint, maintains low voltages, and reduces the inevitable RF propagation losses associated with long traveling wave electrode structures, which would then result in high-speed operation.

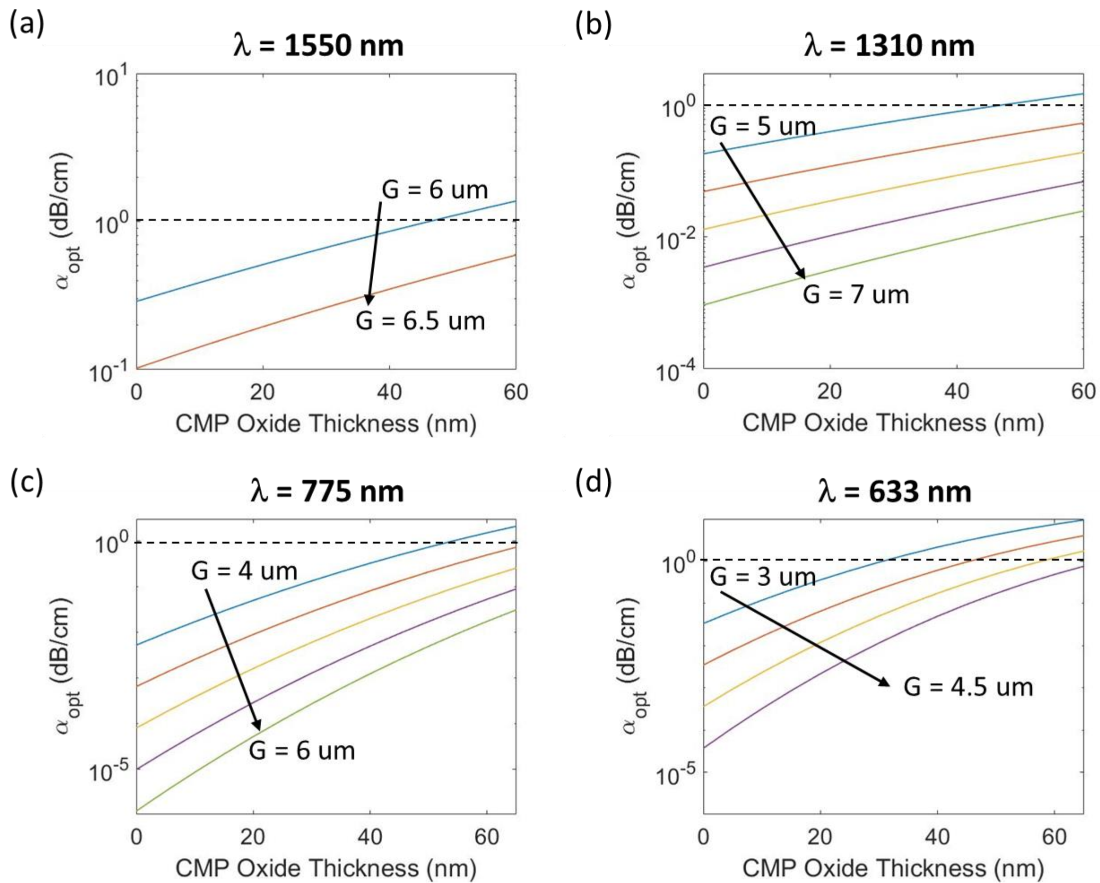

Figure 2.26: The simulated α_{opt} of SiN/LN MZMs designed for the following operation wavelengths and different G: (a) 1550 nm, (b) 1310 nm, (c) 775 nm, and (d) 633 nm. The MgO:LN film thickness is 200 nm and the SiN waveguide is 900 nm wide by 180 nm thick for all four panels. The dashed horizontal lines correspond to an α_{opt} of 1.0 dB/cm.

Figure 2.27 shows the simulated n_g as a function of CMP oxide thickness and G for the same four wavelengths. The increase in n_g as the operational wavelength gets shorter is a classical indication of chromatic dispersion from the cross-sectional materials (SiN, MgO:LN,

and SiO_2). The simulated n_g ranges from 2.05 to 2.37 across the CMP oxide thicknesses and wavelengths considered here when the MgO:LN film is 200 nm wide and the SiN waveguide is 900 nm by 180 nm. This means that a single chip can host an optimized modulator in each of these wavelength regimes as long as the traveling wave electrodes are designed in such a way to achieve velocity matching to each of these MZMs (separately), a method of which will be further discussed in Section 3.2.

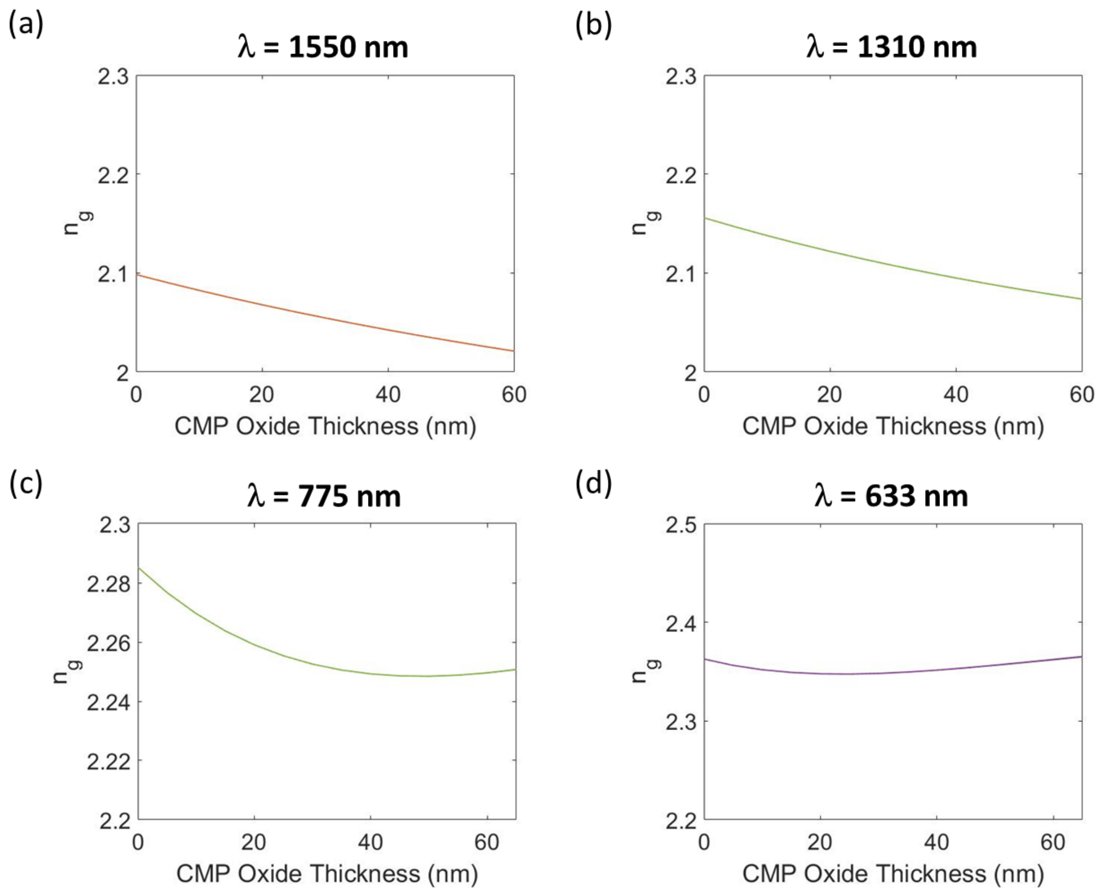

Figure 2.27: The simulated n_g of SiN/LN MZMs designed for the following operation wavelengths: (a) 1550 nm, (b) 1310 nm, (c) 775 nm, (d) 633 nm. The MgO:LN film thickness is 200 nm and the SiN waveguide is 900 nm wide by 180 nm thick for all four simulations.

While the SiN waveguide dimensions in the hybrid region can be identical for each of the wavelengths considered and still achieve high bandwidth and low voltage, this is not the case for the rest of the MZM structure. In particular, the 3-dB MMI couplers are wavelength dependent

and are not “one size fits all” for all wavelengths. Eq. (2.16) details that the length required for a 3-dB splitting ratio is inversely proportional to the operational wavelength; thus, shorter wavelengths require a longer MMI core. Using EME, the L_{3dB} for 780 nm and 633 nm wavelengths are found to be 95.9 µm and 120.6 µm, respectively, when W_{mmi} = 8 µm. Furthermore, the single-mode condition of the feeder waveguides will be different for the visible wavelength structures because of the reduced mode field size. Figure 2.28(a) and Figure 2.28(b) show the modal dispersion of 200 nm thick SiN waveguides for λ = 775 nm and 633 nm, respectively. From these simulations it is seen that the single mode condition is when the SiN waveguide width is less than 600 nm as opposed to greater than 1100 nm for telecom wavelengths.

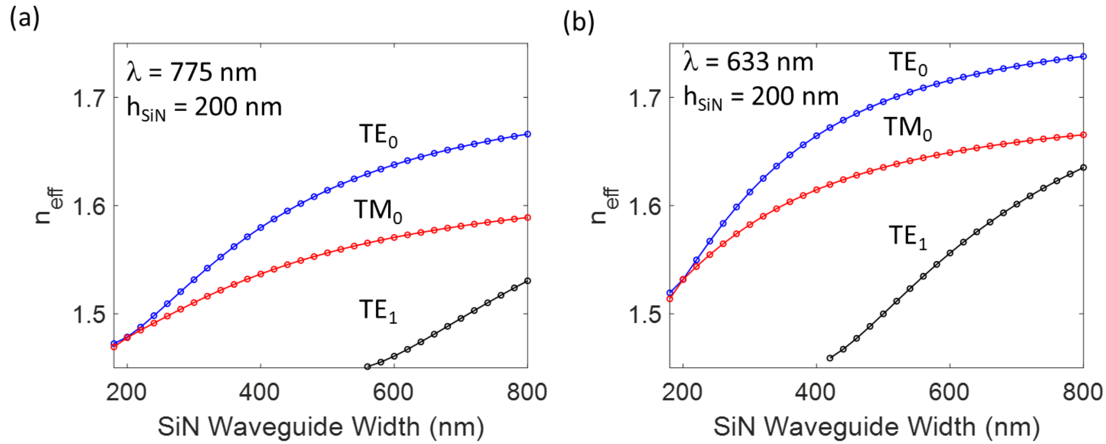

Figure 2.28: The simulated n_{eff} of the first three guided modes of a 200 nm thick SiN feeder waveguide clad in 2 mm of SiO2 at (a) λ = 775 nm and (b) λ = 633 nm. A cross section of the waveguide is in Figure 2.19(d).

2.5 Acknowledgments

Chapter 2, in part, is a reprint of the material that appears in the following: Peter O. Weigel, Forrest Valdez, Jie Zhao, Huiyan Li, and Shayan Mookherjea, “Design of high-bandwidth, low-voltage and low-loss hybrid lithium niobate electro-optic modulators”, Journal

of Physics: Photonics 3, no. 1 (2020) The dissertation author, together with his advisor and colleagues, led the research efforts for this work and co-authored the paper.

Chapter 3

Hybrid Bonded LN EOM: RF Modelling

Section 2.1.1 briefly touched on the three main design criteria one must adhere to in order to achieve high-speed EO modulation when using traveling wave electrodes:

1) The RF and optical waves must be traveling at the same velocities.
2) The source, transmission line, and load impedances must be equal.
3) Th RF propagation loss must be minimized.

These three rules not only must be met but should be maintained over as wide a frequency range as possible, e.g, 1 to 220 GHz. The characteristics of the RF transmission line mode, namely the RF index, impedance, and loss, must be designed well while also preserving the design for low voltage operation, i.e, minimizing the electrode gap G.

3.1 Coplanar Waveguides

As x-cut TFLN is used in all the devices reported in this dissertation, the driving RF field should be oriented primarily in the crystal z-direction (extraordinary axis) to ensure that the higher EO coefficient is being utilized. For such an orientation, coplanar waveguide (CPW) traveling wave electrodes are most suitable. CPW structures consist of three electrode transmission lines separated by the gap distance G, the outer lines are the grounds (GNDs), while the center line is the signal (S) electrode (G-S-G configuration).

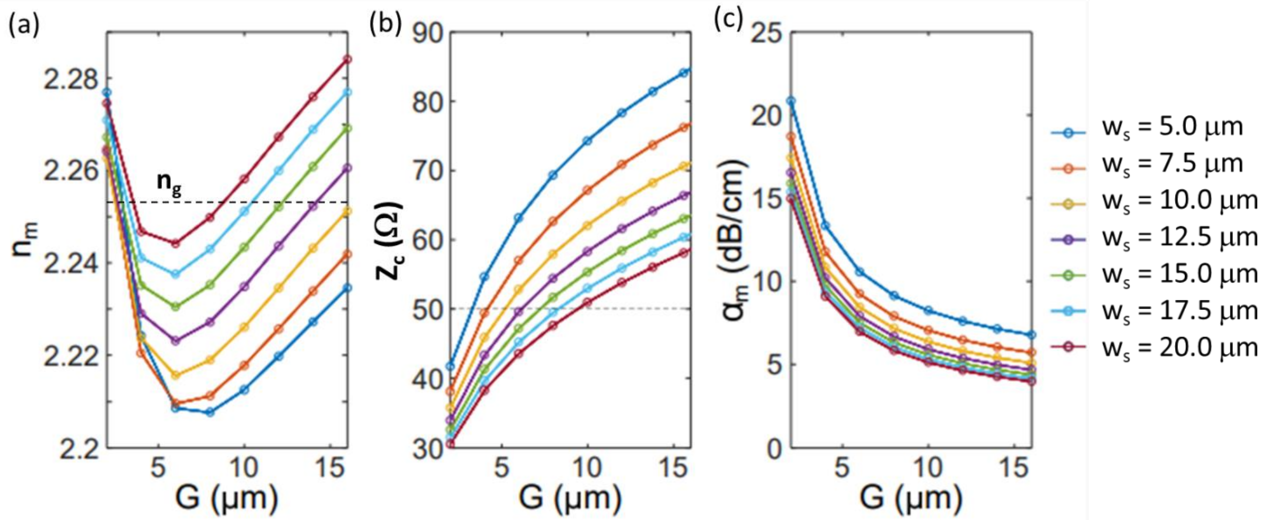

Figure 3.1: The simulated (a) n_m, (b) Z_c, and (c) α_m as a function of electrode gap distance, G, and signal width, w_s, when f_{RF} = 100 GHz, h_{LN} = 600 nm, h_{BOx} = 2 µm, he = 1 µm for a Si/LN cross section with an HR-Si substrate. The dashed line is panel (a) corresponds to an example n_g of 2.252. The dashed line in panel (b) corresponds to target of 50 Ω load impedance.

The CPW RF characteristics are primarily dependent on the material properties of the underlying dielectric layers and the electrode geometry [53,80]. Figure 3.1 shows the simulated n_m, Z_c, and α_m at 100 GHz of 1 µm thick gold CPW structures on a Si/LN platform as a function of G and the signal width, w_s, when the LN thickness is 600 nm and the BOx thickness is 2 µm. These simulations clearly show the interdependence that w_s and G have on the RF characteristics. If one wanted to only minimize the driving voltage, then the designer would choose a G of 4 µm; however, this leads to high RF losses of 15 to 20 dB/cm due to current crowding effects at such narrow spacings. Additionally, this gap spacing results in an impedance mismatch of 10 to 20 Ω (depending on w_s), generally 50 Ω is the target impedance as most RF cables, sources, and equipment are designed to have a 50 Ω impedance. If the impedances are mismatched, then RF power can be reflected to the source, and it can potentially be damaged. To ensure high-speed operation, all three RF characteristics must be considered at once. As an

example, if n_g is 2.25, then index matching at 100 GHz is achieved for G > 8 µm and w_s > 15 µm. However, to achieve impedance matching G < 10 µm and w_s > 17 µm. Finally, to minimize the RF loss, the wider signal electrode should be chosen of 20 µm. Thus, the final design in this example would be G = 8 µm and w_s = 20 µm which yields index matching, impedance matching, minimized RF loss, and minimized $V_\pi L$ for this specific case.

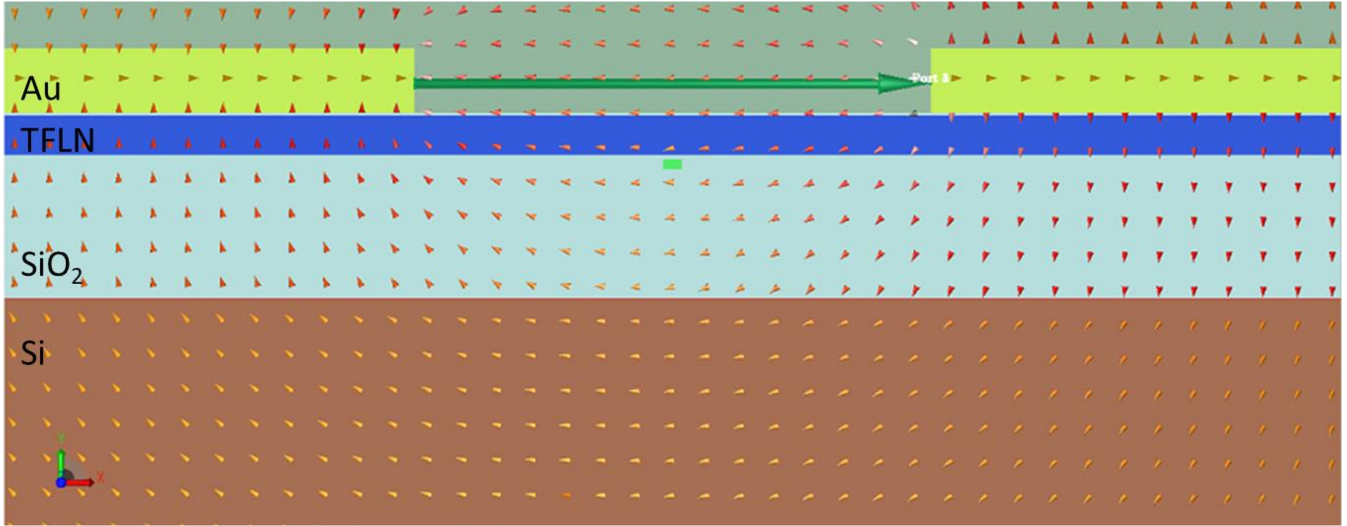

Figure 3.2: An example of a simulated CPW mode at 100 GHz for a Si/LN MZM cross section from EMPro. The color of the vector points correspond to the E_{RF} magnitude and the arrow dictates the direction. The green arrow in between the electrodes is an 'impedance line' defined in EMPro to guide the solver in finding the CPW mode.

One aspect of the design that was overlooked in the previous example was the frequency dependence of the CPW transmission line. In practical real devices, the RF index, loss, and impedance will not be constant for all frequencies and thus it is important to model the dispersion of the RF traveling wave electrodes. To capture the frequency dependent effects, a 3D FEM simulation tool [Keysight Technologies' PathWave EM Design (EMPro)] is used. Like Lumerical FDE, EMPro allows the user to model the entire MZM structure, but in the RF wavelength domain. Figure 3.2 shows an example of the CPW mode simulated in EMPro for a Si/LN cross section at 100 GHz of one arm of the MZM (i.e, between the signal and ground

electrodes). A magnetic symmetry boundary condition is employed to achieve the S-parameters of the full CPW mode. The hybrid phase shifter designs can be evaluated as a function of modulation frequency by simply performing a frequency sweep simulation in EMPro. It then calculates the RF index, characteristic impedance, and loss from the simulated S-parameters of the CPW structure. Figure 3.3(a)-(c) are the simulation results (n_m, Z_c, and α_m) as a function of frequency for that same cross section, but assuming Si substrates with varying resistivities (Low = 1 Ω.cm, Mod(erate) = 20 Ω.cm, High = 10 kΩ.cm).

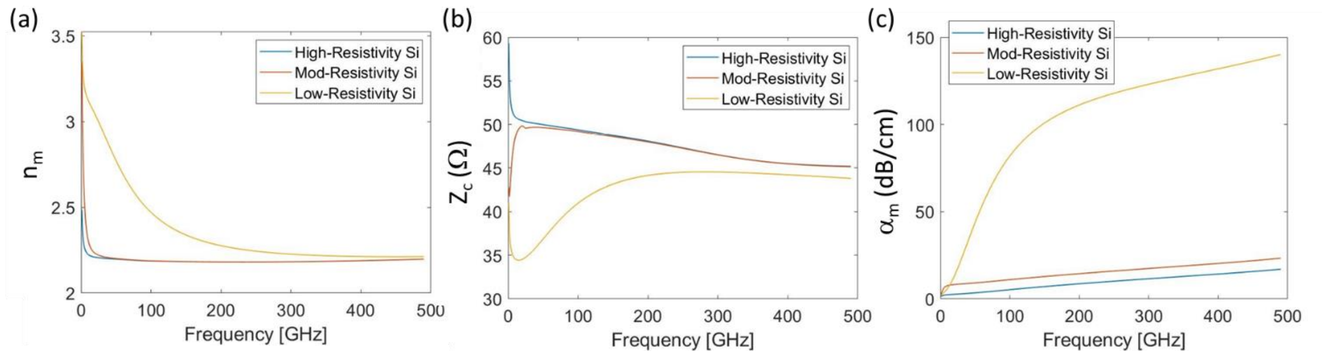

Figure 3.3: The simulated (a) $n_m(f)$, (b) $Z_c(f)$, and (c) $\alpha_m(f)$ assuming three different Si substrate resistivities.

Figure 3.3(a)-(c) show two important points in high-speed traveling wave design. Firstly, the RF dispersion has an impact on the RF characteristics. Typically, there is an increase of n_m and Z_c at low frequencies due to the skin effect [81]. RF loss generally follows a square-root dependence with frequency (from conductor loss) and a linear relationship from dielectric loss [53], which is verified in Figure 3.3(c) by the High-Resistivity (HR) Si and Moderate-Resistivity (MR) Si substrate simulations (blue and red traces, respectively). Secondly, is the importance of the dielectric stack materials, and most notably the substrate properties. The LR-Si substrate results in the highest RF loss of the three examples because at high frequencies the LR-Si substrate begins acting as a conducting plane. Higher resistivity materials, such as quartz or

sapphire have been commonly used as substrates for high-speed RF applications for their low dielectric loss tangents and low optical losses [82,83]. Here I focus on Si substrates as the SOI wafer is procured from a CMOS facility and thus this substrate material is fixed. However, the resistivity of the Si substrate can be chosen, and as such, the HR-Si substrate will perform best due to the lower RF propagation losses.

The RF characteristics of the EO system also depend on where the traveling wave electrodes are relative to the substrate and the LN thin film. In the previous example, the gold electrodes were above the LN film and in direct contact. Figure 2.22(a) is a cross section of an MZM which has the driving electrodes buried in the SOI circuit above the BOx layer (in this case 3 μm above the HR-Si substrate with 200 nm thick TFLN). Such metal layers are regularly offered as part of the CMOS process line and can be patterned in the SOI wafer. Such a device would be more CMOS-compatible as no Au metal would be used. Only the hybrid bonding of the LN film and the opening of the electrode pads would need to be performed. Having the buried metal closer to the HR-Si substrate results in a simulated n_m (~2.0 at 110 GHz) as shown in Figure 3.4(a). The electrode thickness, h_e, also impacts the RF characteristics of the CPW mode. Thicker electrodes typically result in lesser RF Ohmic losses due to a decreased surface resistance [81,84]. This is also predicted with EMPro as shown in Figure 3.4(c) where an h_e of 0.9 um results in α_m(110 GHz) = 9 dB/cm, whereas when h_e = 0.4 um α_m(110 GHz) is 16 dB/cm.

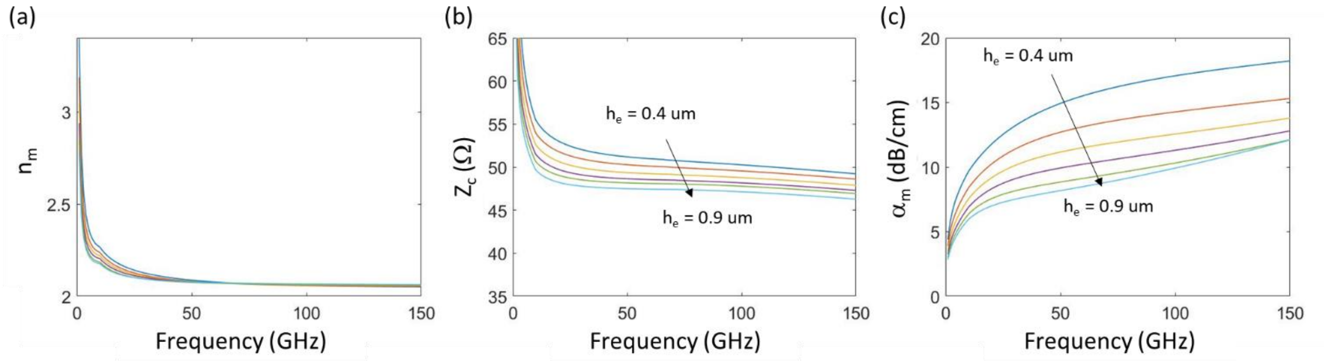

Figure 3.4: The simulated (a) n_m, (b) Z_c, and (c) α_m of a SiN/LN MZM phase shifter using buried electrodes (see Figure 2.22(a) for cross section) of varying thickness from 1 GHz to 150 GHz. The assumed cross-sectional parameters are h_{LN} = 200 nm, G = 4 um, w_s = 12 um, h_{BOx} = 3 um, and h_{buff} = 250 nm.

Figure 3.5(a) and Figure 3.5(b) are the calculated 3-dB bandwidths as a function of the SiN/LN MZM V_π (inverse to phase-shifter length) when using buried M1 standard CPW electrodes with 200 nm thick LN at λ = 1550 nm and 1310 nm, respectively. Also shown is the impact of electrode thickness on the high-speed performance by varying from 0.4 um to 0.9 um. The thicker electrodes result in similar index and impedance matching conditions, but with lesser RF losses, which yields a more efficient modulator per length saving nearly 2 V to achieve 100 GHz in both the C-band and O-band devices.

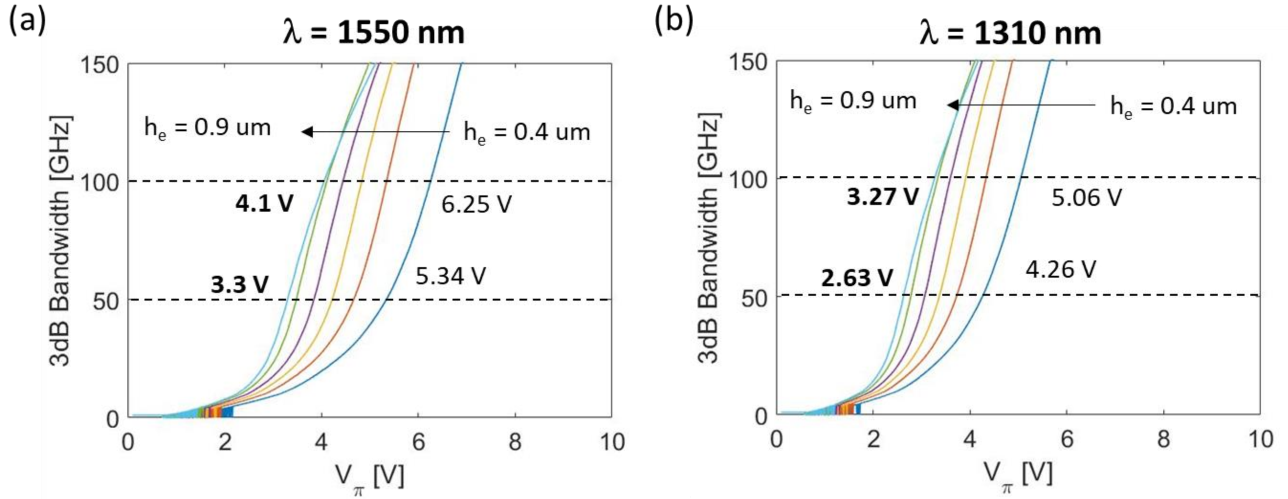

Figure 3.5: The calculated 3-dB bandwidth vs V_{π} of SiN/LN MZMs using buried electrodes at (a) 1550 nm operational wavelength and (b) 1310 nm operational wavelength. The different traces correspond to different thicknesses of electrode, h_e. The assumed cross-sectional parameters are h_{LN} = 200 nm, G = 4 um, w_s = 12 um, h_{BOx} = 3 um, and h_{buff} = 250 nm. The dashed lines correspond to the 50 GHz and 100 GHz levels. The V_{π} that result in 50 GHz and 100 GHz for the thinnest and thickest electrodes are labelled.

3.2 Slow-wave Electrodes for High-speed Modulation

In the previous section a CPW design was considered to achieve index and impedance matching while minimizing the RF propagation losses. However, this example was only for a SiN/LN MZM with buried metal electrodes. This metal layer is closer to the high-index Si substrate which made velocity matching to the hybrid mode simple. If the electrodes were above the LN film instead then the CPW mode would be further from the substrate (which is the majority of the dielectric stack: 600 μm of Si vs 3 μm of SiO_2 and 100s nm of LN) and n_m would reduce. Additionally, in the Si/LN MZM scenario the hybrid mode ng can range from 2.3 to 2.6 (depending on the CMP oxide thickness and Si waveguide width), which is 13-23% larger than the simulated n_m in Figure 3.3(a). While the index matching can be achieved by tuning the Si(N) waveguide width to decrease n_g, as shown in Figure 2.13, this has altercations on the optical loss per electrode interaction. Furthermore, to increase n_m via electrode design, G would need to be

increased (see Figure 3.1(a)), which is non-ideal as that would directly increase the driving voltage of the modulator.

This issue of an undermatched RF wave velocity to the optical wave velocity is not a new problem in high-speed RF design. For III-V modulators, such as GaAs based devices, the optical group index is almost always higher than the RF index ($n_g > n_m$) [85–88]. To alleviate the optical waveguide constraints, researchers had developed slow-wave electrodes (SWEs) to achieve velocity matching. SWEs are traveling wave electrodes which have periodic inductively loading elements (such as slots, see Figure 3.6(a)), capacitively loading elements (such as T-rails, see Figure 3.6(b)), or a combination of both [89]. These periodic elements act as an RF Bragg grating which slow the traveling RF wave and thus increase n_m. Traditional LN-based modulators have generally not needed SWEs because the optical wave tended to have the faster velocity ($n_g < n_m$). On the other hand, LNOI is primarily SiO_2 and the substrate material (in the cases presented here, HR-Si), and thus can utilize SWE design to optimize the index and impedance matching conditions. More recently, SWEs have been shown to be useful on LNOI-based modulators when using low-permittivity substrates such as quartz [90], and also for locally removed substrates [42,91]. Here, SWE introduce several more design parameters to adjust the RF dispersion in conjunction with the dispersion control offered by tapering the underlying Si(N) waveguides of the hybrid optical mode. This is particularly useful when the Si waveguides are wider (and confine more of the hybrid mode) and for shorter wavelength operation ($\lambda < 1$ µm) as chromatic dispersion usually incurs a higher refractive index as the wavelength decreases.

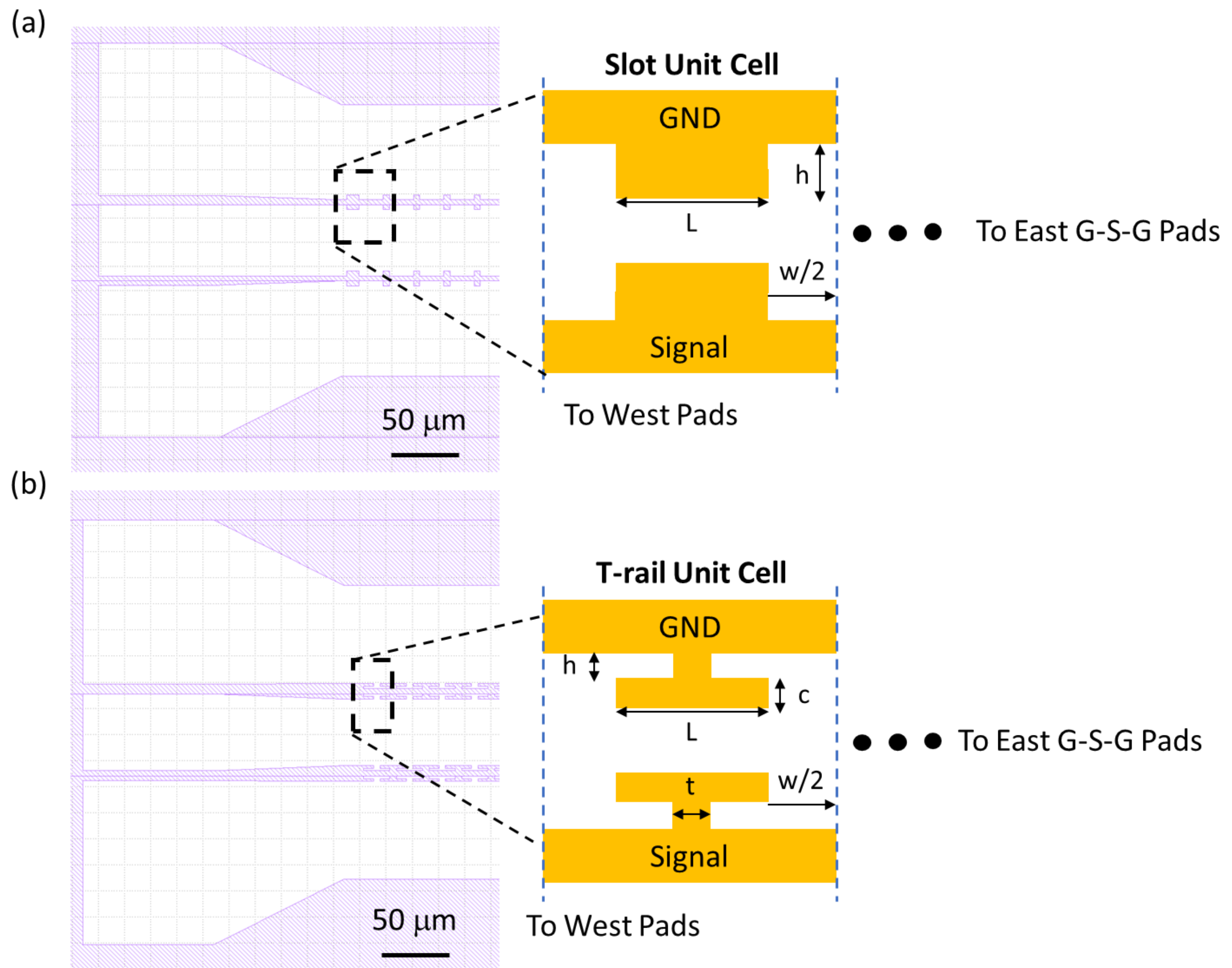

Figure 3.6: A top-view layout of the (a) Slot SWE and (b) T-rail SWE with G-S-G probing pads with 100 μm pitch and 100 μm tapers to the main phase shifting section. The zoomed in diagrams detail the (a) Slot and (b) T-rail parameters of the periodic unit cells.

Figure 3.6(a) and Figure 3.6(b) are top-view diagrams of G-S-G pads that taper to the SWE sections with either inductively loading elements (referred to as Slots in this dissertation) and capacitively loading elements (referred to as T-rails in this dissertation), respectively. Tapers from the G-S-G pads are included to allow for appropriate probe pitches on the order of 100 – 150 μm in these works. The relevant parameters that allow tuning of the RF dispersion are labelled accordingly in Figure 3.6. As the distance between the inner electrode edge and the inner T-rail edge increases (h in Figure 3.6), the RF wave becomes slower which results in a

larger RF effective index. Furthermore, the T-rail stem width (t, in Figure 3.6) also affects the RF wave velocity, with narrower t corresponding to a slower RF field [87]. The parameters L and w dictate the period of the SWE unit cells. There can eventually be a cut-off frequency due to the periodic nature of these SWE designs; however, with periods on the order of 20 – 50 µm, the cut-off frequency is approximated to be much greater than 300 GHz which is well beyond our measuring capabilities.

To accurately model the slow-wave effect of the periodically loaded structures in EMPro, the following simulation procedure is performed. 3D FEM simulations in EMPRo result in the complex S-parameters of the SWE as a function of frequency and electrode length. Two simulations are performed of different lengths which correspond to a different number of T-rail or Slot unit cells. From these results, the RF SWE index is calculated as

$$n_m(f) = \frac{c\beta_{SWE}}{2\pi f} \tag{3.1}$$

$$\beta_{SWE} = \frac{d\phi}{dL} = \frac{\phi_2 - \phi_1}{L_{cell}(N_2 - N_1)} \tag{3.2}$$

where L_{cell} is the period of the unit cell, $N_{1,2}$ is the total number of unit cells in the two simulated SWEs, and $\phi_{1,2}$ is the simulated S-parameter phase of the two SWEs. The SWE Z_c can be evaluated from the simulated S-parameters by first converting them into the ABCD parameters [92]:

$$A = \frac{(1 + S_{11})(1 - S_{22}) + S_{12}S_{21}}{2S_{21}} = \cosh\,(\gamma_m L) \tag{3.3}$$

$$B = Z_L \frac{(1 + S_{11})(1 + S_{22}) - S_{12}S_{21}}{2S_{21}} = Z_c \sinh(\gamma_m L) \tag{3.4}$$

$$C = \frac{1}{Z_L}\frac{(1 - S_{11})(1 - S_{22}) - S_{12}S_{21}}{2S_{21}} = \frac{1}{Z_c}\sinh(\gamma_m L) \tag{3.5}$$

$$D = \frac{(1 - S_{11})(1 + S_{22}) + S_{12}S_{21}}{2S_{21}} = \cosh(\gamma_m L) \tag{3.6}$$

From these set of equations,

$$Z_c = \frac{B}{\sqrt{A^2 - 1}}. \tag{3.7}$$

The RF propagation loss can then be calculated using the calculated n_m, and Z_c along with the simulated transmission, $|S_{21}|$, by fitting skin-depth loss coefficients and dielectric loss coefficients to the following equations:

$$P_{thru} = \exp(-2\alpha_m L)\, T_{in} \tag{3.8}$$

$$T_{in} = 200\frac{Re(Z_{in})}{|Z_{in} + 50|^2}. \tag{3.9}$$

Figure 3.7(a) and Figure 3.7(b) is the simulated n_m at a frequency of 110 GHz as a function of t and h for both Slot and T-rail structures. The assumed parameters for the T-rail SWE are L = 30 µm, t = 6 µm, c = 2 µm, w = 5 µm, G = 8 µm, and w_s = 55 µm; whereas the assumed parameters for the Slot SWE are L = 24 µm, t = 24 µm, c = 2 µm, w = 5 µm, G = 8 µm, and w_s = 55 µm. By simply altering these two parameters of the SWE the resulting RF index can be tuned in the range of $2.3 < n_m(110\text{ GHz}) < 2.82$ which overlaps well with the range of n_g for the Si(N)/LN hybrid platforms at operational wavelengths in the range of 400 nm < λ < 2000 nm. The hybrid mode index has both geometric and chromatic dispersion which dictates the value of n_g (typically shorter λ's result in higher n_g). The precise optical-RF index matching that

is necessary for very high EO bandwidths (>100 GHz) can be achieved in each wavelength band, firstly, by precisely tailoring the Si(N) waveguide width, and secondly, by adjusting the RF traveling wave electrode based on measurements of the layer thicknesses that are specific to each reticle of the wafer.

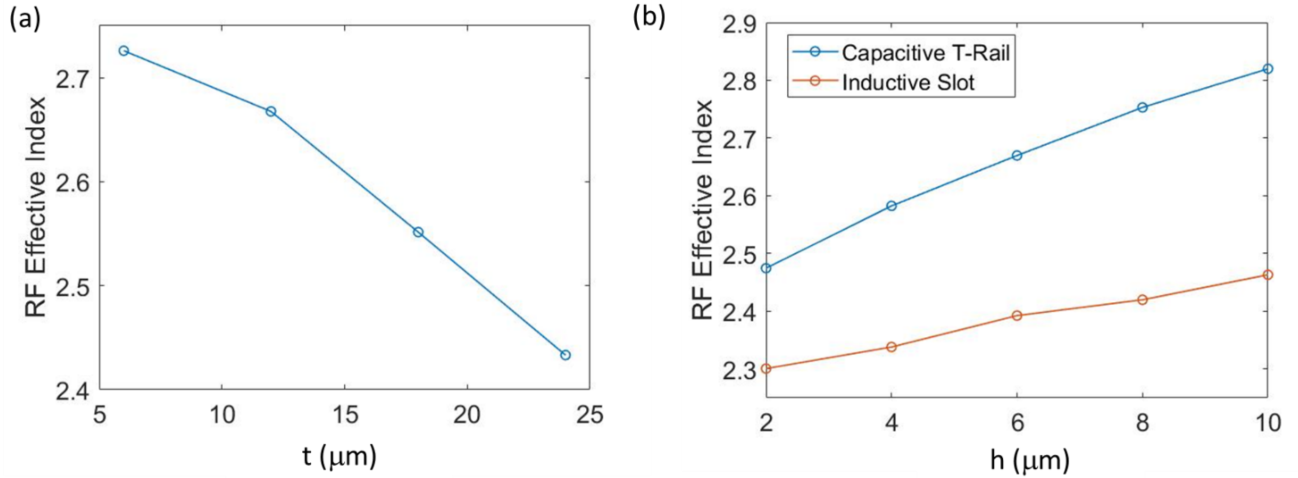

Figure 3.7: The simulated n_m as a function of SWE parameters (a) t and (b) h for T-rail and Slot structures at 110 GHz. The other T-rail parameters are L = 30 μm, t = 6 μm, c = 2 μm, w = 5 μm, G = 8 μm, and w_s = 55 μm. The other parameters for the Slot SWE are L = 24 μm, t = 24 μm, c = 2 μm, w = 5 μm, G = 8 μm, and w_s = 55 μm.

3.3 Modelling the EO Response with CPW and SWE Traveling Wave Electrodes

Now that the design of high-speed traveling wave electrodes is understood, both with and without periodic slow-wave features, the voltage-optimized hybrid Si(N)/LN phase shifters can be evaluated in terms of their EO response. The slow-wave parameters allow wide tunability of the RF characteristics which can aid in achieving the velocity matching condition between the RF and optical waves. The simulated $n_m(f)$, $Z_c(f)$, $\alpha_m(f)$, and optical n_g can then be input to Eq. (2.1) to determine the EO response of modulators as a function of frequency and phase-shifter length. Figure 3.8(d) is the calculated EO response of a Si/LN MZM using the RF characteristics

of the Slot SWE structure in Figure 3.8(a)-(c) assuming $n_g = 2.32$ and $L = 0.5$ cm (blue trace) and $L = 1.0$ cm (red trace). Because the index matching and impedance matching conditions are met, the only thing limiting the high-speed performance of the modulator is the RF propagation loss. Based on the RF loss, the length of the modulator to achieve a specific 3-dB bandwidth and/or V_π can be designed. Figure 3.8(e) is the calculated 3-dB bandwidth of a Si/LN MZM using the same RF characteristics but for different phase-shifter lengths, which results in different V_π (x-axis). Using models like this predicts that a 100 GHz 3-dB bandwidth can be obtained with a V_π of 3.45 V which corresponds to a phase-shifter length of 0.9 cm.

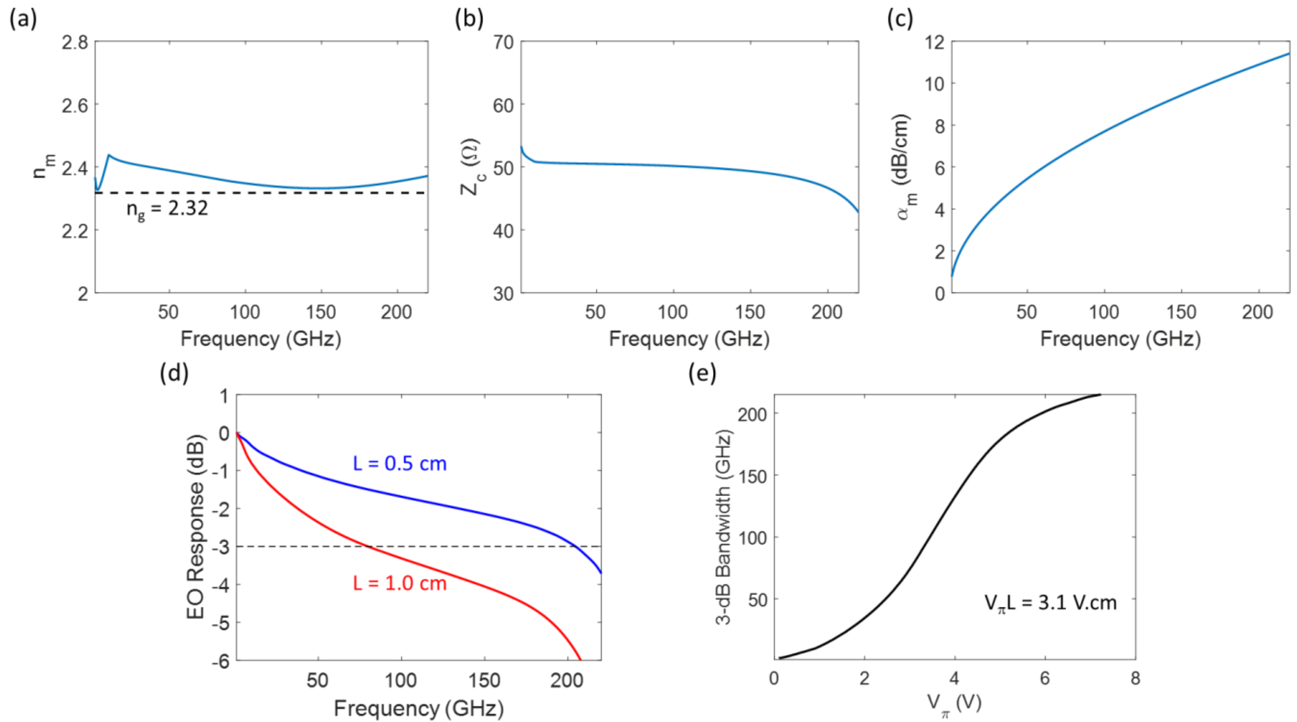

Figure 3.8: The simulated RF (a) n_m, (b) Z_c, and (c) α_m for a Si/LN MZM with Slot SWEs ($L = 20$ µm, $t = 20$ µm, $h = 4$ µm, $w = 5$ µm, $G = 9$ µm) and 600 nm TFLN. The dashed line in panel (a) corresponds to the simulated n_g of a Si/LN mode at 1550 nm. (d) The calculated EO response using the results of panels (a)-(c) assuming phase-shifter lengths of 0.5 cm (blue trace) and 1.0 cm (red trace) and $n_g = 2.32$. The dashed line is at the 3-dB point. (e) The calculated 3-dB bandwidth as a function of MZM V_π (inverse phase-shifter length) using the same simulated RF characteristics in panels (a)-(c), $n_g = 2.32$, and $V_\pi L = 3.1$ V.cm.

Such SWEs can also be used to achieve velocity matching in the visible-to-NIR wavelength ranges as discussed above. Figure 3.9(a)-(c) show the simulated RF characteristics of a SiN/LN MZM made with T-rail (for the blue to red wavelengths) and Slot (for the NIR wavelength) SWEs designed in the buried metal layer (see the cross section in Figure 2.22). As can be seen in Figure 3.9(a), Δn is below 1% for each SWE design and the characteristic impedance is around 50 Ω as well [Figure 3.9(b)]. Assuming an electrode gap of 4 μm, the calculated 3-dB bandwidths as a function of V_π (inverse phase-shifter length) is shown in Figure 3.9(d) for the wavelengths inset. These SiN/LN MZMs with buried electrode SWE designs predict 100 GHz modulation speeds with sub-volt V_π, which would be the most efficient modulators demonstrated to date.

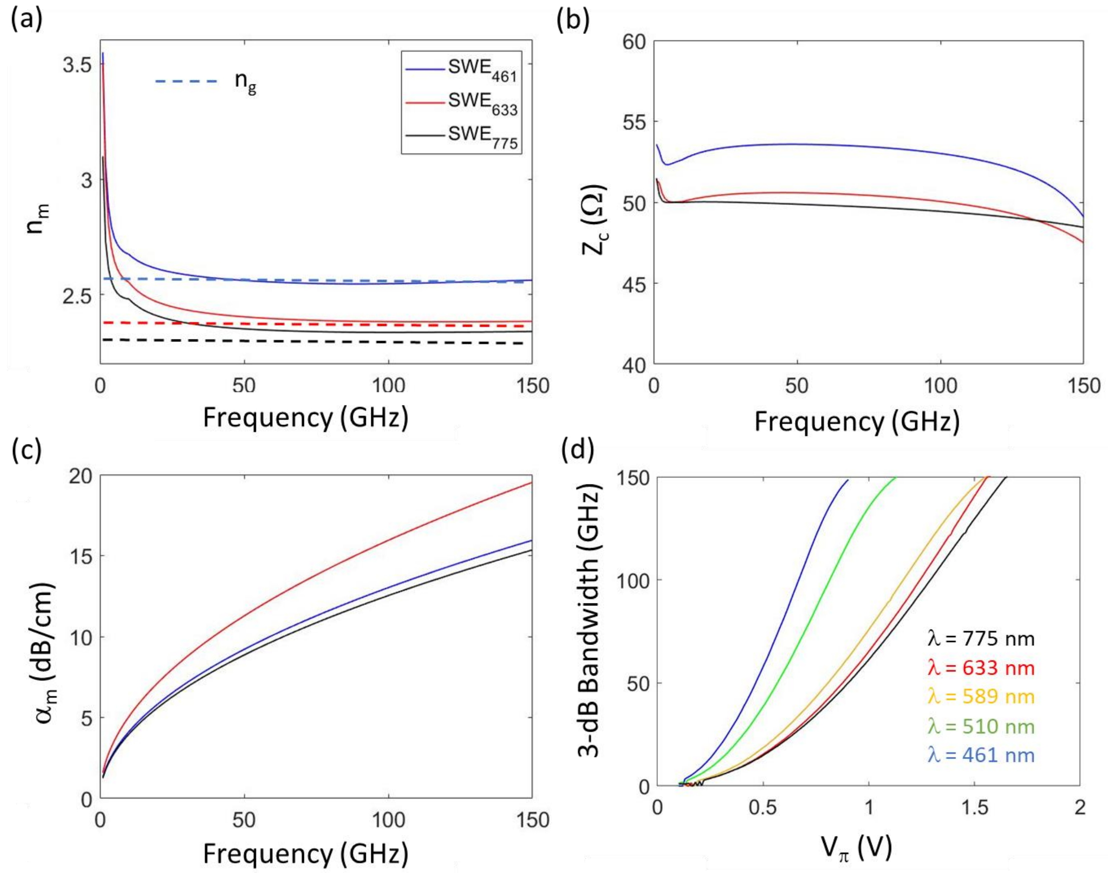

Figure 3.9: (a)-(c) The simulated RF characteristics of a SiN/LN MZM with buried T-rail (blue to red λs) and Slot (λ = 775 nm) electrodes (250 nm below the SiN waveguides). (d) The calculated 3-dB bandwidth as a function of V_π (inverse phase shifter length) for the visible to NIR wavelength designs resulting in greater than 100 GHz speeds with less than 1 V V_π. The assumed constants are h_{LN} = 200 nm, h_{buff} = 250 nm, G = 4 μm, h_{cmp} = 50 nm, and h_e = 0.4 μm.

3.4 SWE Impact on $V_\pi L$?

While the periodicity of the SWEs has shown to help achieve velocity matching and impedance matching for the Si(N)/LN hybrid modulators, there is a question of whether it impacts the modulation efficiency, i.e, driving voltage required for phase-shifting. The periodic elements along the propagation length are varying the electrode gap between the ground and signal planes to slow the RF wave. Can this gradation thus increase V_π over the modulator length? To determine this, the overlap integral between the RF and optical waves must be

considered a 3D integral as opposed to a 2D cross-sectional integral in Eq. (2.8) because it varies over propagation distance:

$$\Gamma_{mo} = \frac{G}{V_A} \frac{\iiint_{LN} E_{RF}(x,y,z)|E_o(x,y,z)|^2 dV}{\iiint |E_o(x,y,z)|^2 dV} \tag{3.10}$$

Assuming that the variation is repeating over every unit cell of total electrode length, then the integral over propagation distance can be approximated as a sum over the total number of unit cells such that

$$\Gamma_{mo} \approx \frac{G\Delta z \sum_{n=1}^{N} \mathrm{A_n}}{\Delta z \sum_{n=1}^{N} \mathrm{V_n B_n}} \tag{3.11}$$

where $A_n = \iint_{LN} E_{RF}(x,y,z_n)|E_o(x,y,z_n)|^2 dA,\ B_n = \iint |E_o(x,y,z_n)|^2 dA$ and V_n is the voltage across the electrodes along a discretized length of the SWE unit cell. Assuming B_n is constant over the length of the unit cell (optical loss is negligible over the unit cell period), then

$$\Gamma_{mo} = \frac{G}{NB} \sum_{n=1}^{N} \frac{A_n}{V_n} \tag{3.12}$$

Plugging Eq. (3.12) into Eq. (2.7) then results in

$$V_\pi L = \frac{n_{eff} \lambda G}{2 n_e^4 r_{33}} \sum_{n=1}^{N} \frac{NB}{G} \frac{V_n}{A_n} \tag{3.13}$$

where N is the total number of SWE unit cells. Thus, the $V_\pi L$ of a SWE structure is the summed average of the calculated $V_\pi L$ along the unit cell length. Figure 3.10(a) shows an example of a T-rail unit cell being discretized over its propagation length. The ERF is determined using EMPro at each of these discretized steps, then used to calculate $V_\pi L$ as shown in Figure 3.10(b). As expected, $V_\pi L$ increases in the regions that have a wider G but decreases where G is narrower.

Because most of the unit cell (80-90%) period has the narrower G, the mean $V_{\pi}L$ (2.52 V.cm) is comparable to the $V_{\pi}L$ calculated for a standard CPW line with the same G of 8 mm (2.5 V.cm in this case).

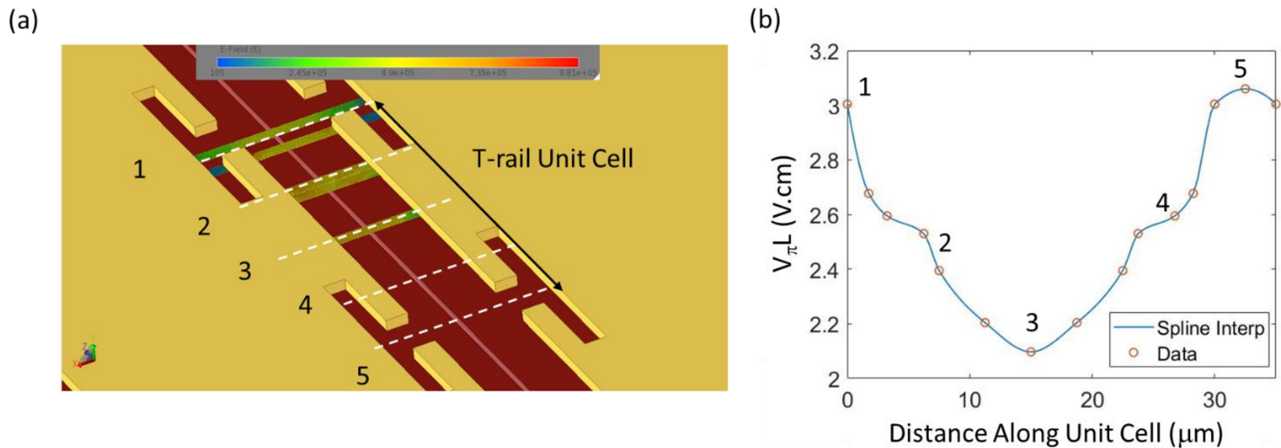

Figure 3.10: (a) A perspective-view of a T-rail unit cell being discretized along the propagation direction. The numbers correspond to the labelled numbers for the (b) calculated VpL as a function of distance along the unit cell.

3.5 Acknowledgments

Chapter 3, in part, is a reprint of the material that appears in the following: Peter O. Weigel, Forrest Valdez, Jie Zhao, Huiyan Li, and Shayan Mookherjea, "Design of high-bandwidth, low-voltage and low-loss hybrid lithium niobate electro-optic modulators", Journal of Physics: Photonics 3, no. 1 (2020) and Forrest Valdez, Viphretuo Mere, Xiaoxi Wang, and Shayan Mookherjea, "Integrated O- and C-band silicon-lithium niobate Mach-Zehnder modulators with 100 GHz bandwidth, low voltage, and low loss" Optics Express 31, no. 4 pg 5273-5289 (2023). The dissertation author, together with his advisor and colleagues, led the research efforts for this work and co-authored the papers.

Chapter 4

Outline of Fabrication and Initial Characterization

4.1 Fabrication of Si/LN Photonic Chips

The hybrid Si(N)/LN EOM chips reported in this dissertation were fabricated by direct hydrophilic bonding without using an intermediate adhesive layer, such as benzocyclobutene (BCB) [35], whose performance and stability at high optical powers is uncertain. The Si waveguides were built on a 200 mm diameter SOI wafer with 150 nm thick Si, 3 µm thick silicon dioxide (SiO_2), and 725 µm thick HR-Si handle. The SOI wafers were developed in a CMOS facility (Sandia National Laboratories). The Si waveguide features were fabricated using deep-UV lithography followed by reactive-ion-etching. SiO_2 was deposited on top of the Si waveguide features and then the surface was planarized using a CMP process to achieve a bondable surface, leaving a thin SiO_2 layer (< 50 nm). The LNOI wafers were procured commercially from NanoLN, Jinan Jingzheng Electronics Co., Ltd. The two LNOI wafers are x-cut 600 and 200 nm thick LN films with 2 µm thick buried SiO_2 and 500 µm thick Si handle.

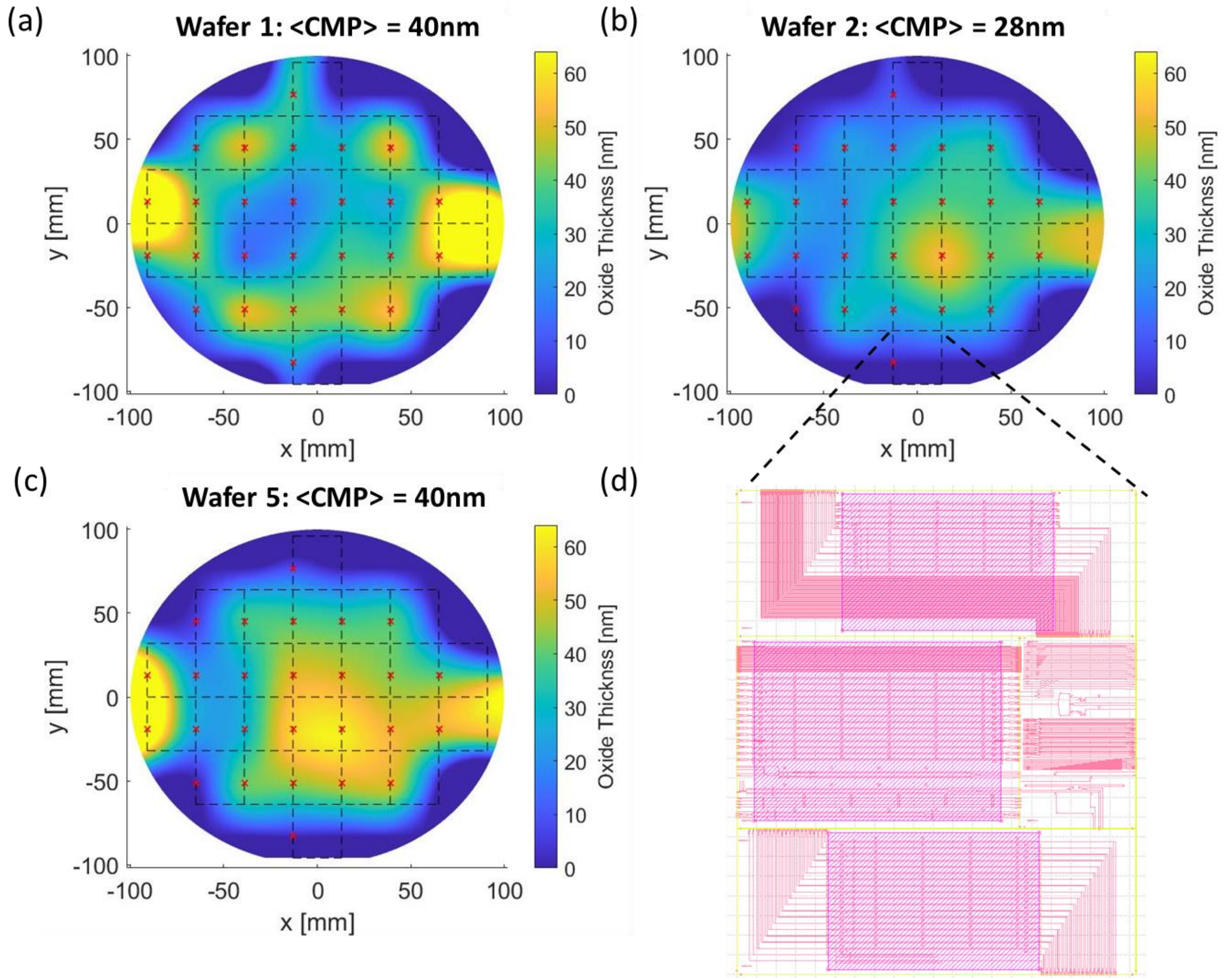

Figure 4.1: The interpolated CMP oxide thickness contour maps of three SOI wafers with single layer Si features after planarization based on ellipsometer measurements (red 'x's). The dashed lines correspond to the individual reticle areas, totaling 26 reticles per wafer. The average CMP oxide thickness is (a) 40 nm, (b) 28 nm, and (c) 40 nm. (d) The 25.4 mm by 30.8 mm reticle layout for the SiN MZMs and passive structures. The purple shaded regions are the expected bonded LN areas.

There is typically some variation of LN film thickness and thin SiO_2 layer of the SOI across the wafers. Section 2.2.1 detailed how variations in the thickness of SiO_2 layer between the bonded Si waveguide and LN film will change the mode fraction (Γ) contained in each region and will also change the modulation efficiency. Furthermore, the CMP thickness variation can impact the A_{eff} of the hybrid mode and the n_g, which can have a direct impact on the high-

speed operation of the modulators. For each reticle of the larger SOI wafer, the thickness of the layer stack was verified by ellipsometry before bonding. Figure 4.1(a)-(c) are contour maps of the SOI CMP oxide variation based on interpolated ellipsometry measurements (red ‘x’s correspond to measurements) for three wafers processed in the same multi-project wafer run. Based on the ellipsometry measurements of both the LN wafer and the processed Si wafer after CMP, a die dicing plan is developed, and specific pairs of diced LN and Si chips are selected for bonding. The electrode design is then also optimized based on the CMP wafer maps (Figure 4.1) where a CPW or SWE design is used as needed per device. In this way, the yield of devices from a wafer is increased, and the EO properties of each hybrid modulator will be closest to optimal.

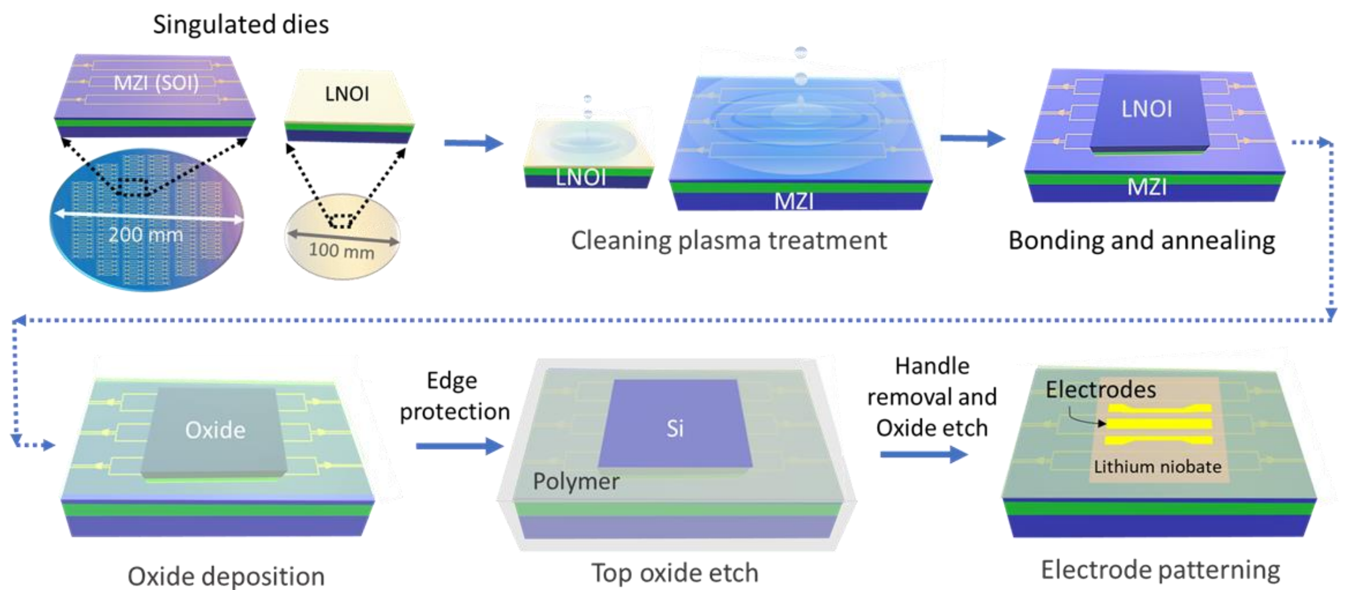

Figure 4.2: The fabrication process flow of the hybrid bonded Si/LN EOM chips.

Figure 4.2 illustrates the direct bonding hybrid Si/LN modulator fabrication process. Before bonding, the surfaces of the LNOI and SOI singulated-dies were cleaned using an RCA-1 process followed by plasma surface activation [51]. After plasma surface activation, the dies were soaked in deionized water. After drying the dies, the bonding was performed by contacting

the two dies at room temperature. To improve the bond strength, the bonded sample was annealed using temperature cycles up to 300 ◦C under an applied pressure of 9.8 $N.cm^{-2}$. At this stage, the bonded samples can be stored for processing at a later stage, if required [51]. A plasma-enhanced-chemical-vapor-deposition (PECVD) was used to deposit a few microns of thick SiO_2 as the top cladding. Before the handle removal step, a polymer coating was applied to protect bonded chips except on top of the LNOI Si handle. Next, the oxide on top of the LNOI Si handle was etched using hydrofluoric acid. The LNOI Si handle was removed using a selective XeF_2-based etching process and then the oxide layer above LN was etched using HF. The polymer was cleaned using a solvent cleaning step, and a direct-laser writer was used to define the traveling wave electrode patterns using a negative photoresist. Finally, titanium and gold of thicknesses 20 nm and 750 nm, respectively, was deposited followed by a lift-off process to complete the fabrication of the electrodes. All steps from bonding of the TFLN chips to the final electrode fabrication were performed either at room temperature or at a modestly-elevated temperatures, not exceeding about 300 ˚C. After the fabrication steps have been completed, the Si/LN chips are mechanically edge polished using a wafer polishing machine (Multiprep, Allied High Tech, Inc.). A recipe of varying diamond lapping film grits was established to reduce optical insertion losses due to rough diced edges of the SOI samples, resulting with upwards of 10 dB loss improvements. Figure 4.3 is an example of the fabricated Si/LN hybrid photonic chip that is integrated with standard Si photonic components via the underlying Si waveguide after all the fabrication steps in Figure 4.2 have been completed.

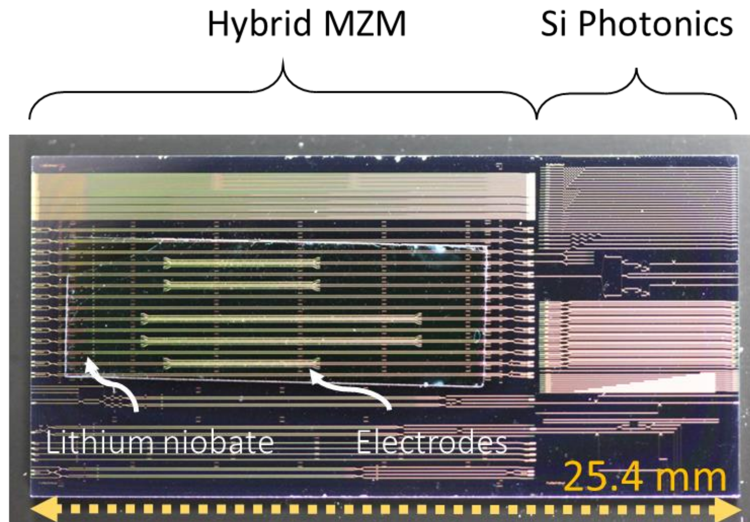

Figure 4.3: A photograph of a hybrid bonded Si/LN photonic chip with a section dedicated to hybrid bonded MZMs and a section dedicated to standard Si photonic components.

4.2 Fabrication of SiN/LN Photonic Chips

From Section 2.3 it was discussed that the SiN wafers can have buried metal layers (M1 layer consisting of a Ti/TiN/Al composite stack) beneath the SiN layer to act as the driving electrodes of the SiN/LN MZMs [see Figure 2.22(a)]. Having the additional metal layers in the SOI wafer requires additional oxide deposition and planarization steps compared to the single layer Si circuits described in Section 4.1. Roughness from one layer of the CMP can cascade to the ascending layers and may impact the overall surface quality of the bonding surface.

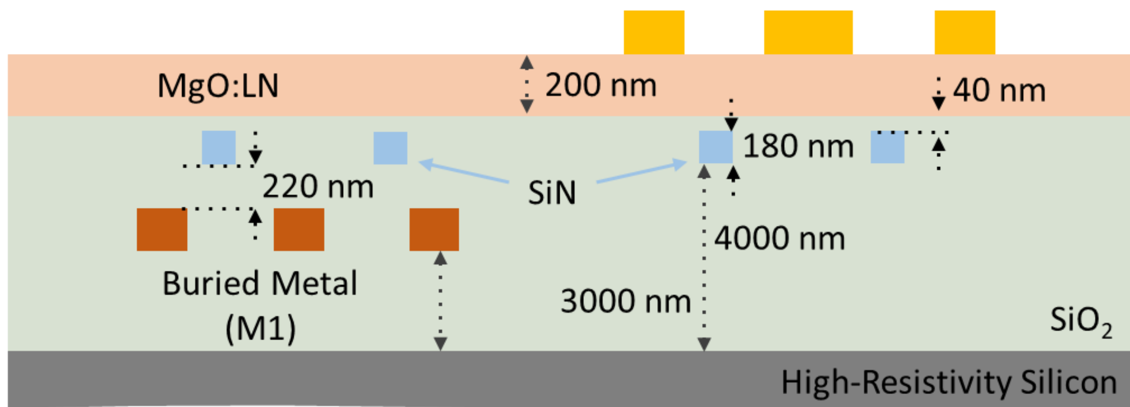

Figure 4.4: A cross-section of the hybrid bonded SiN/LN MZM showing that the traveling wave electrodes can be formed with the buried metal layer (M1) during the SOI wafer development, or post-fabricated using a gold layer above the bonded LN surface.

Figure 4.4 shows the cross section of the hybrid bonded SiN/LN sample including both M1 (Ti/TiN/Al) buried metal and optional top Au metal layers, SiN waveguides, and a 200 nm thick 5% MgO co-doped LN film on a HR-Si substrate. MgO doped LNOI is used rather than standard LN here due to its higher tolerance to photorefractive damage at high optical powers (particularly in the visible regime) [93]. A similar hydrophilic bonding process as Section 4.1 was used to integrate the LNOI and SOI chips together, where no etching or patterning of the LN film was performed [51], but with some modifications described in detail in the following publication [94]. The buried metal layer is also fabricated in the same CMOS foundry wafer process which yielding a 0.87 mm thick patterned Ti/TiN/Al CPW structures. A high-density plasma (HDP) SiO_2 is deposited after metal patterning and then CMP is performed to flatten the surface. The 180 nm thick SiN layer was deposited and patterned to form all the optical routing, tapering, bending, and splitting. A final HDP SiO_2 layer was deposited, and final CMP process was performed to achieve a smooth surface. Figure 4.5(a)-(c) show the interpolated contour maps of the buffer SiO_2 layer thickness (between M1 and SiN layers), SiN layer thickness, and the CMP SiO_2 layer thickness of one 8-inch SOI wafer produced through a multi-project wafer

run at Sandia National Laboratories I designed for use as hybrid bonded SiN/LN MZMs [reticle gds shown in Figure 4.5(d)]. As can be seen there is larger variation in the layer thicknesses when compared to the simpler Si wafers in Figure 4.1, which could be due to the multiple stages of CMP (the errors of which stack in each consecutively processed layer). To account for such variations, an improved bonding procedure of the SiN chips was developed to improve yield [94].

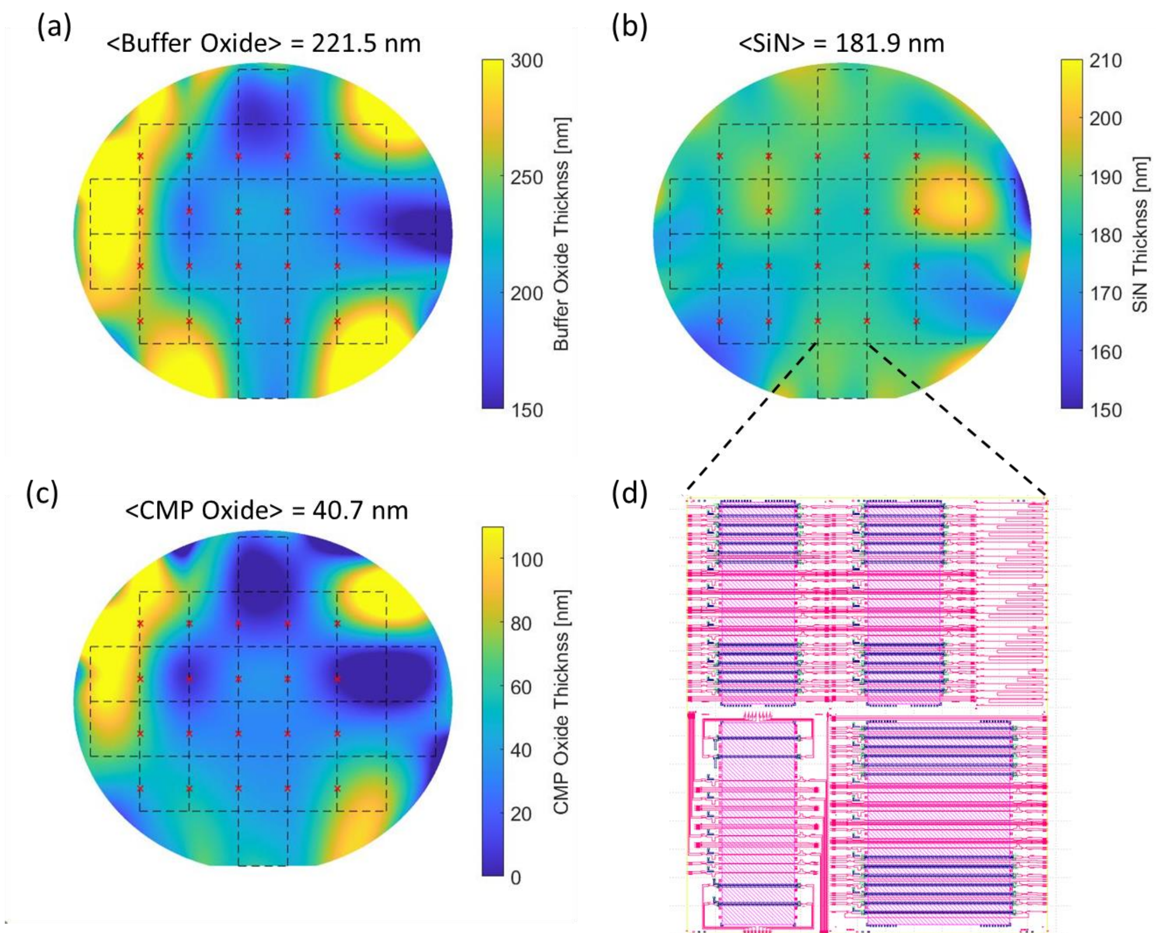

Figure 4.5: The interpolated contour maps of the (a) buffer oxide thickness, (b) SiN layer thickness, and (c) CMP oxide layer thickness based on ellipsometer measurements (red 'x's) of the 8-inch SiN wafer with buried metal. (d) The 25.4 mm by 30.8 mm reticle layout for the SiN MZMs and passive structures. The purple shaded regions are the expected bonded LN areas.

After the bonding and annealing steps, PECVD was used to deposit 4 μm SiO_2, which acts as a cladding layer for the SiN waveguides outside the bonded region. A polymer coating was performed to protect the edges and the SiO_2 on top LNOI Si handle was etched using BHF, to access the LNOI Si handle. The Si handle was then etched away using a highly selective XeF_2 gas at 3.0 torr, followed by SiO_2 etch in BHF to access the LN surface. Finally, the top Au electrodes are defined and patterned, similarly explained in Section 4.1 to complete the MZM fabrication. Alternatively, the SiO_2 cladding can be etched to reveal the buried M1 electrode pads to contact for modulation. Figure 4.6(a) and Figure 4.6(b) show examples of the hybrid bonded SiN/LN chips after all the fabrication steps are completed.

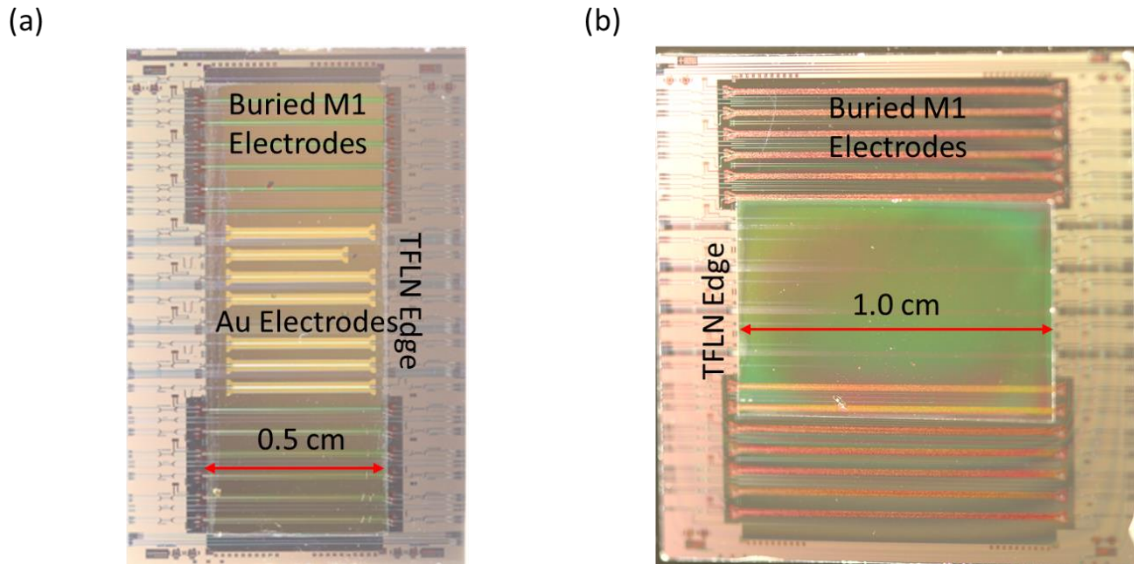

Figure 4.6: Examples of the hybrid bonded SiN/LN photonic chips with (a) 0.5 cm long phase-shifters and (b) 1.0 cm long phase-shifters.

4.3 Passive Feature Characterizations

Before performing full EO measurements of the fabricated Si(N)/LN chips, it is important to verify that the devices transmit light, and work passively as expected. To do so, a tunable laser is edge coupled to the modulators using lensed tapered fibers. The optical

transmission function can then be measured by tuning the operation wavelength. Figure 4.7(a) shows an example of the optical transmission function of an asymmetric Si/LN MZM designed for the C-band. The deep 28 dB extinction ratios (ERs) over the 100 nm span indicate that the two MZM arms are well-balanced in optical amplitude and phase, meaning that the MMI couplers are working as intended. Furthermore, the wide optical bandwidth of low insertion loss indicates that the MMI couplers also have low additional losses over 50 nm.

Passive Si test structures were also fabricated in a section of the wafer reticles which have cutback waveguides and MMI test structures. The cutback waveguides are simple 'paperclip' like waveguides of varying length which are measured to determine the optical propagation loss per length in the feeder sections of the modulators (w_{Si} = 650 nm). Figure 4.7(b) shows the measured transmission of multiple cutback waveguides of different lengths fit to a linear equation, resulting in a propagation loss of 0.8 dB/cm for the Si feeder sections.

The 2x2 MMI couplers were measured and compared to a reference straight waveguide of the same length to evaluate the coupling ratio, additional loss, and imbalance between the arms as shown in Figure 4.7(c)-(d) for couplers designed in the C-band. A common figure of merit for couplers is the wavelength range over which an additional 1 dB of loss is incurred at the outputs, called the 1 dB bandwidth. For the targeted 3 dB splitting ratio this is the 4 dB point, which is 70 nm for the measured 6 μm wide Si MMIs. These MMIs result in an output imbalance (defined as $10\log_{10}(\frac{|S_{31}|^2}{|S_{41}|^2})$) of less than 1 dB over the C and L bands. This means that the C-band MZMs can work in the L-band with well-balanced outputs as well, but with an additional IL due to the dispersion of the couplers.

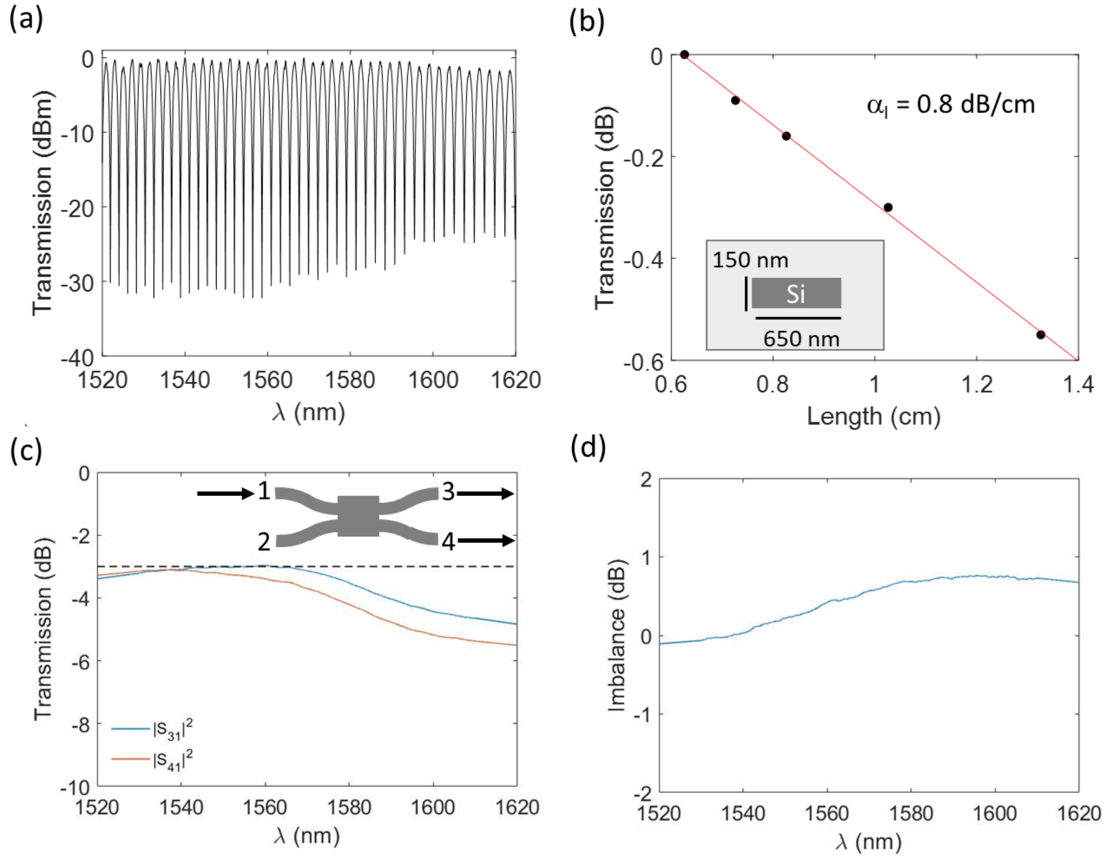

Figure 4.7: (a) The normalized measured passive optical transmission as a function of laser l for a Si/LN asymmetric MZM (no voltage bias applied) showing a 30 dB ER. (b) The normalized transmission of cutback waveguides of varying length to determine the linear absorption loss of the feeder Si waveguides (650 nm wide by 150 nm thick clad in SiO_2 as shown by the inset). (c) The output transmission of a 2x2 MMI 3-dB splitter designed around 1550 nm referenced to a straight waveguide. (d) The measured imbalance of the two output MMI ports in the C+L bands.

Similar measurements were performed on the hybrid SiN/LN chips to evaluate the MZMs before active EO measurements. Figure 4.8(a) and Figure 4.8(b) show the measured passive transmission of asymmetric and symmetric MZMs designed for O-band operation before edge polishing the chip. The well-balanced MMIs (designs discussed in Section 2.2.5) result in deep ERs of 42 dB and and 25 dB for the asymmetric and symmetric MZMs, respectively. We did not have a tunable laser in the visible to NIR regime during these experiments so the modulators made for those wavelengths could not be passively measured as a function of wavelength.

Paperclip waveguides of the SiN feeder section (1200 nm wide by 180 nm thick for the O-band and 500 nm wide by 180 nm thick for the NIR wavelengths) were measured resulting in Figure 4.8(c) and Figure 4.8(d). Although the waveguides are not very long, we are able to extract the waveguide loss. Using a linear fit, the optical propagation loss is about 0.34 dB/cm at 1310 nm and 1.6 dB/cm at 784 nm for the feeder sections. The fiber-waveguide edge coupling loss at the input and output of the chip were determined to be 2.7 dB/facet in the O-band and 3.7 dB/facet in the NIR regime from these measurements.

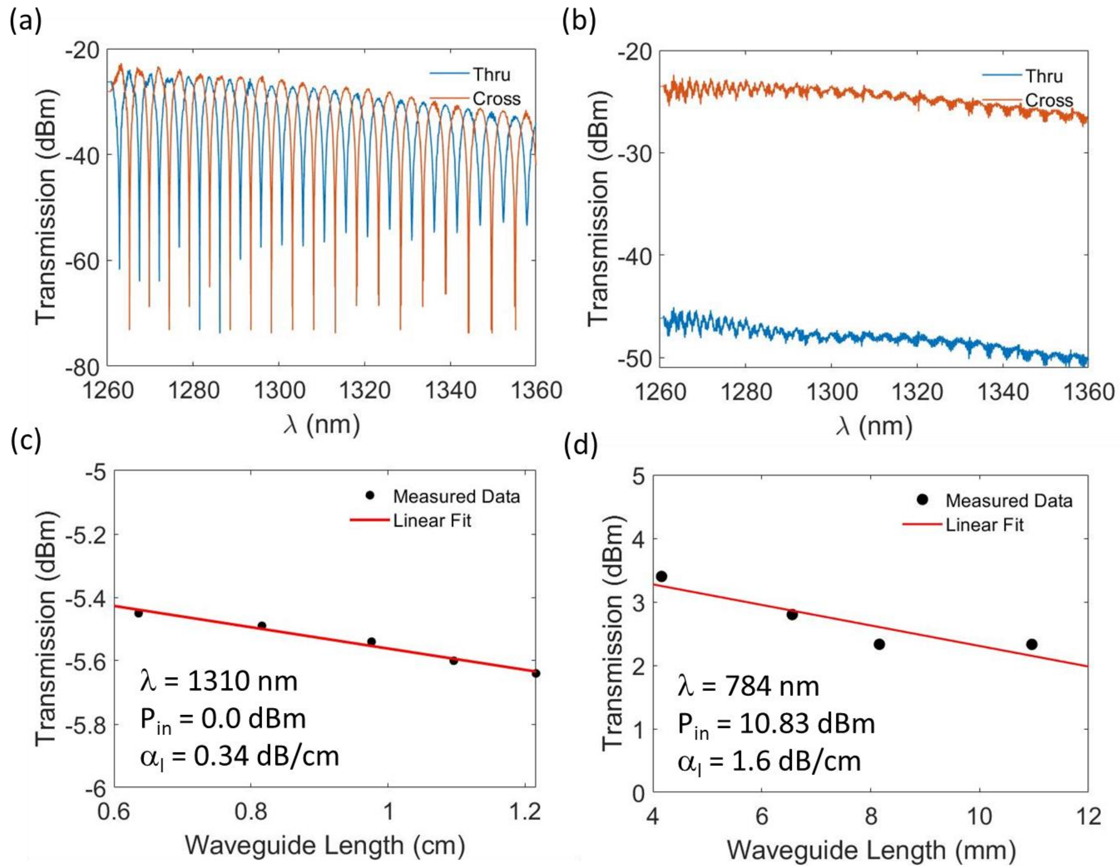

Figure 4.8: (a) The measured passive transmission of the Thru (blue trace) and Cross (orange trace) ports of an asymmetric SiN/LN MZM before edge polishing in the O-band. (b) The measured passive transmission of the Thru (blue trace) and Cross (orange trace) ports of a symmetric SiN/LN MZM before edge polishing in the O-band. (c) The optical transmission as a function of SiN feeder waveguide (1200 nm wide) length at 1310 nm, resulting in a linear loss of 0.34 dB/cm. (d) The optical transmission as a function of SiN feeder waveguide (500 nm wide) length at 784 nm, resulting in a linear loss of 1.6 dB/cm.

4.4 Acknowledgments

Chapter 4, in part, is a reprint of the material that appears in the following: Forrest Valdez, Viphretuo Mere, Nicholas Boynton, Thomas A. Friedmann, Shawn Arterburn, Christina Dallo, Andrew T. Pomerene, Andrew L. Starbuck, Douglas C. Trotter, Anthony L. Lentine, and Shayan Mookherjea, "110 GHz, 110 mW hybrid silicon-lithium niobate Mach-Zehnder modulator", Scientific Reports 12, 18611, (2022), Viphretuo Mere, Forrest Valdez, Xiaoxi Wang, and Shayan Mookherjea, "A modular fabrication process for thin-film lithium niobate modulators with silicon photonics" Journal of Physics: Photonics 4, no. 2 (2022). The dissertation author, together with his advisor and colleague, led the research efforts for this work and co-authored the papers.

Chapter 5

Hybrid Si/LN EOMs in the Telecom Regime

While the majority of TFLN based modulators have been designed for the low-loss C-band (around 1550 nm) for long-haul communication applications, the O-band (around 1310 nm) is important for short-range optical fiber communications and has lower dispersion [95]. When designing devices for different wavelengths on a common platform, it is challenging to achieve precise RF-optical index matching, since sub-micron-scale waveguides in high-index contrast platforms are highly dispersive (i.e., n_{eff} and A_{eff} vary with wavelength) compared to diffused LN waveguides. There have already been some notable efforts to design TFLN MZ-EOM devices using a common approach at both these bands, e.g., by Stenger et al. [96] and Sun et al. [97]; however, state-of-the-art performance has not yet been demonstrated in this way. A unified O-band and C-band 100-GHz-class, few-volt integrated EOM device platform may not only benefit wideband optical communications, but also help in optical signal processing, analog-to-digital conversion, frequency shifting, and EO instrumentation throughout the wider spectral range at which integrated lasers and photodetectors are now available in various photonics platforms [98–105].

Faced with the need to increase capacity, communications researchers are studying multiband optical networks which extend wavelength coverage beyond the C and L bands to other wavelength ranges such as the S, E and O bands [106]. This requires new components, including switches and transceivers. Modulators in standard C-band transceivers show impaired performance when tested at other wavelengths. While mitigation using digital signal processing (DSP) compensation is being studied [107,108], this strategy adds to the cost and complexity.

Complementary to software-based solutions are hardware (i.e., device) improvements, such as improving the modulator design. LN modulators have been compared favorably to InP-based modulators for multiband operation, and TFLN modulators, in particular, have been identified as a potential future solution to the known limitations of current-generation LN modulators [107,108]. However, these modulators are not yet mature, and many fundamental aspects of the new device platform are under study.

A perspective cartoon diagram of the fabricated Si/LN MZM devices are shown in Figure 5.1(a), with an inductively-loaded Slot SWE design. As described in Section 2.2, different Si waveguide widths are used in the input, transition, and phase shifter sections. The wider Si sections can confine nearly all the optical power to ensure low optical loss transitions across the bonded LN edges [48]. We can include both O- and C-band designs in the same Si mask by thinning the Si layer from the standard 220 nm thickness to 150 nm thick. The thickness of this layer is nearly constant across the wafer; however, as shown by Figure 4.1, the CMP oxide thickness (h_{cmp}) can vary across the wafer. As shown in Figure 4.1(a), h_{cmp} was measured in each reticle after CMP was completed by performing ellipsometry on test features. The CMP oxide thickness was about 40 nm for the reticle that produced this specific chip.

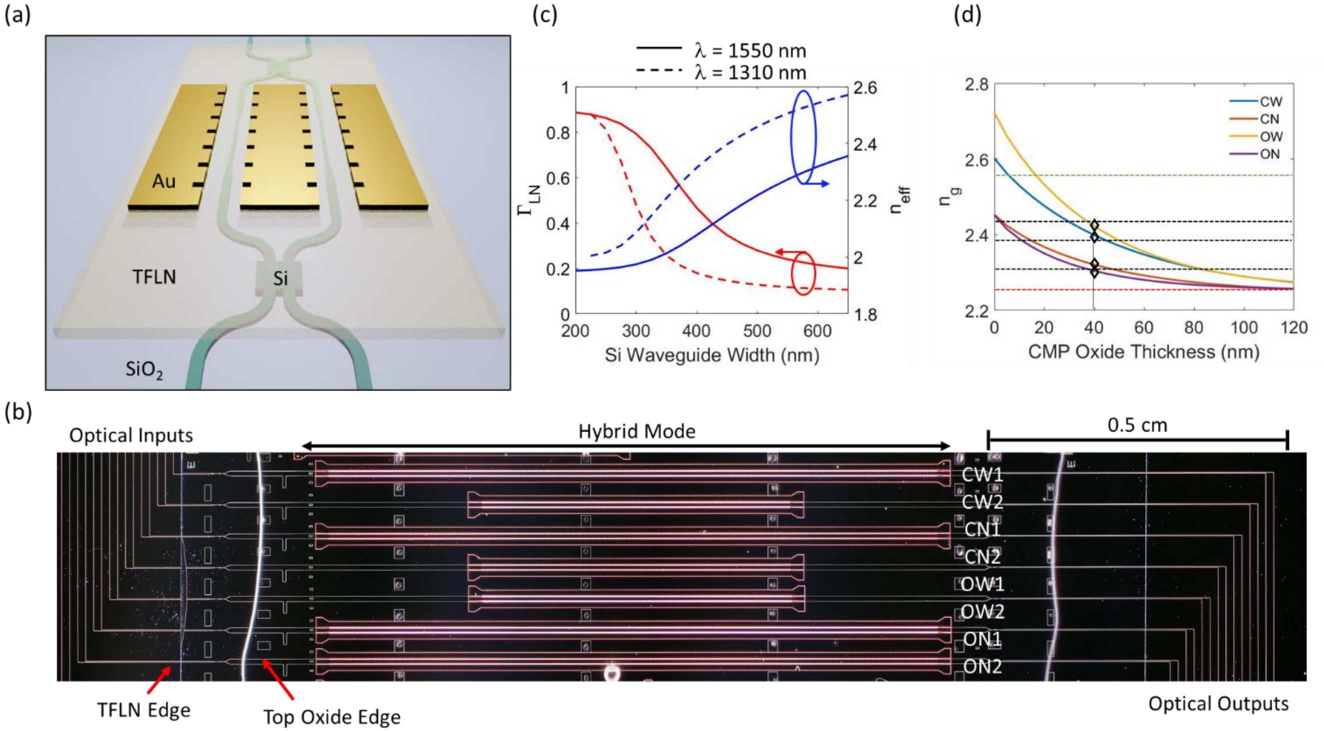

Figure 5.1: (a) A perspective-view schematic (not to scale) of the hybrid bonded Si/LN MZM with slow-wave electrodes (SWEs). (b) An image of the fabricated chip with C-band (labeled Cxy) and O-band (labeled Oxy) MZM devices. (c) The simulated confinement factor of light in the LN film (left) and the effective index (right) of the fundamental TE0 mode as a function of the Si waveguide width. (d) The simulated optical group index of the hybrid mode as a function of h_{cmp} for the four Si waveguide dimensions (Cx and Ox). The black diamonds mark the h_{cmp} of the fabricated devices. The black dashed lines correspond to the simulated RF index of the slow-wave electrodes.

Figure 5.1(b) shows a top-view darkfield optical microscope image of the fabricated hybrid bonded Si/LN chip. The edge couplers for fiber coupling are to the north-west and south-east edges (not shown in this reduced area image), whereas the electrodes are to be probed orthogonally (east-west direction). The TFLN layer thickness is about 580 nm, and it is transparent and cannot be easily seen in this image, but the perimeter of the bonded film is labelled “TFLN Edge” in Figure 5.1(b). An SiO_2 cladding was deposited using a PECVD process and the oxide edge is shown in Figure 5.1(b). Other relevant fabrication details are described in Section 4.1 as well as the following publication [51]. As described in Section 2.2.5, different MMI lengths are designed to yield 3-dB splitting and coupling for the O- and C-band devices to

maintain high extinction ratios (ERs). Based on EME simulations, the 3-dB 2x2 MMI lengths were designed to be 49 µm and 39 µm for the O-band and C-band devices, respectively, [see Figure 2.20(b)-(c)]. The corners of the MMIs were angled to reduce optical reflections back to the source [70]. Note that in this chip, as opposed to the MMIs described in Section 2.2.5, the bonded LN film is over the MMI couplers [see Figure 5.1(a) and Figure **5.1**(b)] and does not affect the coupling ratio due to the high optical confinement in the Si layer for such wide features.

After the MMI coupler, the Si waveguide width is adiabatically tapered down from the feeder section (650 nm width) to a smaller value (between 225 nm and 300 nm, depending on the design) for the phase-shifter section. This results in increasing the fraction of optical power that resides in the LN film. This effect is shown by the fraction (Γ_{LN}) of the integral over the cross-sectional profile of the Poynting power which resides in the LN region, as shown in Figure 5.1(c). The Si waveguide width also affects the optical group index, n_g, of the hybrid mode, where the wider waveguide has a larger n_g and this will matched by the RF electrode design. To compare their performance, we selected two Si waveguide widths for each wavelength band: The C-band modulators have a hybrid Si waveguide width of either 300 nm or 275 nm (labelled as devices CW: C-band, wide; and CN: C-band, narrow, respectively), while the O-band modulators have a width of 250 nm or 225 nm (labelled as devices OW: O-band, wide; ON: O-band, respectively).

As part of the wafer development processes, the wafers undergo CMP to achieve a planar surface for bonding. The CMP oxide thickness was measured across the wafer using ellipsometry and varies less than 2 nm in the bonded regions which are about 2 cm x 1 cm in size. In the bonded stack, the CMP oxide layer is between the Si waveguide and the bonded LN film and

impacts n_g as shown in Figure 5.1(d). Thinner CMP oxide results in a tighter confinement of the optical mode to the Si waveguide, and increases n_g and decreases the effective modal area. For both Si and LN, the optical refractive index increases as the wavelength of light decreases. The optical group index of the hybrid mode was calculated as a function of chromatic (operating wavelength) and geometric dispersion (the cross-sectional parameters), namely the Si dimensions, TFLN thickness, and the amount of oxide between the Si strip and TFLN layer [see Figure 5.1(d)].For the measured chip, the CMP oxide thickness is about 40 nm, resulting in a simulated n_g of 2.38, 2.31, 2.43, and 2.30 for the CW, CN, OW, and ON devices respectively at 1550 nm and 1310 nm. Two different widths of the Si waveguide in each wavelength band were chosen (OW, ON, CW, and CN), to study RF-optical index matching with either Si waveguide tapering or RF electrode design via slow-wave features.

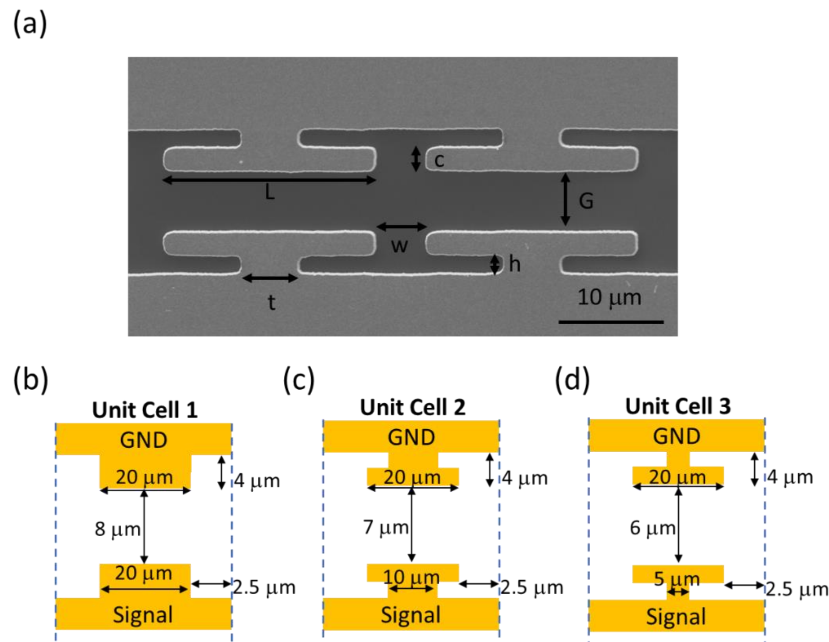

Figure 5.2: (a) An SEM image of a T-rail SWE design used in this work with the SWE parameters labelled. (b) The top-view schematic of the periodic inductively loaded slot feature with slow-wave design parameters used for devices CN and ON. (c) The top-view schematic of the periodic capacitively loaded T-rail feature used for the CW devices. (d) The top-view schematic of the periodic capacitively loaded T-rail feature used for the OW devices.

Figure 5.2(a) is an SEM image of one of the T-rail SWEs used in this work with the design parameters labelled. These additional parameters allow the RF dispersion (variation with frequency) to be adjusted. These three different SWE structures were designed to achieve index matching to the four different MZM designs as shown in Figure 5.2(b)-(d): a slot structure (L = t = 20 μm) for the CN and ON devices, a wider width T-rail for CW (L = 20 μm, t = 10 μm), and a narrow width T-rail for OW (L = 20 μm, t = 5 μm). The dashed lines in Figure 5.1(d) show the simulated n_m of the three SWEs at 110 GHz fabricated on this chip.

The versatile electrode design offers a useful functionality in overcoming the effects of minor imperfections in the fabrication of the hybrid devices. The layer thicknesses were measured after planarization of the silicon and oxide layers was completed, and we observed some variations in layer thicknesses from die-to-die across the wafer. Before fabricating the electrodes, the optical transmission was also measured through an asymmetric MZI structure on the bonded chip, from which the optical refractive index of the target structure can be verified. As Figure 5.1(d) shows, the index matching condition can be achieved over a wide range of Si waveguide widths, CMP oxide thickness, or operational wavelengths by tuning the SWE parameters and tuning n_m to match n_g. In this way, the electrode design was slightly altered for each pattern to trim devices and achieve the highest EO modulation bandwidths in each case. Table 5.1 summarizes the eight hybrid bonded MZM design parameters on this single chip.

Table 5.1: The Si/LN MZM design parameters for the O-band and C-band structures on the chip

Device	λ-band	Si WG Width	L_{ps}	G	SWE Design
CW1	C-band	300 nm	1.0 cm	7 μm	T-rail [Figure 5.2(c)]
CW2	C-band	300 nm	0.54 cm	7 μm	T-rail [Figure 5.2(c)]
CN1	C-band	275 nm	1.0 cm	8 μm	Slot [Figure 5.2(b)]
CN2	C-band	275 nm	0.54 cm	8 μm	Slot [Figure 5.2(b)]
OW1	O-band	250 nm	0.54 cm	6 μm	T-rail [Figure 5.2(d)]
OW2	O-band	250 nm	1.0 cm	6 μm	T-rail [Figure 5.2(d)]
ON1	O-band	225 nm	1.0 cm	8 μm	Slot [Figure 5.2(b)]
ON2	O-band	225 nm	0.54 cm	8 μm	Slot [Figure 5.2(b)]

5.1 High-speed SWE Electrical Characterization

The electrical response of the modulators was measured using a two-port Keysight PNA-X network analyzer with broadband frequency extenders, allowing for RF signals from 100 MHz up to 118 GHz to be applied to the SWEs [see Figure 5.3(a)]. High speed ground-signal-ground (GSG) probes (FormFactor Infinity Probes) sourced and terminated the slow-wave transmission lines of the MZMs. Figure 5.3(b)-(d) show the measured electrical S-parameters of each of the three SWE designs (T-rail structure with G = 6 μm, T-rail structure with G = 7 μm, and slot structure with G = 8 μm) with both 1.0 cm and 0.54 cm length electrodes. The measured RF $|S_{21}|^2$ of the 1.0 cm long electrodes have a -6 dB drop at 75 GHz, while the 0.54 cm long electrodes have a -6 dB drop at greater than 118 GHz.

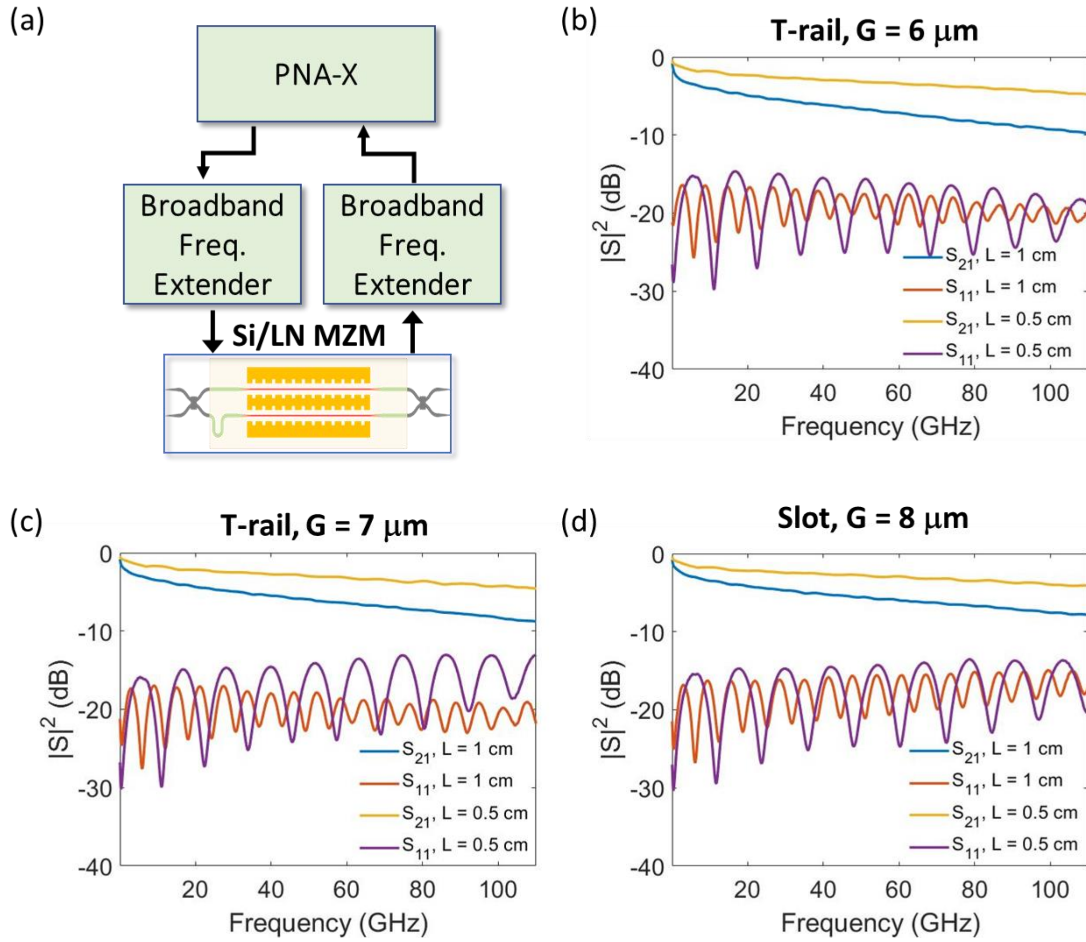

Figure 5.3: (a) A block diagram of the RF S-parameter measurements using a Keysight 2-port PNA-X and frequency extenders to measure from 100 MHz to 118 GHz. The measured S-parameters of the 1.0 cm and 0.54 cm long SWEs with the following designs: (a) T-rail and G = 6 µm, (b) T-rail and G = 7 µm, and (c) Slot and G = 8 µm.

The RF index, loss, and impedance of the transmission lines extracted from the measured S-parameters are shown in Figure 5.4(a)–(f) for each of the four electrode designs using Eqs. (3.3)-(3.7) [92]. Figure 5.4(a) and Figure 5.4(d) show that the SWE structures result in an RF-optical index mismatch of less than 1% for both the C-band and O-band devices for both electrode lengths, where the dashed lines correspond to the simulated n_g of the four respective designs. This proves that the models used to design the SWEs in Section 3.2. result in structures that will be broadband and not index-mismatch-limited. The α_m for each of the lines is less than

9 dB/cm at 110 GHz for all the structures [Figure 5.4(b) and Figure 5.4(e)], which is within the range of high-speed modulator performance when assuming velocity and impedance matching is met [Figure 2.2]. The measured Z_c of the devices was about 40 Ω across the measured frequency range [Figure 5.4(c) and Figure 5.4(f)]. As discussed later in Section 5.6, this deviation from perfect 50 Ω impedance, which is characteristic of the source and detector, slightly lowers the measured EO 3-dB bandwidth. The RF back-reflection ($|S_{11}|^2$) is around -15 dB, and in some cases, around -20 dB as shown in Figure 5.3(b)-(d). The skin-loss coefficient of the fabricated T-rail and Slot SWEs is 0.7-0.8 dB/cm-GHz$^{1/2}$, when the extracted RF loss is fit to Eq. (2.6). As there is less than 1% index mismatch between the RF and optical traveling waves, the devices are RF loss limited. For these devices the gold electrodes are 0.75 µm thick. The RF losses can be reduced by increasing the electrode thickness via electroplating [109]. Alternatively, the Si substrate can be locally removed [91], or a lower loss material can be used as the substrate (such as quartz [90]); however, this will require further fabrication steps than needed here.

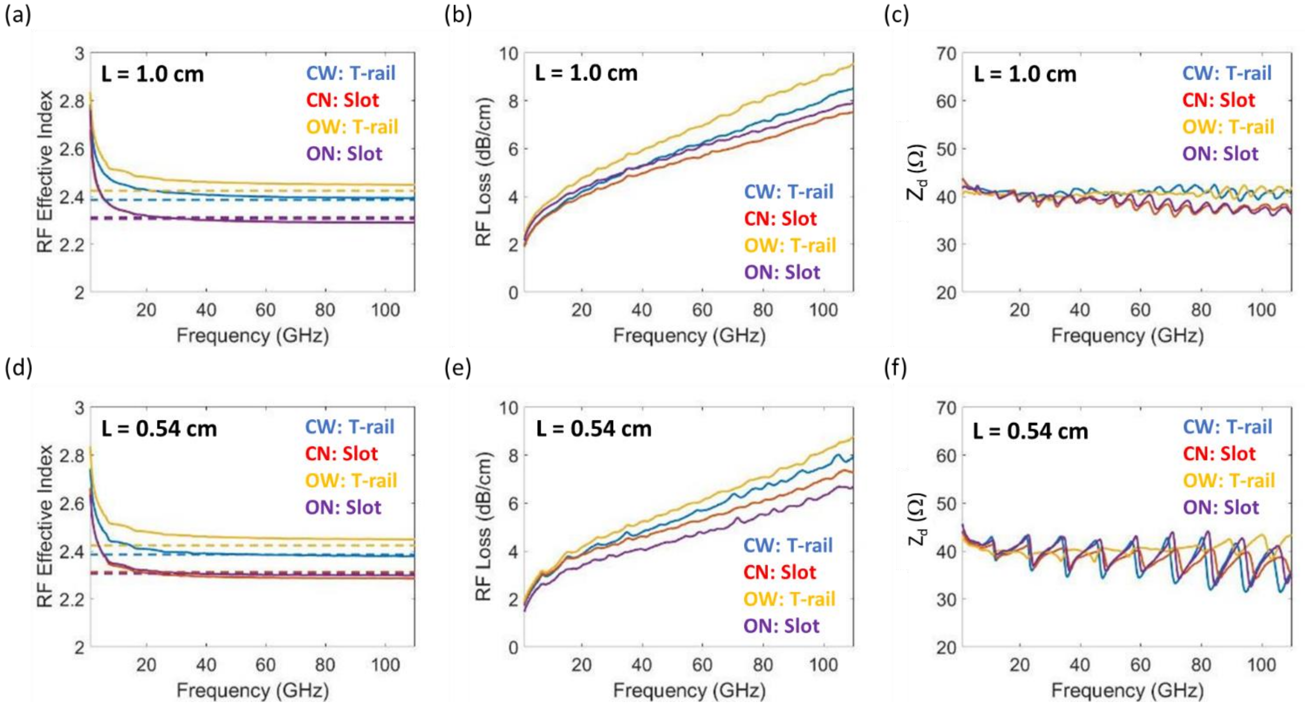

Figure 5.4: The extracted RF characteristics of each of the SWE devices from the measured S-parameters. (a) RF effective index of the four 1.0 cm long SWEs. (b) RF propagation loss of each of the four 1.0 cm long SWEs. (c) RF driving impedance of each of the four 1.0 cm long SWEs. (d) RF effective index of the four 0.54 cm long SWE. (e) RF propagation loss of each of the four 0.54 cm long SWEs. (f) RF driving impedance of each of the four 0.54 cm long SWEs. The dashed lines in panels (a) and (d) correspond to the simulated n_g for each of the C and O-band MZMs.

5.2 Si/LN On-chip Insertion Loss

Light from separate O- and C-band instrument-grade lasers was edge coupled to the chip using a lensed fiber with a 4 µm nominal spot size. The laser wavelengths were set such that the asymmetric MZMs were biased at quadrature. The optical input power from the O- and C-band lasers was +12 dBm and +9 dBm, respectively. No optical amplifiers were used in the measurements. The propagation loss of the wide Si feeder sections and hybrid mode sections have been previously reported in the C-band as 0.8 dB/cm [see Figure 4.7(b)] [110] and 0.6 dB/cm [50], respectively. The wider feeder sections of the chip (only Si) that route from the input/output edge couplers to the hybrid phase-shifter section is 1.48 cm long; thus, 1.2 dB of the

insertion loss is attributed to the feeder sections alone. The MMI couplers contribute to 0.2 dB of the total loss per coupler [see Figure 4.7(c)], while there is about 0.1 dB of loss per LN edge. The optical loss attributed to the phase-shifter section of the device (hybrid mode along the electrode length) was estimated by comparing identical devices with different phase shifter lengths. For example, devices CN1 and CN2 are identical in optical design (Si waveguide, LN film) and RF design (SWE parameters), but the SWE length is 0.46 cm longer for CN1. Assuming all other losses are common, the loss from the phase-shifter would then be 1.5 dB/cm. The edge coupling losses are then estimated to be 4.2 dB per edge and 4.8 dB per edge for the C- and O-band, respectively. Although the waveguide taper tip width of 180 nm was limited by the resolution requirements of the foundry process, lower edge coupling losses can be achieved with smaller resolution or by using different types of edge couplers [59–61]. The insertion loss of the phase-shifter section, 3-dB MMI couplers, and LN transitions are thus calculated to be 1.6 dB and 2.1 dB for the 0.54 cm and 1.0 cm long phase-shifters, respectively.

5.3 High-speed Si/LN EO Response

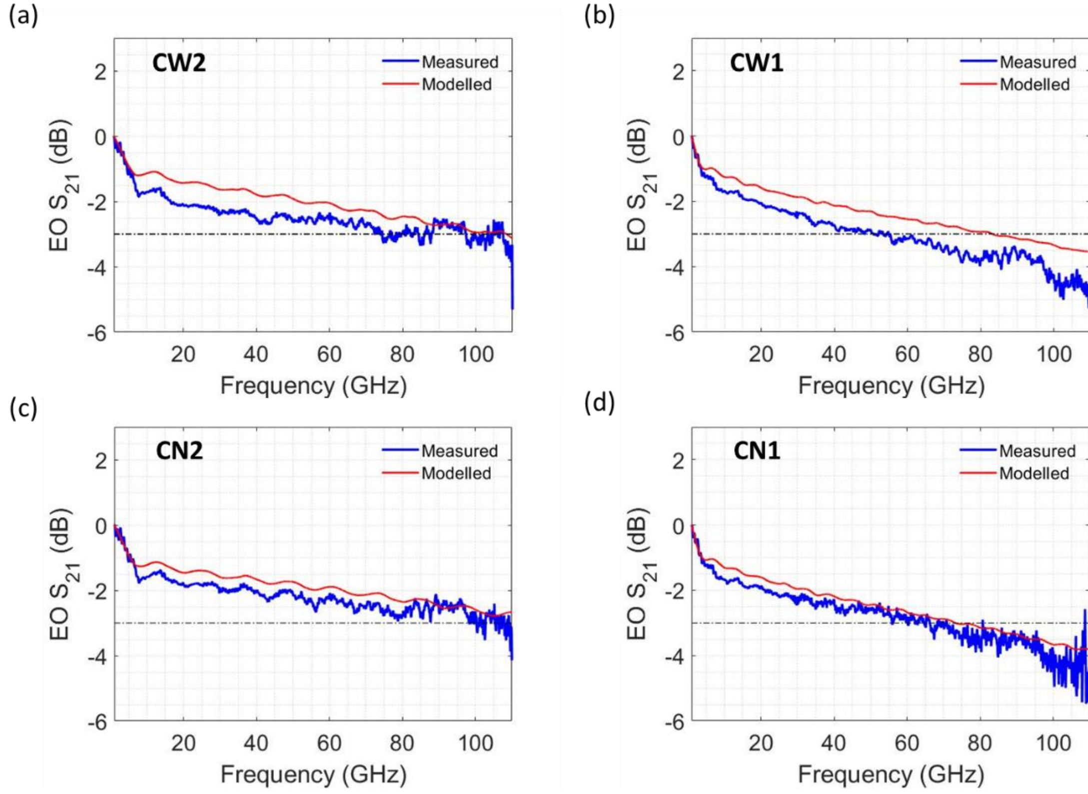

Figure 5.5: The measured (blue) and modelled (red) EO responses of the hybrid bonded Si/LN MZMs designed for C-band. (a) T-rail SWE with G = 7 μm and L = 0.54 cm. (b) T-rail SWE with G = 7 μm and L = 1.0 cm. (c) Slot SWE with G = 8 μm and L = 0.54 cm. (d) Slot SWE with G = 8 μm and L = 1.0 cm.

To measure the EO performance, a 50 Ω load resistor was used to terminate the lines and a 110 GHz Keysight lightwave component analyzer (LCA) was used after full calibration of the probing setup. Figure 5.5(a)-(d) and Figure 5.6(a)-(d) show the measured EO S_{21} normalized to 1 GHz for the four C-band and four O-band MZMs, respectively. The red curves in Figure 5.5 and Figure 5.6 are the modelled EO responses for each device that was calculated using the simulated n_g [dashed lines in Figure 5.4(a) and Figure 5.4(d)], with the measured electrical RF characteristics (n_m, α_m, and Z_c) from Figure 5.4(a)-(f) in Eq. (2.1).

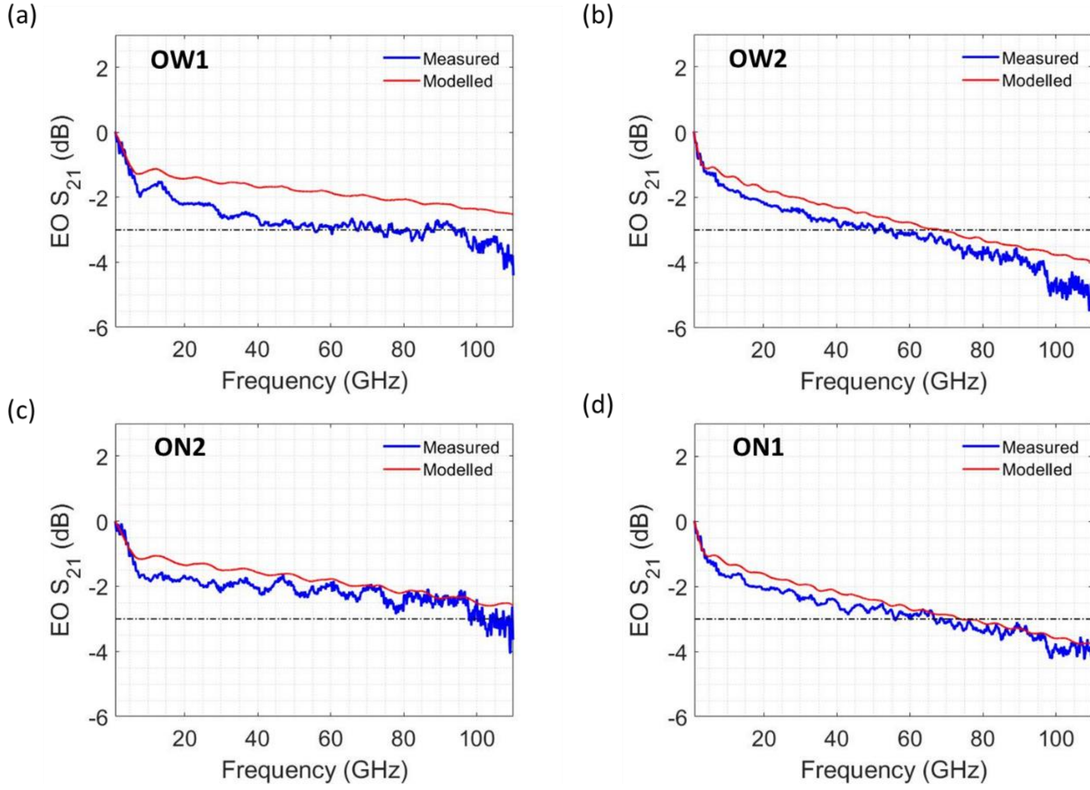

Figure 5.6: The measured (blue) and modelled (red) EO responses of the hybrid bonded Si/LN MZMs designed for O-band. (a) T-rail SWE with G = 6 μm and L = 0.54 cm. (b) T-rail SWE with G = 6 μm and L = 1.0 cm. (c) Slot SWE with G = 8 μm and L = 0.54 cm. (d) Slot SWE with G = 8 μm and L = 1.0 cm.

The measured RF S-parameters from an electrical only measurement (Figure 5.4) were used to model the EO response using Eq. (2.1). However, because the impedance of our SWE was not 50 Ω, the electrical measurements show oscillations versus RF frequency [Figure 5.4(c) and Figure 5.4(f)] that result from the impedance mismatch from the 50-40-50 Ω system (Source-Transmission line-Termination) [111]. To approximately infer the "true" EO response, because the magnitude of the ripples is relatively small (much less than 0.5 dB), the frequency-dependent $Z_c(f)$ data obtained from the PNA-X measurements was fit to a linear curve from 5 GHz to 110 GHz. Based on the agreement of the data and the simulated performance to within a fraction of a dB over a wide range of RF frequencies, I conclude that the EO model described by

Eq. (2.1) together with this linear approximation captures the EO behavior adequately well. The initial drop-off at sub-10 GHz frequencies is due to a combination of skin-loss and the impedance mismatch to the 50 Ω source and load. The decaying oscillations that can be seen in Figure 5.5 and Figure 5.6 is also indicative of an impedance mismatch between the SWEs and the source and termination loads [53]. Furthermore, the measured EO S_{21} traces in Figure 5.5 and Figure 5.6 have a gentle slope and none reach the -6 dB point (where the V_π of the device would increase by a factor of two), nor the frequency cutoff regime.

5.4 Low-speed $V_\pi L$ Measurements

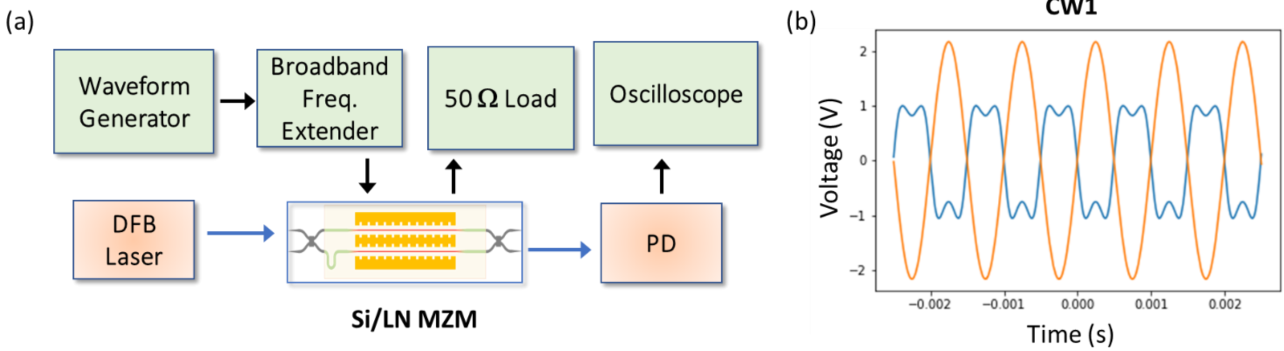

Figure 5.7: (a) A block diagram of the V_π measurement of the Si/LN MZMs using sinusoidal frequencies from a waveform generator. The modulated signals were detected with a photodetector (PD: Newfocus 1611-FC). (b) The applied electrical signal (orange trace) and the modulated signal (blue trace) were monitored with an oscilloscope (Agilent Infinium Digital Signal Analyzer). Device CW1 is shown here as an example.

To measure the near-DC (1 kHz) V_π of the O- and C-band modulators, these asymmetric MZMs were biased to quadrature by varying the laser wavelength. A waveform generator (Keysight 33600A) was used to apply 1 kHz sinusoidal signals to the devices, and the modulated optical signal was captured with a photodetector and an oscilloscope as diagramed in Figure 5.7(a). The voltage levels applied to the modulators were set higher than the expected V_π as to

ensure that the full π phase shift was induced. Overdriving the devices results in 'dips' in the peaks and nulls of the modulated signal because there are higher order harmonics affecting the sinusoidal output [see Figure 5.7(b) for an example of device CW1]. The waveform captured on the oscilloscope was post-processed using software to map the optical transmission to the applied voltage as shown in Figure 5.8. From this relationship, a cosine-squared fit was used to evaluate V_{π}. The value of L is taken from the design: there are two phase-shifter interaction lengths of each of the four MZMs for L = 0.54 cm and 1.0 cm (the blue and red traces, respectively in Figure 5.8).

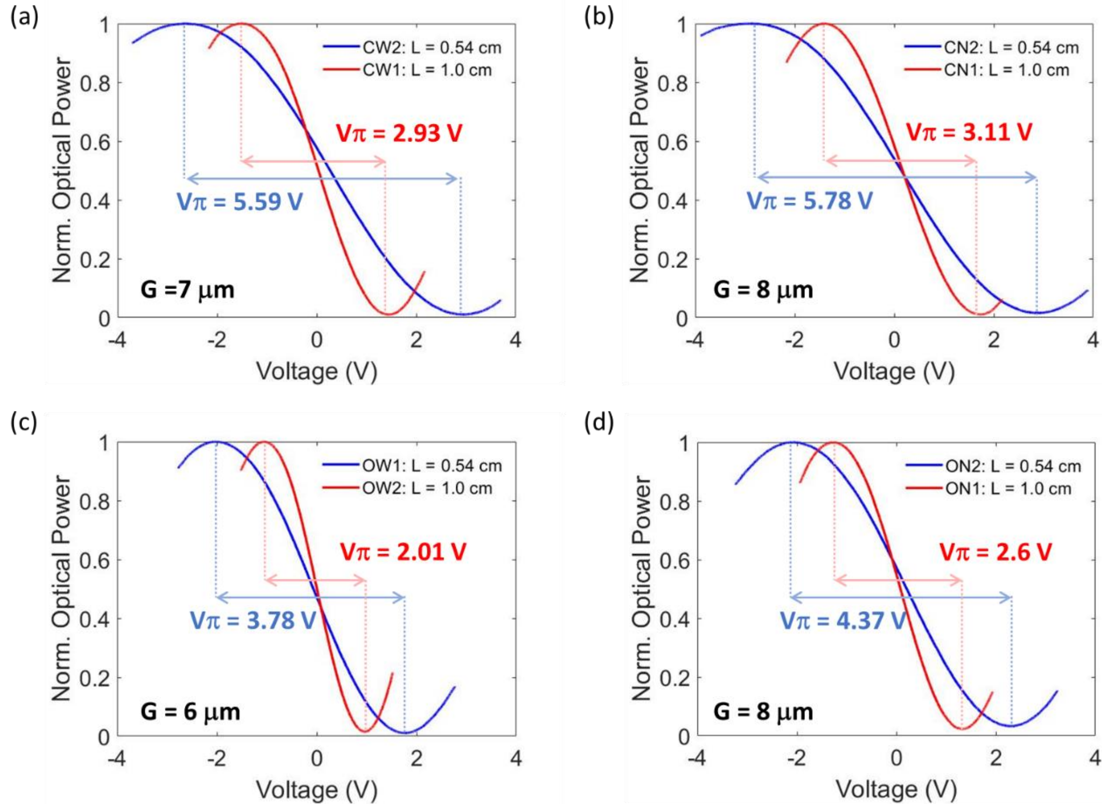

Figure 5.8: The measured normalized optical power as a function of applied voltage to the hybrid bonded Si/LN MZMs for (a) CW MZMs with G = 7 µm. (b) CN MZMs with G = 8 µm, (c) OW MZMs with G = 6 µm, (d) and ON MZMs with G = 8 µm. The blue traces correspond to the 0.54 cm long modulators and the red traces correspond to the 1.0 cm long modulators.

Eq. (2.7) shows that the required driving voltage for a π phase-shift reduces as the operation wavelength decreases. Furthermore, the A_{eff} of the shorter wavelength optical modes is smaller, which implies that G can be reduced without incurring higher optical loss from optical absorption in the metal electrodes. Thus, the OW designs show the most efficient V_π of the group of devices reported here, as shown in Figure 5.8(c) with V_π of 3.78 V and 2.01 V for the 0.54 cm and 1.0 cm long devices, respectively, which is a more efficient scaling of V_π than would be predicted by the ratio of λ at 1310 nm and 1550 nm.

When considering the overall system requirements to drive an EOM, it is important to know V_π as a function of the modulation frequencies (> 1 GHz), because the impact of RF loss, velocity mismatch, and impedance mismatch will also affect the needed voltage for a π phase-shift [112]. The driving voltage as a function of modulation frequency is given by

$$V_\pi(\omega) = V_\pi(DC)10^{-m(\omega)/20} \tag{5.1}$$

where $m(\omega)$ is the measured normalized (for example, to 1 GHz) EO S_{21} or calculated response from Eq. (2.1). Here $V_\pi(DC)$ is taken as the measured V_π at 1 kHz as shown in Figure 5.8 for each MZM. While a more accurate representation would be to normalize $m(\omega)$ to the same frequency as $V_\pi(DC)$, this approximation is valid as the modulator responses are flat for frequencies less than 1 GHz (see Figure 5.12 below). Figure 5.9 shows the calculated RF V_π which shows the effect of the SWE RF propagation loss, velocity, and impedance mismatch on the required driving voltage for the C- and O-band MZMs. An increase of the $V_\pi(DC)$ by a factor of $\sqrt{2}$ and 2 correlate to the EO S_{21} of the modulator decreasing by 3-dB and 6-dB, respectively.

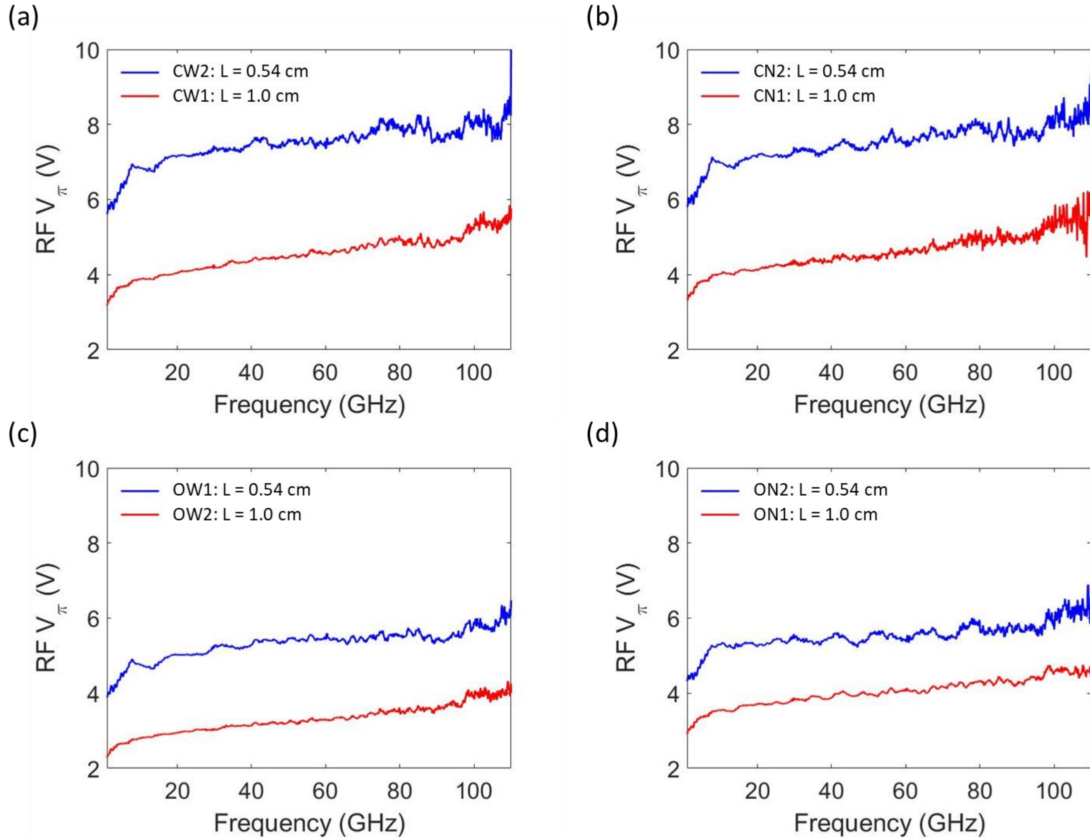

Figure 5.9: The calculated RF V_π as a function of driving frequency using Eq. (5.1) for the following Si/LN MZMs: (a) CW MZMs with G = 7 μm. (b) CN MZMs with G = 8 μm, (c) OW MZMs with G = 6 μm, (d) and ON MZMs with G = 8 μm. The blue traces correspond to the 0.54 cm long modulators and the red traces correspond to the 1.0 cm long modulators.

5.5 O-band and C-band Si/LN EOM Comparison

Both the O-band and C-band devices show high bandwidth and low voltage. As shown in Figure 5.10(a), the C-band modulators have a $V_\pi L$ of 2.9 V.cm to 3.1 V.cm, whereas the O-band modulators have a lower $V_\pi L$ of 2.0 V.cm to 2.3 V.cm. This is because the higher extraordinary index of refraction of LN, and the tighter optical mode confinement which allows for a reduced electrode gap at shorter wavelengths. The reduced gap has a more efficient EO effect, without incurring excess optical propagation loss from the proximity of the metal structures to the mode. These O-band devices can be further improved to have the Si waveguide width narrowed further

and still maintain single mode operation and similar confinement factor (Γ_{LN}) as the C-band devices as shown in Figure 5.1(c).

The wide-Si modulators (CW and OW) have a hybrid optical mode which allows for an electrode gap spacing of G = 7 µm and 6 µm for CW and OW, respectively, instead of 8 µm for the narrow-Si modulators (CN and ON). The hybrid mode is more confined in the Si region than the LN film compared to the narrower designs (CN and ON), but the A_{eff} is smaller. This tighter confinement allows for the electrode gap distance to be decreased, which also increases the modulation efficiency.

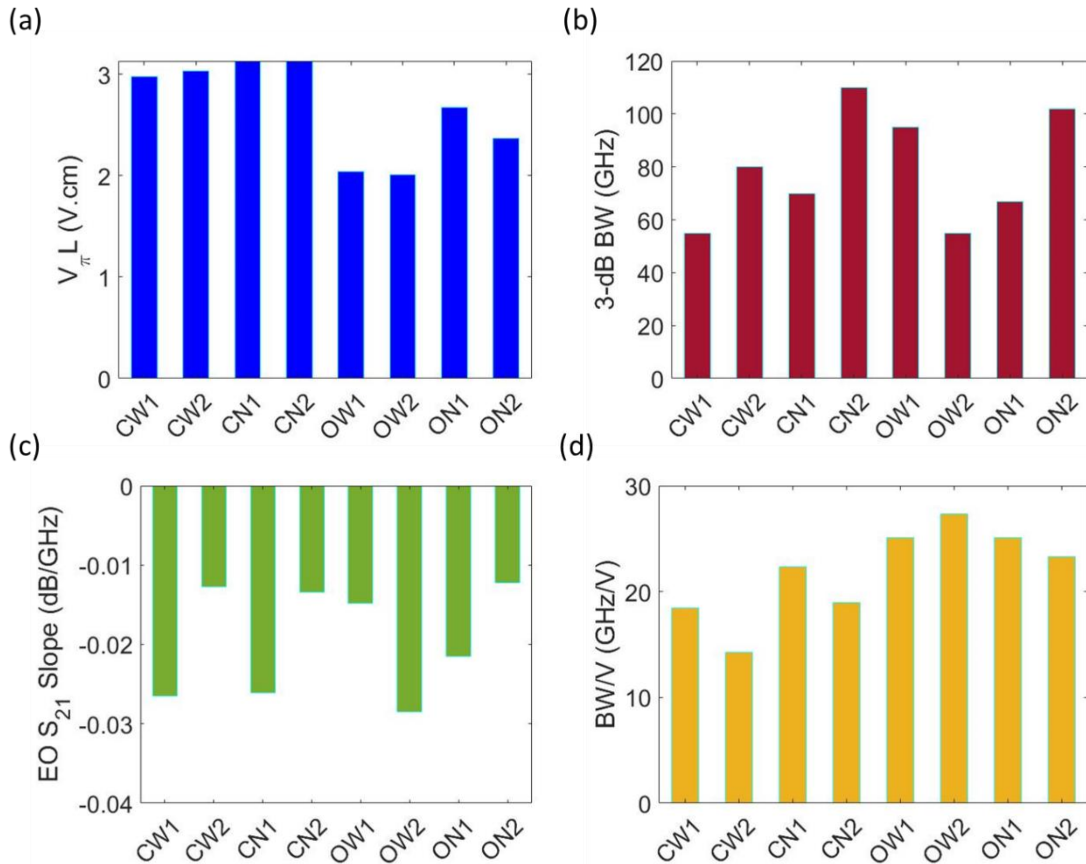

Figure 5.10: Summary bar graphs of the measured (a) $V_\pi L$, (b) 3-dB bandwidth (BW), (c) EO S_{21} slope (from 10 GHz to 110 GHz), and (d) 3-dB BW-to-V_π ratio for the hybrid bonded Si/LN C-band and O-band MZMs of the fabricated chip.

As seen in Figure 5.10(b), the 3-dB bandwidths of the 0.54 cm and 1.0 cm long MZMs are greater than 100 GHz and greater than 60 GHz, respectively for both O and C band designs. Note that although the initial 3-dB point of the wide Si waveguide 0.54 cm long MZMs (CW and OW in Figure 5.5(a) and Figure 5.6(a), respectively) occurs at 75 GHz, the response remains flat until 100 GHz with a slope of -0.013 dB/GHz (meaning a 1 dB drop over 100 GHz). An effective EO response slope from 10 GHz to 110 GHz is shown in Figure 5.10(c) and ranges between -0.012 dB/GHz and -0.029 dB/GHz. This indicates that the modulators still have usable bandwidth up to, and probably higher than, 110 GHz. Figure 5.10(d) summarizes the combined figure-of-merit, 3-dB bandwidth-to-V_π ratio (BW/V_π), of each modulator which shows the advantage of the O-band devices over the C-band counterparts. While both sets of modulators have been optimized for high-speed performance, the reduction of driving voltage for the O-band set allows for a higher BW/V_π which in turn reduces the power needed per high-speed modulation in a RF-photonic link. This may be helpful since communications in data centers and passive optical networks is energy-constrained.

5.6 RF Impedance Mismatch

The drop in EO response by about 2 dB at low frequencies (around 1-10 GHz) that is seen in the EO measurements [see Figure 5.5 and Figure 5.6] is attributed to the characteristic impedance of these traveling SWEs. Due to a design error, the impedance is around 40 Ω [see Figure 5.4(d) and Figure 5.4(f)], and is not matched to the source and load impedances, which are both 50 Ω. The shorter devices (L = 0.54 cm) show this effect more clearly than the longer devices (L = 1.0 cm), where the additional RF loss reduces the back-reflection, and a similar effect has been seen in traditional LN modulators [111]. The impedance is sensitive to the

electrode signal width to electrode gap ratio [53,80] and the mismatch in these devices can be corrected by redesigning the separation distance between the arms of the MZM. This would require a new round of lithography in the Si layer followed by planarization, bonding, handle removal and electrode formation (i.e., a complete process flow). Alternatively, to avoid the cost of full refabrication, an on-chip termination can be fabricated on these devices to provide a customized matching condition to the SWE lines [109,113] . A smaller load impedance (for example, 30 Ω) would result in peaking the response (when normalized to a certain frequency such as 1 GHz); however, this would be at the cost of causing larger back-reflections to the RF source, which is undesirable.

In the future, I believe that achieving a better match to 50 Ω source and termination loads, while maintaining the same levels of index matching and RF propagation loss that have already been achieved, should substantially improve the EO bandwidth. Figure 5.11 is similar to the traces shown in Figure 5.5 and Figure 5.6, with the addition of a yellow trace which corresponds to the modelled EO responses with $Z_L = 40\ \Omega$ to match the characteristic impedance of the fabricated SWEs. In this case, the 3-dB EO bandwidths of the O- and C- band MZMs would be around 110 GHz for the 1.0 cm long modulators, and greater than 110 GHz for the 0.54 cm long modulators. This, in turn, will also decrease the RF V_π (Figure 5.9).

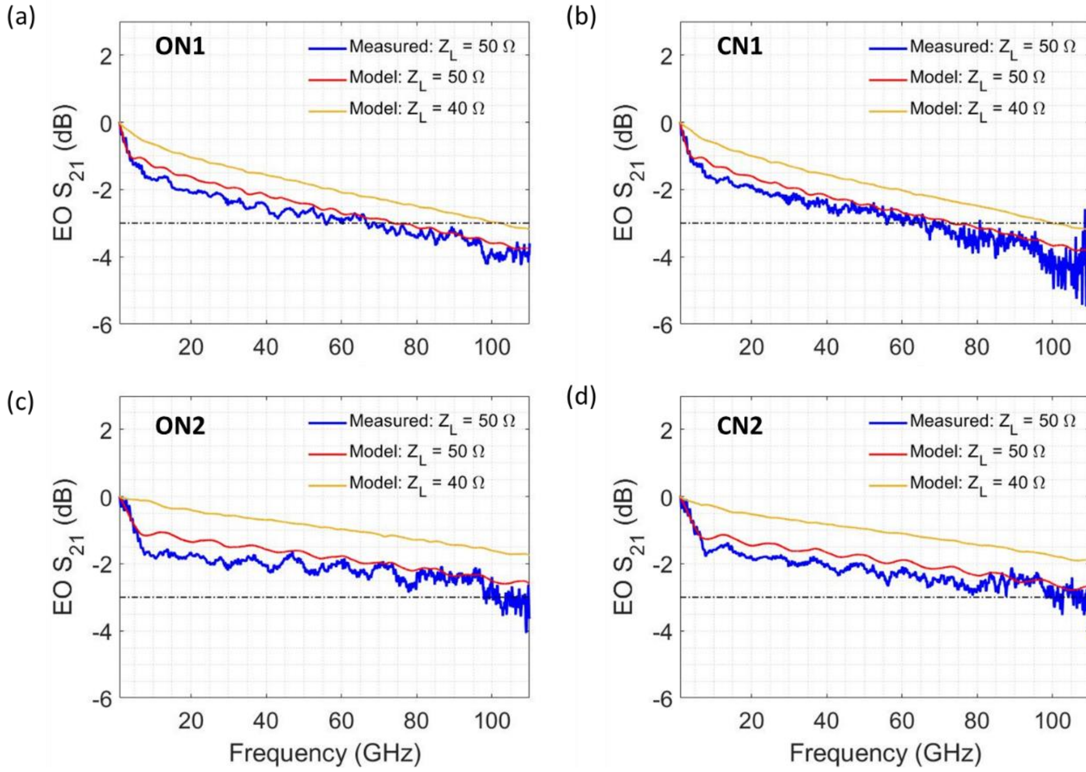

Figure 5.11: The measured (blue) EO responses of the hybrid bonded Si/LN MZMs designed for: (a) O-band, Slot SWE with G = 8 µm and L = 1.0 cm. (b) C-band, Slot SWE with G = 8 µm and L = 1.0 cm. (c) O-band, Slot SWE with G = 8 µm and L = 0.54 cm. (d) C-band, Slot SWE with G = 8 µm and L = 0.54 cm. The red and yellow curves correspond to the modelled EO response using Eq. (2.1) and the measured RF characteristics in Figure 5.4(d)-(f), assuming Z_L of 50 Ω and 40 Ω, respectively.

The EO response was measured over 100 MHz to 110 GHz using the available range of the LCA known, it is usually taken as the value at 1 GHz [51,90,114,115] though values as high as 5 GHz have also been used [116]. For the devices (ON1 and ON2) shown in Figure 5.12, the EO response changes by +0.11 dB from 100 MHz to 1 GHz for an L = 0.54 cm device, and by -0.77 dB for an L = 1.0 cm device. Often-quoted parameters such as the 3-dB bandwidth do depend on the reference point, which should therefore be clearly stated. Since the half-wave voltage V_π can be shows a direct relationship to both m(ω) through Eq. (5.1), and graph the trend all the way from measured down to very low frequencies, it is convenient to plot $V_\pi(\omega)$ as shown in Figure 5.9, which near DC to the highest modulation frequencies measured by the LCA.

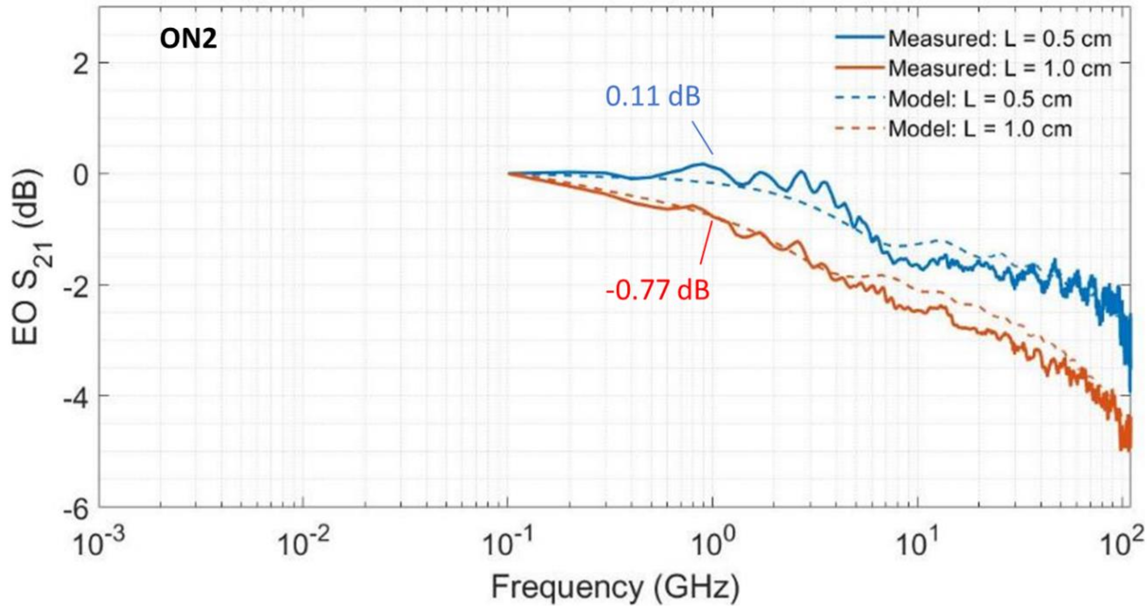

Figure 5.12: The measured (solid) and modelled (dashed) EO response normalized to 0.1 GHz for the ON devices with 8 µm gap slot SWEs.

5.7 Integrated O-band and C-band Si/LN MZMs Summary

In conclusion, we have demonstrated that a hybrid bonded Si/TFLN platform can be used for high-speed and low voltage EOMs in both the O and C wavelength bands using the same fabrication process, a common layer stack, and on the same chip. Standard Si manufacturing processes were used to define the optical routing, splitting, and tapering of the waveguides. The top oxide layer of the SOI wafer was chemical-mechanically polished to provide a bondable surface and no etching or patterning of the LN layer is required. We show that the velocity matching condition for high-speed modulation can be precisely achieved (to less than 1%) by changing the Si waveguide width (tuning n_g) and the parameters of the travelling slow-wave electrode structures (tuning n_m) across different wavelength bands to account for both chromatic dispersion and local variations in geometry. Four designs were reported here, two in the O-band and two in the C-band, which differ only in the widths of the features in Si layer and in the

traveling slow-wave electrode designs. The high-frequency EO response of the 0.54 cm and 1.0 cm long devices cross the 3 dB line (referenced to 1 GHz) at about 100 GHz and 60 GHz, respectively, for both O and C bands. However, a single number such as 3 dB bandwidth may not fully capture the device performance, since the gentle slopes of the modulator response, and the fact that the EO response has not reached the cut-off frequency regime indicates useful EO bandwidth beyond 110 GHz in both cases. While all eight reported modulators are shown to have high electro-optic modulation bandwidth, the O-band devices prove to have a higher modulation efficiency, and the combination of high bandwidth and low voltage can greatly benefit short-range communications in data centers.

5.8 Acknowledgments

Chapter 5, in part, is a reprint of the material that appears in the following: Forrest Valdez, Viphretuo Mere, Xiaoxi Wang, and Shayan Mookherjea, “Integrated O- and C-band silicon-lithium niobate Mach-Zehnder modulators with 100 GHz bandwidth, low voltage, and low loss” Optics Express 31, no. 4 pg 5273-5289 (2023). The dissertation author, together with his advisor and colleague, led the research efforts for this work and co-authored the papers.

Chapter 6

Hybrid Si/LN EOMs at High Optical Power

6.1 Introduction

In recent years, TFLN EOMs with a high EO 3-dB bandwidth of at least 100 GHz have been reported with a $V_\pi L$ product and low optical insertion loss [36,41,117,118]. However, these demonstrations have been performed at relatively low optical power levels less than 10 mW. The ability to handle high optical powers without increasing V_π would be beneficial, by increasing the RF link gain and reducing the noise figure of an analog communications system [1,56,119]. For a given photodiode responsivity, reducing V_π and increasing the optical power are both important in the noise figure of an RF photonic link. Recently, a higher optical power level, around 25 mW, was shown using TFLN MZM with about 50 GHz bandwidth [120]. Here, we report the first TFLN MZM which achieves both above-100 GHz bandwidth and above-100 mW optical power handling capability, while also achieving a low $V_\pi L$ product and low on-chip optical insertion loss, and integration with silicon photonics.

By carefully designing the Si layer dimensions and tapers of the Si/LN MZM, the amount of optical power in the Si region can be minimized while remaining in the single-mode regime, which is necessary for a high-bandwidth MZM. The narrowing of the underlying Si waveguide not only minimizes the percentage of the hybrid mode that resides in the Si region (where TPA would impact greatest in the C-band), but also optimizes the EO phase-shifting effect of the hybrid Si/LN mode from the modal interaction with the driving RF electric field. While this strategy does not completely eliminate the nonlinear loss of Si, it can keep the impairments of

the hybrid mode adequately low for practically useful optical power levels over the device lengths needed for a high-bandwidth, low-voltage MZM.

6.1 High Optical Power Handling: Theory

The ability of an MZM to handle high optical input powers without increasing V_π can be beneficial to overall system performance in an RF-photonic link, such as the RF link gain and NF increase and decrease, respectively (Section 2.1.3). At higher optical powers, Si waveguides suffer from two-photon absorption (TPA) and free carrier absorption (FCA) and dispersion (FCD) effects [121–124]. These nonlinear, intensity dependent effects can, in principle, limit the intrinsic MZM EO bandwidth, insertion loss (IL), and V_π. The density of photo-generated electronic carriers caused by TPA is

$$N_{TPA}(P) = G_{TPA}\tau_e = \frac{\beta\tau_e}{2hf}\left(\frac{P}{A_{eff}}\right)^2 \tag{6.1}$$

where G_{TPA} is the photogeneration rate from TPA, β is the TPA coefficient of Si (assumed to be 1.0 cm/GW [123]), hf is the photon energy, and P is the optical power in the waveguide mode. The electronic carrier lifetime, τ_e, in crystalline Si waveguides is typically in the range of 1 to 100 ns and is dependent on the waveguide geometry and surface properties [125]. These photogenerated carriers lead to additional optical losses and a shift in refractive index in the Si waveguide via the plasma dispersion effect [10] given by,

$$\alpha_{FC}(P) = 1.45 \times 10^{-17} N_{TPA}(P) \tag{6.2}$$

$$\Delta n_{FC}(P) = -8.8 \times 10^{-22} N_{TPA}(P) - 8.5 \times 10^{-18} N_{TPA}^{0.8}(P) \tag{6.3}$$

TPA induced FCA and FCD plague all Si-based devices and as such can impact the hybrid bonded Si/LN MZMs proposed in this dissertation. However, the carriers generated by high intensities will only occur in the Si rib waveguide because LN and SiO_2 do not exhibit large TPA coefficients in the telecom wavelength regimes. This is where our Si/LN platform shines, because in order to optimize the phase shifting capabilities of the hybrid region the Si waveguide width has to be narrowed (see Section 2.2.1) which pushes the optical mode into the EO region (TFLN) and out of the higher refractive index Si waveguide. This is reiterated here as Figure 6.1 which shows the simulated n_{eff} and Γ for the Si and LN regions of the hybrid mode as a function of Si waveguide width. As the Si waveguide width is narrowed (which can be done very precisely in a CMOS fabrication process) Γ_{LN} increases to 84%, while Γ_{Si} decreases to about 2% when w_{Si} = 275 nm, h_{Si} = 150 nm, and h_{cmp} = 50 nm at λ = 1550 nm. This is still enough confinement to guide the hybrid mode and maintain single-mode operation in the MZM as shown by the simulated optical mode ($|E_o|^2$) in Figure 2.14(c). Therefore, the nonlinear impairments can be expected to be much lower than for a conventional Si carrier depletion MZM where most of the light is in the Si waveguide [126]. Because the amount of light in Si is so small, the hybrid TFLN phase shifter does not have a significant nonlinear optical penalty compared to an etched or deposited TFLN modulator.

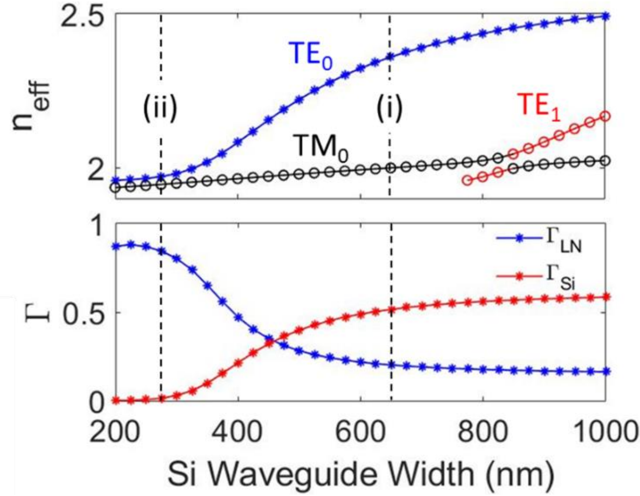

Figure 6.1: The simulated n_{eff} (top) of the first three modes of the Si/LN hybrid waveguide and confinement factor (bottom) in the LN film (blue) and Si waveguide (red) regions as a function of Si waveguide width.

To account for the percentage of Poynting vector magnitude that resides outside the Si waveguide of the Si/LN MZM, Γ_{Si} is introduced to the nonlinear power differential equation which describes the evolution of power along the waveguide:

$$\frac{dP(y)}{dy} = -(\alpha_l + \alpha_{FC}\Gamma_{Si})P - \frac{\beta}{A_{eff}}\Gamma_{Si}P^2 \tag{6.4}$$

where α_l is the linear absorption loss and the change in modal cross-sectional area (A_{eff}) is assumed to be negligible. Figure 6.2(a) shows the calculated change in IL due to these nonlinear effects (TPA induced FCA) by numerically solving Eq. (6.4) for different lengths of hybrid waveguide (solid lines) and transition waveguide (dashed lines). The A_{eff} of the transition and hybrid modes are calculated to be 0.24 μm^2 and 1.48 μm^2, respectively. The carrier lifetime, τ_e, upper limit is estimated to be 15 ns for the 150 nm thick strip Si waveguides [127]. For the maximum considered lengths of 2 cm and 0.15 cm for the hybrid and transition waveguides in Figure 6.2(a), the 1 dB IL penalty from TPA and FCA occurs at an optical power ten times

higher in the hybrid section than the transition section. Thus, to maintain high optical handling capabilities, the hybrid waveguide section must be made as long as possible (i.e, push the light into the hybrid mode immediately after reaching the LN region) and the transition and feeder waveguide should be kept as short as possible. If the transition section is reduced to 100 µm (which is approximately the minimum for an adiabatic taper [128]), then the total additional IL should be less than 1 dB for optical powers up to 0.6 W

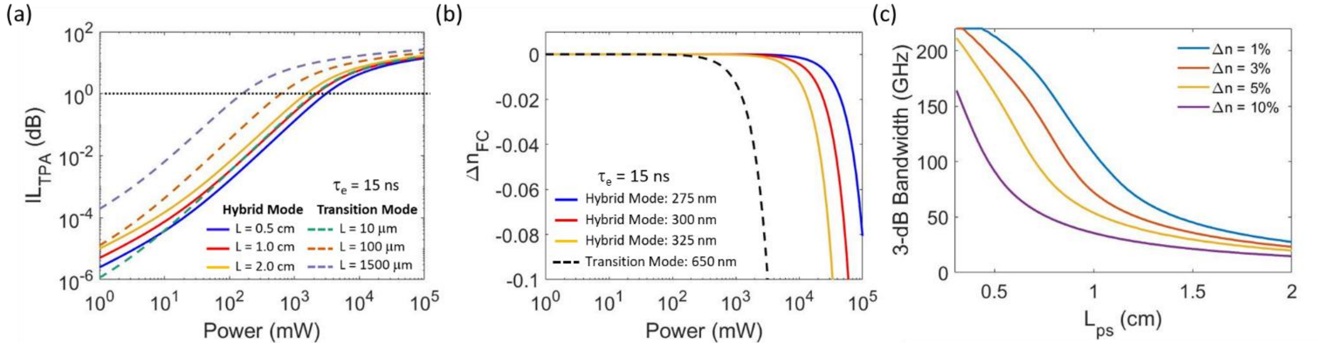

Figure 6.2: (a) The calculated IL due to TPA as a function of peak optical power in the hybrid waveguide mode (solid) and the transition mode (dashed) assuming different lengths. (b) The change in refractive index due to additional carriers generated via TPA as a function of peak optical power for different waveguide widths. (c) The calculated 3-dB bandwidth of a traveling wave MZM as a function of L_{ps} assuming impedance matching to a 50 Ω load and for different values of index mismatch, Δn, from TPA induced FCD.

The carriers introduced by TPA not only increases the absorption and overall IL of the Si/LN MZM, but also impart a change in refractive index as described by Eq. (6.3). This local change in the refractive index of Si will also change the n_{eff} and n_g of the hybrid mode, and thus may affect the velocity matching condition to achieve high-speed modulation. To account for this potential impact, Eq. (2.1) is adjusted here to include optical power dependence:

$$m(\omega, P) = \frac{R_L + R_G}{R_L} \left|\frac{Z_{in}}{Z_{in} + Z_G}\right| \left|\frac{(Z_L + Z_c)F(u_+(P)) + (Z_L - Z_c)F(u_-(P))}{(Z_L + Z_c)\exp[\gamma_m L_{ps}] + (Z_L - Z_c)\exp[-\gamma_m L_{ps}]}\right| \quad (6.5)$$

$$F(u_\pm(P)) = \frac{1 + \exp[u_\pm(P)]}{u_\pm(P)} \quad (6.6)$$

$$u_{\pm}(P) = \pm\alpha_m L_{ps} + \frac{j\omega}{c}\left(\pm n_m - n_g(P)\right)L_{ps} \tag{6.7}$$

where $n_g(P)$ is the associated FCD from photogenerated carriers. There will be a similar shift in $V_\pi L$ due to FCD, where the effective modulator length may be limited by the additional nonlinear losses and phase shift, and thus impact V_π. These effects can be expressed as:

$$V_\pi L_{ps}(P) = \frac{n_{eff}(P)\lambda G}{2n_e^4 r_{33}\Gamma_{mo}} \tag{6.8}$$

Figure 6.2(b) shows the change in n_{eff} from TPA induced FCD. These changes will affect the index matching condition ($\Delta n = (1 - n_m/n_g) \times 100\%$) between the travelling RF and optical waves. Since the hybrid mode is predominantly in localized in the LN film, the effect is expected to be negligible for optical peak powers less than 10 W in theory. Although the high intensity optical input can also result in an increase in the local temperature (and cause an associated thermo-optic effect), the time scales of such thermal shifts are much longer compared to the modulation speeds [129] and can be compensated by a bias controller. Additionally, the photorefractive effect of TFLN at a wavelength of 1550 nm results in a Δn_{eff} on the order of 10^{-5}[130], which would only change Δn by 0.005%.

Assuming the impedance matching condition is met, the 3-dB bandwidth of a traveling wave hybrid TFLN MZM is plotted as a function of phase shifter length for different values of Δn in Figure 6.2(c) using Eq. (6.5). If L_{ps} is 0.5 cm, then the Δn caused by nonlinear high-power effects would need to be about 10% in order to reduce the bandwidth by a factor of 2, which corresponds theoretically to an input power greater than 100 W. An MZM using a longer phase

shifting section (1 cm, say) would have its bandwidth decreased by 3 dB for a Δn of 5%. Thus, by optimizing the hybrid region for low-voltage operation, the Si/LN MZM has simultaneously been optimized to handle high optical powers which benefit RF-photonic links.

6.2 High Optical Power Handling: Measurements

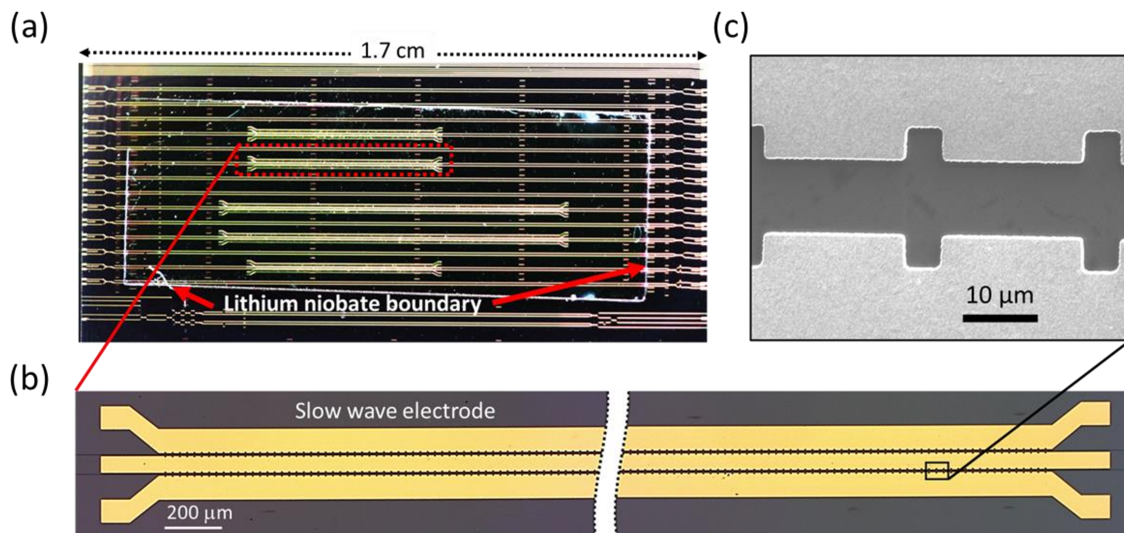

Figure 6.3: (a) An optical microscope image of the hybrid bonded Si/LN chip with gold SWEs used for high optical power modulation measurements with short feeder sections. (b) A stitched optical microscope image of the 5 mm long SWE. (c) A scanning electron microscope image of the inductively loaded slot features of the SWE.

The Si/LN MZMs in Chapter 5 (Figure 5.1, Table 5.1) were chosen to have orthogonal probing, i.e the optical fibers contact the north and south of the chip, while the RF probes contact the east and west, for easier testing setup. Thus, the MZMs were designed with rather long feeder Si sections (about 1.4 cm long) to get from the chip edges to the phase-shifter section. These wider Si waveguide sections would incur large amounts of intensity dependent nonlinear losses over such lengths as shown in Figure 6.2(a). To minimize such losses, the feeder sections need to be kept as short as possible. Figure 6.3(a) is an image of a fabricated hybrid bonded Si/LN chip

with the total length of the MZM about 1.7 cm, which includes the edge couplers, MMIs, transition region (L_{Tr} = 0.14 cm), and the hybrid region (L_{Hb} = 1.4 cm). Here the optical and RF probing are parallel (both east-west directions) to facilitate the shorter feeder sections. To overcome testing issues the RF probes are placed on lifted and movable platforms so that the RF probe tips can reach the electrode pads without touching the lensed tapered fibers underneath [see Figure 6.4]. In the hybrid bonded region, the transition waveguides are adiabatically tapered down from a width of 650 nm to a width of 275 nm over a length of 300 μm which pushes the optical mode up into TFLN. These transition sections were intentionally made longer than necessary to simplify our bonding process.

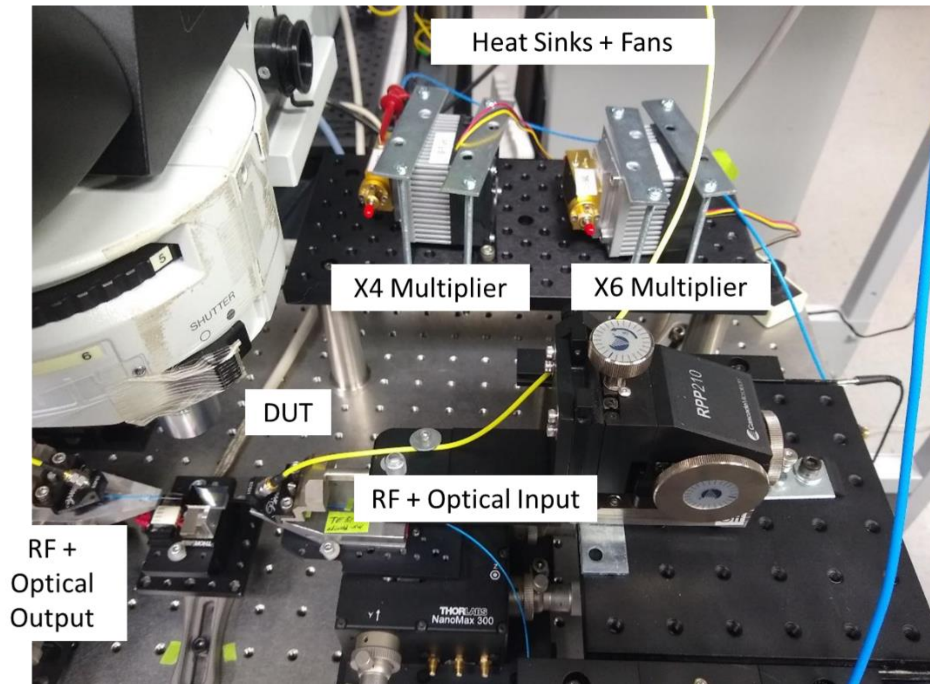

Figure 6.4: A photograph of the hybrid bonded MZM EO test station.

For this device, an inductively loaded SWE structure [Figure 6.3(b)-(c)] was designed to achieve velocity matching to the hybrid Si/LN optical mode. The gap between the signal and ground electrodes is 9 μm, and the signal width is 55 μm. The inductive loading feature is a

periodic slot that is 5 µm wide (w) and 4 µm deep (h) with a period of 25 µm, as shown in Figure 6.3(c). In this case, the hybrid Si/LN group index is simulated to be 2.32 and the slow-wave RF index is 2.34 at 110 GHz, resulting in Δn < 1% between the optical and RF waves before the intensity dependent nonlinear change of the index [Eq. (6.3)] is taken into account. For the fabricated structures with about 40 nm of CMP SiO_2 thickness, the estimated peak electric field strength at 110 mW optical power in the thin SiO_2 region of to be about 5.4×10^4 V.cm^{-1} and 1.3×10^4 V.cm^{-1}, which is smaller than the estimated breakdown field strength of SiO_2 (about $5\text{x}10^6$ V.cm^{-1}).

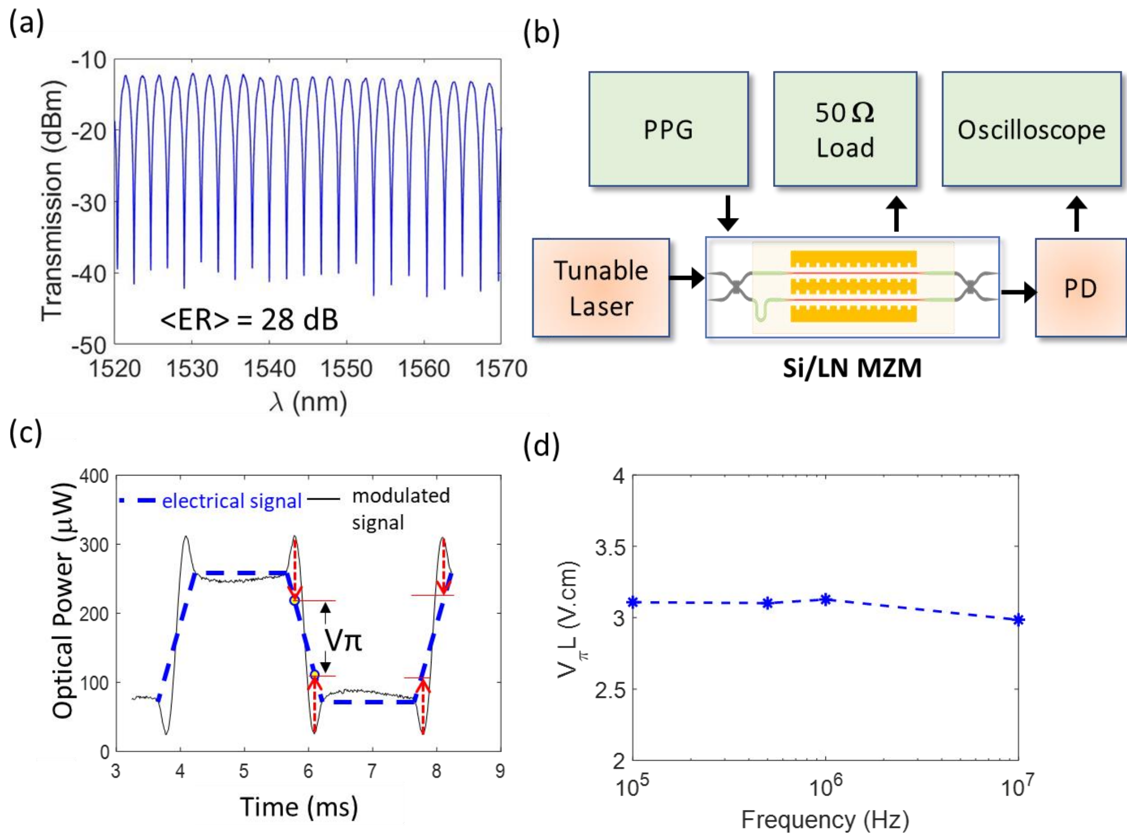

Figure 6.5: (a) The measured passive (no voltage applied) transmission of the asymmetric Si/LN MZM in the C-band. (b) The block diagram of the V_π measurement for the Si/LN MZM using a pulse pattern generator to drive the device. (c) An example of the trapezoidal driving signal (blue dashed trace) and the measured modulated signal (black solid trace). The V_π of the device is measured from the overshoots in the measured signal as shown by the red arrows. (d) The measured $V_\pi L$ of the 0.5 cm long Si/LN phase shifter as a function of the trapezoidal signal frequency.

The asymmetric MZM under test was measured using a tunable CW C-band laser source which resulted in a free spectral range (FSR) of 2.3 nm, a mean ER of 28 dB over 50 nm (maximum of 31 dB at λ = 1560 nm), and a fiber-to-fiber IL of 12.2 dB as shown in Figure 6.5(a) (without applied voltage). After characterizing the transmission curve of the MZM, the laser wavelength was fixed at the quadrature-point, and the value of $V\pi$ was measured by applying trapezoidal waveforms using a pulse pattern generator (PPG), as depicted in Figure 6.5(b). Trapezoidal waveforms are similar to triangular waveforms used in other reports [20,131], but also allow the slew rate and level-hold times to be adjusted independently for further detailed studies of bias drift and stability [see Chapter 10]. The half-wave voltage of the Si/LN modulator with L_{ps} = 0.5 cm was measured by overdriving it with a trapezoidal signal of peak-to-peak voltage greater than the expected V_π, and projecting the overshoots of the modulated signal as demonstrated in Figure 6.5(c). This was repeated as a function of the driving signal frequency resulting in an average $V_\pi L$ of 3.1 V.cm in the range of 0.1 to 10 MHz, which is shown in Figure 6.5(d).

To determine the low power (1 mW) IL of the hybrid bonded Si/LN MZM, a CW tunable laser was coupled to the device using lensed tapered fibers (2.5 µm nominal mode field diameter). As shown in Figure 6.6, the hybrid bonded Si/LN MZM consists of edge couplers, MMIs, wide Si transition sections and a narrow Si hybrid section. The IL of the phase shifter section was measured by subtracting the transmission spectra of the test device and an identical reference device, but without electrodes. Therefore, the IL of the L_{ps} = 5 mm long phase shifter is 0.4 dB. From these measurements, the individual component losses of the MZM were subtracted from the total transmission, resulting in an edge coupling loss of 5.2 dB/facet and an on-chip loss of 1.8 dB (assuming 0.1 dB of loss per LN edge transition) as shown in Figure 6.6. These losses,

as well as the fiber, splitter, and connector losses were factored in to calculate the peak power out of the PM-EDFA for the high-power setup described below. The power levels labeled in Figure 6.8 and in this discussion refer to the on-chip optical power levels in the feeder waveguide before the start of the MZM section. A peak power level of 110 mW corresponds to an intensity of 460 kW/mm^2 and 74 kW/mm^2 in the transition and hybrid waveguides, respectively.

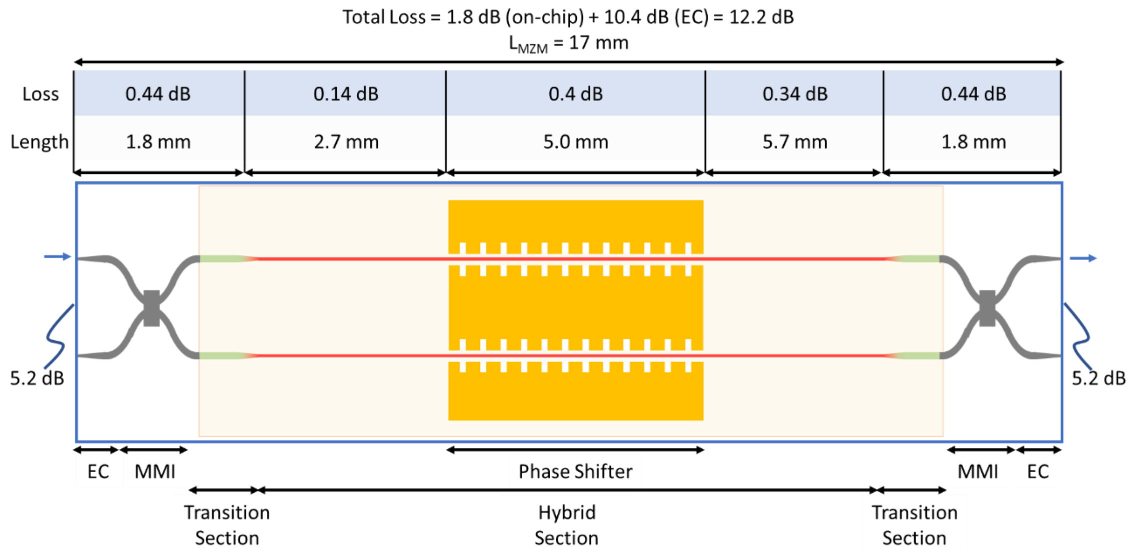

Figure 6.6: A (not to scale) schematic of the hybrid bonded Si/LN MZM showing the total measured insertion loss and the loss attributed to the edge coupler (EC), transition, hybrid, and phase shifter sections.

Figure 6.7 details a block diagram of the quasi-CW high power modulation experiment. An external commercial LN modulator (labelled Pulse Carver in Figure 6.7) with 30 dB extinction ratio was used to carve the CW laser source into quasi-CW pulses. The pulse carver was driven by a pulse pattern generator, setting voltages with a pulse width of 1 µs and a period of 100 µs. This corresponds to a pulse length greater than 100 m, which is much greater than the length (1.7 cm) of the chip. A polarization maintaining erbium-doped fiber amplifier (PM-EDFA) was used to amplify the quasi-CW pulses to the Si/LN MZM. Quasi-CW pulses were

used to extract maximum gain from the PM-EDFA by reducing the average power and gain saturation. Also, the lower average power reduces the likelihood of damage to the lensed fibers used in the experiments. The amplified pulses were characterized by monitoring the PM-EDFA output using a PM 90-10 splitter, where a sampling oscilloscope (Keysight DCA 81600D) verified the pulse shape and peak power, while an optical power monitor measured the average power of the pulses as a function of the PM-EDFA current. Optical attenuators were placed before the DCA and optical spectrum analyzer (OSA, Finisar WaveAnalyzer 1550s) to avoid damage.

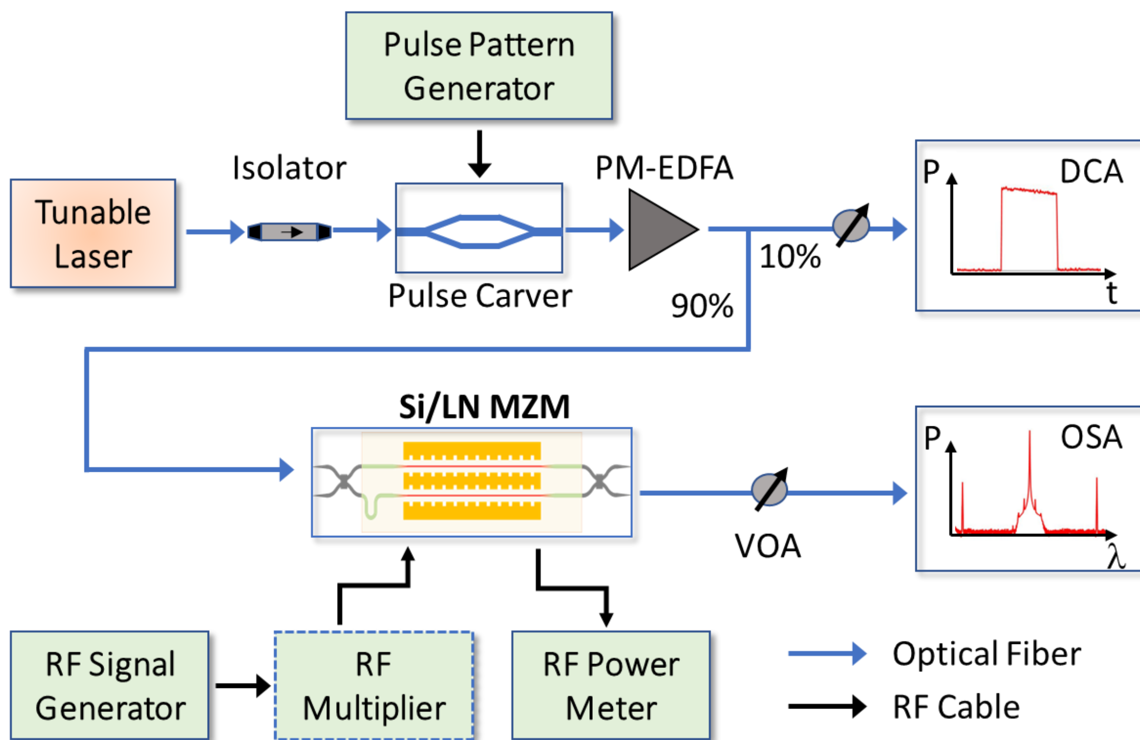

Figure 6.7: A schematic block diagram of the quasi-CW high power electro-optic response measurement setup. Active RF multipliers were used for generating f > 50 GHz. PM-EDFA: Polarization Maintaining Erbium Doped Amplifier. VOA: Variable Optical Attenuator.

The high-power quasi-CW pulses were then coupled to the device and modulated with varying frequency sinusoidal waves using an RF signal generator. A high-resolution OSA

(Finisar WaveAnalyzer 1500s) was used to detect the generated sidebands and carrier signal as the frequency was swept [132] (see Appendix B.1 for more information). This high-speed modulation measurement was performed in three frequency bands: 1 to 50 GHz, 47 to 78 GHz, and 72 to 110 GHz, where active RF multipliers (Eravant SFA-503753420-15SF-E1 and 753114616-10SF-E1) were used to reach the latter two bands. A CS-5 calibration substrate (GGB Industries, Inc.) and a 110 GHz RF power sensor were used to de-embed the cables and probes used in the experiment and determine the RF power delivered. These calibration measurements were then used to extract the measured EORs of the modulator at relatively low power CW optical input (4mW), and at input peak powers of 110mW, as shown in Figure 6.8(a) and 6.8(b), respectively. In both cases, the measured EOR has a 3-dB bandwidth of 110 GHz. The overlapping measured data between the bands was averaged and shifted accordingly to stitch the frequency responses together. Furthermore, the EO S_{21} of an identically designed hybrid bonded MZM on a different chip (the chip presented in Section 4.3) was independently verified at low CW optical power using an LCA. The LCA consisted of a Keysight PNA-X network analyzer, frequency extenders, and a 110 GHz photodetector which allowed us to measure modulated signals ranging from 100 MHz to 110 GHz, similar to the measurements described in Section 5.3. As can be seen in Figure 6.8(a), the OSA-measured response (blue marks) and LCA-measured response (cyan line) agree in both slope and 3-dB bandwidth. The 3-dB bandwidth is limited from impedance matching as discussed in Section 5.6. Due to the fixed separation between the Si waveguides of the fabricated SOI chip, the signal electrode to electrode gap spacing is also fixed. This specific MZM was fabricated with an electrode gap of 9 µm, resulting in a transmission line impedance of 42 Ω. If the Si waveguide separation is changed to

accommodate a more optimal signal electrode width, then the impedance will be better matched to a 50 Ω load, and further increase the 3-dB bandwidth of the MZM as shown in Figure 5.11.

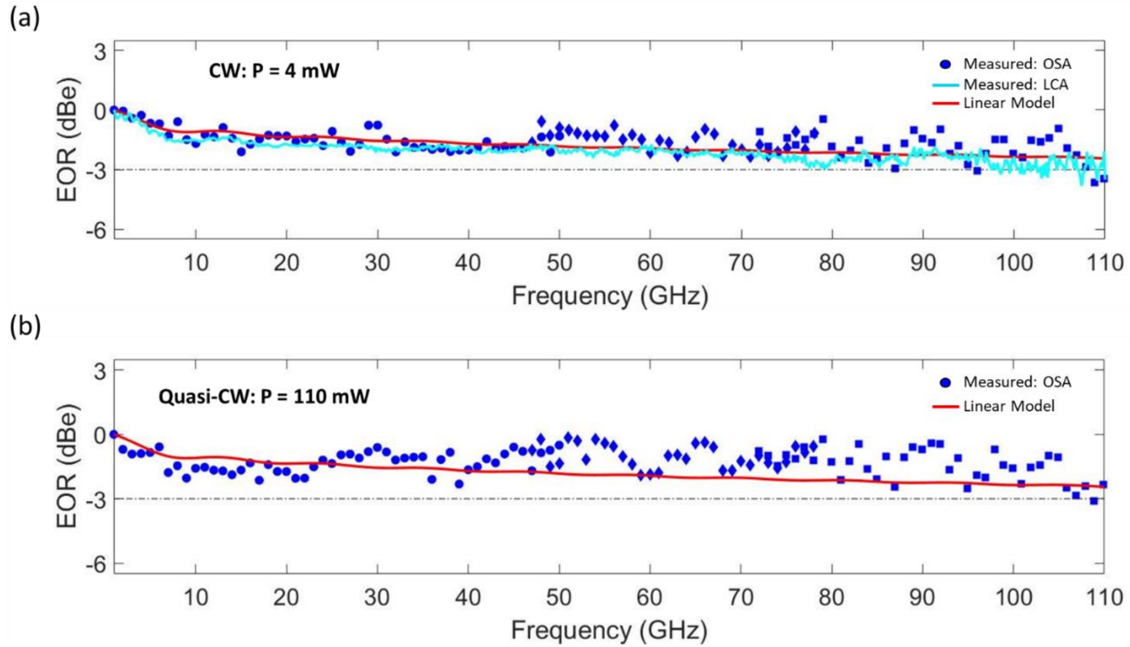

Figure 6.8: The OSA-measured (blue points) EOR of the hybrid bonded Si/LN MZM with Lps = 0.5 cm using no RF multiplier (circles), a 4x multiplier (diamonds), and a 6x multiplier (squares) resulting in a measured 3-dB bandwidth of 110 GHz for both: (a) Low power, CW optical input with 4 mW of power; and (b) Quasi-CW optical input with peak power of 110 mW. The solid red line is the calculated linear model using Eq. (2.1) with no nonlinearities. The cyan line in panel (a) is the EOR of an identically designed Si/LNMZM using a high speed LCA.

6.3 High Optical Power Handling: Discussion

The red lines in Figure 6.8(a) and Figure 6.8 (b) are the calculated EO responses using a linear model of the response function of a traveling wave MZM with no intensity dependent nonlinear effects using Eq. (2.1). The theoretical EOR predicts a 3-dB bandwidth above 110 GHz (approximately 156 GHz) for this 0.5 cm long modulator, which is agreement with the measured frequency responses in both the low and high optical power regimes. A large concentration of free carriers overlapping with the optical mode would cause a free-carrier dispersion effect which would decrease the 3-dB bandwidth. However, since the hybrid mode

has only 2% of light in the Si waveguide, there is an insignificant impairment in our device, and the response at 110 mW is effectively the same as that at low (4 mW) power levels. Table 6.1 lists performance metrics of recent TFLN-based MZM. The present device is the first (to our knowledge) TFLN MZM that demonstrates greater than 100 GHz modulation of high optical power inputs greater than 100 mW. FOM_{NF} (units: dB) in Table 6.1 is defined as

$$FOM_{NF} = 20\log_{10}(V_\pi) - 20\log_{10}(P_{opt} r_d R_s) \quad (6.9)$$

where r_d is the detector responsivity, assumed to be 1 A/W, and R_s is the source resistance, assumed to be 50 Ω. FOM_{NF} is that portion of the NF expression for an RF photonic link [Eq. (2.10)] which represents the contribution to the NF from the modulator V_π and optical power level. In addition, the laser RIN plays an important role in the overall NF in a practical system, but is not considered here in the FOM for the modulator alone.

Lower values of the modulator FOM_{NF} are preferable because they reduce the minimum achievable NF of the link. This shows the benefits of increasing P_{opt} while keeping V_π low. The on-chip IL of our hybrid Si/LN device is comparable to that of other TFLN devices. The $V_\pi L$ can be slightly improved by introducing a buffer SiO_2 layer between the electrodes and LN film, which will reduce the optical loss due to electrode interaction and allow for a narrower electrode spacing. In comparison to these TFLN MZM devices, a traditional Si depletion-mode MZM made with 250 nm thick Si rib waveguide (90 nm slab height and 650 nm width) will have 75% of the Poynting energy confined in Si and an A_{eff} on the order of 0.2 μm^2. Both the linear and nonlinear optical propagation loss coefficients are high, and will limit the high-power handling capabilities of a Si MZM. Furthermore, the modulation speed of carrier depletion MZMs is typically RC-limited, with reported 3-dB electro-optic bandwidths < 60 GHz [11–14,133].

Table 6.1: Comparison of recent TFLN-based MZM Performance Metrics

Device	3-dB BW (GHz)	$V\pi L$ (V.cm)	IL (dB)	Lps (cm)	Popt (mW)	FoM_{NF} (dB)
Etched LNOI [36]	100	2.2	0.5	0.5	1	38.9
Etched LNOI [41]	>110	2.4	18 (f-f)	0.5	1	39.6
Etched LNOI [120]	50	2.2	NR	0.5	25	10.9
Etched LNOI [40]	>67	1.7	17 (f-f)	0.5	NR	-
Etched LNOI [42]	>67	2.2	0.2	1	0.03	63.3
Bonded (BCB-assisted) Si/LN [91]	>70	2.1	3	1.25	NR	-
Polished LNOI [134]	>50	2.2	0.6	0.7	NR	-
Bonded (BCB-assisted) Si + Etched LN [39]	>70	2.5	2.5	0.5	NR	-
Bonded (Direct) SiN/LN [20]	37	6.7	13 (f-f)	0.5	4	36.5
Bonded (Direct) Si/LN – This Work	110	3.1	1.8	0.5	110	1.04

The experimental observations are consistent with the theoretical predictions shown in Figure 6.2(b). Using Eq. (6.8), the effect of TPA induced carriers on the $V_{\pi}L$ through FCD [Figure 6.2(b)] is insignificant at 110 mW, and would contribute less than 1% change in modulation efficiency assuming thermo-optic and photorefractive effects in the TFLN layer are

negligible. The change in IL due to carrier effects in the Si regions are predicted to be under 1 dB as shown by Figure 6.2(a). Practically, such small changes are indistinguishable from other losses in this study, such as repeatability of fiber coupling in these bare-die test chips. Fiber-pigtailing the device will allow for easier testing. Although these tests were performed using long quasi-CW pulses, we expect similar performance, when packaged, under CW optical excitation as well.

As the modulators scale to longer phase shifters (L_{ps} >1 cm) to reduce the voltage, the walk-off between the RF and optical phases can occur from smaller velocity differences. Therefore, the changes caused by higher optical power can have a larger effect on the 3-dB bandwidth. However, our calculations show that the majority of the impairments will occur in the mode transition region rather than the phase-shifter region. The theoretical minimum length for a low-loss adiabatic taper between the transition mode and hybrid mode in this design is about 100 μm [128]. In this batch of test chips, the transition waveguides were intentionally made longer for fabrication ease, and therefore the nonlinear losses will inevitably be higher. The feeder waveguide and taper lengths could be reduced, which in turn will minimize the TPA-induced FCA of the transition section. If the combined input and output transition sections were only 100 μm long instead of 1.4 mm long as in these chips, then the additional insertion loss due to TPA would incur a 1 dB penalty only for optical powers greater than 0.6 W. For higher power operation, other materials with lower multiphoton absorption effects can be used. As an example, SiN is another CMOS-compatible material, does not experience TPA in the telecom wavelength regime, and has been shown to be suitable for hybrid bonding with unpatterned LNOI [20].

Greater than 110 mW, upwards of 150 mW, on-chip optical power was also coupled to the Si/LN MZMs; unfortunately, damage was incurred during the modulation response

measurement. Figure 6.9(a)-(c) detail the optically induced damage to the Si/LN MZM when 150 mW of on-chip peak pulsed power was used. Figure 6.9(a) are stitched infrared (IR) camera images with a 20x objective showing CW low-power (0 dBm) input light at 1550 nm propagating from left-to-right. There are large amounts of scattering just before the TFLN bonded edge (dashed vertical line) due to the high-power damage. Still light in the top MZM arm propagates through the hybrid mode to the SWEs and output, but the bottom arm shows an indiscernible amount of light. This is verified by optical transmission measurements in Figure 6.9(b) where the blue trace is the measured low-power CW transmission before damage, showing the deep 30 dB ER which is indicative of well-balanced MZM arms. After the damage, the transmission (red trace) becomes constant with the tunable laser wavelength and has an additional IL of 10 dB. This damage is further confirmed via the SEM images in Figure 6.9(c). The damage seems to originate from the top PECVD oxide cladding being partially etched near the feeder Si waveguides just before the TFLN interface. These air-clad Si waveguides would then have poor thermal conductivity when high optical powers propagate through and resulted in a damaged waveguide as seen by the inset in Figure 6.9(c). This potentially means that the MZM no longer is an amplitude modulator, but instead a phase modulator (via the top MZM arm) with additional IL. With a more protected sample during the fabrication stages, this oxide etching can be mitigated, and thus higher optical powers can be modulated in the future.

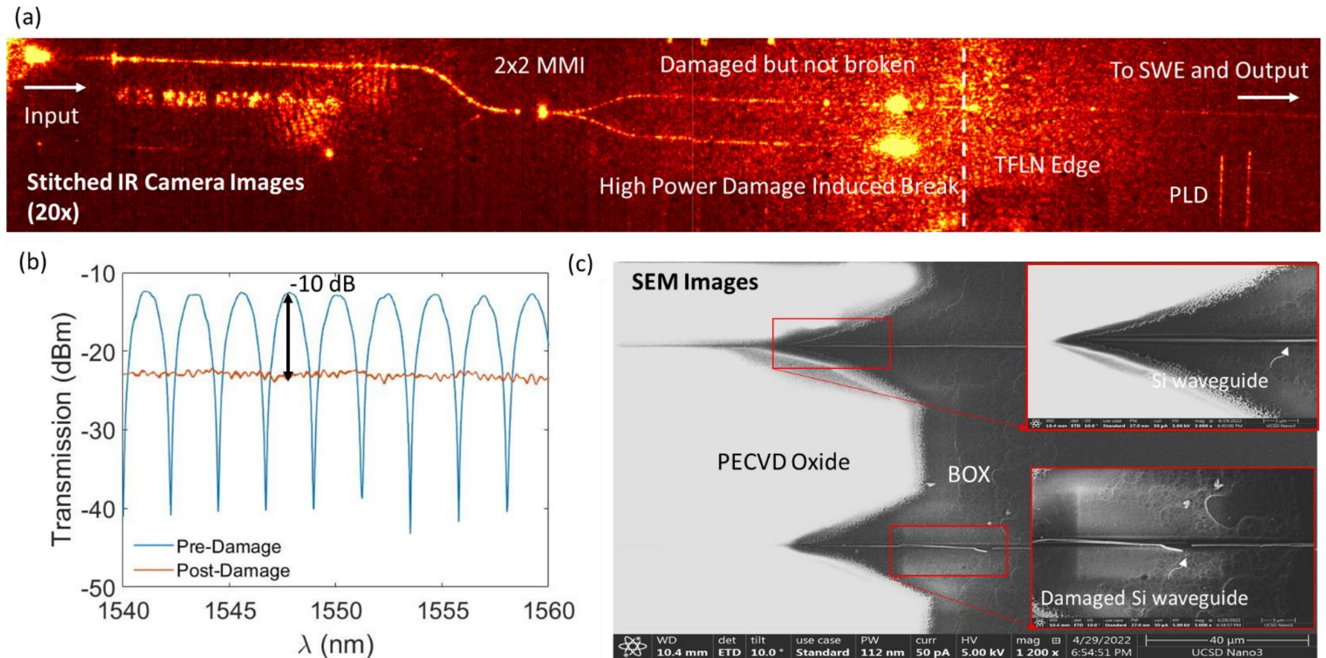

Figure 6.9: (a) Stitched IR camera images (20x objective) of the propagating light through the damaged Si/LN MZM after 150 mW of peak on-chip optical power was coupled. Large scattering before the TFLN edge (dashed line) indicates the points of damage. (b) The optical transmission measurements as a function of laser wavelength before (blue trace) and after (red trace) optical damage. The damage results in only one MZM arm functioning, hence the ER collapsing to near 0 dB and the additional 10 dB of IL. (c) SEM images of the damaged area. The top PECVD oxide cladding was unintentionally etched leaving the Si waveguides air-clad with poor thermal conductivity. The bottom Si waveguide was damaged and severed due to the high optical power; whereas the top waveguide was damaged but remains intact.

A separate Si/LN MZM was also tested at high optical input powers, but not modulated. This MZM had an SiO_2 cladding that covered just past the bonded LN edge and thus did not get etched during the fabrication process. Using an EDFA, the on-chip optical power was increased to 479 mW before the MZM suffered optical induced damage. The optical damage occurred at the input edge coupler inverse taper as shown by the IR camera images in Figure 6.10(a) and (b). Studies have shown that optically induced damage tends to happen at the edge coupling section of Si waveguide circuits because this is where the most of the optical power resides [135]. This test proves that our hybrid Si/LN MZMs can withstand and modulate even higher optical power than demonstrated here.

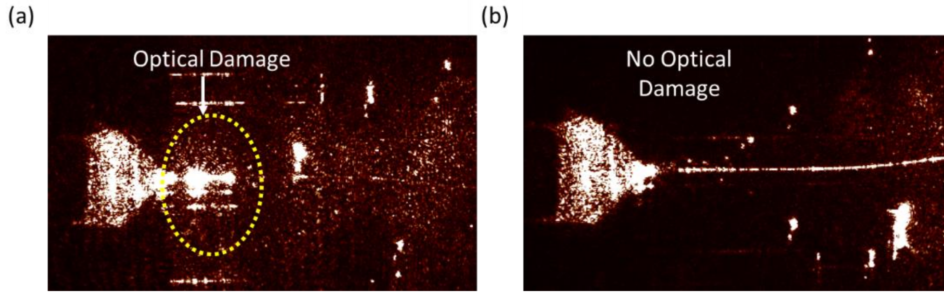

Figure 6.10: (a) An IR camera image of the input edge coupler of a Si/LN MZM that has experienced optically induced damage which causes large amounts of scattering (encircled). (b) An IR camera image of the other port of the Si/LN MZM which has not experienced damage and propagates the light to the device.

In summary, we have demonstrated that hybrid TFLN MZMs, which use an unetched TFLN layer bonded to planarized crystalline Si waveguides, can withstand high optical input powers of 110 mW while maintaining high speed modulation bandwidths of 110 GHz. A high EO bandwidth was achieved by using an inductively loaded SWE design to achieve velocity matching between the RF and optical waves. The hybrid Si/LN device design was optimized to achieve a high modulation efficiency ($V_\pi L$ = 3.1 V.cm) while minimizing the nonlinear intensity dependent effects of Si. The on-chip IL of the hybrid MZM structure including the MMI couplers, transitions into and out of the bonded region and electrode interaction loss was measured to be 1.8 dB. High optical power operation was tested by amplifying quasi-CW pulses with a pulse width of 1 μs and at power levels of up to 110 mW, we did not observe degradation of the EO bandwidth compared to measurements made at a conventional power level (4 mW). Compared to measurements made at an input power of 6 dBm, the additional nonlinear insertion loss was less than 1 dB at 20.4 dBm optical power. Our work demonstrates the integration of MZMs with high bandwidth and power handling capabilities well beyond the capabilities of traditional Si photonics.

6.4 Acknowledgments

Chapter 6, in part, is a reprint of the material that appears in the following: Forrest Valdez, Viphretuo Mere, Nicholas Boynton, Thomas A. Friedmann, Shawn Arterburn, Christina Dallo, Andrew T. Pomerene, Andrew L. Starbuck, Douglas C. Trotter, Anthony L. Lentine, and Shayan Mookherjea, “110 GHz, 110 mW hybrid silicon-lithium niobate Mach-Zehnder modulator”, Scientific Reports 12, 18611, (2022). The dissertation author, together with his advisor and colleague, led the research efforts for this work and co-authored the papers.

Chapter 7

Hybrid Bonded SiN/LN EOMs in the Telecom Regime

Section 4.2 described the methods of which to fabricate SiN/LN hybrid modulator chips. The cross-section of the SiN/LN phase-shifter is shown in Figure 4.4 where either a buried metal layer or a post-fabricated Au layer can be used to facilitate the traveling wave electrodes. In this Chapter I will focus on modulators utilizing this top Au layer for applying the RF signals. As alluded to in Section 4.2, the additional buried metal layers and consecutive CMP processes had an impact on the quality of the final SiO_2 surface that bonds with the TFLN. Initial bonded samples of SiN circuits with LNOI resulted in a large amount of "chemical voids" produced from trapped gas byproducts between the bonded layers [136]. These voids can degrade the mechanical, optical, and electrical performance of the hybrid SiN/LN devices by adversely affecting the optical waveguides. Including in-plane outgassing channels in the SiN photonic chip surface has demonstrated to drastically reduce the number of voids by about 99% [94] and increases the yield of SiN/LN devices per fabricated chip.

7.1 High-speed O-band SiN/LN MZM Characterization

After inspection, a bonded SiN/LN sample with minimal voids was processed through the remaining steps of electrode definition and fabrication using a lift-off process, as described earlier. Slot SWEs with L = 20 μm, h = 4 μm, w = 5 μm, and G = 5.5 μm were designed to achieve index and impedance matching to the SiN/LN optical mode with 200 nm thick MgO:LN. Figure 7.1(a) shows an image of the microchip which contains several MZM structures. Each

MZM device addresses a different wavelength band. Measurements from devices in the O-band (around 1310 nm) are reported here, with a more detailed report on the other devices, and a comparison of their performance are reported in Chapter 9. Lensed-tapered fibers and multi-axis micropositioners were used to couple light from an O-band tunable laser diode to the microchip. The optical transmission of both asymmetric and symmetric MZMs were measured using a swept laser source, as shown in Figure 7.1(b) and Figure **7.1**(c). The intentional path-length difference between the two arms in this asymmetric MZM device resulted in a measured FSR of 4.7 nm; the asymmetric MZM design allows this modulator to be either wavelength- or voltage-biased at quadrature for testing purposes. For the asymmetric device, the optical ER was seen to be about 30 dB, which shows that light propagation along both of the two interferometric pathways (about 1 cm long) was well balanced, due to the effective elimination of voids in the vicinity of the optical modes. Figure 7.1(c) shows the symmetric MZM flat broadband response with wavelength as there is no path-length difference in the MZM arms. The red dotted lines in Figure 7.1(b) and Figure 7.1(c) are the optical transmission spectra of MZMs (asymmetric and symmetric) with many voids along the waveguides (from sample A) normalized to the transmission of MZMs with no voids for comparison (blue solid lines). The voids act as scatterers which impact the loss and relative phase of the two MZM arms, increasing the insertion loss by 50-60 dB compared to the MZMs with no voids.

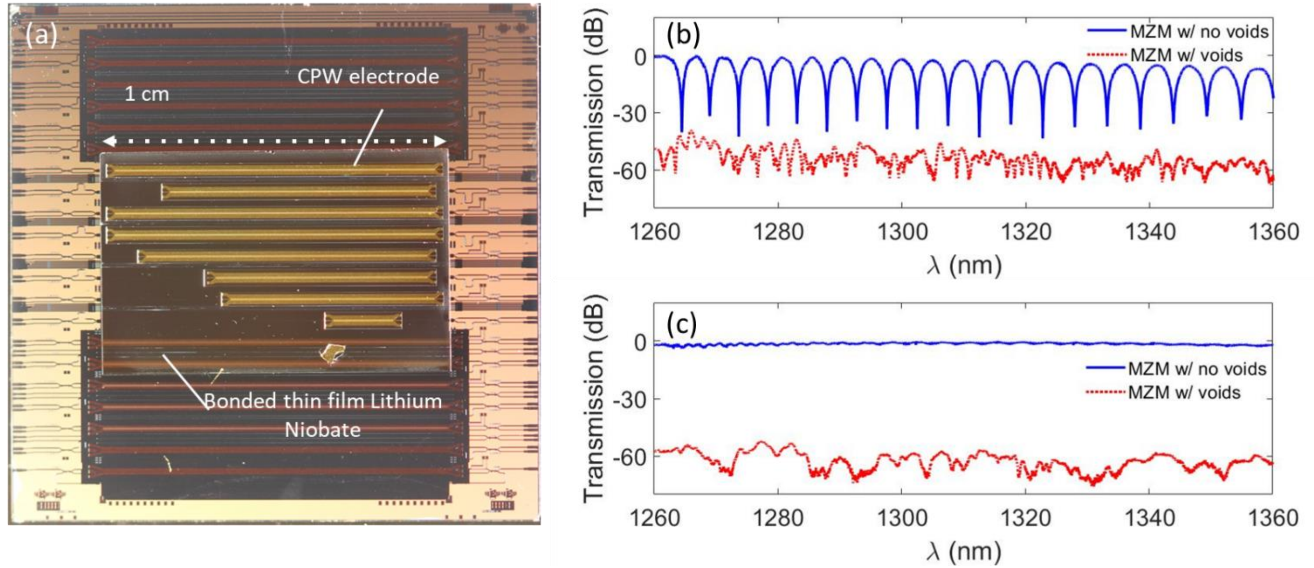

Figure 7.1: (a) A digital camera image of the fabricated SiN/LN bonded MZM chip. (b) Passive normalized transmission measurements of the hybrid EOM (b) asymmetric and (c) symmetric devices in the O-band with (red dotted lines) and without (blue solid lines) voids.

To measure the low-speed (100 kHz) V_π, G-S-G probes rated to 110 GHz were landed on the launch and termination pads of the 0.93 cm long SWE. The gap between the signal and ground electrodes was 5.5 µm, with a signal width of 16 µm. Trapezoidal waveforms were applied to the devices with a peak-to-peak voltage greater than the expected V_π to capture more than the full modulation range [similarly described in Figure 6.5(b)-(c)]. The modulated optical waveforms were detected using fiber-coupled InGaAs photodetector (ThorLabs DET02AFC) and sampling oscilloscope (Keysight InfiniiVision DSOX4022A). Figure 7.2 shows the measured normalized optical power and a cosine-squared fit (blue trace) as a function of applied peak-to-peak voltage, yielding a V_π = 2.9 V (L = 0.93 cm, hence $V_\pi L$ = 2.7 V.cm) and a voltage-driven ER of 25 dB at 1310 nm. A more precise scan of the transmission null may result in a higher measured ER.

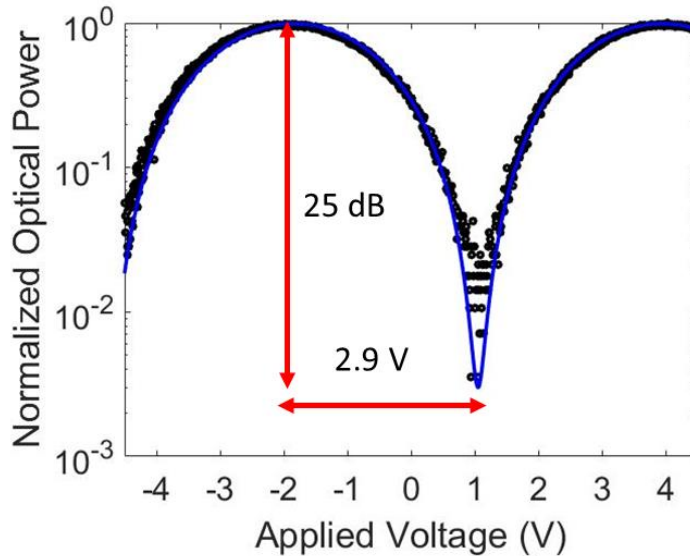

Figure 7.2: The measured normalized optical power as a function of applied voltage using a pulse pattern generator at 1310 nm, resulting in a voltage-driven ER of 25 dB and a V_π of 2.9 V for the 0.93 cm long phase-shifter. The blue trace is a cosine-squared fit to the data (black circles).

The high-speed (> 1 GHz) modulator response was measured by driving the SiN-LN MZM with sinusoidal waveforms generated by an RF frequency synthesizer (sweeper). As opposed to the O-band devices demonstrated on a Si/LN platform in Chapter 5, a high-speed LCA was not available for the EO response characterization of this device. In fact, instrumentation to measure the high-speed EO response of modulators in the shorter wavelengths is limited. For example, OSAs with high resolution on the order of 20 MHz are not available in the visible or O-band regime unlike in the C-band. Due to the limited resolution of the OSA at hand (0.01 nm, Ando AQ6317B), the generated sideband peaks could not be discerned from the main carrier signal peak at frequencies less than 10 GHz. However, as the modulation frequency increases, the sidebands are adequately separated from the carrier and thus the peaks can be accurately tracked to evaluate the modulator's performance as seen by the examples of 10, 15, 20, 30, 40, and 50 GHz modulation signals in Figure 7.3(b).

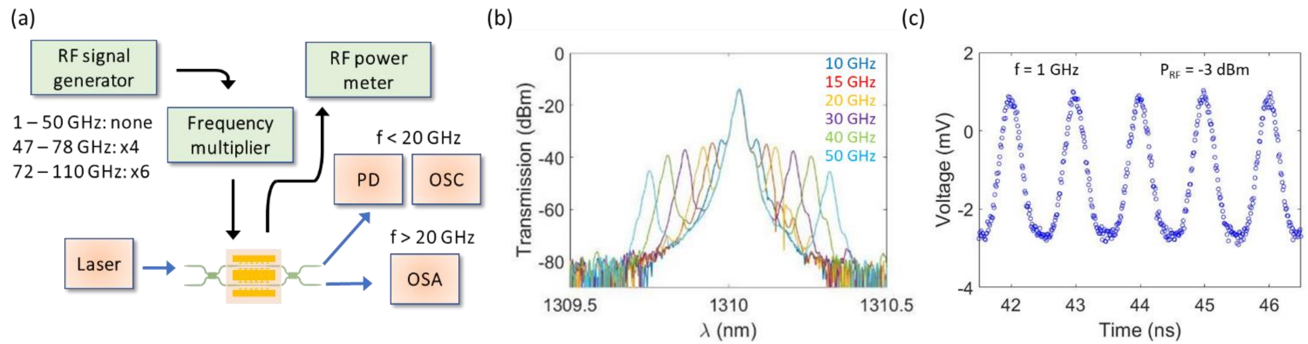

Figure 7.3: A block diagram detailing the different equipment used to measure the EO modulator response from 1 to 110 GHz of a SiN/LN MZM designed for wavelengths in the O-band. For frequencies greater than 10 GHz the OSA method can be used to track the modulated sideband peaks. For frequencies less than 10 GHz a 40 GHz photodetector (PD) and high-speed sampling oscilloscope (OSC, DCA-X) are used to track the modulated signal peak-to-peak voltages. (b) Measured OSA traces at different modulation frequencies of the O-band SiN/LN MZM before factoring out the RF power delivered to the device. Frequencies less than 10 GHz are lost in the carrier signal width. (c) An example of the measured modulated signal at 1 GHz using a photodetector and oscilloscope.

As a result of this limitation, four different frequency ranges were measured to obtain the full modulator response from 1 to 110 GHz as diagramed in Figure 7.3(a). At lower frequencies (< 30 GHz), the peak-to-peak amplitude of the modulated optical signals was detected with a high-speed photodetector (40 GHz bandwidth) and sampling oscilloscope (Keysight DCA-X 86100D) (see Appendix B.2 for more information). An example of this measured modulated signal with the photodetector and oscilloscope is demonstrated in Figure 7.3(c) when the device is driven at 1 GHz. For higher frequencies, the optical spectra were measured using the Ando OSA with 10 pm resolution (see Appendix B.1 for more information). Active RF multipliers driven by the RF sweeper were used to generate frequencies between 50 - 75 GHz and 75-110 GHz. The amount of RF power delivered to the device was calibrated for each band of the measurements (see Appendix B.3 for more information).

Figure 7.4 shows the measured EO response referenced to 1 GHz where the different colors correspond to the four measurements described above. Inductively loaded slow-wave electrodes were designed to achieve index matching between the RF and hybrid optical waves as

well as impedance matching to a 50 Ω load. This is evident by the flat response at frequencies less than 20 GHz. The 3-dB bandwidth of the O-band SiN-LN MZM is about 80 GHz; however, the EO response does not roll off significantly below the 3-dB line even at 100 GHz and is about -4.2 dB at 110 GHz.

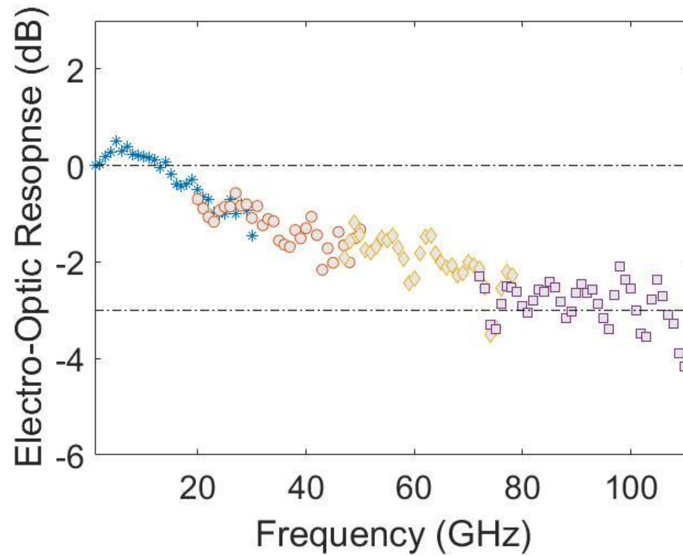

Figure 7.4: Measured EO response of the 0.93 cm long SiN-LN MZM referenced to the 1 GHz value using a high-speed sampling oscilloscope (blue stars), an OSA (red circles), and active multipliers (yellow diamonds and purple squares).

In summary, these results show that a SiN/LN hybrid MZM can have similar high-speed (3-dB bandwidth > 80 GHz), high ER (25 dB), and low-voltage ($V_\pi = 2.9$ V) performance compared to a Si/LN MZM in the O-band (Chapter 5) as well as etched TFLN modulators [97] and deposited SiN/LN modulators [115]. Unfortunately, due to the single-layer SiN transitions used at the bonded TFLN edges, the insertion losses were quite high (15 - 20 dB). In theory, the SiN/LN platform could offer an alternative to the Si/LN structures demonstrated in Chapter 6 for high optical power handling as SiN has a much smaller TPA coefficient than Si. However, with such insertion losses we could not perform a high-power study with the EDFA available in our

lab. In the future, alternative transition sections could be employed, such as multi-layer vertical couplers, to reduce these transition losses.

7.2 Acknowledgments

Chapter 7, in part, is a reprint of the material that appears in the Journal of the Optical Society of America B: Viphretuo Mere, Forrest Valdez, and Shayan Mookherjea, “Improved fabrication of scalable hybrid silicon nitride – thin-film lithium niobate electro-optic modulators”, JOSAB 40, no. 5 (2023). The dissertation author, together with his advisor and colleague co-authored the paper.

Chapter 8

Hybrid Bonded SiN/LN EOMs with CMOS Buried Electrodes

8.1 Introduction

All the devices demonstrated in this dissertation to this point were driven using Au electrodes which were fabricated above the bonded TFLN layer and developed outside of the CMOS facility. While these structures work to show independent modulator performance, it can be more difficult to integrate such a device with other active components (lasers, detectors, isolators) that also require electrical contacts and drivers. A more general CMOS processed circuit can contain multiple layers of materials including metal, Si(N) waveguides, dopants, and multiple layers of planarized oxides. Alternatively, one may instead define the electrodes using the same buried metal layer that is part of the CMOS-compatible fabrication of the Si or SiN layer stack in a foundry Si photonics process, and is used for the electrodes in Si carrier-depletion modulators [11,13,71,126]. Earlier hybrid bonded MZM devices of this type demonstrated a 3-dB electro-optic bandwidth of about 30 GHz and half-wave voltage (V_π) of 13.6 V [20]. Here, we demonstrate an integrated hybrid bonded SiN/LN modulator for the O-band (1310 nm) which uses these buried electrodes (BEs) and shows a greatly improved EO 3-dB bandwidth greater than 110 GHz, and a half-wave voltage of 5.6 V ($V_\pi L$ = 2.8 V.cm) with a high optical extinction ratio exceeding 28 dB. Also, this device is compared to a similar hybrid

MZM with gold electrodes fabricated on top of the TFLN layer, which shows similar performance.

8.2 BE vs TE SiN/LN: Comparison of RF Design

Figure 4.4 shows the cross-sectional schematic of the buried-electrode (BE) and top-electrode (TE) MZM designs which were fabricated on the same chip. The stack includes 5 mol-% MgO-codoped TFLN of 200 nm thickness as the EO layer. The BE design uses the "M1" composite-metal layer which is made of Ti/TiN/Al (primarily Al of thickness 870 nm) with a conductivity of 2.6e7 S/m, and the TE design uses Au of thickness 750 nm and a conductivity of 4.1e7 S/m. The optical mode is confined to a small region in the vicinity of the SiN rib waveguide and is the same for both designs (900 nm wide by 180 nm thick). The RF materials properties and the position of the electrodes in the stack are both different and impact the optimal electrode device design in each case.

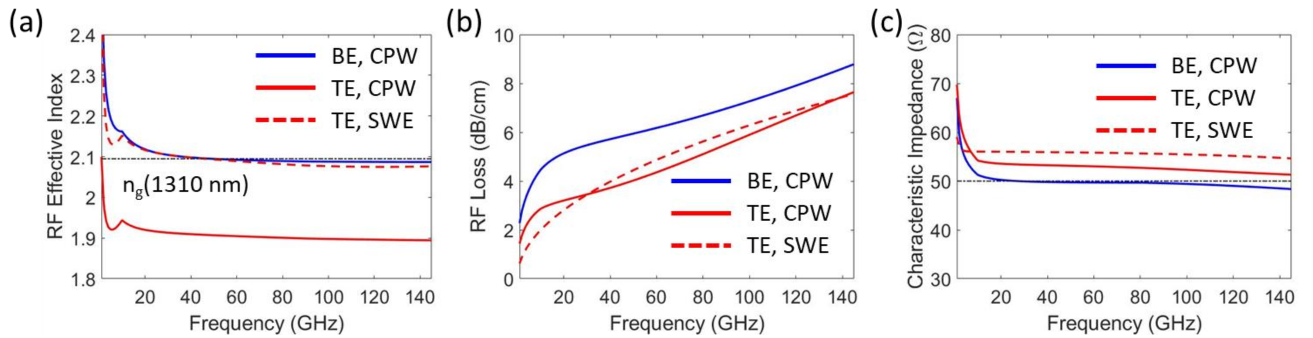

Figure 8.1: The simulated (a) RF effective index, n_{RF}, (b) RF loss, and (c) characteristic impedance of a SiN-LN MZM with buried electrodes (BE) CPW structure (solid) and top Au electrodes (TE) using standard CPW structures (dotted line) and a SWE structure (dashed line). The dash-dot black line in (a) corresponds to the simulated optical group index, n_g, at 1310 nm.

Figure 8.1(a) shows the simulated n_m, as a function of frequency using the buried metal layer (solid blue trace) and the top Au layer (dotted red trace). The electrode gaps, G, are 6 µm

and 5.5 µm wide for the BE and TE structure, respectively and the signal width, w_s, is 16 µm. The buried metal layer is 3 µm away from the HR-Si substrate, whereas the Au layer is 4.1 µm from the substrate. Because the Au layer is farther from the high index substrate, the well-confined CPW mode in the TE design sees more of the oxide, resulting in an n_m of 1.89 at 110 GHz. The optical group index, n_g, is simulated to be 2.095 at 1310 nm, and is shown by the black dash-dot line in Figure 8.1(a). This results in near-perfect index matching for the BE device, but a 10% mismatch for the TE design when using a standard CPW structure with electrode gap of 6 µm and a signal electrode width of 16 µm [see Figure 8.1(a)]. Since the baseline TE design results in $n_m < n_g$, a SWE design can be implemented to achieve the required index match, similarly described in Section 3.2. The dotted red curve in Figure 8.1(a) is the simulated n_m using an inductively loaded SWE design using the top Au layer, resulting in a less than 1% index mismatch to the O-band hybrid mode, similar to the BE device. Figure 8.2(a) and Figure **8.2**(b) depict the BE standard CPW structure and TE inductively loaded SWE structure, respectively. The design parameters of the SWE used to achieve index matching are h = 2 µm, L = 20 µm, and w = 5 µm. With similar electrode thicknesses, the higher conductive CPW (gold) is expected to have less RF propagation loss compared to the M1 CPW as shown by the red traces in Figure 8.1(b).

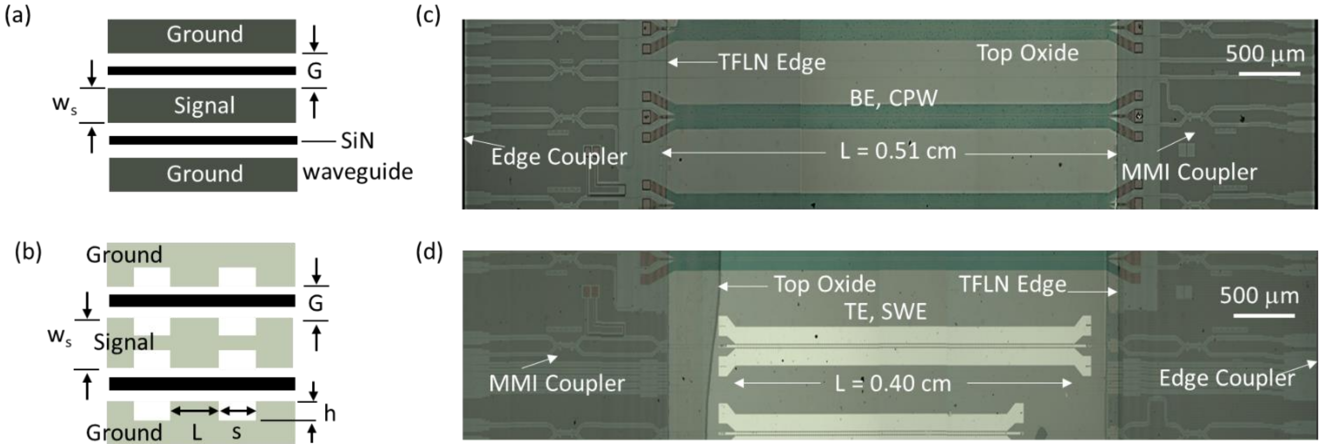

Figure 8.2: A top-view schematic of the (a) BE CPW MZM and (b) TE SWE MZM. (c) A stitched optical microscope image showing the 0.5 cm long SiN-LN MZM with buried M1 electrodes. (d) A stitched optical microscope image showing the 0.4 cm long SiN-LN MZM with top Au electrodes.

Figure 8.2(c) and Figure 8.2(d) show the fabricated BE and TE devices, respectively. The SiN layer was deposited using a PECVD process as part of the silicon photonics fabrication at Sandia National Labs. The hydrophilic bonding and electrode formation steps were performed as described in Section 4.2. The LNOI substrate was removed after bonding to access the LN film and deposit the Au layer. The active electrode length of the TE device (0.4 cm) is shorter than the BE device (0.51 cm). This is because the Au layer must remain within the bonded region on top of the TFLN section, while the buried metal must extend beyond the perimeter of the TFLN section so that RF probes can be physically landed in contact with the G-S-G pads after a pad-opening etch to access the buried metal layer.

8.3 BE vs TE SiN/LN: Comparison of EO Operation

A tunable O-band laser (+10 dBm optical power at the source) was edge-coupled to the chip using lensed tapered fibers. The end-to-end optical insertion loss was measured to be about 16 dB for both designs. Cutback waveguides of the feeder section (1200 nm wide by 180 nm

thick) were measured, resulting in an optical propagation loss of 0.34 dB/cm [see Figure 4.8(c)]. From these measurements, the losses from edge coupling for these devices were determined to be 2.7 dB/facet. From Lumerical Mode simulations the optical loss of the phase-shifter section is expected to be 0.2 dB/cm and 0.005 dB/cm for the TE and BE structures, respectively. Thus, most of the loss is estimated to be from the optical mode traversing the edge of the bonded TFLN section. Compared to the hybrid Si-LN devices in Chapter 4, where the feeder waveguide in the underlying high-index Si layer confines most of the light away from the index discontinuity at the unbonded-to-bonded edge interface, the low refractive index of SiN incurs high transition losses. The SiN layer must be close to the surface for the hybrid mode design in the phase-shift EO segment. Other reports have shown lower transition loss using a bilayer vertical SiN coupler [20] but a bilayer SiN process was not available here. This additional loss does not affect the measurements of the EO section as it originates before and after the hybrid mode and phase-shifter.

A similar method as demonstrated in Figure 6.5(b) was used here to determine the low-speed (100 kHz) V_π of the modulators. Figure 8.3(a) shows the measured modulated light from the BE device as a function of applied voltage when the measured and applied signals are folded over each other. A cosine-squared function (red line) was fit to the data (black dots), resulting in a V_π of 5.6 V and voltage-driven ER of 28 dB. Figure 8.3(b) shows a measurement similar to Figure 8.3(a) but for the TE device, resulting with V_π equal to 6.4 V. In addition, the inset to Figure 8.3(b) shows the measured $V_\pi L$ as a function of applied signal frequency resulting in an average $V_\pi L$ equal to 2.5 V.cm and negligible change in $V_\pi L$ over four decades of frequency range from 100 Hz to 1 MHz. The lengths of the BE and TE devices are 0.51 cm and 0.4 cm, which result in a $V_\pi L$ product of 2.8 V.cm and 2.5 V.cm, respectively. For a fairer comparison,

the measured $V_\pi L$ should be normalized by the electrode gap because they are slightly different (6 μm vs 5.5 μm). The $V_\pi L/G$ for the BE and TE MZMs is 0.48 V.cm/μm and 0.46 V.cm/μm, respectively. These results correspond extremely well with the simulations presented in Figure 2.11(d) and Figure 2.23(b). The vertical separation (h_{buff} = 220 nm) between the buried metal and the TFLN film slightly reduces the RF-optical mode overlap, which leads to a slightly less (2.6% less $V_\pi L/G$) efficient MZM device in the BE case when fabricated using the same cross-sectional stack.

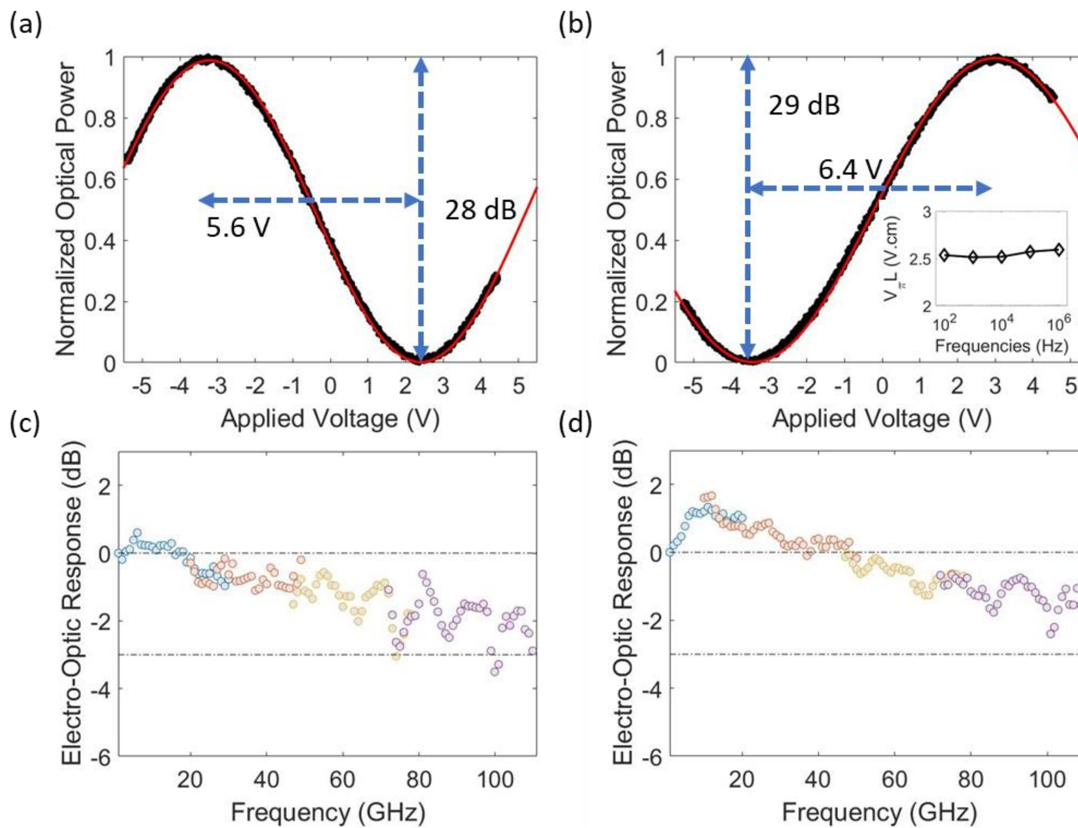

Figure 8.3: The normalized measured optical power (black) as a function of applied voltage when driven with a 100 kHz trapezoidal waveform for the (a) BE and (b) TE SiN/LN devices. The electro-optic response (referenced to 1 GHz) of the (c) BE and (d) TE SiN/LN devices.

The high-speed EO modulator responses of these O-band devices were measured using the frequency banded method described in Figure 7.3(a). For frequencies greater than 20 GHz,

the OSA method in Appendix B.1 was used, whereas, due to the limited resolution (0.01 nm) of the OSA, the time-domain method in Appendix B.2 was used for frequencies less than 30 GHz. Figure 8.3(c) and Figure 8.3(d) are plotted with different symbols for the range of frequencies generated directly by the RF synthesizer or with X4 and X6 active RF mixers. The measurements were normalized to the RF power delivered to the chip, and the photodetector response versus RF frequency as calibrated by the manufacturer (see Appendix B.3). Both devices show a 3-dB EO bandwidth of over 110 GHz when referenced to 1 GHz. The initial increase in the EO response for sub-10 GHz frequencies in Figure 8.3(d) is a trait of the characteristic impedance of the SWE transmission line being greater than 50 Ω, which can be seen in Figure 8.1(c). While both these devices are essentially similar in performance, longer MZM devices of both types on the same chip have not yet been fabricated and may reveal further insights into the difference between the TE and BE designs in the future. Accounting for the 0.5 μm variation in electrode gap between the two devices, the BE MZM achieves similar performance to the TE MZM, but with a simpler back-end fabrication process, at the cost of additional front-end processing steps. These results show that high-speed hybrid bonded TFLN modulators can be incorporated with a CMOS-compatible silicon-photonics process for future scalability and integration, and in fact, both TE and BE designs can be conveniently incorporated on the same chip if desired.

8.2 Acknowledgments

Chapter 8, in part, has been submitted for publication of the material as it may appear in Photonic Technology Letters 2023. Forrest Valdez, Viphretuo Mere, Nicholas Boynton, Thomas A. Friedmann, Shawn Arterburn, Christina Dallo, Andrew T. Pomerene, Andrew L. Starbuck, Douglas C. Trotter, Anthony L. Lentine, Ashok Kodigala, and Shayan Mookherjea, “Buried-

electrode Hybrid Bonded Thin-film Lithium Niobate Electro-optic Mach-Zehdner Modulators" PTL 2023 (under review). The dissertation author, together with his advisor and colleague, led the research efforts for this work and co-authored the paper.

Chapter 9

Hybrid Bonded SiN/LN EOMs at Near-Infrared Wavelengths

9.1 Introduction

Historically, electrically driven modulation of laser light at near-infrared (NIR) wavelengths around 0.8 μm was used in compact disc technology [137], spectroscopy [72] and optical communications [138,139]. These wavelengths are less absorbed by water and penetrate more deeply into skin, and are used in sensors, biological and chemical applications [75,76] and phototherapy [140,141]. NIR optical modulators are used to generate pulse sequences in quantum optics [142] and for qubit readout [143]. In communications, externally modulated lasers have not outperformed directly modulated lasers in optical interconnects at NIR wavelengths, whereas the opposite is true in the telecom band [144]. Improved performance, integration, and scalability of NIR EO modulators can thus benefit many applications including communications and information processing, sensing and spectroscopy, biomedical sciences, and laser technology.

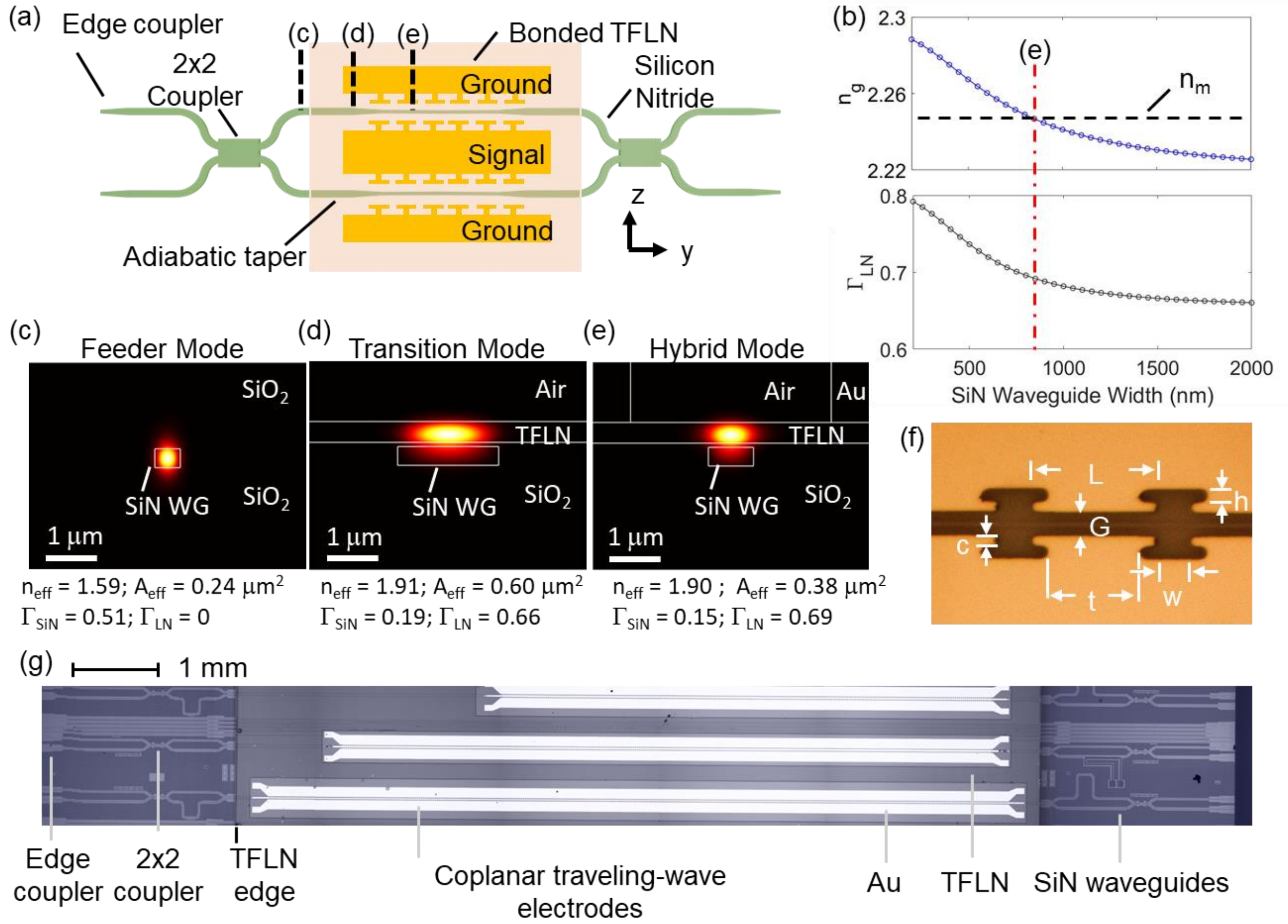

Figure 9.1: (a) A top-view schematic of the hybrid bonded SiN-TFLN modulator (not to scale). (b) The simulated n_g, and Γ_{LN} as a function of the SiN waveguide width. The vertical dot-dashed red line corresponds to the mode shown in panel (e). The horizontal dashed black line corresponds to the simulated RF index at 110 GHz for the RF transmission line. The cross-sectional Poynting vector magnitude is shown of the (c) feeder SiN waveguide (no TFLN), (d) transition SiN waveguide, and (e) the phase-shifter section hybrid waveguide when λ = 784 nm. (f) A section of the RF transmission line with dimensions discussed in the text. (g) An optical microscope image of hybrid chip with a few different MZM structures.

Figure 9.1(a) shows a top-down schematic of the hybrid MZM device. The optical index and mode fraction contained in TFLN can be varied by changing the SiN width (more details in Section 2.4), as shown in Figure 9.1(b). In contrast to hybrid Si waveguides, the lower refractive index of SiN requires a different transition design. The input and output sections are defined in thin SiN waveguides whose height is 0.18 µm and width is 0.5 µm with an oxide cladding, and

whose TE-polarized fundamental optical mode profile is shown in Figure 9.1(c). The feeder waveguide makes a two-stage transition, with a first mode-expansion stage implemented before the edge of the bonded TFLN region to the mode profile shown in Figure 9.1(d), where the SiN width is increased to 2.0 μm. The second part of the transition is past the bonded edge, where the waveguide is adiabatically narrowed down over a length of 100 μm to a width of 0.9 μm, which results in pushing most of the light into the TFLN region. This mode, shown as Figure 9.1(e), is used in the EO phase shift section with the x-cut TFLN. The RF traveling-wave electrodes were designed as slow-wave structures as described in Chapter 3.2. A section of the electrode structure is shown in Figure 9.1(f) and the indicated dimensional parameters can be varied to achieve RF-optical index matching. The EOM devices reported here used G = 4 μm, h = 2 μm, L = 20 μm, and t = 15 μm. The dashed lines in the top sub-panel of Figure 9.1(b) shows the simulated RF index (n_m = 2.24) which matches the optical group index of the mode shown in Figure 9.1(e).

Figure 9.1(g) is a stitched microscope image of a portion of one of the microchips, showing a few EOM devices fabricated along the east-west direction. The MZM shown in the center of Figure 9.1(g) is the 0.8 cm long device described here. The SiN feeder waveguides are visible outside the bonded region, and transition seamlessly to the hybrid waveguides under the bonded region. The 2x2 couplers at the input and output sections are designed as MMI couplers using the feeder mode shown in Figure 9.1(g) and are 8 μm wide by 96 μm long to facilitate a 3-dB splitting ratio. While not affecting the design or performance of the EO phase-shift section, the overall insertion loss can be improved by using multiple SiN layers in the transition region [20]. Also, the waveguide-fiber edge couplers were defined here as inverse tapers in a single SiN layer and were not optimized for stand-alone performance.

9.2 NIR SiN/LN EO Measurement Results

To measure the EO performance, a distributed feedback laser (784 nm wavelength; ThorLabs, Inc.) was coupled to the chip with lensed tapered fibers. The on-chip optical power was about 0 dBm (1 mW). High-speed ground-signal-ground RF probes rated to 110 GHz (Picoprobe Model 110, GGB Industries) sourced and terminated the traveling-wave electrodes and were used with standard low-loss 1.0 mm RF cables and connectors.

A similar measurement scheme shown in Figure 6.5(b) was used to measure V_{π} of these NIR MZMs, but with a visible photodetector (FPD610-FC-VIS, MenloSystems). A 4 Vpp trapezoidal signal was used to overdrive the devices. This waveform is post-processed to map the modulated signal to the applied voltage and fit to a cosine-squared function. Figure 9.2(a) and Figure 9.2(b) show these mappings resulting in a V_{π} of 2.0 V and 1.0 V for the 0.4 cm and 0.8 cm long MZMs, respectively ($V_{\pi}L$ = 0.8 V.cm). Compared to devices at telecom wavelengths, the NIR hybrid MZM achieves a smaller $V_{\pi}L$ = 0.8 V.cm because of three factors: the direct role of λ in the numerator of Eq. (2.7), the higher refractive index n_e at shorter wavelengths, and a reduced G (4 μm in this case) which is permitted by the tighter mode confinement without incurring higher optical propagation loss from interacting with the metal electrodes [see Figure 2.26(c)]. This measured $V_{\pi}L$ compares well with the simulated $V_{\pi}L$ of 0.75 V.cm in Figure 2.25(c), which gives a good indication that the MZMs designed for 633 nm wavelengths can be even more efficient (Figure 2.25(d) predicting $V_{\pi}L$ of 0.45 V.cm). In Section 6.2, the $V_{\pi}L$ of a hybrid Si/LN MZM designed around 1550 nm was 3.1 V.cm; the reduced $V_{\pi}L$ of 0.8 V.cm of this device implies a power reduction of about 12 dB may be achieved by electrical driver circuits at NIR wavelengths. A portion of the trace shown in Figure 9.2(b) is converted to the

logarithmic scale for the vertical axis in Figure 9.2(c), from which an ER of about 31 dB was measured. This high degree of interferometric cancellation confirms that the couplers are well balanced and the mode transitions to the hybrid mode preserve the TE polarization state.

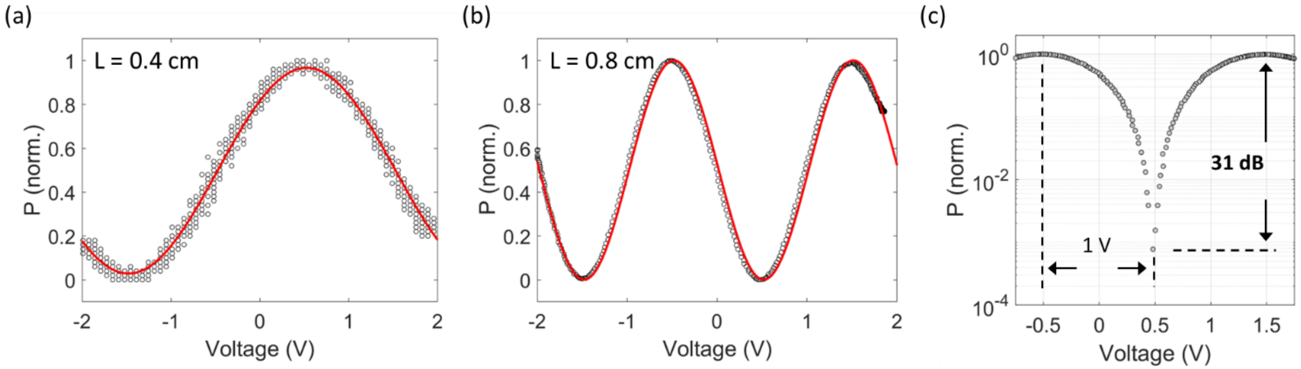

Figure 9.2: (a,b) The normalized optical power measured as a function of applied voltage for the hybrid MZM with length 0.4 cm [panel (a)] and 0.8 cm [panel (b)]. The solid lines are fits to the data using the squared-cosine functional form, which yields V_{π}. (c) A magnified portion of the data in panel (b) with a logarithmic vertical scale to quantify the ER.

Similar to the O-band SiN-LN MZMs reported in Chapter 7 and Chapter 8, a combination of measurements was used to characterize the high frequency EO response from 1 to 110 GHz as shown in Figure 9.3(a). In this case, the time-domain method is used for frequencies less than 30 GHz to ensure enough points overlap between the two methods in the NIR regime. At short wavelengths, combinations of techniques have been used since the earliest reports of modulators [145]. From 20 GHz to 110 GHz, the OSA method described in Appendix B.1 was used to measure the spectra of the modulated signals, where X4 and X6 active RF multipliers were used to achieve frequencies greater than 50 GHz. For frequencies less than 30 GHz, the modulated signals were measured with a high-speed 35 GHz visible photodetector (Model 1471, Newport Corporation) and a high-speed sampling oscilloscope (DCA-X, Keysight Technologies). A fiber-pigtailed semiconductor optical amplifier (BOA785S, ThorLabs, Inc.) was used after the chip to amplify the optical waveform. The peak-to-peak voltage of the

detected signal was recorded for each modulation frequency in steps of 1 GHz. For each of the four measurement bands the amount of RF power delivered to the devices was calibrated out [see Appendix B.3]. Measurements made in the overlapping RF frequency ranges show smooth continuity to within a small fraction of a dB with no artificial manipulation or stitching.

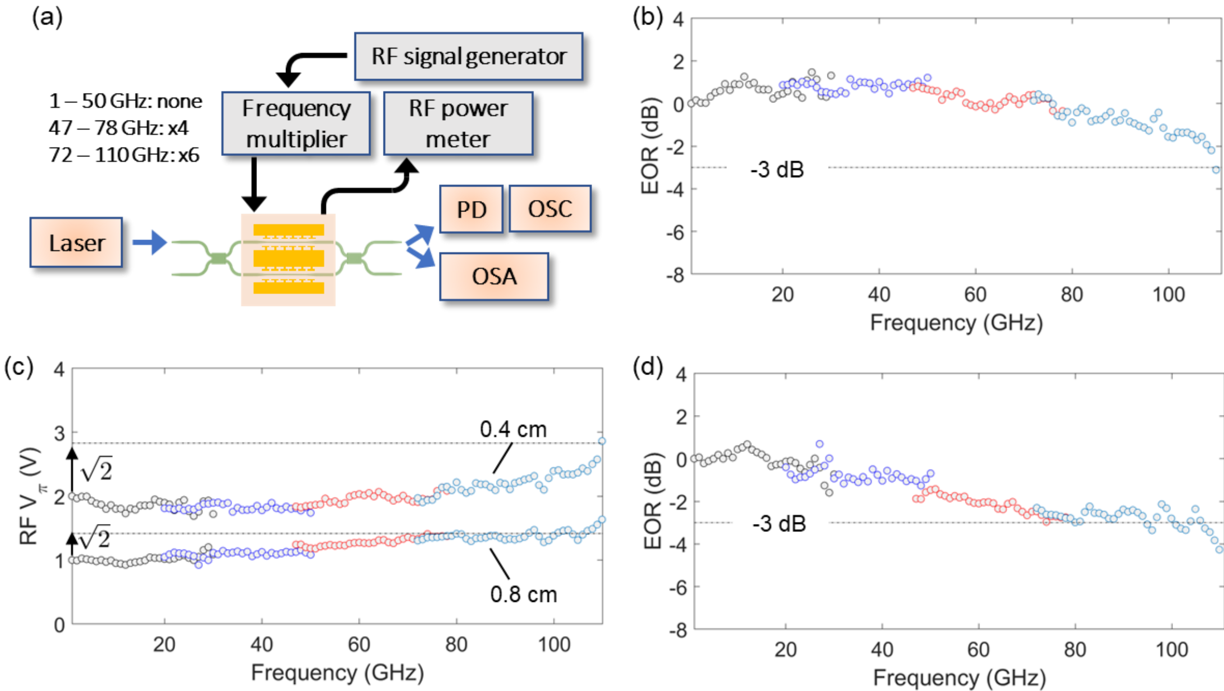

Figure 9.3: (a) Schematic for measurement of the EO response. (b,d) EO response measurements over 1 to 110 GHz of a hybrid TFLN-SiN MZM with phase-shift length 0.4 cm and 0.8 cm, respectively. The four colors for the data points represent the four RF measurement bands as described in the text. Each trace is normalized to the corresponding EO response at 1 GHz. (c) $V_\pi(f)$ normalized to 100 kHz for the two MZMs. The dashed lines show $\sqrt{2}\ V_\pi(DC)$ in each case.

The EOR for two MZMs, with phase-shifter lengths 0.4 cm and 0.8 cm, are shown in Figure 9.3(b) and Figure 9.3(d), respectively. The four colors in each curve represent the EOR measurements from the four overlapping RF frequency bands: 1 GHz to 30 GHz in black color, 20 to 50 GHz in blue, 47 GHz to 78 GHz in red, and 72 GHz to 110 GHz in cyan. Generally, a small amount of noise was present at the last two or three points of each range where use the components slightly past their stated range. We have not removed or averaged out these artifacts

for clarity, but they can usually be dropped in favor of the data points from the next band. The significance of the 3-dB frequency f_0 is that the EO response rolls off as $\left[1+\left(\frac{f}{f_0}\right)^2\right]^{-1}$ as f increases above f_0. The EOR response does not roll off below 3 dB (shown as a dashed line) except at the far edge of the measured RF range, above 100 GHz, which we therefore take as the 3-dB roll-off frequency.

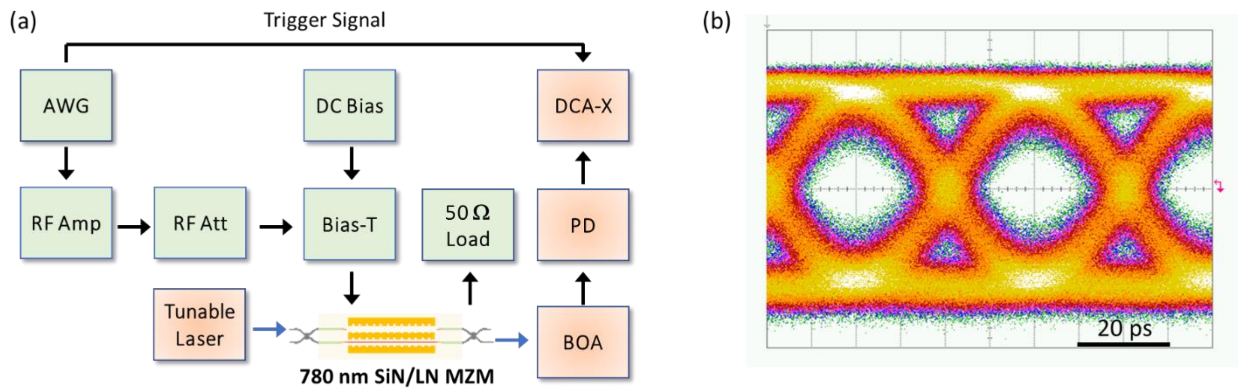

Figure 9.4: (a) A block diagram of the high-speed serial PRBS-15 data measurement using the NIR SiN/LN MZM. (b) The measured eye diagram from a PRBS-15 signal at 25 Gbps with no precompensation or signal processing.

To further test the NIR hybrid bonded SiN/LN MZM, a high-speed serial data measurement was performed as diagramed in Figure 9.4(a). An arbitrary waveform generator (AWG, Tektronix AWG70002) provided a pseudorandom bit sequence (PRBS)-15 signal with 500 mV peak-to-peak voltage at a data rate of 25 Gbps (highest voltage limit and data rate of the current AWG available in our lab). This signal was amplified to ensure that about 1.3 Vpp was applied to the chip by using an RF amplifier (Keysight N4985A) and inline fixed RF attenuators rated to 18 GHz. The modulator was biased with a DC voltage of 1.2 V using a high-speed bias-T. The modulated optical signal was amplified using a 780 nm optical amplifier (ThorLabs, BOA 785S) and detected using a 35 GHz visible photodetector (PD, Newport 1474-A) and a sampling oscilloscope (Keysight DCA-X 86100D) to generate the open eye diagram shown in Figure

9.4(b) with a measured signal-to-noise ratio of 6.2 dB. No pre-emphasis, compensation or signal processing was done on the measurement.

9.3 NIR SiN/LN Discussion

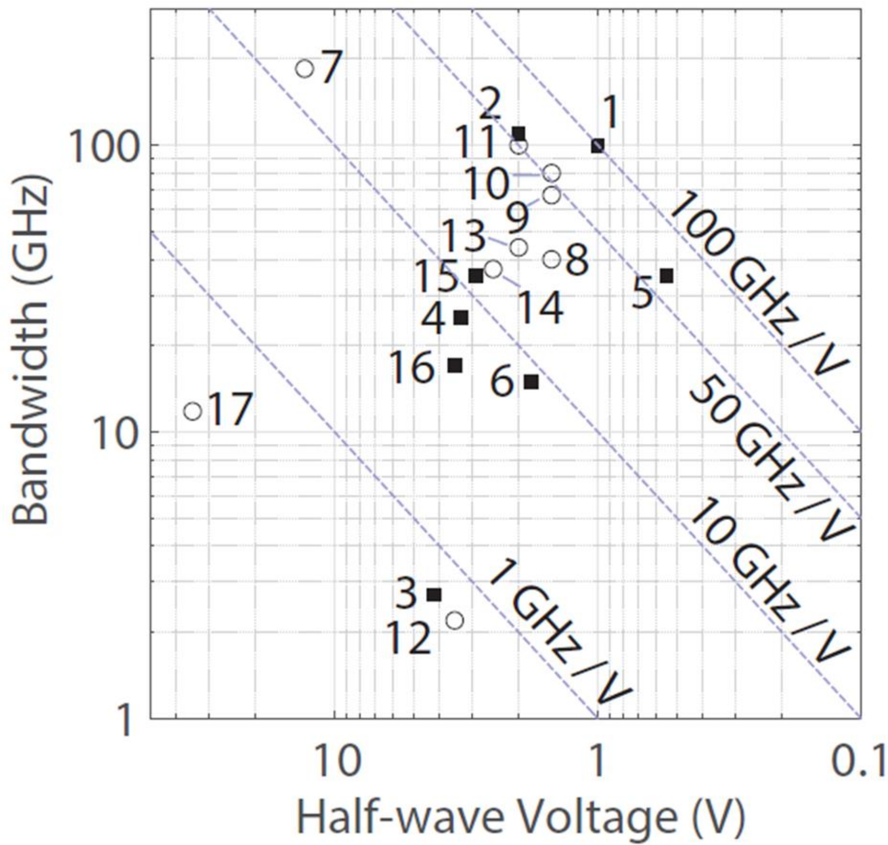

Figure 9.5: Scatter plot of 3-dB EO Bandwidth (GHz) versus half-wave voltage (V) for various MZM devices with slope lines at 1, 10, 50 and 100 GHz/V indicated. The correspondence between the numerical labels for the data points and the citation-list numbers is provided in Table 9.1. Labels 1 and 2 are this work. Black squares represent short-wavelength modulators (wavelengths below 1 um) whereas open circles are at longer wavelengths (typically, 1310 nm or 1550 nm).

The hybrid MZM with L = 0.8 cm is the first modulator, to our knowledge, that achieves 100 GHz EO bandwidth and $V_\pi = 1$ V simultaneously. Figure 9.5 shows a collection of reported MZM performance as a two-dimensional scatter plot with half-wave voltage on the horizontal

axis (right to left) and 3-dB EO bandwidth on the vertical axis. In this representation, points to the upper-right (north-east) section are desirable, and dashed lines with various slope efficiencies are indicated. The data points in Figure 9.5 are labelled with numbers which correspond to the references in Table 9.1. This device uses the Pockels field effect in a push-pull MZM configuration [146] which can offer very high bandwidths and high on-off extinction ratio and is complementary to other field-effect modulators [147–150]. Although MZM devices are longer, the length is less than a centimeter, which is much shorter than traditional LN modulators. While a lower value of the $V_{\pi}L$ product can be achieved in TFLN modulators with plasmonic effects [151], it is important to achieve a low V_{π} which dictates the driver requirements and energy dissipation cost, and thus, voltage is used as the horizontal axis of Figure 9.5.

Resonant EO modulators, which use different design principles and operate in a different portion of the performance space, are not shown in Figure 9.5. Among these, two notable EOMs are the graphene and plasmonic ring resonators [152,153]. The former uses only a monolayer of EO material and yet has shown an efficiency of about 3 GHz/V (30 GHz / 7.5 V driving voltage). The latter can achieve very high modulation bandwidths (possibly exceeding 1 THz), and at the measurement limit, an efficiency of about 33 GHz/V (110 GHz / 3.3 V). On the other hand, a microresonator based device may exhibit spectral ripple from the cavity free-spectral range, is sensitive to wavelength (or bias) and may have a smaller extinction ratio compared to MZM devices.

The achieved 3-dB bandwidth to half-wave voltage ratio of 100 GHz/V from this SiN/LN MZM establishes a new benchmark in EO modulator performance. NIR photonics applications including communications and signal processing may now benefit from having as much EO bandwidth as the best telecom band MZM's, but with an order-of-magnitude lower electrical

power requirement. Scalability of NIR integrated photonics will be facilitated by the simple fabrication method of these hybrid MZM devices with today's silicon photonics platforms.

Table 9.1: References for data points in Figure 9.5.

Figure Label	Ref. #
1	This Work
2	This Work
3	[154]
4	[155]
5	[156]
6	[157]
7	[158]
8	[159]
9	[160]
10	[161]
11	[162]
12	[163]
13	[164]
14	[165]
15	[166]
16	[145]
17	[167]
18	[145]
19	[168]
20	[169]

9.4 Acknowledgments

Chapter 9, in part, is a reprint of the material that appears in arxiv 2022 and has been submitted for publication of the material as it may appear in Optica. Forrest Valdez, Viphretuo Mere, and Shayan Mookherjea, “100 GHz, 1 V Near-infrared Electro-optic Mach-Zehnder Modulator” arXiv:2211.13348 2022. The dissertation author, together with his advisor and colleague, led the research efforts for this work and co-authored the paper.

Chapter 10

Summary and Outlook

The findings of this dissertation have demonstrated that high-speed, > 110 GHz class, and low-voltage, CMOS level, EOMs are feasible on a Si photonics wafer process by heterogeneously integrating with TFLN. We have pushed the envelope of modulator performance by showing the world's first modulator that achieves 100 GHz 3-dB bandwidth with 1 V driving voltage (100 GHz/V efficiency). These hybrid modulators take the 'best-of-both-worlds' approach by leveraging the high EO Pockels effect of LN with the robustness, scalability, and lithographic control of Si photonics. Optimizing the hybrid mode design for minimal V_π simultaneously minimized the impact of high intensity nonlinear optical effects in Si/LN such as TPA, FCA and FCD. This resulted in a Si/LN MZM that can modulate at greater than 110 GHz speeds while handling greater than 110 mW of optical power, which can greatly benefit the gain and NF of an RF-photonic link.

Using the LN film in specified regions dedicated for EO phase-shifting allows for additional integration with other photonic components. This was demonstrated using our Si/LN MZM platform integrated with high Q-factor Si microresonators (Q-factor of 1.14×10^5) to enable photon pair generation and the control of the two-photon JSI [51,114]. A SiN/LN MZM was also developed using the CMOS fabricated buried metal layer with comparable high-speed and low-voltage performance to a post-fabricated Au driven SiN/LN MZM. This work lays the foundation for the hybrid bonded Si(N)/LN platform to be co-integrated with other active components, such as a Si/III-V gain sections, Si/Ge photodetectors, and SiN/AlN acousto-optic

isolators as demonstrated by Figure 10.1 for a fully integrated, CMOS-compatible system on a chip.

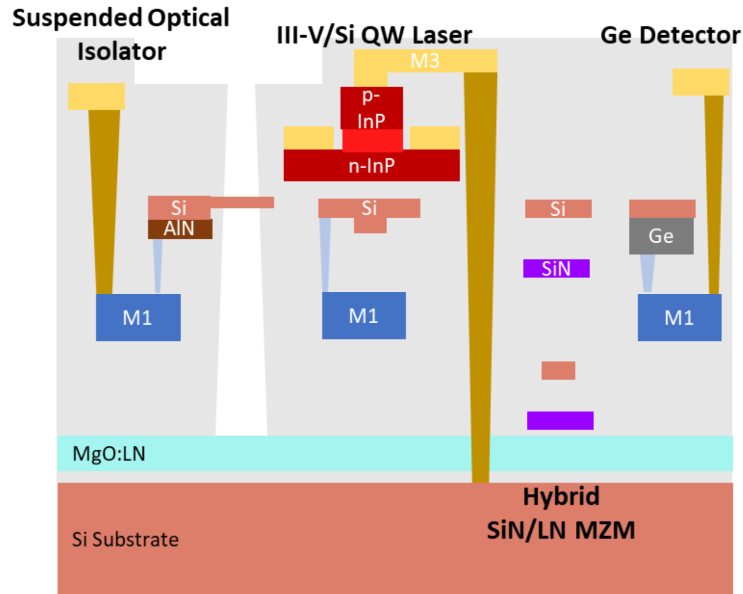

Figure 10.1: A cross-sectional example of an integrated system with a suspended optical isolator, III-V/Si quantum well laser, hybrid SiN/LN MZM, and Ge photodetector.

10.1 DC Bias Drift: Preliminary Study and Observations

EO MZMs have a transfer function that varies sinusoidally with the applied DC bias voltage, V_{dc}, to the device [see Figure 2.5(b)]. In the measurements presented in this dissertation, we did not use a DC bias but instead, tuned the wavelength with a tunable laser, as most of the modulators had an asymmetric path-length difference or were already at the quadrature wavelength by design (symmetric). When a DC voltage is used to bias a modulator at a particular point on the sinusoidal transfer function (e.g, the quadrature, the null, or the peak), there is a phase, ϕ, that is applied to the modulator. This phase can change with time [$\phi(t)$] due to trapped charges, thermal effects (thermo-optic and pyroelectric), or strain-induced charges which lead to a built-in E-field that can screen the applied voltages [170]. Low frequency bias drift has been

shown to affect x-cut LN modulators when there is a buffer oxide layer between the driving electrodes and LN surface [170–173]. There is no such oxide layer in our top electrode devices since the gold (Au) electrodes are patterned directly on the LN surface. While we do not know if surface charge accumulation plays a significant role, we think it is unlikely as there are large Au ground planes in contact with the surface. If there is, then the long-term stability of our hybrid bonded MZMs could be impacted while biasing at a particular V_{dc}.

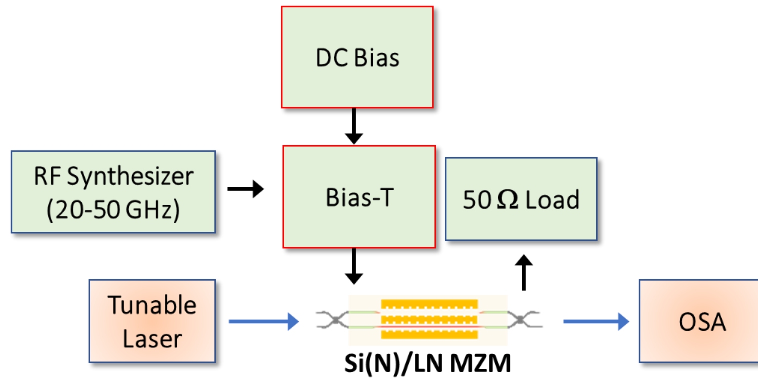

Figure 10.2: A schematic block diagram showing the measurement of the DC bias drift of a hybrid bonded Si(N)/LN MZM using a high-speed bias-t and a programmable DC bias source. The modulated signals are monitored using the OSA method described in Appendix B.1.

To determine if there is long term bias drift that may impact the hybrid bonded MZM performance, a bias-t rated up to 50 GHz is used in conjunction with a DC voltage source (Keysight E3611A) and the RF synthesizer to drive the devices as diagramed in Figure 10.2. The output of the modulators is fed to an OSA to see the carrier signal and generated sidebands. By monitoring the first-order and second-order sidebands over time the modulation index, $m = \frac{\pi}{2}\frac{V_{RF}}{V_\pi}$, and the imparted phase can be evaluated and tracked using Eqs. (B.5) and (B.6) from Appendix B.1.

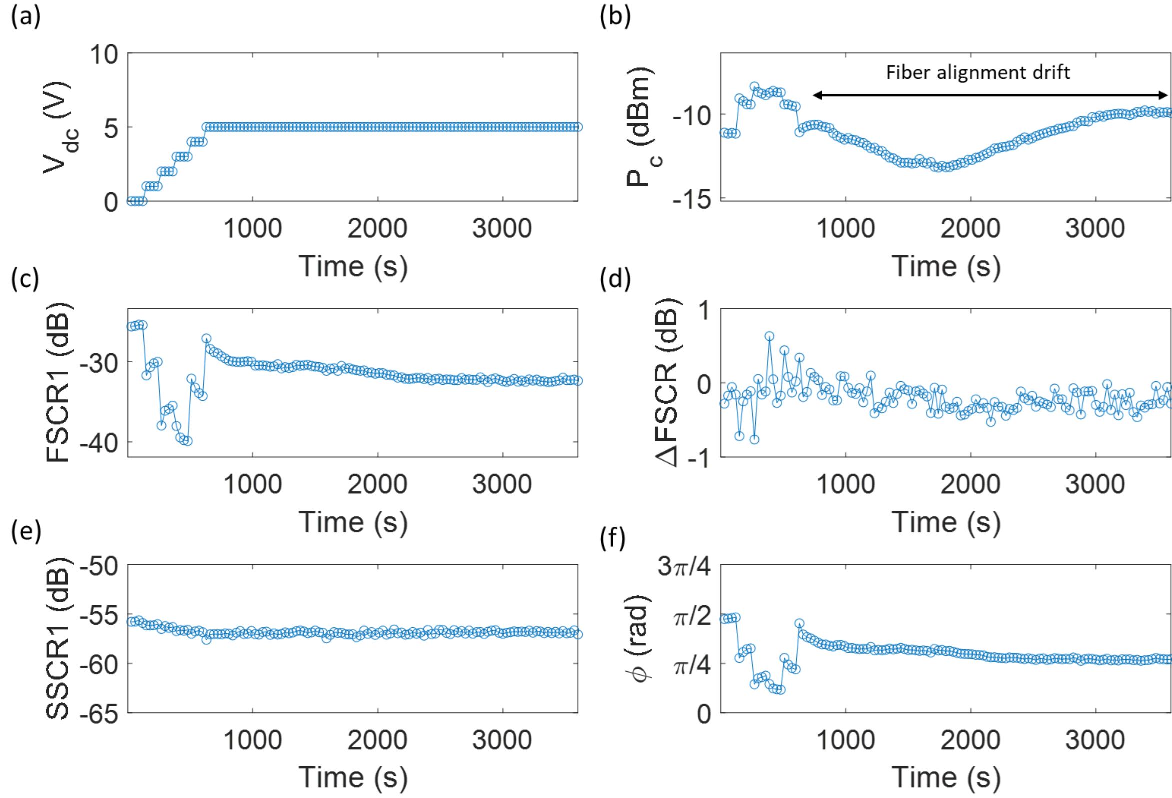

Figure 10.3: (a) The applied DC bias voltage as a function of time. It is stepped from 0 V to 5 V in 1 V increments and held for 2 minutes before each consecutive step. V_{dc} = 5 V is held for the remainder of the measurement. (b) The tracked carrier signal peak as a function of time. From 630 seconds onward, the variation in Pc is from mechanical drift of the fibers coupling light to the chip. (c) The FSCR of the first sideband (shorter wavelength) as a function of time and V_{dc}. (d) The difference between the measured FSCRs (shorter vs longer wavelength) which are measured a few seconds apart showing there is minimal drift during the OSA scans. (e) The measured SSCR as a function of time and V_{dc}, which is constant (as expected from Eq. (B.6)). (f) The calculated phase, ϕ, from the measured FSCR and SSCR as a function of time and V_{dc}.

Figure 10.3 shows an example of a SiN/LN MZM with top Au electrodes modulating a carrier signal at 1310 nm at 30 GHz with varying DC bias over the course of 1 hour. Figure 10.3(a) is the voltage ramp showing that V_{dc} was stepped in 1 V intervals, held for 2 minutes at each DC bias, then stopped at V_{dc} = 5 V for over 45 minutes. As seen by the measured FSCR and extracted phase, ϕ, in Figure 10.3(c) and Figure **10.3**(f) there is an exponential drift upon the change in DC bias over 5 minutes which then stabilizes. There is, however, phase drift on the

order of 0.1-0.2 radians over 15 minutes (see the zoomed region in Figure 10.4) which then settles for the remainder of the measurement.

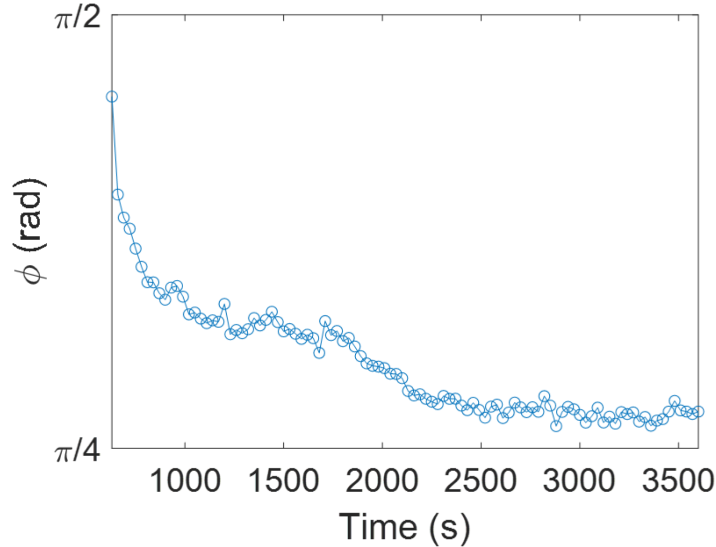

Figure 10.4: The same measured ϕ from Figure 10.3(f) but zoomed into the 'hold' regime (V_{dc} = 5 V for 3000 s). There is an initial overshoot in ϕ in the first 4.5 minutes from changing the bias from 4 to 5 V (seen in every step). Then ϕ is stable at 1.0 ± 0.01 radian for 12 minutes before decaying by 0.2 radians over a span of 12 minutes. It is then stable for the remaining 19.5 minutes.

From this initialization measurement it can be inferred that the drift direction depends on where the initial bias begins. For example, if the device is biased on the rising slope of the MZM transfer function, then FSCR > 0; whereas FSCR < 0 when biased on the falling slope. Furthermore, the mechanical drift of the lensed tapered fibers used to couple light onto the chip can be seen in Figure 10.3(b) by monitoring the carrier signal peak while holding the bias voltage constant. While this fiber alignment drift does change the overall optical power delivered to the OSA, it does not impact the change in FSCR, SSCR, of ϕ because these values are normalized to the carrier signal peak.

Figure 10.4 proves that a form of long-term drift can impact the hybrid bonded SiN/LN MZMs. This drift must be accounted for and controlled if the devices will be used in any long-

term (multiple hours) experiments or used commercially. In a practical setting, the majority of the modulated signal should be routed to the RF-photonic system link detector as opposed to an OSA. For this, an external 90-10 tap can be used to both monitor the phase drift as well as use the modulation for practical applications such as generating eye diagrams. Figure 10.5 describes the logic flow for monitoring and controlling the bias drift of our hybrid bonded Si(N)/LN MZMs using spectral domain measurements. This method is generalized in the sense that the devices V_π and bias voltage to achieve the target phase setting (i.e, quadrature, null, etc) are assumed to be unknown. In this example the target bias is in the linear regime of the transfer function (quadrature, $\phi = \pi/2$). First, a coarse DC voltage sweep is performed to map the MZM transfer function at the user-selected input wavelength (blue data points in Figure 10.6). This gives a general idea of the V_{dc} to set to the target phase. Secondly, the quadrature voltage is determined by finding the V_{dc} that achieves a phase that is closest to $n\pi/2$, where n is an odd integer. Then a fine(r) bias sweep is performed around this initial quadrature V_{dc} to better lock-on to quadrature point in steps of 0.25 V (red data points in Figure 10.6). From here, the DC voltage will remain constant at the quadrature point unless ϕ (when compared to the previous OSA scans) has changed by a user-determined threshold, for example $\pm$ 0.05 radians. If so, then V_{dc} is changed accordingly to adjust the phase back to within the threshold range. This can be applied to peak or null bias points as well by setting the desired phase to 0 or π radians instead of $\pi/2$. An example of this is shown by the voltage ramps in Figure 10.6(a).

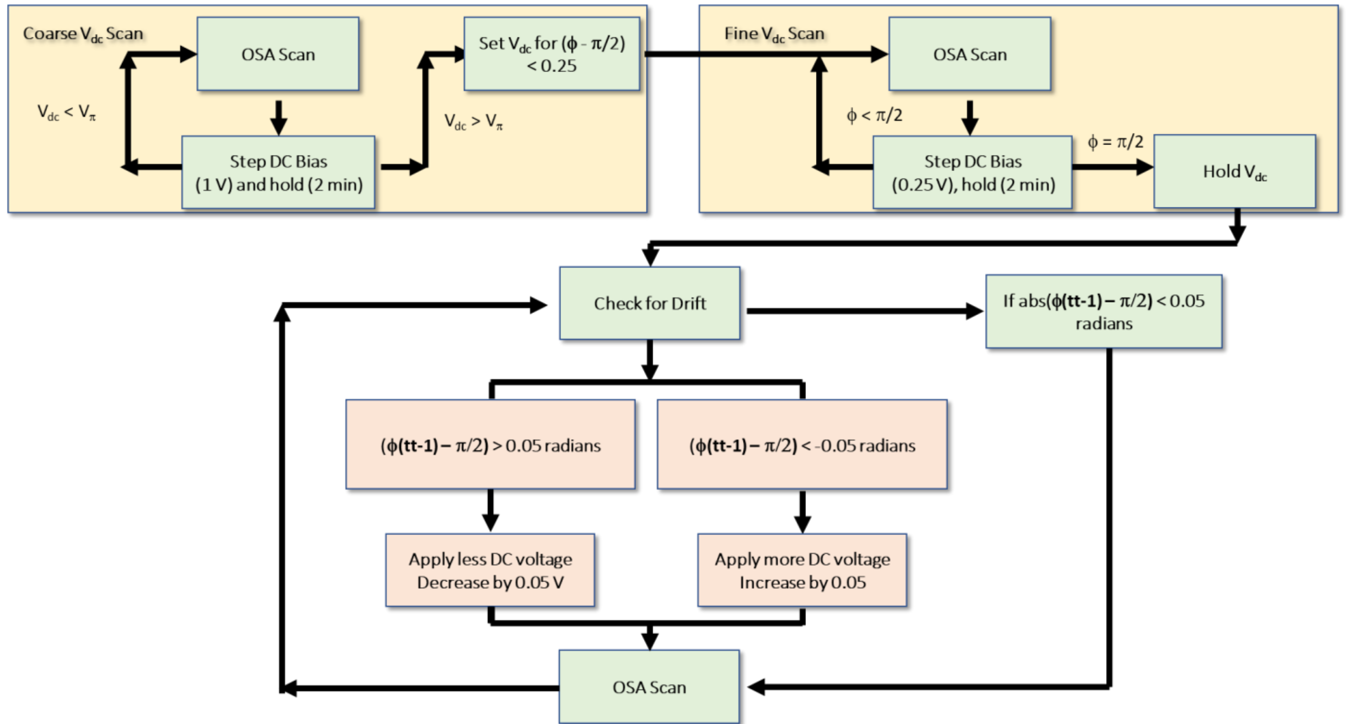

Figure 10.5: The flow-chart diagram of the Si(N)/LN MZM DC bias drift control using an OSA to monitor the modulated sidebands and resulting phase.

Figure 10.6(b) shows the extracted phase as a function of time over the course of 9000 seconds (2.5 hours) when the control scheme described in Figure 10.5 is enabled for a SiN/LN MZM with top Au electrodes. The target bias point is quadrature in this case ($\phi = \pi/2$) and the control method is able to lock on to this bias after the coarse and fine voltage sweeps (blue and red traces). After, the bias is maintained to within ±3% of $\pi/2$ for 2 hours (yellow data points) by slightly adjusting V_{dc} as the phase drifts out of bounds (see the insets in Figure 10.6). The proposed control scheme shows phase stability over the course of two hours with no signs of losing control. In contrast, Figure 10.7(a) and Figure 10.7(b) shown the results when the phase is not controlled over time and the bias voltage is held constant for two hours (yellow data points). The quadrature point is only maintained for about 5 minutes before drift occurs. Note that the oscillations that occur after 8000 s in Figure 10.7(b) are not from DC bias drift, but from the

edge coupling lensed tapered fibers drifting from optimal power coupling to the device. This reduced the power measured at the OSA and at this moment the modulated second sidebands were lost to the noise floor of the OSA, causing the oscillations in the extracted phase.

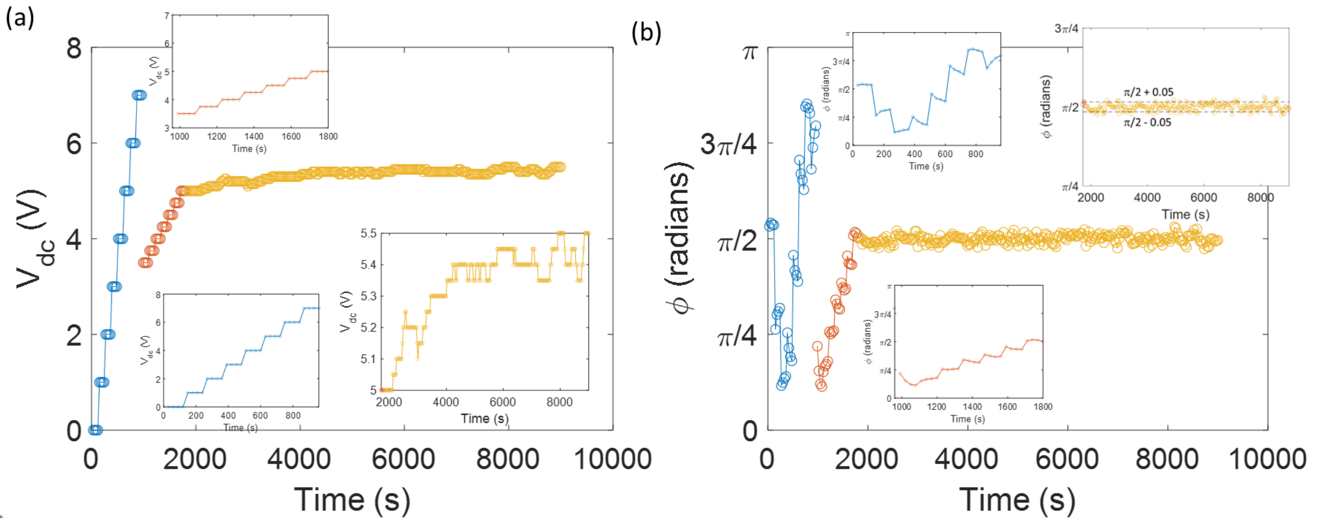

Figure 10.6: (a) The applied DC voltage and (b) extracted phase as a function of time to the symmetric SiN/LN MZM under test. First a coarse voltage sweep is done to map out the MZM transfer function (blue data points). Then a finer sweep (red data points) is performed around the quadrature point (3.5 V to 5 V in this case). Lastly, the phase is locked to the desired target, π/2 and maintained by applying slight 0.1 V adjustments as needed based on succeeding OSA measurements (yellow data points). The insets are zoomed sections of each voltage ramp and resulting phase.

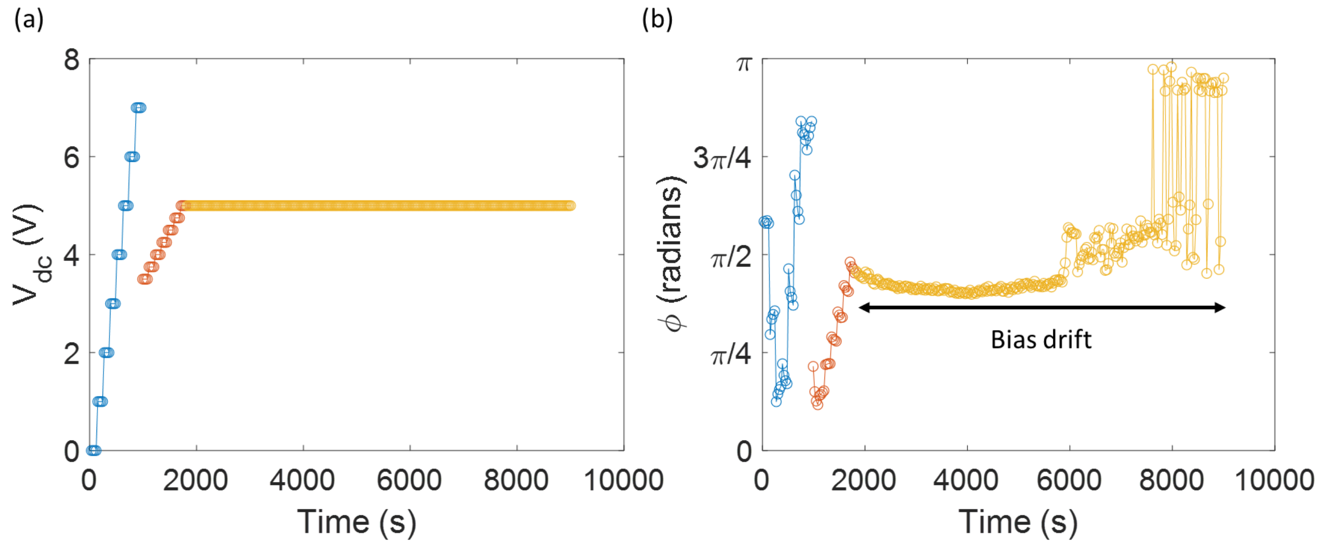

Figure 10.7: (a) The applied DC voltage and (b) extracted phase as a function of time to the symmetric SiN/LN MZM under test. First a coarse voltage sweep is done to map out the MZM transfer function (blue data points). Then a finer sweep (red data points) is performed around the quadrature point (3.5 V to 5 V in this case). The phase is not locked, and a constant voltage of 5 V is applied for 2 hours, quickly leading to bias drift.

While these results are preliminary, they do offer valuable insight into the DC drift effects of TFLN based MZMs. Even though there is long-term drift on the minutes-to-hour time scale, this drift in the target bias phase can be controlled by monitoring the modulated signal spectra. This control is maintained for multiple hours to within 3% of the target phase. With minor adjustments to the control algorithm, our hybrid bonded Si(N)/LN MZMs could be utilized in commercial applications with no worry of malfunction with biasing via wavelength (asymmetric MZMs) or via DC voltage as shown here.

10.2 Integration of Hybrid MZMs with Silicon Photonic Devices

10.2.1 Integrated High Quality Factor Microrings

The separation of the SOI and LN layer and their respective functionalities allows for a wide range of device customization, as the Si layer can host a multitude of passive and active

devices fabricated in a CMOS process at the same time as having a hybrid region dedicated to high bandwidth voltage-driven optical modulation. There may be some changes required in the device design or fabrication process to facilitate this modular approach. For example, the standard Si-photonic optical devices are implemented on a SOI platform with 220 nm Si thickness, while this hybrid bonded platform uses a 150 nm thick Si layer, and therefore the rings, gaps and transitions must be redesigned. As an example, we demonstrate high-Q single microring resonators for narrow band single photon generation [174] and a cascaded three stage second-order coupled microring filters [175–178] in a SOI platform which is outside of the hybrid bonded MZM region [Figure 10.8(a)] but part of the same chip. Figure 10.8(b) shows the transmission spectrum through the cascaded symmetric MZM (without modulation signal), single microring resonator and the three stage second-order coupled microring filters (Port 1 to Port 5 in Figure 10.8(a)). The FSR, insertion loss, and the extinction ratio of the high-order filter are 5.0 nm, less than 1 dB, and greater than 40 dB, respectively. The measured filter FSR agrees precisely with the design target, and the filter extinction ratio is high, and is likely limited in Figure 10.8(b) by the detection noise floor. The inset in Figure 10.8(b) shows the transmission spectrum of the inline microring resonator with a loaded quality-factor (Q-factor) of 1.14 × 105, at 1556.96 nm. This is comparable to a standard high-Q Si microring resonator we have previously fabricated using conventional 230 nm Si thickness and used for photon-pair generation using spontaneous-four-wave-mixing [179].

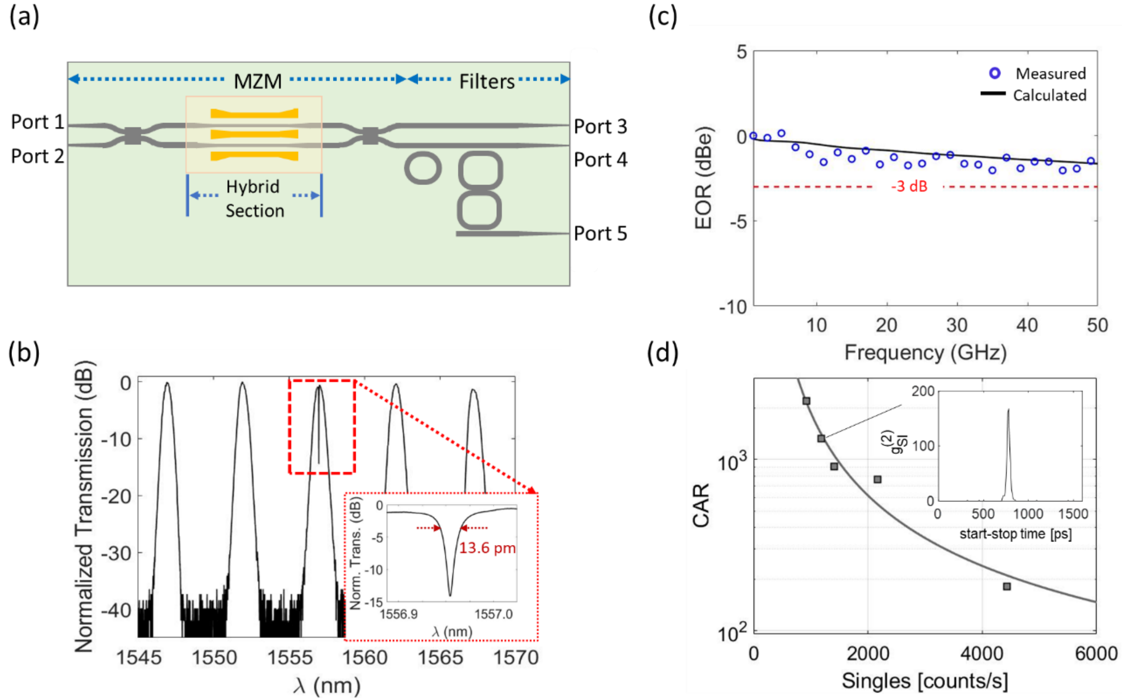

Figure 10.8: (a) Schematic representation of a hybrid bonded thin-film MZM integrated with microring resonator based filters. (b) The measured transmission of a three stage second-order coupled microring filter cascaded with a ring resonator and symmetric hybrid bonded MZI fabricated using 150 nm thick Si waveguides. The inset shows the transmission spectrum of the micro-ring off-resonance from the filters, showing 3 dB bandwidth greater than 50 GHz. (d) The measured CAR values from the high-Q Si resonator with a loaded Q-factor of 1.14×10^5. (c) The measured EOR of the MZM from Port 1 to Port 4 such that the light was microring at varying single photon rates. The inset shows a corresponding histogram of the signal and idler cross-correlation coincidence peak.

To determine the performance of the hybrid bonded symmetric MZM, the input laser wavelength was positioned away from the single microring and higher-order microring filter resonances [Port 1 to Port 4 of Figure 10.8(a)] and a DC bias voltage of 2.8 V was applied to set the quadrature bias point. The EO response was measured using the same method described in Appendix B.2, resulting with a 3-dB bandwidth greater than 50 GHz, as shown in Figure 10.8(c). For testing purposes only, the microring resonator section was diced out to separately measure the coincidence-to-accidentals ratio (CAR) versus the single photon count rate. High CAR values were measured as shown in Figure 10.8(d). The measurement to characterize the single photons

from this portion of the chip was performed with superconducting nanowire single-photon detectors similar to a setup used in [179]. The photon rates and CAR were limited in this case by the coupling losses of the chip segment after dicing (17 dB). These promising early results indicate that our hybrid bonded platform, which brings LN and SOI devices together, can open new avenues for gated photon-pair generation, filtering, switching, wavelength-shifting of photons and quantum pulse gate operations [6].

10.3 A Design for Si/LN EO Modulators Integrated with Lasers

One of the strengths of the demonstrated hybrid bonded Si(N)/LN platform in this dissertation is its compatibility with CMOS fabrication processes and integration of high-speed low-voltage EO modulators in a region only where they are needed via the bonded LN films. As shown in Section 10.2, this gave the possibility of integrating a 110 GHz class Si/LN hybrid MZM with other Si photonic components outside of the bonded region such as high-Q Si microrings for photon pair generation. This is only one such example of Si/LN MZM integration with other photonic devices. Si photonics is a well-established platform that has been used with heterogeneously combination of other materials to provide functionalities that Si cannot normally exhibit such as lasing (III-V integration [99,100,180,181]), telecom range photodetection (Ge integration [98]) and visible range photodetection [182]. Thus, a fully integrated Si/III-V laser with high-speed Si/LN MZM is possible on the same Si photonic chip. Figure 10.9 is an example of a potential fabrication flow to jointly integrate III-V quantum well (QW) structures and TFLN with a single layer of patterned Si features.

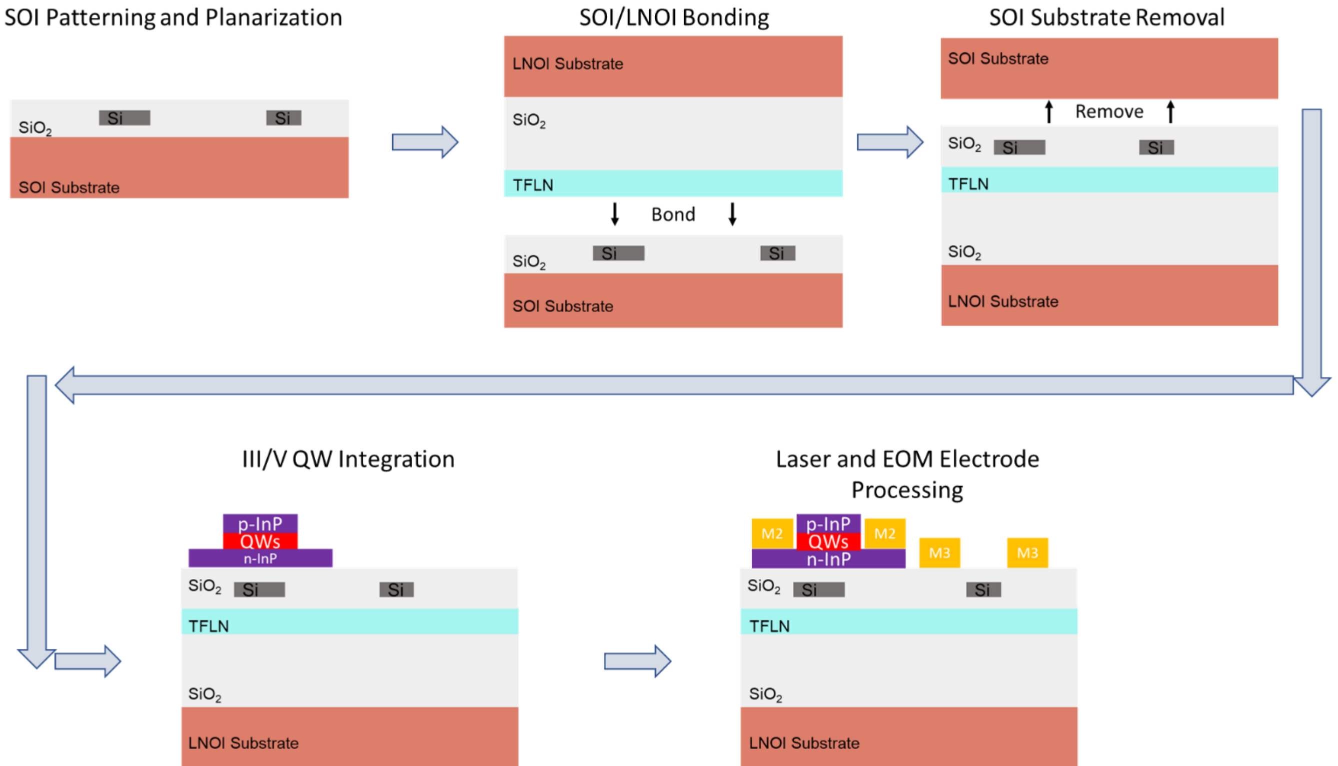

Figure 10.9: A fabrication process flow for integrating hybrid Si/LN EO modulators with hybrid Si/III-V gain sections with the same single layer patterned SOI.

This fabrication flow example would utilize the same layer of Si waveguides that would taper in and out of the III-V gain region as the hybrid mode section of the EO region. This means that the hybrid Si/LN mode design is constrained by the design of the hybrid Si/III-V laser. Typical Si waveguide thicknesses for such lasers are on the order of 250 nm, unlike the 150 nm thick Si layer used for the Si/LN modulators presented in this dissertation. Figure 10.10(a)-(d) are the simulated n_{eff}, n_g, α_{opt}, and Γ_{LN} of the fundamental TE_0 and TM_0 modes for the hybrid Si/LN cross section shown in Figure 10.9 with 400 nm thick TFLN. Because of the 250 nm thick Si layer, there is some mode competition for widths less than 250 nm between the two orthogonal polarizations. To ensure there is no coupling from the wanted TE_0 mode to the unwanted TM_0 mode (does not interact with the applied RF field in this x-cut LN configuration),

the waveguide width should be 250 nm or greater. However, if the waveguide is too wide (greater than 350 nm), then the confinement of the mode in the LN film reduces to below 20%.

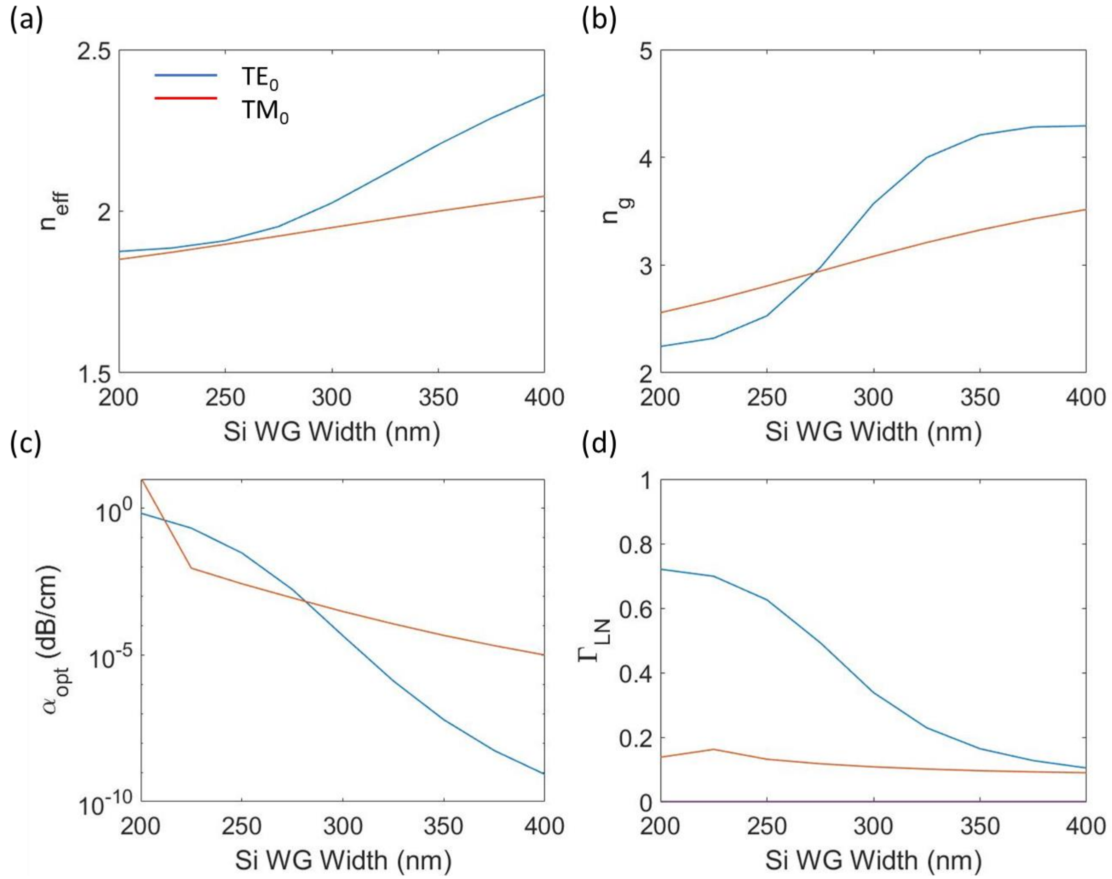

Figure 10.10: The simulated (a) n_{eff}, (b) n_g, (c) α_{opt}, and (d) Γ_{LN} of the fundamental TE_0 and TM_0 Si/LN hybrid modes as a function of Si waveguide width. The waveguide thickness is 250 nm, LN film is 400 nm, G = 4 μm, and λ = 1550 nm for these calculations.

Figure 10.11(a) shows the simulated hybrid Si/LN mode with such a waveguide and a LN film 400 nm thick with 50 nm of SiO_2 above and below the Si waveguide. Au electrodes with a gap of 4 μm are assumed here. If the Si waveguide is set to 250 nm wide and thick, then that would maximize the mode overlap [Γ_{LN} ~ 62%, see Figure 10.11(b)] without interference with the TM_0 mode. Following the fabrication process in Figure 10.9, the TFLN is now 'below' the patterned Si waveguides, whereas in Chapter 4 it was the inverse. This causes the larger area of the hybrid mode to be further from the driving electrodes [labelled 'Au' in Figure 10.11(a)] and

results in less α_{opt} as shown by Figure 10.11(c) for different G, which can be reduced to 4 μm before α_{opt} is on the order of 1 dB/cm. Figure 10.11(d) shows the simulated $V_{\pi}L$ as a function of G for this system resulting with 2.2 V.cm at G = 4 μm. These initial findings show that not only is integration of a hybrid bonded Si/LN MZM with a hybrid Si/III-V laser possible, but it will also result with voltages which are comparable to state-of-the-art TFLN EO modulators at 1550 nm.

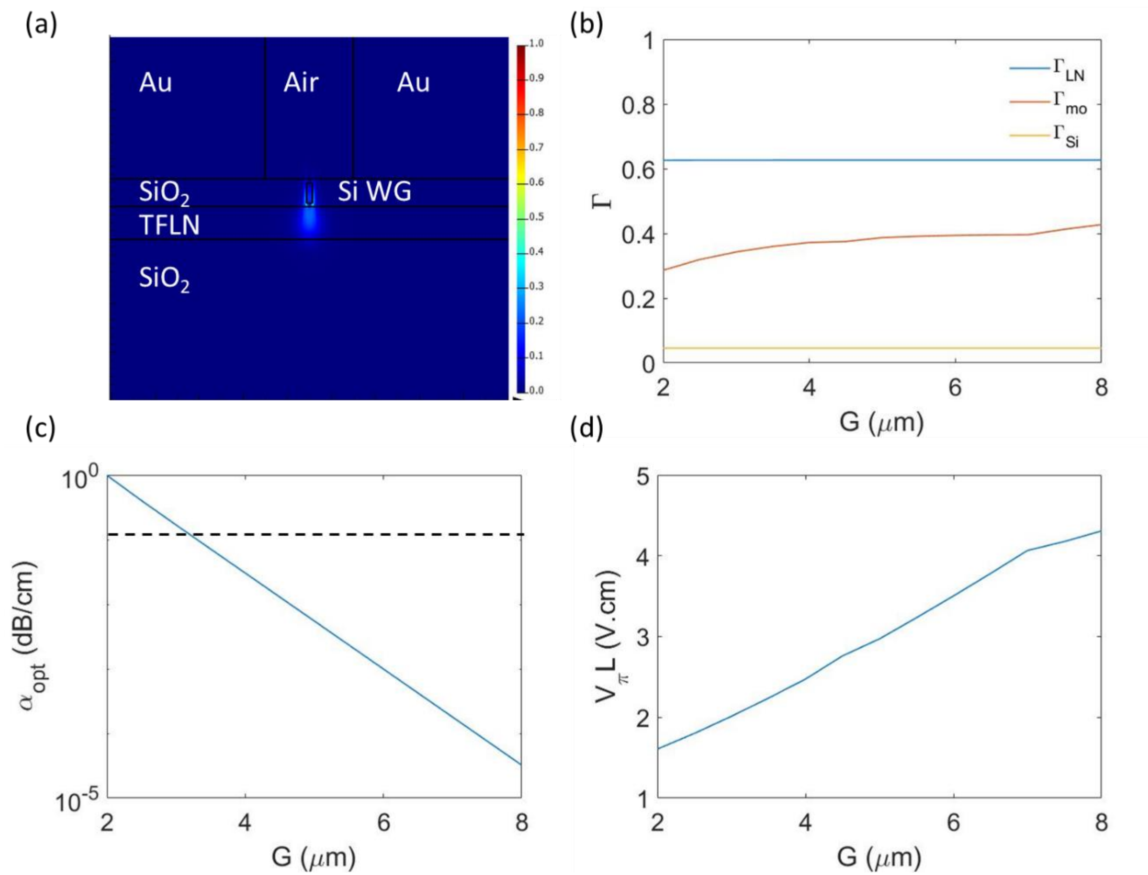

Figure 10.11: (a) The simulated Si/LN hybrid mode cross-sectional |E|2 with a 250 nm wide by 250 nm thick Si waveguide, 400 nm thick LN film, Au electrodes spaced 4 μm apart, operating at λ = 1550 nm. The simulated (b) Γ_{LN}, Γ_{mo} and Γ_{Si}, (c) α_{opt}, and (d) $V_{\pi}L$ as a function of G.

10.4 Acknowledgments

Chapter 10, in part, is a reprint of the material that appears in the following: Viphretuo Mere, Forrest Valdez, Xiaoxi Wang, and Shayan Mookherjea, “A modular fabrication process for thin-film lithium niobate modulators with silicon photonics” Journal of Physics: Photonics 4, no. 2 (2022). The dissertation author, together with his advisor and colleagues, led the research efforts for this work and co-authored the papers.

Appendix A

A.1 Half-wave Voltage-length Derivation

Consider a MZM configuration as shown in Figure 2.1(a) with a x-cut TFLN region for an applied phase shift (via voltage). The Helmholtz wave equation of light propagating through this MZM is:

$$\nabla_t E_o + \left[n^2 k_0^2 - \beta_{eff}^2\right] E_o = 0 \tag{A.1}$$

where E_o is the electric field of the optical wave, $k_0 = 2\pi\lambda_0$, and $\beta_{eff} = 2\pi n_{eff}\lambda_0$ is the propagation constant of the fundamental TE-like mode. This is the unperturbed wave equation, i.e no voltage applied to the phase shifter. When a driving voltage is applied to the MZM, the linear Pockels effect of LN produces a phase shift via index variation: n becomes $n + \Delta n$ and β_{eff} becomes $\beta_{eff} + \Delta\beta_{eff}$. Assuming this index change is small, then n^2 can be approximated as $n^2 + 2n\Delta n$.

The perturbed wave equation is thus given by:

$$\nabla_t E_o{}' + \left[(n^2 + 2n\Delta n)k_0^2 - (\beta_{eff}^2 + 2\beta_{eff}\Delta\beta_{eff})\right] E_o{}' = 0 \tag{A.2}$$

Assuming that the perturbed field $E_o' = E_o$, then the two wave equations can be put together and simplified to

$$[2n\Delta n k_0^2 - 2\beta_{eff}\Delta\beta_{eff}]|E_o|\hat{}2 = 0 \tag{A.3}$$

The electro-optic effect happens over the entire transverse domain, meaning Eq. (A.3) must be integrated over the x-z plane:

$$\iint \left[2n\Delta n k_0^2 - 2\beta_{eff}\Delta\beta_{eff}\right]|E_o|^2 dxdz = 0 \tag{A.4}$$

Substituting $\beta_{eff} = k_0 n_{eff}$ and rearranging Eq. (A.4) yields

$$\Delta n_{eff} = \frac{1}{n_{eff}} \frac{\iint n(x,z)\Delta n(x,z)|E_o(x,z)|^2 dxdz}{\iint |E_o(x,z)|^2 dxdz} \tag{A.5}$$

Because the index change from an applied voltage only occurs in the thin-film LN region, the integral in the numerator is zero outside of the LN domain. The refractive index change of LN is well known, as is the change in refractive index from applied voltage:

$$\Delta n_e = -\frac{1}{2} n_e^3 r_{33} E_{RF} \tag{A.6}$$

where n_e is the extraordinary index of LN, r_{33} = 30.8 pm/V is the electro-optic coefficient of LN, and E_{RF} is the applied electric microwave field. Only the extraordinary index is being considered here as the hybrid optical mode in x-cut LN is primarily polarized along the crystal axis of LN and thus would only interact with the extraordinary index. Plugging this index change and a normalization factor of $\frac{V_A}{G}\frac{G}{V_A}$, Eq. (A.5) becomes:

$$\Delta n_{eff} = \frac{n_e^4 r_{33}}{2n_{eff}} \frac{V_A}{G} \frac{G}{V_A} \frac{\iint E_{RF}(x,z)|E_o(x,z)|^2 dxdz}{\iint |E_o(x,z)|^2 dxdz} \tag{A.7}$$

where G is the electrode gap spacing and V_A is the applied voltage to the coplanar electrodes. Letting

$$\Gamma_{mo} = \frac{G}{V_A}\frac{\iint_{LN} E_{RF}(x,z)|E_o(x,z)|^2 dxdz}{\iint |E_o(x,z)|^2 dxdz}, \tag{A.8}$$

the effective index change of the hybrid optical mode is simplified to

$$\Delta n_{eff} = \frac{n_e^4 r_{33}}{2n_{eff}}\frac{V_A}{G}\Gamma_{mo} \tag{A.9}$$

The phase shift accumulated over a propagated distance L from the changing index is $\Delta\phi = 2\pi\Delta n_{eff} L\lambda_0$. To achieve a π phase shift,

$$\pi = \frac{2\pi}{\lambda_0}\frac{n_e^4 r_{33} V_A \Gamma_{mo} L}{2_{neff} G} \tag{A.10}$$

Thus, the half-wave voltage-length product needed to obtain a π phase shift is

$$V_\pi L = \frac{n_{eff}\lambda_0 G}{2n_e^4 r_{33}\Gamma_{mo}} \tag{A.11}$$

where a factor of 1/2 is included to account for push-pull configuration of the MZM arms.

The above derivation had an assumption that only the z-component of the RF mode interacts with the TE polarized hybrid optical mode (only E_x). However, the applied electric field via the coplanar electrodes may not be uniform or polarized entirely in the z direction. If this is the case, then other components of the electro-optic tensor will contribute to the overall index change caused by the applied voltage. In general, the index change due to the linear electro-optic effect (Pockels Effect) is related to the applied electric field via:

$$\Delta n_{ii}^2 = \frac{n_{ij}^3}{2} \sum_{k=1}^{3} r_{ijk} E_k \tag{A.12}$$

where each index corresponds to the x, y, z rectangle coordinates. Thus r_{ijk} is a matrix with 27 elements! However, due to reciprocity, only 18 of these elements are independent. The 18 elements are arranged into a 3x6 matrix by using a contracted index representation. LN is a trigonal group 3m crystal, so its electro-optic coefficient matrix is given by

$$\begin{bmatrix} 0 & -r_{22} & r_{13} \\ 0 & r_{22} & r_{13} \\ 0 & 0 & r_{33} \\ 0 & r_{42} & 0 \\ r_{42} & 0 & 0 \\ -r_{22} & 0 & 0 \end{bmatrix} \tag{A.13}$$

where r_{22} = 3.4 pm/V, r_{13} = 8.6 pm/V, r_{42} = r_{51}= 26 pm/V, and r_{33} = 30.8 pm/V [23].

It was also assumed above that $E_{RF} = E_z$, thus according to Eq. (A.12), only the r_{13} and r_{33} components contribute to the phase shift. Furthermore, it is assumed that only the r_{33} term has an effect due to the optical field being TE polarized, and thus only the extraordinary index is being modulated. If instead a general microwave field with components in each direction is applied, then the total index change due to the applied voltage would be

$$(-\frac{n_5^3}{2} r_{42} + \frac{n_o^3}{2} r_{22}) E_1 - \frac{n_4^3}{2} r_{42} E_2 + \left(-n_o^3 r_{13} - \frac{n_e^3}{2} r_{33}\right) E_3. \tag{A.14}$$

Following a similar derivation for Eq. (A.9), the cross section of the phase shifter must be integrated. This time there are three different microwave field components, meaning there must be three different overlap integrals, and the total effective index variation becomes:

$$\Delta n_{\mathrm{eff}} = \frac{V}{2n_{eff}G}((n_5^4 r_{42} - n_o^4 r_{22})\Gamma_{mo1} + n_4^4 r_{42}\Gamma_{mo2} + (2n_o^4 r_{13} + n_e^4 r_{33})\Gamma_{mo3}) \quad \text{(A.15)}$$

where $\Gamma_{mo,i}$ corresponds to the overlap integral between the i-th component of the RF mode and the TE optical mode. To achieve a $-\pi$ phase shift, the required voltage-length product is then

$$\mathrm{V}_{\pi}L = \frac{n_{eff}\lambda_0 G}{(n_5^4 r_{42} - n_o r_{22})\Gamma_{mo1} + n_4^4 r_{42}\Gamma_{mo2} + (2n_o^4 r_{13} + n_e^4 r_{33})\Gamma_{mo3}} \quad \text{(A.16)}$$

Assuming a ground-signal-ground coplanar electrode configuration on x-cut LN, Γ_{mo1} and Γ_{mo2} are both much less than Γ_{mo3} and can be neglected. Furthermore, if the optical mode is purely a TE mode, then the field is polarized along the extraordinary axis when using x-cut LN and then the modulation occurs along the extraordinary axis (meaning the r_{13} term does not interact). Under these assumptions Eq. (A.16) simplifies to Eq. (A.11).

Appendix B

B.1 Measuring the Modulator Response using an OSA

Consider an EO MZM with an input optical amplitude E_i and optical carrier frequency ω_0 that is split into two equal paths and modulated with a sinusoidal RF modulation of frequency ω_m. Ignoring optical loss, the output modulated optical field after recombination is

$$E_o = \frac{E_i}{2}\exp\,(\mathrm{j}\omega_0 \mathrm{t})[\exp\,(jm_1\cos(\omega_m t) + \exp(jm_2\, cos(\omega_m t)) + j\phi] \tag{B.1}$$

where $m_{1,2}$ are the phase modulation amplitudes in the two MZM arms and ϕ is a constant phase difference between the arms, which can be imposed from either a length difference, an applied DC voltage, or both. For an MZM driven with G-S-G electrodes in a push-pull configuration, $m_1 = -m_2 = m$ and

$$m = \frac{\pi}{2}\frac{V}{V_\pi} \tag{B.2}$$

where V is the applied voltage and V_π is the half-wave voltage of the modulator. Eq. (B.1) can be expanded into the following Fourier series in the frequency domain:

$$E_o = \frac{E_i}{2}\exp(j\omega_0 t)\sum_k (j)^k[J_k(m) + J_k(m)\exp\,(j\phi)]\exp\,(jk\omega_m t) \tag{B.3}$$

where and $J_k(m)$ is the k-th order Bessel function of the first kind. Thus, the output modulated signal results in a carrier signal at ω_0 and an infinite number of sidebands at $\omega_0 + k\omega_m$ with the output optical intensity of

$$I(\omega_0 + k\omega_m) = \frac{1}{2} I_i J_k^2(m)[1 + (-1)^k \cos(\phi)] \tag{B.4}$$

where I_i is the input optical intensity. An OSA can thus be used to measure the carrier signals and generated sidebands from modulation. An example of such spectra are shown in Figure B.1 when a Si/LN MZM operating at 1550 nm is modulated with sinusoidal tones from 1 GHz to 50 GHz in 1 GHz steps (all overlaid in the plot, not at the same time). In the small signal (i.e, $m \ll 1$) only the first order sidebands are generated; thus, to determine the EO modulation response, the carrier peak power to first sideband peak power ratio, $\left(\frac{J_1(m)}{J_0(m)}\right)^2$, is measured as a function of modulation frequency (e.g, 1 GHz to 110 GHz). However, due to the various RF cables, connectors, potential multipliers, and probes used to contact the modulator, each with its own frequency response, the amount of RF power delivered to the chip is not constant at each frequency. To determine the true EO response of the modulator, the amount of RF power delivered to the chip must be calibrated out of the measurements. This becomes even more evident when multiple different in-line components are used to generate the RF driving signals.

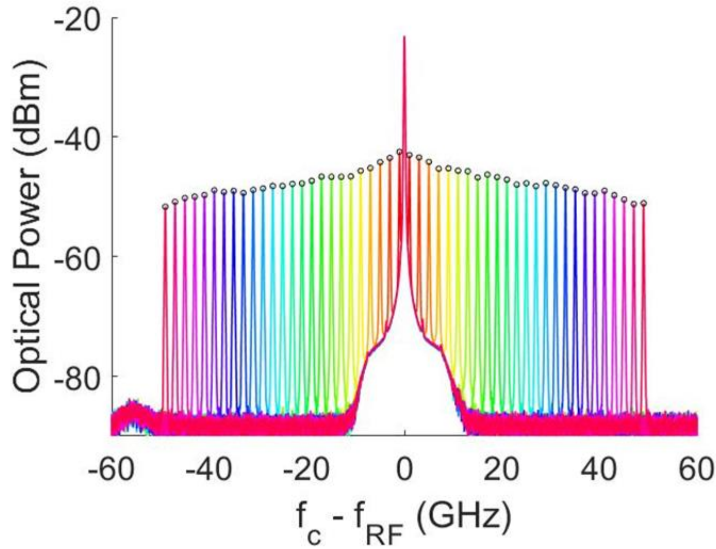

Figure B.1: The measured spectra of a 1550 nm Si/LN MZM being modulated with tones from 1 to 50 GHz in 1 GHz steps (overlaid) using a high-resolution OSA. Modulating at f_{RF} GHz generates first-order sidebands at $\pm f_{RF}$ from the carrier frequency (f_c). Each color pair represents one modulation tone. The black circles are the peak powers at each generated sideband.

As the input RF power increases or, conversely, as the modulator V_π decreases, higher order modulation sidebands will become visible and measurable via an OSA and the small-signal approximation previously made no longer holds. This calls for a modification to the method of measuring the EO response. Figure B.2 shows a measured spectrum from modulating a 1 V V_π SiN/LN MZM operating at 784 nm at 100 GHz using active RF multipliers, showing the carrier, first, and second order sidebands. Comparing Figure B.2 and Figure B.1 it is clearly seen that the linewidths are limited by the OSA resolution (limited for λ not in the C-band), but the peak powers are clearly distinguishable from the carrier peak and are well above the noise floor. From this measurement, the first-sideband to carrier ratio (FSCR), $I(\omega_0 \pm \omega_m)/I_i$, and the second-sideband to carrier ratio (SSCR), $I(\omega_0 \pm 2\omega_m)/I_i$, can be calculated and the unknown parameters m and $\cos(\phi)$ can be inferred using the following equations:

$$FSCR = \left(\frac{J_1(m)}{J_0(m)}\right)^2 \frac{1-\cos(\phi)}{1+\cos(\phi)} \tag{B.5}$$

$$SSCR = \left(\frac{J_2(m)}{J_0(m)}\right)^2 \tag{B.6}$$

Once m is determined at each modulation frequency, Eq. (B.2) can be used to solve for $V_\pi(f)$:

$$20\log_{10}(m(f)) = 20\log_{10}\frac{\pi}{2} + 20\log_{10}V(f) - 20\log_{10}V_\pi(f). \tag{B.7}$$

Furthermore from Eq. (5.1),

$$EOR(f) = 20\log_{10}V_\pi(DC) - 20\log_{10}V_\pi(f) \tag{B.8}$$

and Eq. (B.7) can be used to write

$$EOR(f) = 20\log_{10}V_\pi(DC) - 20\log_{10}\frac{\pi}{2} + 20\log_{10}m(f) - 20\log_{10}V(f). \tag{B.9}$$

The EOR curve is referenced to its value at a low frequency and thus, the frequency-independent terms on the first line of Eq. (B.9) can be dropped when calculating how EOR rolls off with f. Two terms remain, the first of which, $20\log_{10}m(f)$, is found from the optical spectrum as described above. The second term, $20\log_{10}V$, is linearly proportional to the RF power delivered to the MZM, labeled $P_{chip}(f)$, which, as explained above, is dependent on the input cables and components used to send the RF signal to the modulator and must be independently measured to determine EOR(f).

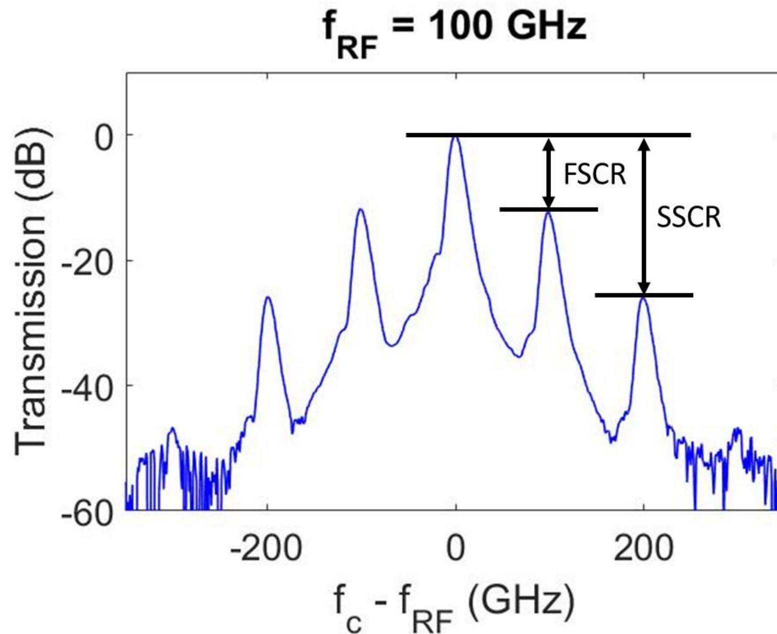

Figure B.2: An example of the measured spectrum using an low resolution OSA (Ando AQ6317B) showing the first sideband o carrier ratio (FSCR) and second-sideband to carrier ratio (SSCR) which were generated by modulating a SiN/LN MZM at 100 GHz.

B.2 Measuring the Modulator Response using a Sampling Oscilloscope

As stated previously, the spectral domain method of measuring an EOM's frequency response is only valid if the generated sideband peak values can be distinguished from the carrier signal peak. However, this may not always be the case if the OSA has a limited wavelength resolution. As the operation wavelength shortens, the corresponding bandwidth also changes. For example, a 20 GHz tone at 1310 nm results in a sideband peak that is 0.114 nm from the carrier, while at 784 nm it is only 0.041 nm from the carrier. This becomes an issue when measuring O-band and visible regime modulators as the modulator response at shorter frequencies ($f < 10$ GHz for O-band and $f < 20$ GHz for NIR, see Chapter 5) is not measurable with the OSA available at the time. To acquire the modulator response for such instances, a time domain method can be

used as shown in Figure B.3. An optical amplifier is used after the chip for the NIR MZM to raise the modulated waveform out of the noise floor on the oscilloscope.

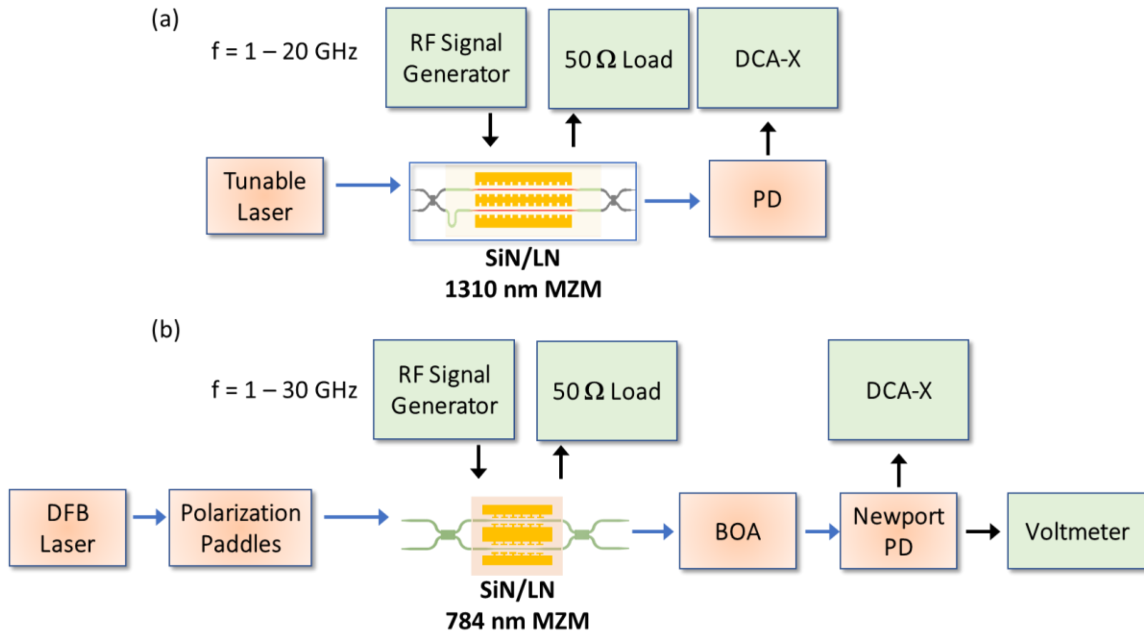

Figure B.3: Time domain method block diagrams for measuring the frequency response of (a) MZMs operating in the O-band and (b) MZMs operating in the NIR. PD: Photodetector, DFB: Distributed Feedback Laser, BOA: Optical Amplifier.

The time domain method requires a high-speed photodetector and sampling oscilloscope (Keysight DCA-X), from which the modulated signals from 1 GHz to 20-30 GHz (depending on the operation wavelength) can thus be analyzed. The visible photodetector (Newport 1474-A) has a DC output monitor that can be connected to a voltmeter (Keithley 2450 Sourcemeter) to verify the optical power measured. The change in the peak-to-peak voltage measured on the oscilloscope as the modulation frequency changes then corresponds to the change in the EO response. Figure B.4 shows the captured sinusoidal modulated optical waveforms using the high-speed detector and oscilloscope at 1 GHz, 10 GHz, 20 GHz, and 30 GHz. Similarly to the spectral domain method described in Appendix B.1, this method also requires the frequency

response of all RF components (cables, connectors and in this case photodetectors) to be calibrated out to accurately determine the device's EO response.

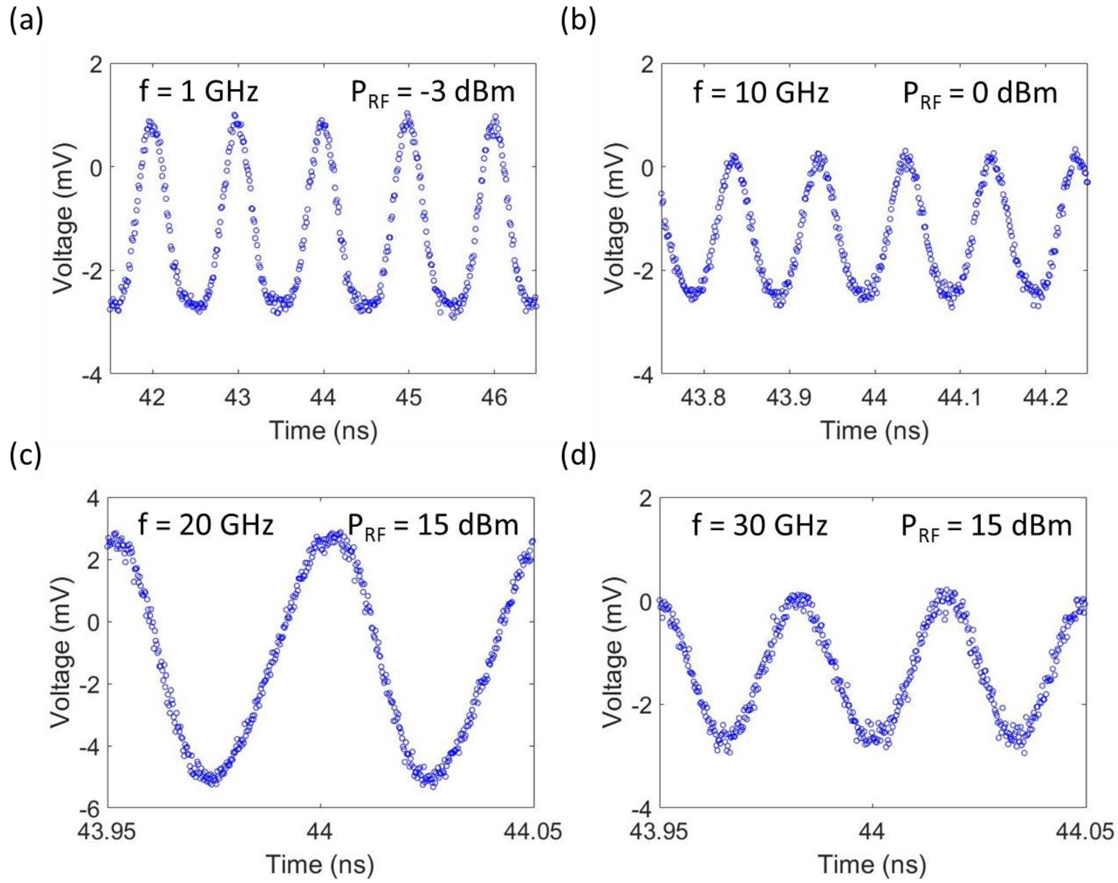

Figure B.4: The modulated optical waveforms measured with a high-speed photodetector and sampling oscilloscope when driven with sinusoidal tones at the following frequencies: (a) 1 GHz, (b) 10 GHz, (c) 20 GHz, and (d) 30 GHz.

B.3 RF Power Calibrations

High-speed RF measurements of EO modulators require multiple connections from the frequency source to the chip, and from the chip to the load or RF power sensor. Depending on the frequency and RF power being applied, different combinations of cables or connections should be used as each component has its own frequency response. To accurately determine the EO response of the hybrid modulators under test, the RF power delivered to the chip as a

function of modulation frequency $P_{chip}(f)$ must be measured and calibrated out, otherwise the EO response will include the response of all RF components in the setup.

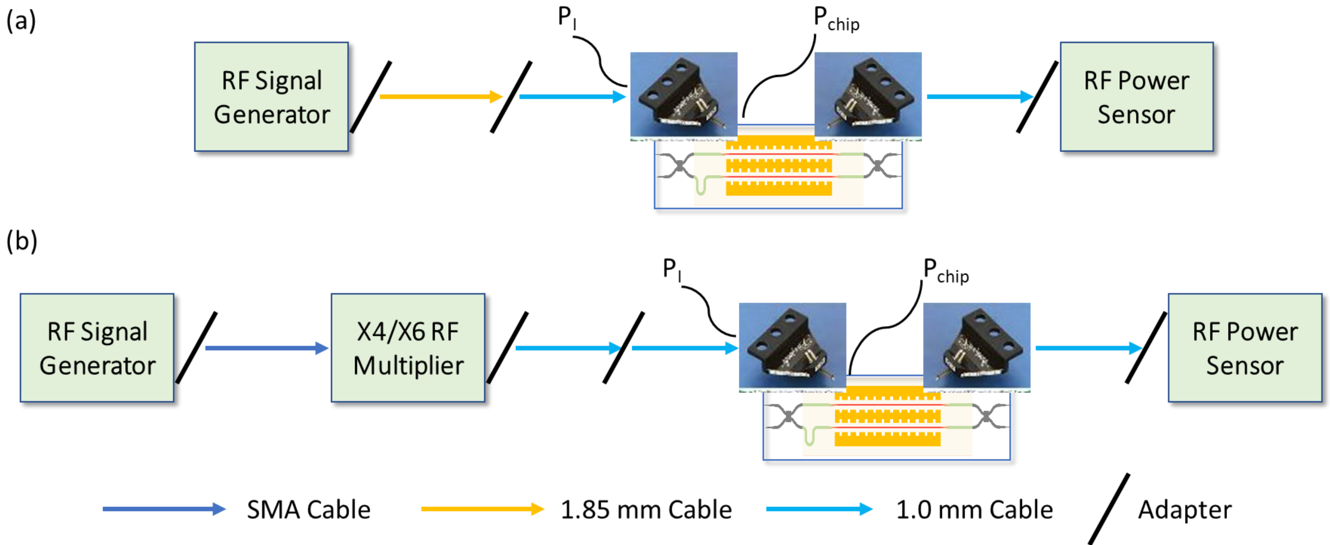

Figure B.5: The RF connection setups for high-speed frequency measurements of EO modulators in the (a) 1 – 50 GHz range and (b) 47 – 111 GHz range using 110 GHz rated G-S-G RF probes with 1.0 mm connectors (Picoprobe 110H). P_I (input RF power) is defined as the RF power before the input-side probe and P_{chip} (power to the chip) is defined as the input RF power including the loss of the probe.

Figure B.5(a) and Figure B.5(b) are schematics of the modulator response measurements for frequencies 1 - 50 GHz, 47 – 72 GHz, and 72 – 111 GHz respectively, showing the RF cables and connectors used for the input and output sides of the device. The RF source used in the EO response measurements has a frequency limit of 50 GHz. To reach frequencies greater than 50 GHz, active RF multipliers are used. These multipliers (Erevant SFA-503753420-15SF-E1 and SFA-753114616-10SF-E1) are banded from 47 – 72 GHz and 72 – 111 GHz, respectively due to the metal waveguide outputs. Figure B.6(a) and Figure B.6(b) show the RF power output from the X4 and X6 multipliers, respectively, as a function of frequency and RF input power. The multipliers have the most stable output when the RF input power is 0 to 3 dBm; however, they also have a fixed gain of about 20 dB. To not overdrive the modulators under test, two 1.0 mm

RF cables (rather than just one) are placed in between the multipliers and the chip to provide additional attenuation.

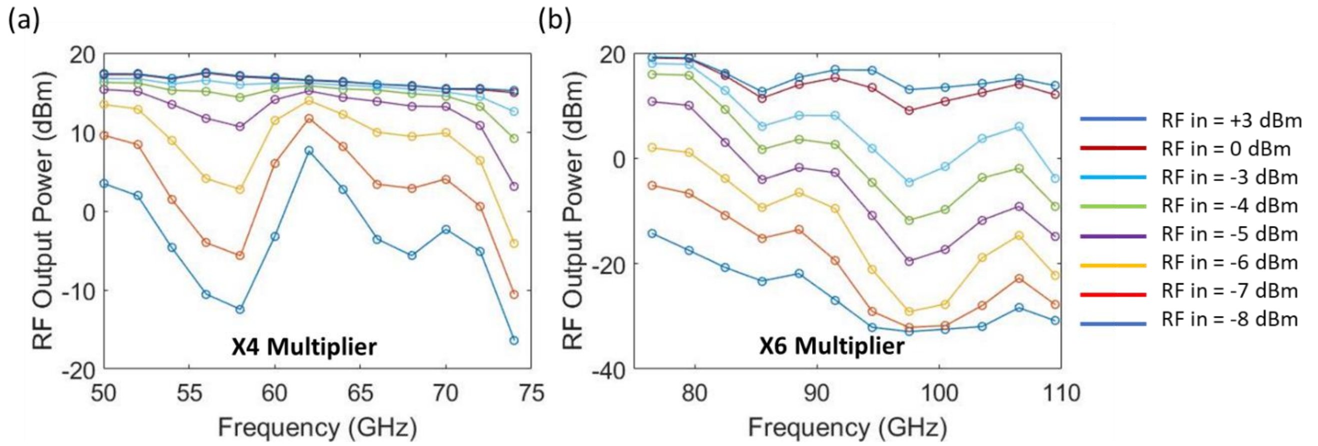

Figure B.6: The measured RF power output from the (a) X4 and (b) X6 active RF multipliers as a function of their respective frequency ranges at various input RF powers. When the RF input power is greater than 0 dBm the output is more stable with frequency.

As RF probes will be contacting the device G-S-G pads throughout each measurement, the same probes must be used for each frequency range. RF cables and components rated to 110 GHz have a standardized 1.0 mm connection, whereas RF cables and components rated to 67 GHz typically have a standardized 1.85 mm connection; thus, adapters are required to connect cables and components of varied size. An RF power sensor (Rhode & Schwarz NRP110T) was used to measure the RF power through the input sections, P_I of the three measurement schemes in Figure B.5. The amount of RF power to the chip would then be

$$P_{chip}(f) = P_I(f) - P_{probe}(f) \tag{B.10}$$

where $P_{probe}(f)$ is the frequency response of the input-side probe (Picoprobe 110H), which was provided by the manufacturer (GGB Industries, Inc.). Examples of $P_{chip}(f)$ for the four measurement configurations in Figure B.5 are shown in Figure B.7 for input RF powers (PRF)

used in the EO response measurements. This calibration data can then be subtracted out from the measured spectra or oscilloscope data from Appendix B.1 and B.2 to obtain the true EO response as a function of frequency for the hybrid bonded MZMs under test.

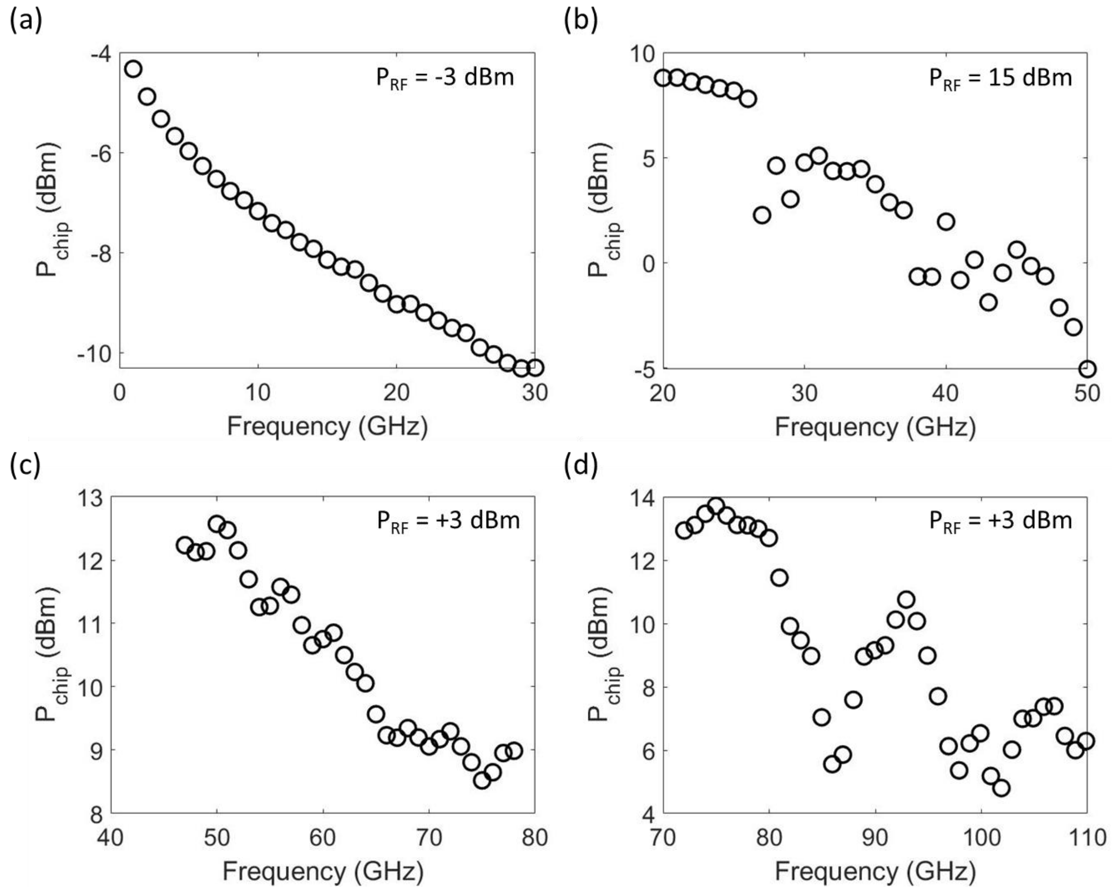

Figure B.7: The RF power delivered to the chip under test (P_{chip}) as a function of frequency for the four different measurement configurations in (a) Figure B.5(a) with an RF input power setting of -3 dBm, (b) Figure B.5(a) with an RF input power setting of 15 dBm, (c) Figure B.5(c) with an RF input power setting of 3 dBm, and (d) Figure B.5(d) with an RF input power setting of 3 dBm. Panel (a) includes the frequency dependence of the 35 GHz photodetector (Newport 1474-A) used in the oscilloscope measurement setup.

B.4 Acknowledgments

Appendix B, in part, is a reprint of the material that appears in arxiv 2022 and has been submitted for publication of the material as it may appear in Optica. Forrest Valdez, Viphretuo

Mere, and Shayan Mookherjea, “100 GHz, 1 V Near-infrared Electro-optic Mach-Zehnder Modulator” arXiv:2211.13348 2022. The dissertation author, together with his advisor and colleague, led the research efforts for this work and co-authored the paper.

Bibliography

1. C. H. Cox, E. I. Ackerman, G. E. Betts, and J. L. Prince, "Limits on the performance of RF-over-fiber links and their impact on device design," IEEE Trans. Microw. Theory Tech. **54**(2), 906–920 (2006).

2. J. S. Fandino, P. Muñoz, D. Doménech, and J. Capmany, "A monolithic integrated photonic microwave filter," Nat. Photonics **11**(December 2016), (2017).

3. S. Jia, X. Pang, O. Ozolins, X. Yu, H. Hu, J. Yu, P. Guan, F. Da Ros, S. Popov, G. Jacobsen, M. Galili, T. Morioka, D. Zibar, and L. K. Oxenlowe, "0.4 THz Photonic-Wireless Link with 106 Gb/s Single Channel Bitrate," J. Light. Technol. **36**(2), 610–616 (2018).

4. I. A. Walmsley, "Quantum optics: Science and technology in a new light," Science (80-.). **348**(6234), 525–530 (2015).

5. J. G. Ren, P. Xu, H. L. Yong, L. Zhang, S. K. Liao, J. Yin, W. Y. Liu, W. Q. Cai, M. Yang, L. Li, K. X. Yang, X. Han, Y. Q. Yao, J. Li, H. Y. Wu, S. Wan, L. Liu, D. Q. Liu, Y. W. Kuang, Z. P. He, P. Shang, C. Guo, R. H. Zheng, K. Tian, Z. C. Zhu, N. Le Liu, C. Y. Lu, R. Shu, Y. A. Chen, C. Z. Peng, J. Y. Wang, and J. W. Pan, "Ground-to-satellite quantum teleportation," Nature **549**(7670), 70–73 (2017).

6. B. Brecht, D. V. Reddy, C. Silberhorn, and M. G. Raymer, "Photon temporal modes: A complete framework for quantum information science," Phys. Rev. X **5**(4), 1–17 (2015).

7. J. Nunn, L. J. Wright, C. Söller, L. Zhang, I. A. Walmsley, and B. J. Smith, "Large-alphabet time-frequency entangled quantum key distribution by means of time-to-frequency conversion," Opt. Express **21**(13), 15959 (2013).

8. T. M. Zhao, H. Zhang, J. Yang, Z. R. Sang, X. Jiang, X. H. Bao, and J. W. Pan, "Entangling different-color photons via time-resolved measurement and active feed forward," Phys. Rev. Lett. **112**(10), 1–5 (2014).

9. ITU-T, "Spectral grids for WDM applications: DWDM frequency grid," **G.694.1**, (2020).

10. R. A. Soref and B. R. Bennett, "Electro-optical effects in ferroelectrics," IEEE J. Quantum Electron. **23**(1), 123–129 (1987).

11. M. R. Watts, W. A. Zortman, D. C. Trotter, R. W. Young, and A. L. Lentine, "Low-Voltage, Compact, Depletion-Mode, Silicon Mach-Zehnder Modulator," IEEE J. Sel. Top. Quantum Electron. **16**(1), 159–164 (2010).

12. P. Dong, L. Chen, and Y. Chen, "High-speed low-voltage single-drive push-pull silicon Mach-Zehnder modulators," Opt. Express **20**(6), 6163–6169 (2012).

13. C. T. DeRose, D. C. Trotter, W. A. Zortman, and M. R. Watts, "High speed travelling

wave carrier depletion silicon Mach-Zehnder modulator," in *2012 Optical Interconnects Conference* (IEEE, 2012), pp. 135–136.

14. X. Xiao, H. Xu, X. Li, Z. Li, T. Chu, Y. Yu, and J. Yu, "High-speed, low-loss silicon Mach–Zehnder modulators with doping optimization," Opt. Express **21**(4), 4116–4125 (2013).

15. M. Li, L. Wang, X. Li, X. Xiao, and S. Yu, "Silicon intensity Mach–Zehnder modulator for single lane 100 Gb/s applications," Photonics Res. **6**(2), 109 (2018).

16. H. Xu, X. Li, X. Xiao, P. Zhou, Z. Li, J. Yu, and Y. Yu, "High-speed silicon modulator with band equalization," Opt. Lett. **39**(16), 4839 (2014).

17. X. Tu, T.-Y. Liow, J. Song, M. Yu, and G. Q. Lo, "Fabrication of low loss and high speed silicon optical modulator using doping compensation method," Opt. Express **19**(19), 18029 (2011).

18. M. J. Shaw, J. Guo, G. A. Vawter, S. Habermehl, and C. T. Sullivan, "Fabrication techniques for low-loss silicon nitride waveguides," Micromach. Technol. Micro-Optics Nano-Optics III **5720**(January 2005), 109 (2005).

19. A. Z. Subramanian, P. Neutens, A. Dhakal, R. Jansen, T. Claes, X. Rottenberg, F. Peyskens, S. Selvaraja, P. Helin, B. Dubois, K. Leyssens, S. Severi, P. Deshpande, R. Baets, and P. Van Dorpe, "Low-Loss Singlemode PECVD silicon nitride photonic wire waveguides for 532-900 nm wavelength window fabricated within a CMOS pilot line," IEEE Photonics J. **5**(6), (2013).

20. N. Boynton, H. Cai, M. Gehl, S. Arterburn, C. Dallo, A. Pomerene, A. Starbuck, D. Hood, D. C. Trotter, T. Friedmann, C. T. DeRose, and A. Lentine, "A heterogeneously integrated silicon photonic/lithium niobate travelling wave electro-optic modulator," Opt. Express **28**(2), 1868 (2020).

21. A. N. R. Ahmed, S. Nelan, S. Shi, P. Yao, A. Mercante, and D. W. Prather, "Subvolt electro-optical modulator on thin-film lithium niobate and silicon nitride hybrid platform," Opt. Lett. **45**(5), 1112 (2020).

22. K. Alexander, J. P. George, J. Verbist, K. Neyts, D. Van Thourhout, J. Beeckman, and B. Kuyken, "Nanophotonic Pockels modulators on a silicon nitride platform," (2018), 4–9 (n.d.).

23. A. Yariv, *Optical Electronics in Modern Communications* (1997).

24. R. C. Alferness and L. L. Buhl, "Waveguide electro-optic polarization transformer," Appl. Phys. Lett. **38**(9), 655–657 (1981).

25. R. O. D. C. Alferness, "Waveguide Electrooptic Modulators," IEEE Trans. Microw. Theory Tech. **MTT-30**(8), 1121–1137 (1982).

26. S. Thaniyavarn, "Wavelength-independent, optical-damage-immune LiNbO_3 TE–TM mode converter," Opt. Lett. **11**(1), 39 (1986).

27. F. Auracher and R. Keil, "Method for measuring the rf modulation characteristics of Mach-Zehnder-type modulators," Appl. Phys. Lett. **36**(8), 626–629 (1980).

28. F. J. Leonberger, "High-speed operation of LiNbO_3 electro-optic interferometric waveguide modulators," Opt. Lett. **5**(7), 312 (1980).

29. K. Noguchi, O. Mitomi, H. Miyazawa, and S. Seki, "A Broadband Ti:LiNbO3 Optical Modulator with a Ridge Structure," J. Light. Technol. **13**(6), 1164–1168 (1995).

30. K. Noguchi, O. Mitomi, and H. Miyazawa, "Millimeter-wave Ti:LiNbO 3 optical modulators," J. Light. Technol. **16**(4), 615–619 (1998).

31. J. B. Lasky, "Wafer bonding for silicon-on-insulator technologies," Appl. Phys. Lett. **48**(1), 78–80 (1986).

32. M. Shimbo, K. Furukawa, K. Fukuda, and K. Tanzawa, "Silicon-to-silicon direct bonding method," J. Appl. Phys. **60**(8), 2987–2989 (1986).

33. R. Stengl, T. Tan, and U. Gösele, "A model for the silicon wafer bonding process," Jpn. J. Appl. Phys. **28**(10 R), 1735–1741 (1989).

34. P. Rabiei and P. Gunter, "Optical and electro-optical properties of submicrometer lithium niobate slab waveguides prepared by crystal ion slicing and wafer bonding," Appl. Phys. Lett. **85**(20), 4603–4605 (2004).

35. G. Poberaj, M. Koechlin, F. Sulser, A. Guarino, J. Hajfler, and P. Günter, "Ion-sliced lithium niobate thin films for active photonic devices," Opt. Mater. (Amst). **31**(7), 1054–1058 (2009).

36. C. Wang, M. Zhang, X. Chen, M. Bertrand, A. Shams-Ansari, S. Chandrasekhar, P. Winzer, and M. Lončar, "Integrated lithium niobate electro-optic modulators operating at CMOS-compatible voltages," Nature **562**(7725), 101–104 (2018).

37. J. Zhao, M. Rüsing, U. A. Javid, J. Ling, M. Li, Q. Lin, and S. Mookherjea, "Shallow-etched thin-film lithium niobate waveguides for highly-efficient second-harmonic generation," Opt. Express **28**(13), 19669 (2020).

38. C. Wang, M. Zhang, B. Stern, M. Lipson, and M. Lončar, "Nanophotonic lithium niobate electro-optic modulators," Opt. Express **26**(2), 1547 (2018).

39. M. He, M. Xu, Y. Ren, J. Jian, Z. Ruan, Y. Xu, S. Gao, S. Sun, X. Wen, L. Zhou, L. Liu, C. Guo, H. Chen, S. Yu, L. Liu, and X. Cai, "High-performance hybrid silicon and lithium niobate Mach–Zehnder modulators for 100 Gbit s -1 and beyond," Nat. Photonics **13**(5), 359–364 (2019).

40. X. Liu, B. Xiong, C. Sun, J. Wang, Z. Hao, L. Wang, Y. Han, H. Li, J. Yu, and Y. Luo, "Wideband thin-film lithium niobate modulator with low half-wave-voltage length product," Chinese Opt. Lett. **19**(6), 060016 (2021).

41. F. Yang, X. Fang, X. Chen, L. Zhu, F. Zhang, Z. Chen, and Y. Li, "Monolithic thin film lithium niobate electro-optic modulator with over 110 GHz bandwidth," Chinese Opt. Lett. **20**(2), 2–6 (2022).

42. G. Chen, K. Chen, R. Gan, Z. Ruan, Z. Wang, P. Huang, C. Lu, A. P. T. Lau, D. Dai, C. Guo, and L. Liu, "High performance thin-film lithium niobate modulator on a silicon substrate using periodic capacitively loaded traveling-wave electrode," APL Photonics **7**(2), 026103 (2022).

43. S. Jin, L. Xu, H. Zhang, and Y. Li, "LiNbO 3 Thin-Film Modulators Using Silicon," IEEE Photonics Technol. Lett. **28**(7), 736–739 (2016).

44. L. Cao, A. Aboketaf, Z. Wang, and S. Preble, "Hybrid amorphous silicon (a-Si:H)-LiNbO3 electro-optic modulator," Opt. Commun. **330**, 40–44 (2014).

45. A. Rao, A. Patil, J. Chiles, M. Malinowski, S. Novak, K. Richardson, P. Rabiei, and S. Fathpour, "Heterogeneous microring and Mach-Zehnder modulators based on lithium niobate and chalcogenide glasses on silicon," Opt. Express **23**(17), 22746 (2015).

46. P. Rabiei, J. Ma, S. Khan, J. Chiles, and S. Fathpour, "Heterogeneous lithium niobate photonics on silicon substrates," Opt. Express **21**(21), 25573 (2013).

47. J. Van Campenhout, W. M. J. Green, S. Assefa, Y. A. Vlasov, X. Liu, and R. M. Osgood, "Silicon-nitride surface passivation of sub-micron silicon waveguides for low-power optical switches," Opt. InfoBase Conf. Pap. **34**(10), 1534–1536 (2009).

48. P. O. Weigel, M. Savanier, C. T. Derose, A. T. Pomerene, A. L. Starbuck, A. L. Lentine, V. Stenger, and S. Mookherjea, "Lightwave Circuits in Lithium Niobate through Hybrid Waveguides with Silicon Photonics," Sci. Rep. **6**(November 2015), 1–9 (2016).

49. L. Chang, M. H. P. Pfeiffer, N. Volet, M. Zervas, J. D. Peters, C. L. Manganelli, E. J. Stanton, Y. Li, T. J. Kippenberg, and J. E. Bowers, "Heterogeneous integration of lithium niobate and silicon nitride waveguides for wafer-scale photonic integrated circuits on silicon," Opt. Lett. **42**(4), 803 (2017).

50. P. O. Weigel, J. Zhao, K. Fang, H. Al-Rubaye, D. Trotter, D. Hood, J. Mudrick, C. Dallo, A. T. Pomerene, A. L. Starbuck, C. T. DeRose, A. L. Lentine, G. Rebeiz, and S. Mookherjea, "Bonded thin film lithium niobate modulator on a silicon photonics platform exceeding 100 GHz 3-dB electrical modulation bandwidth," Opt. Express **26**(18), 23728 (2018).

51. V. Mere, F. Valdez, X. Wang, and S. Mookherjea, "A modular fabrication process for thin-film lithium niobate modulators with silicon photonics," JPhys Photonics **4**(2), (2022).

52. M. Churaev, A. Riedhauser, R. N. Wang, C. Möhl, T. Bkésin, M. A. Anderson, V. Snigirev, A. Siddharth, Y. Popoff, U. Drechsler, D. Caimi, S. Hönl, J. Riemensberger, J. Liu, P. Seidler, and T. J. Kippenberg, "Heterogeneously integrated lithium niobate photonics," 2022 Conf. Lasers Electro-Optics, CLEO 2022 - Proc. **1**(c), 2022–2023 (2022).

53. G. Ghione, *Semiconductor Devices for High-Speed Optoelectronics* (2009).

54. E. Chen and S. Y. Chou, "Characteristics of coplanar transmission lines on multilayer substrates: modeling and experiments," IEEE Trans. Microw. Theory Tech. **45**(6), 939–945 (1997).

55. H. Yu and W. Bogaerts, "An equivalent circuit model of the traveling wave electrode for carrier-depletion-based silicon optical modulators," J. Light. Technol. **30**(11), 1602–1609 (2012).

56. E. Ackerman, G. Betts, W. Burns, J. Prince, M. Regan, H. Roussell, and C. Cox, "Low noise figure, wide bandwidth analog optical link," Int. Top. Meet. Microw. Photonics, MWP 2005 **2005**, 325–328 (2005).

57. C. Cox, "Techniques and performance of intensity-modulation direct-detection analog optical links," IEEE Trans. Microw. Theory Tech. **45**(8 PART 2), 1375–1383 (1997).

58. A. S. Alam, M. Girardi, A. Caut, A. Larsson, M. Galili, Y. Ding, and K. Yvind, "LiNbO 3 / Si 3 N 4 -Bilayer Vertical Coupler for Integrated Photonics," in *Conference on Lasers and Electro-Optics* (2020), pp. 1–2.

59. J. Wang, Y. Xuan, C. Lee, B. Niu, L. Liu, G. N. Liu, and M. Qi, "Low-loss and misalignment-tolerant fiber-to-chip edge coupler based on double-tip inverse tapers," 2016 Opt. Fiber Commun. Conf. Exhib. OFC 2016 19–21 (2016).

60. L. Jia, C. Li, T.-Y. Liow, and G.-Q. Lo, "Efficient Suspended Coupler With Loss Less Than -1.4 dB Between Si-Photonic Waveguide and Cleaved Single Mode Fiber," J. Light. Technol. **36**(2), 239–244 (2018).

61. X. Wang, X. Quan, M. Liu, and X. Cheng, "Silicon-nitride-assisted edge coupler interfacing with high numerical aperture fiber," IEEE Photonics Technol. Lett. **31**(5), 349–352 (2019).

62. X. Mu, S. Wu, L. Cheng, and H. Y. Fu, "Edge couplers in silicon photonic integrated circuits: A review," Appl. Sci. **10**(4), (2020).

63. M. J. Picard, Y. Painchaud, C. Latrasse, C. Larouche, F. Pelletier, and M. Poulin, "Novel spot-size converter for optical fiber to sub-μm silicon waveguide coupling with low loss, low wavelength dependence and high tolerance to alignment," Eur. Conf. Opt. Commun. ECOC 1–3 (2015).

64. R. S. Tummidi and M. Webster, "Multilayer Silicon Nitride-based Coupler Integrated into

a Silicon Photonics Platform with < 1 dB Coupling Loss to a Standard SMF over O , S , C and L optical bands," in *2020 Optical Fiber Communications Conference and Exhibition (OFC)* (2020), pp. 1–3.

65. J. R. Ong, T. Y. L. Ang, G. Alagappan, C. H. Son, S. T. Lim, and C. E. Png, "Silicon nitride double-tip fiber-to-waveguide edge couplers at visible wavelengths," in *Conference on Lasers and Electro-Optics Pacific Rim* (2017), p. s1840.

66. Z. Lin and W. Shi, "Broadband , low-loss silicon photonic Y-junction with an arbitrary power splitting ratio," **27**(10), 14338–14343 (2019).

67. N. S. Lagali, "The Generalized Mach-Zehnder Interferorneter using Multimode Interference Couplers for Optical Communications Networks," (2000).

68. L. B. Soldano and E. C. M. Pennings, "Optical Multi-Mode Interference Devices Based on Self-Imaging: Principles and Applications," J. Light. Technol. **13**(4), 615–627 (1995).

69. E. C. M. Pennings, R. Van Roijen, M. J. N. Van Stralen, P. J. de Waard, R. G. M. P. Koumans, and B. H. Verbeek, "Reflection Properties of Multimode Interference Devices," IEEE Photonics Technol. Lett. **6**(6), 715–718 (1994).

70. J. Zhang, L. Han, B. P.-P. Kuo, and S. Radic, "Broadband Angled Arbitrary Ratio SOI MMI Couplers With Enhanced Fabrication Tolerance," J. Light. Technol. **38**(20), 5748–5755 (2020).

71. A. Rahim, T. Spuesens, R. Baets, and W. Bogaerts, "Open-Access Silicon Photonics : Current Status and Emerging Initiatives," **106**(12), (2018).

72. G. P. Barwood, P. Gill, and W. R. C. Rowley, "Frequency measurements on optically narrowed Rb-stabilised laser diodes at 780 nm and 795 nm," Appl. Phys. B Photophysics Laser Chem. **53**(3), 142–147 (1991).

73. C. Lee, C. Shen, H. M. Oubei, M. Cantore, B. Janjua, T. K. Ng, R. M. Farrell, M. M. El-Desouki, J. S. Speck, S. Nakamura, B. S. Ooi, and S. P. DenBaars, "2 Gbit/s data transmission from an unfiltered laser-based phosphor-converted white lighting communication system," Opt. Express **23**(23), 29779 (2015).

74. F. Zafar, M. Bakaul, and R. Parthiban, "Laser-Diode-Based Visible Light Communication: Toward Gigabit Class Communication," IEEE Commun. Mag. **55**(2), 144–151 (2017).

75. M. G. Allen, "Diode laser absorption sensors for gas-dynamic and combustion flows," Meas. Sci. Technol. **9**(4), 545–562 (1998).

76. D. Yoo, K. L. Gurunatha, H. K. Choi, D. A. Mohr, C. T. Ertsgaard, R. Gordon, and S. H. Oh, "Low-Power Optical Trapping of Nanoparticles and Proteins with Resonant Coaxial Nanoaperture Using 10 nm Gap," Nano Lett. **18**(6), 3637–3642 (2018).

77. J. A. Holguin-Lerma, M. Kong, O. Alkhazragi, X. Sun, T. Khee Ng, and B. S. Ooi, "480-nm distributed-feedback InGaN laser diode for 10.5-Gbit/s visible-light communication," Opt. Lett. **45**(3), 742 (2020).

78. C. Lee, C. Shen, C. Cozzan, R. M. Farrell, J. S. Speck, S. Nakamura, B. S. Ooi, and S. P. DenBaars, "Gigabit-per-second white light-based visible light communication using near-ultraviolet laser diode and red-, green-, and blue-emitting phosphors," Opt. Express **25**(15), 17480 (2017).

79. B. Janjua, H. M. Oubei, J. R. D. Retamal, T. K. Ng, C.-T. Tsai, H.-Y. Wang, Y.-C. Chi, H.-C. Kuo, G.-R. Lin, J.-H. He, and B. S. Ooi, "Going beyond 4 Gbps data rate by employing RGB laser diodes for visible light communication," Opt. Express **23**(14), 18746 (2015).

80. A. Honardoost, R. Safian, A. Rao, and S. Fathpour, "High-speed modeling of ultracompact electrooptic modulators," J. Light. Technol. **36**(24), 5893–5902 (2018).

81. E. P. Sinulinnga, "Modelling and Characterisations of Wideband Coplanar Waveguide MMIC Components for Nano-scale Device Applications," (2014).

82. R. G. Geyer and J. Krupka, "Microwave Dielectric Properties of Anisotropic Materials at Cryogenic Temperatures," IEEE Trans. Instrum. Meas. **44**(2), 329–331 (1995).

83. T. P. McKenna, J. D. Witmer, R. N. Patel, W. Jiang, R. Van Laer, P. Arrangoiz-Arriola, E. A. Wollack, J. F. Herrmann, and A. H. Safavi-Naeini, "Cryogenic microwave-to-optical conversion using a triply resonant lithium-niobate-on-sapphire transducer," Optica **7**(12), 1737 (2020).

84. G. Ghione, "A CAD-Oriented Analytical Model for the Losses of General Asymmetric Coplanar Lines in Hybrid and Monolithic MICs," IEEE Trans. Microw. Theory Tech. **41**(9), 1499–1510 (1993).

85. N. A. F. Jaeger and Z. K. F. Lee, "Slow-Wave Electrode for Use in Compound Semiconductor Electrooptic Modulators," IEEE J. Quantum Electron. **28**(8), 1778–1784 (1992).

86. R. Spickermann and N. Dagli, "Millimetre Wave Coplanar Slow Wave Structure on GaAs Suitable for use in Electro-Optic Modulators," Electron. Lett. **29**(9), 774–775 (1993).

87. S. R. Sakamoto, R. Spickermann, and N. Dagli, "Narrow gap coplanar slow wave electrode for travelling wave electro-optic modulators," Electron. Lett. **31**(14), 1183–1185 (1995).

88. J. Shin, S. R. Sakamoto, and N. Dagli, "Conductor loss of capacitively loaded slow wave electrodes for high-speed photonic devices," J. Light. Technol. **29**(1), 48–52 (2011).

89. Á. Rosa, S. Verstuyft, A. Brimont, D. Van Thourhout, and P. Sanchis, "Microwave index engineering for slow-wave coplanar waveguides," Sci. Rep. **8**(1), 1–8 (2018).

90. P. Kharel, C. Reimer, K. Luke, L. He, and M. Zhang, "Breaking voltage-bandwidth limits in integrated lithium niobate modulators using micro-structured electrodes," 1–7 (2020).

91. Z. Wang, G. Chen, Z. Ruan, R. Gan, P. Huang, Z. Zheng, L. Lu, J. Li, C. Guo, K. Chen, and L. Liu, "Silicon-Lithium Niobate Hybrid Intensity and Coherent Modulators Using a Periodic Capacitively Loaded Traveling-Wave Electrode," ACS Photonics **9**(8), 2668–2675 (2022).

92. D. M. Pozar, *Microwave Engineering* (John wiley\& sons, 2011).

93. D. A. Bryan, R. Gerson, and H. E. Tomaschke, "Increased optical damage resistance in lithium niobate," Appl. Phys. Lett. **44**(9), 847–849 (1984).

94. V. Mere, F. Valdez, and S. Mookherjea, "Improved fabrication of scalable hybrid silicon nitride – thin-film lithium niobate electro-optic modulators," J. Opt. Soc. Am. B **40**(5), 5–14 (2023).

95. "Physical layer specifications and management parameters for 40 gb/s and 100 gp/s operation over fiber optic cables," IEEE Stand. Ethernet (n.d.).

96. V. Stenger, J. Toney, A. Pollick, J. Busch, J. Scholl, P. Pontius, and S. Sriram, "Engineered thin film lithium niobate substrate for high gain-bandwidth electro-optic modulators," 2013 Conf. Lasers Electro-Optics, CLEO 2013 5–6 (2013).

97. S. Sun, M. He, S. Yu, and X. Cai, "Hybrid Silicon and Lithium Niobate Mach-Zehnder Modulators with High Bandwidth Operating at C-Band and O-Band," Conf. Proc. - Lasers Electro-Optics Soc. Annu. Meet. **2020-May**(MMI), 4–5 (2020).

98. M. Piels and J. E. Bowers, *Photodetectors for Silicon Photonic Integrated Circuits* (Elsevier Ltd, 2016).

99. A. W. Fang, H. Park, O. Cohen, R. Jones, M. J. Paniccia, and J. E. Bowers, "Electrically pumped hybrid AlGaInAs-silicon evanescent laser," Opt. Express **14**(20), 336–340 (2006).

100. G. Duan, S. Member, C. Jany, A. Le Liepvre, A. Accard, M. Lamponi, D. Make, P. Kaspar, G. Levaufre, N. Girard, J. Fedeli, A. Descos, B. Ben Bakir, S. Messaoudene, D. Bordel, S. Menezo, G. De Valicourt, S. Keyvaninia, G. Roelkens, D. Van Thourhout, D. J. Thomson, F. Y. Gardes, and G. T. Reed, "Hybrid III – V on Silicon Lasers for Photonic Integrated Circuits on Silicon," IEEE J. Sel. Top. Quantum Electron. **20**(4), (2014).

101. X. Luo, Y. Cao, J. Song, X. Hu, Y. Cheng, C. Li, C. Liu, T. Y. Liow, M. Yu, H. Wang, Q. J. Wang, and P. G. Q. Lo, "High-throughput multiple dies-to-wafer bonding technology and III/V-on-Si hybrid lasers for heterogeneous integration of optoelectronic integrated circuits," Front. Mater. **2**(April), 1–21 (2015).

102. D. Shin, J. Cha, S. Kim, Y. Shin, K. Cho, K. Ha, G. Jeong, H. Hong, K. Lee, and H.-K. Kang, "O-band DFB laser heterogeneously integrated on a bulk-silicon platform," Opt.

Express **26**(11), 14768 (2018).

103. K. Li, Z. Liu, M. Tang, M. Liao, D. Kim, H. Deng, A. M. Sanchez, R. Beanland, M. Martin, T. Baron, S. Chen, J. Wu, A. Seeds, and H. Liu, "O-band InAs/GaAs quantum dot laser monolithically integrated on exact (0 0 1) Si substrate," J. Cryst. Growth **511**(January), 56–60 (2019).

104. D. Colucci, M. Baryshnikova, Y. Shi, Y. Mols, M. Muneeb, Y. De Koninck, D. Yudistira, M. Pantouvaki, J. Van Campenhout, R. Langer, D. Van Thourhout, and B. Kunert, "Unique design approach to realize an O-band laser monolithically integrated on 300 mm Si substrate by nano-ridge engineering," Opt. Express **30**(8), 13510 (2022).

105. P. Wen, P. Tiwari, S. Mauthe, H. Schmid, M. Sousa, M. Scherrer, M. Baumann, B. I. Bitachon, J. Leuthold, B. Gotsmann, and K. E. Moselund, "Waveguide coupled III-V photodiodes monolithically integrated on Si," Nat. Commun. **13**(1), (2022).

106. N. Sambo, V. Curri, G. Shen, M. Cantono, J. Pedro, and E. Pincemin, "Guest Editorial: Multi-Band Optical Networks," J. Light. Technol. **40**(11), 3360–3363 (2022).

107. G. Di Rosa, R. Emmerich, M. Sena, J. K. Fischer, C. Schubert, R. Freund, and A. Richter, "Characterization, Monitoring, and Mitigation of the I/Q Imbalance in Standard C-Band Transceivers in Multi-Band Systems," J. Light. Technol. **40**(11), 3470–3478 (2022).

108. R. Emmerich, M. Sena, R. Elschner, C. Schmidt-Langhorst, I. Sackey, C. Schubert, and R. Freund, "Enabling S-C-L-band systems with standard C-band modulator and coherent receiver using nonlinear predistortion," Opt. InfoBase Conf. Pap. **40**(5), 1360–1368 (2022).

109. X. Liu, B. Xiong, C. Sun, Z. Hao, L. Wang, J. Wang, Y. Han, H. Li, and Y. Luo, "Capacitively-loaded Thin-film Lithium Niobate Modulator with Ultra-flat Frequency Response," IEEE Photonics Technol. Lett. **34**(16), 1–1 (2022).

110. X. Wang, F. Valdez, V. Mere, and S. Mookherjea, "Integrated thin-silicon passive components for hybrid silicon-lithium niobate photonics," Opt. Contin. **1**(10), 2233–2244 (2022).

111. G. K. Gopalakrishnan, R. W. McElhanon, W. K. Burns, C. H. Bulmer, and A. S. Greenblatt, "Performance and Modeling of Broadband LiNb03 Traveling Wave Optical Intensity Modulators," J. Light. Technol. **12**(10), 1807–1819 (1994).

112. M. M. Howerton and W. Burns, *Broadband Traveling Wave Modulators in LiNb03* (Cambridge University Press, 2002).

113. X. Huang, Y. Liu, Z. Li, Z. Fan, and W. Han, "High-performance and compact integrated photonics platform based on silicon rich nitride-lithium niobate on insulator," AIP Adv. **6**(11), (2021).

114. X. Wang, F. Valdez, V. Mere, and S. Mookherjea, "Monolithic Integration of 110 GHz

Thin-film Lithium Niobate Modulator and High-Q Silicon Microring Resonator for Photon-Pair Generation," in *CLEO: QELS Fundamental Science* (2022), pp. JTh6B--9.

115. S. Nelan, A. Mercante, S. Shi, P. Yao, E. Shahid, B. Shopp, and D. W. Prather, "Integrated lithium niobate intensity modulator on a silicon handle with slow-wave electrodes," IEEE Photonics Technol. Lett. **PP**, 1 (2022).

116. S. Alam, E. Berikaa, and D. V Plant, "Net 350 Gbps / λ IMDD Transmission Enabled by High Bandwidth Thin-Film Lithium Niobate MZM," IEEE Photonics Technol. Lett. **PP**, 1 (2022).

117. X. Wang, P. O. Weigel, J. Zhao, M. Ruesing, and S. Mookherjea, "Achieving beyond-100-GHz large-signal modulation bandwidth in hybrid silicon photonics Mach Zehnder modulators using thin film lithium niobate," APL Photonics **4**(9), (2019).

118. M. Xu, Y. Zhu, F. Pitalla, J. Tang, M. He, W. C. Ng, J. Wang, Z. Ruan, X. Tang, M. Kuschnerov, L. Liu, S. Yu, B. Zheng, and X. Cai, "Dual-polarization thin-film lithium niobate in-phase quadrature modulators for terabit-per-second transmission," Optica **9**(1), 61–62 (2022).

119. R. C. Williamson and R. D. Esman, "RF photonics," J. Light. Technol. **26**(9), 1145–1153 (2008).

120. A. Shams-Ansari, D. Renaud, R. Cheng, L. Shao, L. He, D. Zhu, M. Yu, H. R. Grant, L. Johansson, M. Zhang, and M. Loncar, "Electrically pumped high power laser transmitter integrated on thin-film lithium niobate," Optica **9**(4), 408–411 (2022).

121. H. K. Tsang, C. S. Wong, T. K. Liang, I. E. Day, S. W. Roberts, A. Harpin, J. Drake, and M. Asghari, "Optical dispersion, two-photon absorption and self-phase modulation in silicon waveguides at 1.5μm wavelength," Appl. Phys. Lett. **80**(3), 416–418 (2002).

122. Q. Lin, O. J. Painter, and G. P. Agrawal, "Nonlinear optical phenomena in silicon waveguides: modeling and applications," Opt. Express **15**(25), 16604 (2007).

123. A. D. Bristow, N. Rotenberg, and H. M. Van Driel, "Two-photon absorption and Kerr coefficients of silicon for 850-2200 nm," Appl. Phys. Lett. **90**(19), (2007).

124. J. Leuthold, C. Koos, and W. Freude, "Nonlinear silicon photonics," Nat. Photonics **4**(8), 535–544 (2010).

125. T. Kuwayama, M. Ichimura, and E. Arai, "Interface recombination velocity of silicon-on-insulator wafers measured by microwave reflectance photoconductivity decay method with electric field," Appl. Phys. Lett. **83**(5), 928–930 (2003).

126. J. Witzens, "High-Speed Silicon Photonics Modulators," Proc. IEEE **106**(12), 2158–2182 (2018).

127. R. Claps, V. Raghunathan, D. Dimitropoulos, and B. Jalali, "Influence of nonlinear

absorption on Raman amplification in Silicon waveguides," Opt. Express **12**(12), 2774 (2004).

128. Y. Fu, T. Ye, W. Tang, and T. Chu, "Efficient adiabatic silicon-on-insulator waveguide taper," Photonics Res. **2**(3), A41 (2014).

129. J.-P. Ruske, B. Zeitner, A. Tunnerman, and A. S. Rasch, "Photorefractive effect and high power transmission in LiNbO3 channel waveguides," Electron. Lett. **39**(14), 1 (2003).

130. H. Jiang, R. Luo, H. Liang, X. Chen, Y. Chen, and Q. Lin, "Fast response of photorefraction in lithium niobate microresonators," Opt. Lett. **42**(17), 3267 (2017).

131. G. E. Betts and J. Cartledge, "Broadband and optical modulators: science, technology, and applications," CRC Press (Ch 4), 93–126 (2011).

132. Y. Shi, L. Yan, and A. E. Willner, "High-Speed Electrooptic Modulator Characterization Using Optical Spectrum Analysis," J. Light. Technol. **21**(10), 2358–2367 (2003).

133. M. Li, L. Wang, X. Li, X. Xiao, and S. Yu, "Silicon intensity Mach–Zehnder modulator for single lane 100 Gb/s applications," Photonics Res. **6**(2), 109 (2018).

134. R. Wu, L. Gao, Y. Liang, Y. Zheng, J. Zhou, H. Qi, D. Yin, M. Wang, Z. Fang, and Y. Cheng, "High-production-rate fabrication of low-loss lithium niobate electro-optic modulators using photolithography assisted chemo-mechanical etching (PLACE)," Micromachines **13**(3), 378 (2022).

135. S. Singer, P. Trocha, H. Zwickel, C. Kieninger, J. Kemal, M. Kaschel, C. Menzel, S. Randel, W. Freude, and C. Koos, "Nonlinear Loss and Damage Threshold in Silicon Photonic Waveguides : Modelling and Experimental Verification," **2**(4), 4–5 (2022).

136. F. Nagano, S. Iacovo, A. Phommahaxay, F. Inoue, F. Chancerel, H. Naser, G. Beyer, E. Beyne, and S. De Gendt, "Void Formation Mechanism Related to Particles During Wafer-to-Wafer Direct Bonding," ECS J. Solid State Sci. Technol. **11**, 063012 (2022).

137. J. P. J. Heemskerk and K. A. S. Immink, "The CD System as Standardized by Philips and Sony," (January 2009), 53–136 (2009).

138. M. J. Hackert, S. M. Sibley, and P. Sendelbach, "Performance of Telecommunication-Grade Multimode Fiber at 780 nm," J. Light. Technol. **10**(6), 712–719 (1992).

139. D. Giggenbach, J. Horwath, and M. Knapek, "Optical data downlinks from Earth observation platforms," Free. Laser Commun. Technol. XXI **7199**(February 2009), 719903 (2009).

140. R. R. Anderson and J. A. Parrish, "Selective photothermolysis: precise microsurgery by selective absorption of pulsed radiation," Science (80-.). **220**(4596), 524–527 (1983).

141. S. H. Yun and S. J. J. Kwok, "Light in diagnosis, therapy and surgery," Nat. Biomed. Eng.

1(1), (2017).

142. V. M. Schäfer, C. J. Ballance, K. Thirumalai, L. J. Stephenson, T. G. Ballance, A. M. Steane, and D. M. Lucas, "Fast quantum logic gates with trapped-ion qubits," Nature **555**(7694), 75–78 (2018).

143. P.-J. Stas, Y. Q. Huan, B. Machielse, E. N. Knall, A. Suleymanzade, B. Pingault, M. Sutula, S. W. Ding, C. M. Knaut, D. R. Assumpcao, Y.-C. Wei, M. K. Bhaskar, R. Riedinger, D. D. Sukachev, H. Park, M. Loncar, D. S. Levonian, and M. D. Lukin, "Robust multi-qubit quantum network node with integrated error detection," Science (80-.). **378**(6619), 557–560 (2022).

144. D. M. Kuchta, *High Capacity VCSEL-Based Links* (2017), (March).

145. C. M. Gee, G. D. Thurmond, and H. W. Yen, "17-GHz bandwidth electro-optic modulator," Appl. Phys. Lett. **43**(11), 998–1000 (1983).

146. M. Thomaschewski and S. I. Bozhevolnyi, "Pockels modulation in integrated nanophotonics," Appl. Phys. Rev. **9**(2), (2022).

147. J. A. Dionne, K. Diest, L. A. Sweatlock, and H. A. Atwater, "PlasMOStor: A metal-oxide-si field effect plasmonic modulator," Nano Lett. **9**(2), 897–902 (2009).

148. N. Youngblood, Y. Anugrah, R. Ma, S. J. Koester, and M. Li, "Multifunctional graphene optical modulator and photodetector integrated on silicon waveguides," Nano Lett. **14**(5), 2741–2746 (2014).

149. Y. Gao, R. J. Shiue, X. Gan, L. Li, C. Peng, I. Meric, L. Wang, A. Szep, D. Walker, J. Hone, and D. Englund, "High-speed electro-optic modulator integrated with graphene-boron nitride heterostructure and photonic crystal nanocavity," Nano Lett. **15**(3), 2001–2005 (2015).

150. X. Liu, K. Zang, J. H. Kang, J. Park, J. S. Harris, P. G. Kik, and M. L. Brongersma, "Epsilon-Near-Zero Si Slot-Waveguide Modulator," ACS Photonics **5**(11), 4484–4490 (2018).

151. M. Thomaschewski, V. A. Zenin, S. Fiedler, C. Wolff, and S. I. Bozhevolnyi, "Plasmonic Lithium Niobate Mach-Zehnder Modulators," Nano Lett. **22**(16), 6471–6475 (2022).

152. C. Haffner, D. Chelladurai, Y. Fedoryshyn, A. Josten, B. Baeuerle, W. Heni, T. Watanabe, T. Cui, B. Cheng, S. Saha, D. L. Elder, L. R. Dalton, A. Boltasseva, V. M. Shalaev, N. Kinsey, and J. Leuthold, "Low-loss plasmon-assisted electro-optic modulator," Nature **556**(7702), 483–486 (2018).

153. C. T. Phare, Y. H. Daniel Lee, J. Cardenas, and M. Lipson, "Graphene electro-optic modulator with 30 GHz bandwidth," Nat. Photonics **9**(8), 511–514 (2015).

154. O. T. Celik, C. J. Sarabalis, F. M. Mayor, H. S. Stokowski, J. F. Herrmann, T. P.

McKenna, N. R. A. Lee, W. Jiang, K. K. S. Multani, and A. H. Safavi-Naeini, "High-bandwidth CMOS-voltage-level electro-optic modulation of 780 nm light in thin-film lithium niobate," Opt. Express **30**(13), 23177 (2022).

155. C. Li, B. Chen, Z. Ruan, H. Wu, Y. Zhou, J. Liu, P. Chen, K. Chen, C. Guo, and L. Liu, "High modulation efficiency and large bandwidth thin-film lithium niobate modulator for visible light," Opt. Express **30**(20), 36394 (2022).

156. D. Renaud, D. R. Assumpcao, G. Joe, A. Shams-Ansari, D. Zhu, Y. Hu, N. Sinclair, and M. Loncar, "Sub-1 Volt and High-Bandwidth Visible to Near-Infrared Electro-Optic Modulators," (2022).

157. C. E. Rogers and P. L. Gould, "Nanosecond pulse shaping at 780 nm with fiber-based electro-optical modulators and a double-pass tapered amplifier," Opt. Express **24**(3), 2596 (2016).

158. M. Lee, H. E. Katz, C. Erben, D. M. Gill, P. Gopalan, J. D. Heber, and D. J. McGee, "Broadband modulation of light by using an electro-optic polymer," Science (80-.). **298**(5597), 1401–1403 (2002).

159. C. Kieninger, Y. Kutuvantavida, D. L. Elder, S. Wolf, H. Zwickel, M. Blaicher, J. N. Kemal, M. Lauermann, S. Randel, W. Freude, L. R. Dalton, and C. Koos, "Ultra-high electro-optic activity demonstrated in a silicon-organic hybrid modulator," Optica **5**(6), 739 (2018).

160. Y. Ogiso, J. Ozaki, Y. Ueda, N. Kashio, N. Kikuchi, E. Yamada, H. Tanobe, S. Kanazawa, H. Yamazaki, Y. Ohiso, T. Fujii, and M. Kohtoku, "Over 67 GHz Bandwidth and 1.5 v Vπ InP-Based Optical IQ Modulator with n-i-p-n Heterostructure," J. Light. Technol. **35**(8), 1450–1455 (2017).

161. H. Yamazaki, M. Nagatani, H. Wakita, Y. Ogiso, M. Nakamura, M. Ida, H. Nosaka, T. Hashimoto, and Y. Miyamoto, "IMDD Transmission at net data rate of 333 Gb/s using over-100-GHz-bandwidth analog multiplexer and Mach-zehnder modulator," J. Light. Technol. **37**(8), 1772–1778 (2019).

162. O. Ozolins, X. Pang, M. I. Olmedo, A. Kakkar, A. Udalcovs, S. Gaiarin, J. R. Navarro, K. M. Engenhardt, T. Asyngier, R. Schatz, J. Li, F. Nordwall, U. Westergren, D. Zibar, S. Popov, and G. Jacobsen, "100 GHz Externally Modulated Laser for Optical Interconnects," J. Light. Technol. **35**(6), 1174–1179 (2017).

163. T. Hiraki, T. Aihara, Y. Maeda, T. Fujii, T. Tsuchizawa, K. Takahata, T. Kakitsuka, and S. Matsuo, "50-GHz-Bandwidth Membrane InGaAsP Electro-Absorption Modulator on Si Platform," J. Light. Technol. **39**(16), 5300–5306 (2021).

164. S. Lange, M. Gruner, C. Meuer, R. Kaiser, M. Hamacher, K. O. Velthaus, and M. Schell, "Low Switching Voltage Mach-Zehnder Modulator Monolithically Integrated with DFB Laser for Data Transmission up to 107.4 Gb/s," J. Light. Technol. **34**(2), 401–406 (2016).

165. K. Prosyk, A. Ait-Ouali, C. Bornholdt, T. Brast, M. Gruner, M. Hamacher, D. Hoffmann, R. Kaiser, R. Millett, K. O. Velthaus, and I. Woods, "High performance 40GHz InP mach-zehnder modulator," Opt. InfoBase Conf. Pap. 50–52 (2012).

166. R. G. Walker, N. I. Cameron, Y. Zhou, and S. J. Clements, "Optimized gallium arsenide modulators for advanced modulation formats," IEEE J. Sel. Top. Quantum Electron. **19**(6), (2013).

167. R. G. Walker, "High-Speed Electrooptic Modulation in GaAs/ GaAlAs Waveguide Devices," J. Light. Technol. **5**(10), 1444–1453 (1987).

168. F. Valdez, V. Mere, X. Wang, N. Boynton, T. A. Friedmann, S. Arterburn, C. Dallo, A. T. Pomerene, A. L. Starbuck, D. C. Trotter, A. L. Lentine, and S. Mookherjea, "110 GHz, 110 mW Hybrid Silicon-Lithium Niobate Mach-Zehnder Modulator," Sci. Rep. **12**(1), 18611 (2022).

169. F. Valdez, V. Mere, X. Wang, and S. Mookherjea, "Integrated O- and C-band Silicon-Lithium Niobate Mach-Zehnder Modulators with 100 GHz Bandwidth, Low Voltage, and Low Loss," Opt. Express **31**(4), 5273–5289 (2023).

170. J. P. Salvestrini, L. Guilbert, M. Fontana, M. Abarkan, and S. Gille, "Analysis and control of the dc drift in LiNbO3-based Mach-Zehnder modulators," J. Light. Technol. **29**(10), 1522–1534 (2011).

171. S. Yamada and M. Minakata, "DC drift phenomena in LiNbO3 optical waveguide devices," Jpn. J. Appl. Phys. **20**(4), 733–737 (1981).

172. C. M. Gee, G. D. Thurmond, H. Blauvelt, and H. W. Yen, "Minimizing dc drift in LiNbO3 waveguide devices," Appl. Phys. Lett. **47**(3), 211–213 (1985).

173. N. Nagata, "Long-term DC drift in x-cut Lil\lbO3 modulators without oxide buffer layer," IEE Proc. Optoelectron. **147**(5), 350–354 (2000).

174. C. Ma, X. Wang, V. Anant, A. D. Beyer, M. D. Shaw, and S. Mookherjea, "Silicon photonic entangled photon-pair and heralded single photon generation with CAR > 12,000 and g^(2)(0) < 0006," Opt. Express **25**(26), 32995 (2017).

175. M. A. Popovic, T. Barwicz, M. R. Watts, P. T. Rakich, L. Socci, E. P. Ippen, M. A. Popovic, F. X. Kärtner, and H. I. Smith, "Multistage high-order microring resonator add-drop filters," Opt. Lett. **31**(17), 2571–2573 (2006).

176. J. R. Ong, R. Kumar, and S. Mookherjea, "Ultra-High-Contrast and Tunable-Bandwidth Filter Using Cascaded High-Order Silicon Microring Filters," Photonics Technol. Lett. IEEE **25**(16), 1543–1546 (2013).

177. K. Xu, J. Y. Sung, C. Y. Wong, Z. Cheng, C. W. Chow, and H. K. Tsang, "Optical Nyquist filters based on silicon coupled resonator optical waveguides," Opt. Commun. **329**, 23–27 (2014).

178. C. L. Manganelli, P. Pintus, F. Gambini, D. Fowler, M. Fournier, S. Faralli, C. Kopp, and C. J. Oton, "Large-FSR Thermally Tunable Double-Ring Filters for WDM Applications in Silicon Photonics," IEEE Photonics J. **9**(1), 1–10 (2017).

179. C. Ma, X. Wang, and S. Mookherjea, "Progress towards a widely usable integrated silicon photonic photon-pair source," OSA Contin. **3**(6), 1398 (2020).

180. B. Szelag, K. Hassan, L. Adelmini, E. Ghegin, P. Rodriguez, F. Nemouchi, P. Brianceau, E. Vermande, A. Schembri, D. Carrara, P. Cavalié, F. Franchin, M. C. Roure, L. Sanchez, C. Jany, and S. Olivier, "Hybrid III-V/Silicon Technology for Laser Integration on a 200-mm Fully CMOS-Compatible Silicon Photonics Platform," IEEE J. Sel. Top. Quantum Electron. **25**(5), (2019).

181. J. M. Ramirez, H. Elfaiki, T. Verolet, C. Besancon, A. Gallet, D. Néel, K. Hassan, S. Olivier, C. Jany, S. Malhouitre, K. Gradkowski, P. E. Morrissey, P. O'Brien, C. Caillaud, N. Vaissière, J. Decobert, S. Lei, R. Enright, A. Shen, and M. Achouche, "III-V-on-Silicon Integration: From Hybrid Devices to Heterogeneous Photonic Integrated Circuits," IEEE J. Sel. Top. Quantum Electron. **26**(2), 1–13 (2020).

182. S. Yanikgonul, V. Leong, J. R. Ong, T. Hu, S. Y. Siew, C. E. Png, and L. Krivitsky, "Integrated avalanche photodetectors for visible light," Nat. Commun. **12**(1), 1–8 (2021).